High resolution solutions for the multipath problem in radar

"HIGH RESOLUTION SOLUTIONS FOR THE MULTIPATH PROBLEM IN RADAR"

by

ALI TAHA, Bsc., Msc.

A DOCTORAL THESIS

Submitted in Partial Fulfilment of the Requirements for the Award of Degree of Doctor of Philosophy of the Loughborough University of Technology

1987

Supervisor: J.E. Hudson
Department of Electronic and Electrical Engineering
Loughborough University of Technology, U.K.

TO MY PARENTS

WIFE

AND CHILDREN

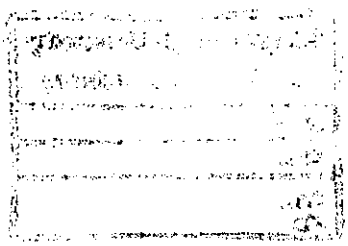

Abstract

The problem of tracking radar targets in the low-angle region where conventional monopulse radars face difficulties due to the presence of multipath waves is considered in this thesis. The emphasis of the presentation is mainly directed towards finding a new simple closed-form solution to the coherent multipath problem over a smooth surface. Another concern is to improve the performance of the three-subapertures maximum-likelihood estimator when the two received signals are in-phase or anti-phase at the centre of the array.

The multipath phenomenon and its modelling for smooth and rough surfaces are discussed and simulation results obtained for different surfaces, subsequently the following are treated:

First, a new four-subapertures technique to improve the in-phase and anti-phase performance of the maximum likelihood estimator above is derived and simulation results are shown. Then, an improved version of this technique is introduced as a part of the new algorithm.

Second, a new three-subapertures trigonometric solution to solve the coherent multipath problem is derived and demonstrated by simulation results. This new method is simpler than the maximum likelihood estimator above and very similar in its estimation accuracy.

Third, the performance of the maximum entropy method is tested for the coherent multipath problem by using the

three-subapertures arrangement of a linear array. Finally the performances of the above three methods and the normal phase monopulse radar are tested and compared for different surfaces when the coherent and noncoherent multipath exist together. Simulation results show that the performances of the maximum entropy method and phase monopulse are much better than the others when the target is low-flying over a rough surface.

AKNOWLEDGEMENT

The author is deeply indebted to his suppervisor, Dr. J.E. Hudson, for his continuous support and encouragement, without which this work could not have been completed.

The author also wishes to thank the people and the Government of the Syrian Arab Republic for the generous financial support.

The patience of my wife Ibtisam and my duaghter Jamila will never be forgotten.

LIST OF SYMBOLS

SW.2	Swerling case 2 for the type of echo signal (fluctuating amplitude)
SW.5	Swerling case 5 for the type of echo signal (nonfluctuating amplitude)
$P(\theta)$	estimated power in the angular direction θ
Q	covariance matrix
$S(\theta)$	steering vector
R_o^h	the reflection coefficient for the horizontal linear polarization from a smooth surface.
R_o^v	the reflection coefficient for the vertical linear polarization from a smooth surface.
γ	the grazing angle
γc	the critical grazing angle
λ	the wave length
σ	the conductivity of the medium in mho/m
D	divergence factor
R	the distance between the radar and the target
G	the ground range
d	interelement (or entersubaperture) spacing
dc	correlation distance
$R^{h,v}$	reflection coefficient for both linear polarizations from a curved earth.
εc	complex dielectric constant of the medium
$\varepsilon 1$	relative dielectric constant
εo	free space dielectric constant

r_1	the slant range between the receiving antenna and the reflection point on the surface.
r_2	the slant range between the target and the reflection point on the surface.
a,b	the radii of curvature
3SA-MLE	three-subapertures maximum likelihood estimator
4SA-MLE	four-subapertures maximum likelihood technique
3SA-TRM	three-subapertures trigonometric solution method
4SA-TRM	four-subapertures trigonometric solution technique
3&4SA-TRM	mutual 3&4 subaperture trigonometric solution tech.
3SA-MEM	three-subapertures maximum entropy method
$\phi^{h,v}$	the phase associated with the reflection coefficient (horizontal and vertical polarization)
h_r	radar height
h_t	target height
h	surface height difference
δ_o	the approximate path difference between the direct and indirect ways at the receiving point.
Ψ	the phase difference between the two signals at the array's centre.
Ψ_1	the phase associated with the direct signal at the array's centre.
Ψ_2	the phase associated with the reflected signal at the array's centre.
Ψ_{to}	the phase of the direct signal at ref. point
Ψ_{ro}	the phase of the reflected signal at ref. point
Ψ_{t1}	the phase of the direct signal at point 1
Ψ_{r1}	the phase of the reflected signal at point 1
$\Delta\Psi$	the change in Ψ

E	the total received field strength.
E_o	direct field strength ($\|a_1\|$)
δ	path difference between the direct wave and reflected one.
Rcs	reflection coefficient for same sense circular polarization.
Rco	reflection coefficient for opposite sense circular polarization.
Φc	circular polarization phase
σ_h^2	rms deviation of the surface heights
σ_w^2	wight noise variance
σ	noise variance in genral
Rs	specular reflection component from a rough surface
Rd	diffuse reflection component from a rough surface
ρ_s	specular scattering coefficient from a rough surface.
ρ_d	diffuse scattering coefficient from a rough surface.
β_o	rms surface slopes
Gt	transmitting antenna gain
Gr	receiving antenna gain
γ_1	grazing angle associated with path r_1
γ_2	grazing angle associated with path r_2
σ^o	bistatic scattering coefficient from γ_1 and γ_2
Pc	clutter reflected power
Pt	transmitted power
Pr	received power from the direct path
θ_t	target elevation angle
θ_r	image elevation angle

θ_B	the bisecting angle of the two sources
θ_D	the angular distance from the bisector angle
X_o	specular reflection point
X_1	projection of r_1 on the ground
X_2	projection of r_2 on the ground
ds	diffused power contributing area
Y	the y axis value of the glistening surface boundry
X_a	the x axis start point of the integration
X_b	the x axis end point of the integration
Fd	roughness factor
Fd_1, Fd_2	roughness factor at local grazing angle γ_1 and γ_2 respectively.
ρ_{s1}	specular reflection associated with γ_1 over rough surface.
ρ_{s2}	specular reflection associated with γ_2 over rough surface.
Δx	integration step length on the x axis
$\Delta\rho_{di}$	patch value of the diffused power from a surface
a_1, a_2	complex amplitudes of the direct signal and its coherent multipath.
a_{1r}, a_{1j}	the real and imaginary parts of a_1
a_{2r}, a_{2j}	the real and imaginary parts of a_2
G_1, G_2	subaperture gains in the direction of the target and its image.
s_m	the output of the m-th subaperture
m,k,M,i,j	integers
K	the relative strength of the two received signals
$w_{k,i}$	the coeffecients represent the phase progression along the array for each angle of arrival.

CM,m	the m-th parameter of the all-pole filter
P_M	the output power of the all-pole filter
S/N	signal-to-noise ratio calculated for the direct signal only as received by the main beam of the array.

Contents

Chapter -1

Chapter -2

Surface Reflection - a survey

Chapter -3

The Maximum Likelihood Estimator

Chapter -4

The Trigonometric High Resolution Method

Chapter -5

The Maximum Entropy Method and Monopulse Radar

Chapter -6

Effect of Surface Roughness on Elevation Angle Estimation in Multipath

Chapter -7

Conclusions and Recommendations for Further Work

Chapter 1

Introduction

This thesis addresses the tracking problem of a low-flying target over different types of surfaces. The main effort is directed toward finding a new simple method to estimate the angle of arrival of the target in the presence of a strong specular multipath component. Additionally, the associated problem with in-phase and anti-phase signals is investigated.

In this chapter we will introduce the reader to the low-flying target tracking problem, review the previous research, and give an outline of the thesis with a summary of the contributions.

1-1 The tracking problem of a low-flying target

The classical form of tracking radar is related to a system which follows the path of a single target and measures its position in a given coordinate system. Usually, the same system provides information about the speed of the target which can be used to estimate its future position.

Various single target tracking methods have been developed and used in the past few decades. These methods are mainly based on either simultaneous or sequential lobing

techniques which require a minimum number of echo pulses to extract the required error signals to drive the servo-control system toward the target's position. These methods are very sensitive to fluctuations in the amplitude of the received signal (pulse to pulse amplitude fluctuations). Thus, a new system which depends on the basis of one pulse to extract the required error signals was found. This monopulse system is basically of two types, an amplitude-comparison monopulse and phase-comparison monopulse (studied in chapter 6). Detailed analysis of this system can be found in many reference books [1-1,2,3]. It is shown that the monopulse system provide an optimum tracking performance as long as just one target is presented within the main lobe of the antenna's pattern. The problem arises when two (or more) signals caused by closely spaced targets (or by a low-flying target with multipath) fall within the main-beam pattern where the tracking system starts to behave erratically in the vertical plane and frequently loses track. One obvious solution to this problem is to increase the resolving power of the antenna by increasing the frequency or the dimensions of the radar antenna. This solution is not always possible practically because of physical and environment limitations.

The main reason for the erratic performance of the tracking radar in following the path of a low-flying target can be related to the following three factors [1-4]:

a- specular multipath reflection component

b- diffuse multipath reflection component

c- energy or clutter reflected on the sea surface from the same range cell as the target.

The contribution of each term above depends on the state of the sea (or the under-lying surface in general) as will be shown next chapter. Figure 1-1 shows the behaviour of a tracking radar in following a low-flying target with constant amplitude and decreasing elevation angle. It can be seen from the first zone (zone A) that when the elevation angle is high and the beam is well above the surface, the tracking accuracy is the optimum obtainable from the system (as, when one target exists). For a smaller elevation angle, where some reflected energy starts to enter through the side lobes, the antenna shows weak oscillation around a mean value (Zone B). After that the oscillation increases rapidly due to the increase in the strength of the reflected signal (mainly specular multipath) making the radar lose track altogether. Figure 1-2 shows the equilibrium positions for a curved earth with a specular reflection coeffecient less than one. It can be seen that the equilibrium positions about the true target are continuous while it breaks up into series of loops about the image. When the reflection coefficient is one (over a smooth, flat surface) then the radar will track the target or its image by jumping from one to the other occasionally. Many classical solutions have been suggested to solve this problem as will be shown in the next section.

1-2 Classic solutions of the multipath problem

In theory, there are many solutions for overcoming the multipath problem in a tracking radar but most of them are not practical, like the increase of the operating frequency

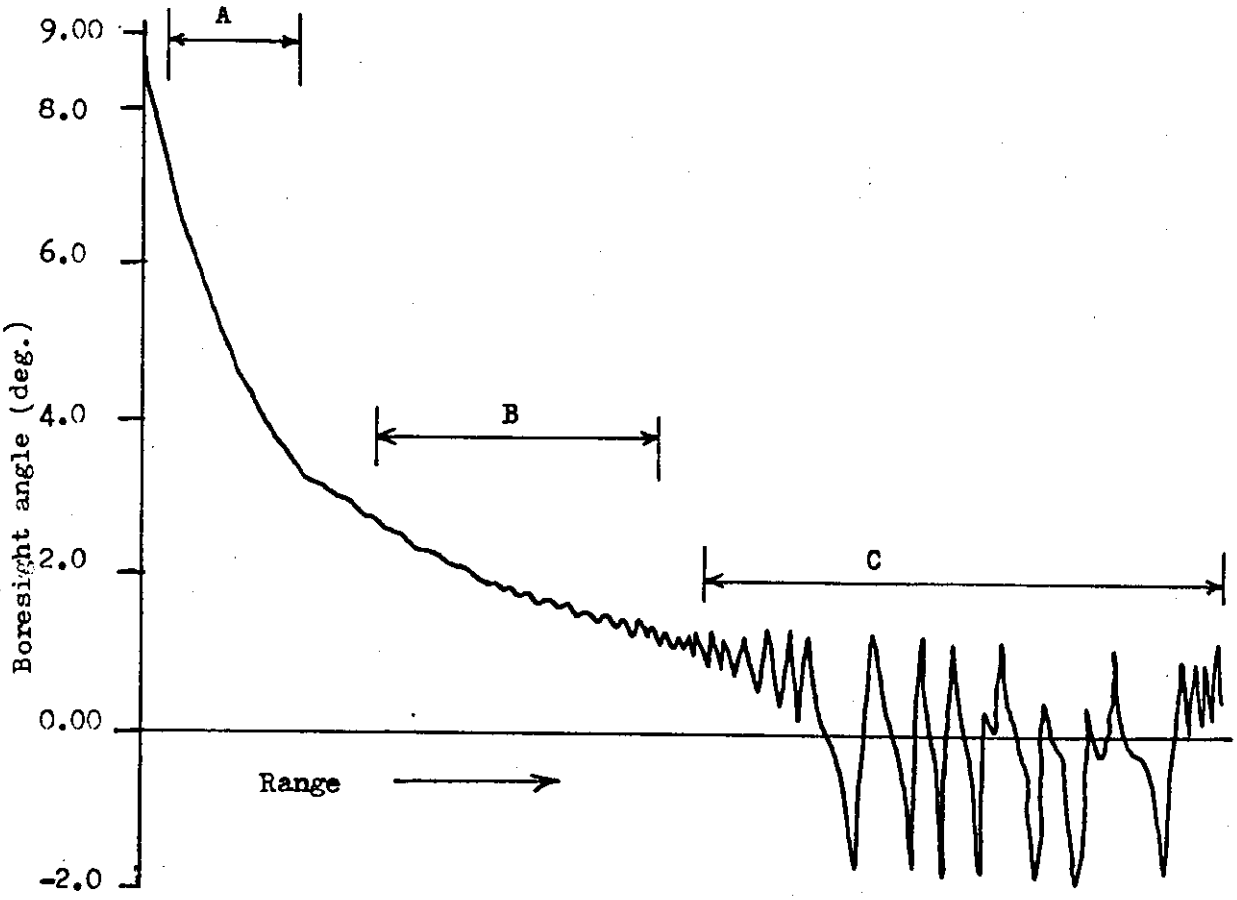

Figure 1-1: Behaviour of a tracking radar, tracking an airborne target, which is opening at constant altitude, shows erratic response as target drops in elevation [1-4].

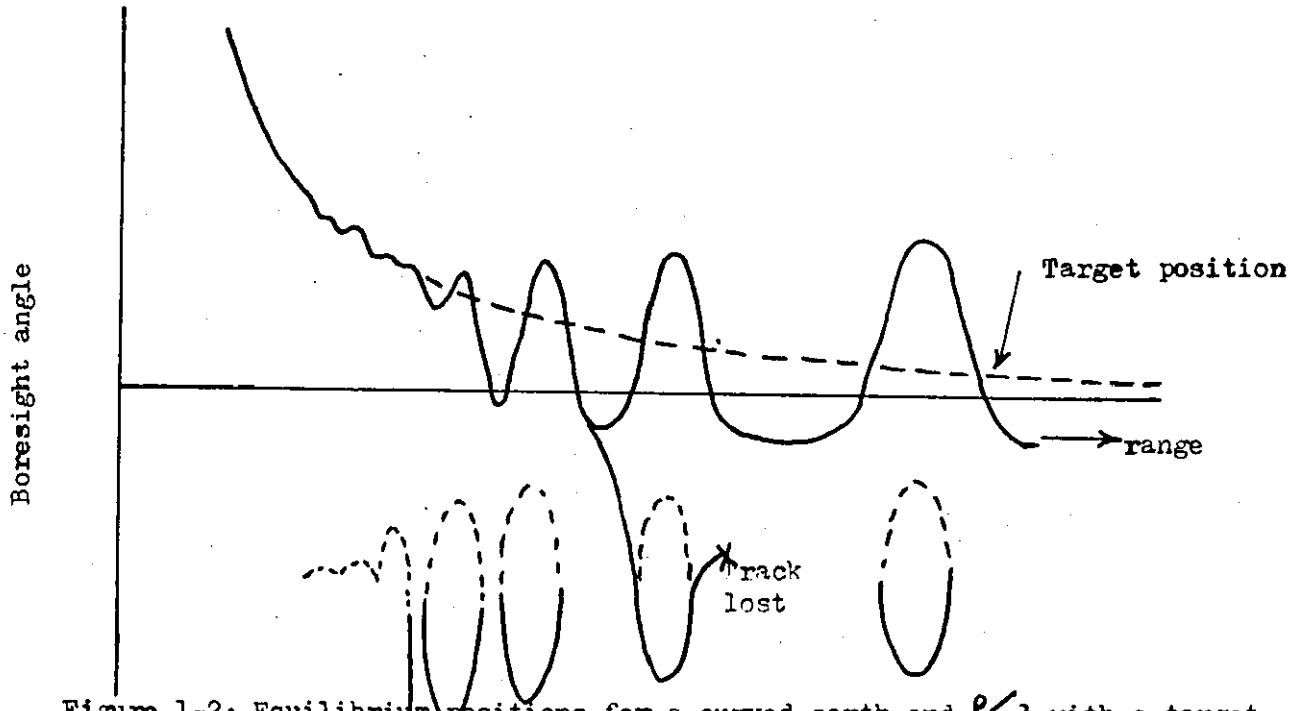

Figure 1-2: Equilibrium positions for a curved earth and $\rho_s < 1$ with a target opening at constant altitude [1-4].

or aperture's length mentioned above. Here, a brief description is made of each solution and its vulnerability to multipath.

1-2.1 Screening: This can be done by placing a fence in front of and below the antenna to intercept the reflection from the surface. It is found that the multipath problem is replaced by a diffraction problem from the top edge of the fence due to illumination by the main beam [1-5].

1-2.2 Polarization: By using vertical polarization the reflected signals in the vicinity of the Brewster angle can be reduced, but this is not applicable for low elevation angles. While the use of circular polarization in reducing rain clutter is widely recognized, it has no real advantages in reducing the surface reflection because it does not reverse its sense for angles less than Brewster angle [1-4], [1-6].

1-2.3 Time of arrival: Theoreticaly, a time lag due to the difference in the propagation paths of the direct and reflected signals can be used to separate them. This time lag is very small in practice (especially for very low elevation angle) which makes it impossible to separate the two signals [1-4].

1-2.4 Doppler frequency: Sometimes the two signals differ in frequency. This difference is very small in practice, and sometimes does not exist. However, to resolve the direct from the reflected signals on the basis of frequency would require exceptional oppler resolution [1-4].

From the above four solutions it is concluded that separation of the direct signal from its specular multipath by simple filtering is not possible.

1-2.5 Off-axis tracker: In this case the beam is tilted upward from horizontal by about 0.7 of a beamwidth, then the reflected signal from the target image under the surface is attenuated by being appreciably closer to the first null of the beam and further off boresight than the signal from the true target. This method reduces the elevation angle error to acceptable accuracy [1-7].

1-2.6 Double null tracker: This tracker is based on generating an antenna pattern which forces the difference function beam to have two symmetrically located nulls about the horizon. The second null (the extra null) is always maintained in the direction of the image target [1-12].

1-2.7 Frequency diversity: This method is usually used to reduce the glint of a target. But, as can be seen from figure 1-1, the angle errors due to specular multipath at low elevation angle are cyclical. This is due to constructive and destructive interference between the two received signals. In changing the operating frequency the phase relationship between these two signals will change accordingly and thus, the angle errors can be averaged by operating the tracking radar over a wide band of frequencies. The main disadvantage of this method is the need for a large bandwidth [1-4].

1-2.8 The complex indicated angle: The normal monopulse uses only the in-phase (or anti-phase) component of the difference signal, but in the presence of multipath additional quadrature components do exist along with the in-phase component. A complex angle error-signal can be derived from

these two components, and a spiral can be drawn in the complex plane with the elevation angle acting as a parameter [1-8,9]. One of the main disadvantages of this method is the ambiguity problem due to the overlapping turns of the spiral. As the antenna height increases (in terms of wavelengths), the number of the turns increases creating more ambiguities. Also, this method is sensitive to surface roughness and the improvement obtained over a rough surface is very marginal [1-10,11].

These are some of the well-known classical solutions to this problem. However, due to the growing adaptive array antenna technology, new high-resolution algorithms are proposed and some of these algorithms will be reviewed in the coming section.

1-3 Modern high-resolution algorithms

During the last few years a great number of high resolution algorithms for multiple target direction finding has appeared in the literature. These algorithms arise from different fields of application such as radar, sonar, seismology, and radio astronomy. The common factor among them is the use of a spatially distributed array of sensors which samples the wavefield in the propagation medium. Nickel [1-13] classified these algorithms into four categories (linear prediction methods, Capon-type algorithms, Projection-type algorithms, and parametric target model fitting), and analysed their possible use in phased array

radar to improve the spectral or angular resolution. The first three categories can also be listed under a more general term called the spectral estimation techniques. An excellent review of the application of these techniques in the frequency domain is shown by Kay and Marple [1-14], and a good survey of the array signal processing applications can be found in many reference books like Hudson [1-15], Clarke [1-16], Haykin [1-17], Childers [1-18], Monzingo [1-19], and a paper by Gabriel [1-20].

1-3.1 The linear prediction methods:

The most popular method in this category is the maximum entropy method (or the autoregressive model fitting) where the spatially sampled data, from the equally spaced linear array, is assumed to be stationary. Burg's method is one of the different ways to calculate the filter coefficient (or the reduced form of the covariance matrix) in order to get the angular power spectrum. The use of this method in radar, as a way to solve the multipath problem associated with a low-flying target, was first reported by Evans [1-21] where he shows a result from a field test which demonstrates that the method works well, but he did not mention the scale of the surface roughness. However this method has many problems such as line splitting, high sidelobes, and best filter length determination [1-14]. In general, fully coherent multipath (or coherent sources) with fixed phase and amplitude relations can not be resolved, as will be seen in chapter 6.

1-3.2 Capon-type algorithms

These methods take the following general form:

$$P(\theta)=(S^{*}(\theta)\ Q^{-v}\ S(\theta))^{-v} \quad ,v \text{ real}$$

Where, * represents the complex conjugate transpose, Q is the array covariance matrix, $P(\theta)$ is the estimated power in the angular direction θ, and $S(\theta)$ the corresponding steering vector. When v=1, the above equation represents the maximum likelihood method of Capon [1-13]. Griffiths [1-22] gives a good summary of the covariance matrix properties, and Mather [1-23] shows simulation results for different methods. Gabriel [1-24] discussed the use of spectral estimation techniques for radar target tracking and detection in the presence of interfering sources. He found that the maximum likelihood method and the sidelobe canceller failed to resolve two partially correleted (95%) sources with half-beamwidth angular spacing and 10 dB signal-to-noise ratio. Evans [1-25] and White [1-26] show the performance of the maximum likelihood method in locating a low-flying target over a smooth surface where specular multipath dominates. They found that this method fails completely over all values of phase difference between the two received signals, while the maximum-entropy method succeeds when the two signals are in phase quadrature. Thus, the method cannot be used to solve fully coherent targets in general. Besides, a minimum number of snapshots (twice the number of array elements) are always

required in order to get satisfactory resolution [1-13]. Thus, the successful use of these types of algorithms in a monopulse-based tracking system is highly unlikely or impossible in practice.

1-3.3 Projection-type algorithms

The general scan pattern of these methods is given [1-13] by:

$$\overset{\perp}{P}(\Theta)=1/[S^{*}(\Theta)\ P^{L}\ S(\Theta)]$$

where, $\overset{\perp}{P}(\Theta)$ is the estimated power in the angular direction Θ, the noise space $P^{L}=I-XX^{*}$, and the matrix X formed by a set of orthogonal vectors $(x^{1},.....,x^{M})$ describes the signal space, where M represents the number of targets. If the columns of X represent the eigenvectors corresponding to the largest eigenvalues of the estimated covariance matrix, then the multiple signal classification method (Music) would result. This method was first found and analysed by Schmidt [1-27]. It is cabable of producing an estimate which contains extremely narrow peaks at signal directions, especially for small number of data vector, i.e in the order of the array elements. Gabriel [1-24] shows that this method could resolve partially correlated signals (95%) with sharp peaks, when the maximum likelihood method failed. However for the case of fully correlated signals, such as the specular multipath problem, this method fails too [1-13].

In general, one concludes that the resolution of two

coherent sources or equivalent radar targets is more difficult for any of the above three categories of spectral estimation technique, because the two coherent sources produce nonstationary fields in the space domain. However, Gabriel [1-28] shows that a solution is possible whenever sufficient relative motion or "Doppler cycles" are available.

The single snapshot case (monopulse) is the most difficult one to solve satisfactorily, because it is a constant-phase coherent case even if the two sources are not nominally coherent. A solution is sometimes possible by using a small moving subaperture along the single snapshot data sample. This synthetic movement of the subaperture is very similar to the action which occurs in Burg's technique of the maximum entropy method [1-28].

1-3.4 Parametric target model fitting

In principle, these are the only methods which can resolve the fully coherent multipath problem or equivalent closely spaced targets on the basis of one snapshot. Even so they have attracted little attention in the literature. The unknown parameters of the received field, such as angular directions, amplitudes, and phases are basically determined by selecting the model which offers the best fit for the collected data. For radar applications, the most convenient model is the point target approach with constant amplitude and phase. The optimization procedure involves the minimization of the mean-squared error between the collected

data and the assumed model for increasing number of targets (starting with 1 and progressing to any possible maximum number of targets) in general, but for two targets only for the coherent multipath problem of concern. The minimization can be done by using some gradient algorithm or by search on a finite net of parameter values [1-13].

Recent publications on the use of this category in solving the specular multipath problem associated with a low-flying target are shown by Reilly et.al. [1-29], and Haykin [1-30]. The best-known closed-form algorithm so far is the maximum likelihood estimator by Cantrell et.al. [1-31] and its modified version by Gordon [1-32]. A linear, equally spaced array, divided into three equal subapertures, is used (explained in chapter 3 in detail).

The common drawback of these algorithms is the massive computer load needed in processing. However, for the specular multipath case this load is as low as for the linear prediction algorithms [1-13], and for the closed-form solution of Cantrell's type above the load is even less. Also, this load can be reduced very much for the symmetric target-image case (i.e. when the target and its image are symmetrically located about the centre of the elevation antenna beam) in comparison with the nonsymmetric case. The first case is usually applicable for a short range low-flying target over a plane surface where the effects of the surface curvature, and the rays bending toward the surface (due to a variation in atmosphere density with altitude) are negligable, and vise versa for the second case [1-33].

The concept of an all digital processing radar system is described by Gabriel [1-24]. A conventional receiver is used prior to the digitizing stage for each element of the receiving array then the baseband in-phase and quadrature video outputs are applied to sample and hold circuits followed by analogue to digital converters. The snapshots are taken according to Nyquist sampling rate corresponding the bandwidth of the baseband video.

1-4 Thesis outline and contributions

Chapter 2 is devoted to a brief survey of the multipath problem for a low-flying target over smooth and rough surfaces respectively. Simulation results for diffused power distributions for a given radar-target geometry and different surface roughnesses and slopes are shown.

Chapter 3 is focused on the study of the closed-form maximum-likelihood estimator where a linear array of three subapertures is used. A new phase estimation, four subapertures technique to improve the in-phase and anti-phase (just anti-phase for the symmetric case) erroneous performance is derived and simulation results are shown. Also, an amplitude comparison four subapertures technique to solve the anti-phase problem for the symmetric case is discussed. This technique depends on the fact that the amplitude of the composite output at the array centre is minimum whenever the two received signals are in phase opposition and vice versa.

Chapter 4 demonstrates a new closed-form method to solve the specular multipath problem in which a simple trigonometric solution is derived and simulation results are shown and compared with their correspondents for the maximum likelihood estimator discussed in chapter 3 (the same array is used). Also, a new method to detect the occurrence of in-phase and anti-phase conditions of the two coherent sources is shown and new three and four subapertures techniqes are introduced with extensive simulation results.

Chapter 5 briefly discusses the performances of the maximum entropy method for spectral estimation (Burg's method) and phase-comparison monopulse radar over a smooth surface.

Chapter 6 is devoted to a study of the performances of the above-mentiond methods in tracking a low-flying target over a rough surface. Simulation results show the effects of the surface roughness parameter, surface slopes, and the array beamwidth. The effects of the off-axis angle on the performance of the phase monopulse radar is shown too.

Chapter 7 includes discussion and recommendations for further work.

The basic contributions of this thesis can be summarised by the following:

1- A new closed-form high resolution method to solve the specular multipath problem associated with a low-flying target over a smooth surface is found.

2- New four-subapertures techniques to improve the performances of the maximum-likelihood and the trigonometric methods when the two received signals from the target and its image are in-phase or anti-phase are derived and validated.

3- The performances of the closed-form maximum likelihood estimator, the trigonometric method, the maximum entropy method, and the phase-comparison monopulse radar are studied and compared for a low-flying target over a rough surface. The effects of surface roughness, surface slopes, and array beamwidth are shown.

Chapter 2

Surface reflection- a survey

2.1 Introduction:

The elevation angle estimation of a low-flying target depends on the amplitude and spatial distribution of the target energy (the reflected power from the illuminated target) forward scattered from the surface between the radar and the target. In particular, the reflection properties of a surface are frequency dependent, so that for long wavelengths, the surface is considered as being perfectly smooth, and for short wav lengths, it is considered to be rough. When the surface is smooth the specular reflection target energy is approximated simply by the target-image model, which obeys the laws of geometrical optics [2-2], [2-10]. In practice, however, most of the surfaces in nature are irregular for microwave frequencies, producing another component (diffuse scattering) which reaches the radar from an extended area lying between the target and the radar "glistening surface" [2-2], [2-5]. Many factors would affect the reflection from a rough surface other than frequency [2-4], like elevation angle, polarization, surface curvature,

wind speed and direction, water vapour.....etc.

Extensive descriptions of multipath phenomena are given in several standard texts [2-1,5]. Many papers are found to address this problem over the sea, but few results are available for over-land operation. Katzin [2-7,8] developed a theory in which the elemental scatterers are taken to be the small patches or "facets" of the sea surface which overlie the main large-scale wave pattern. At low grazing angles the destructive interference between direct and specular reflected waves gives rise to the so-called "critical angle" and spiky apearances of the sea scatterers. Mrstik and Smith [2-14] gave particular attention to the effects of target motion, which permit rejection of multipath components falling outside the radar tracker's passband. Twersky [2-15] studied the reflection from a rough surface, showing that when the grazing angle approaches zero the reflection coefficients approaches unity. Court [2-10] used the optical analogy to study the radar-coverage in elevation over the sea surface. Beard and Katz [2-12] used a vector presentation of the total received field over a calm ocean. By interpreting practical data according to this model, it has been possible to relate the surface roughness to the sea state. Katz [2-6] extended the vector model to include circular polarization. Barton [2-9], [2-13] developed a theory for low-angle tracking over the surface depending on the rough surface scattering theory. A detailed model of the diffuse scattering is produced, which takes care of surface roughness, spikiness, masking, geometrical

correction factor.....etc, and which agree with experimental data in [2-17].

The refraction of electromagnetic waves at low angles of elevation is known to be troublesome, especially at or near the horizon where an error in measuring the elevation angle is introduced [2-18]. This phenomenon is not of interest in this study and a homogeneous atmosphere is considered (for more detail about refraction and deffraction, see references [2-3], [2-18]).

In this chapter, it is intended to give a brief survey of the multipath problem for a low-flying target over the sea surface, to be used in later chapters to evaluate various algorithm's performances.

2.2 Reflection from a smooth surface:

Specular reflection takes place only over a smooth, plane surface, where the laws of geometrical optics are valid. The reflection coefficient is normally defined as the ratio of the reflected wave amplitude to the incident wave amplitude, and the classical formulas for it are the following [2-1].

$$Ro^{h} = \frac{\sin(\gamma) - \sqrt{\varepsilon c - \cos^2(\gamma)}}{\sin(\gamma) + \sqrt{\varepsilon c - \cos^2(\gamma)}} \qquad (2\text{-}1)$$

$$Ro^{V} = \frac{\varepsilon c \sin(\gamma) - \sqrt{\varepsilon c - \cos^2(\gamma)}}{\varepsilon c \sin(\gamma) + \sqrt{\varepsilon c - \cos^2(\gamma)}} \qquad (2\text{-}2)$$

Where, Ro^{h} and Ro^{V} are the reflection coefficients for the horizontal and vertical linear polarizations respectively; γ is the grazing angle of incident and εc is the complex dielectric constant of the medium given by [2-1], [2-3].

$$\varepsilon c = \varepsilon_1 - j\,\varepsilon_2 \qquad (2\text{-}3)$$

$$\varepsilon_2 = 60\,\lambda\,\sigma \qquad (2\text{-}4)$$

where, λ is the wave length of the incident wave; σ is the conductivity of the medium in S/m; $\varepsilon_1 = \varepsilon/\varepsilon_o$ is the relative dielectric constant of the medium (ε_o is the free space dielectric constant). Figure 2-1, shows the geometry of the reflection from a smooth surface.

In the above paragraph the polarization is referred to as being horizontal when the electric field vector of the incident wave is horizontal (parallel to the plane of incidence) and vertical when the electric field vector is lying in the vertical plane containing the incident and reflected rays.

The value of εc depends on the electrical properties of the medium, which depends on too many factors to be discused in this research (for more information, see ref.[2-3]). In practice εc is much larger than unity, which allows us to introduce an approximation to equations (2-1) and (2-2) above which become as follows:

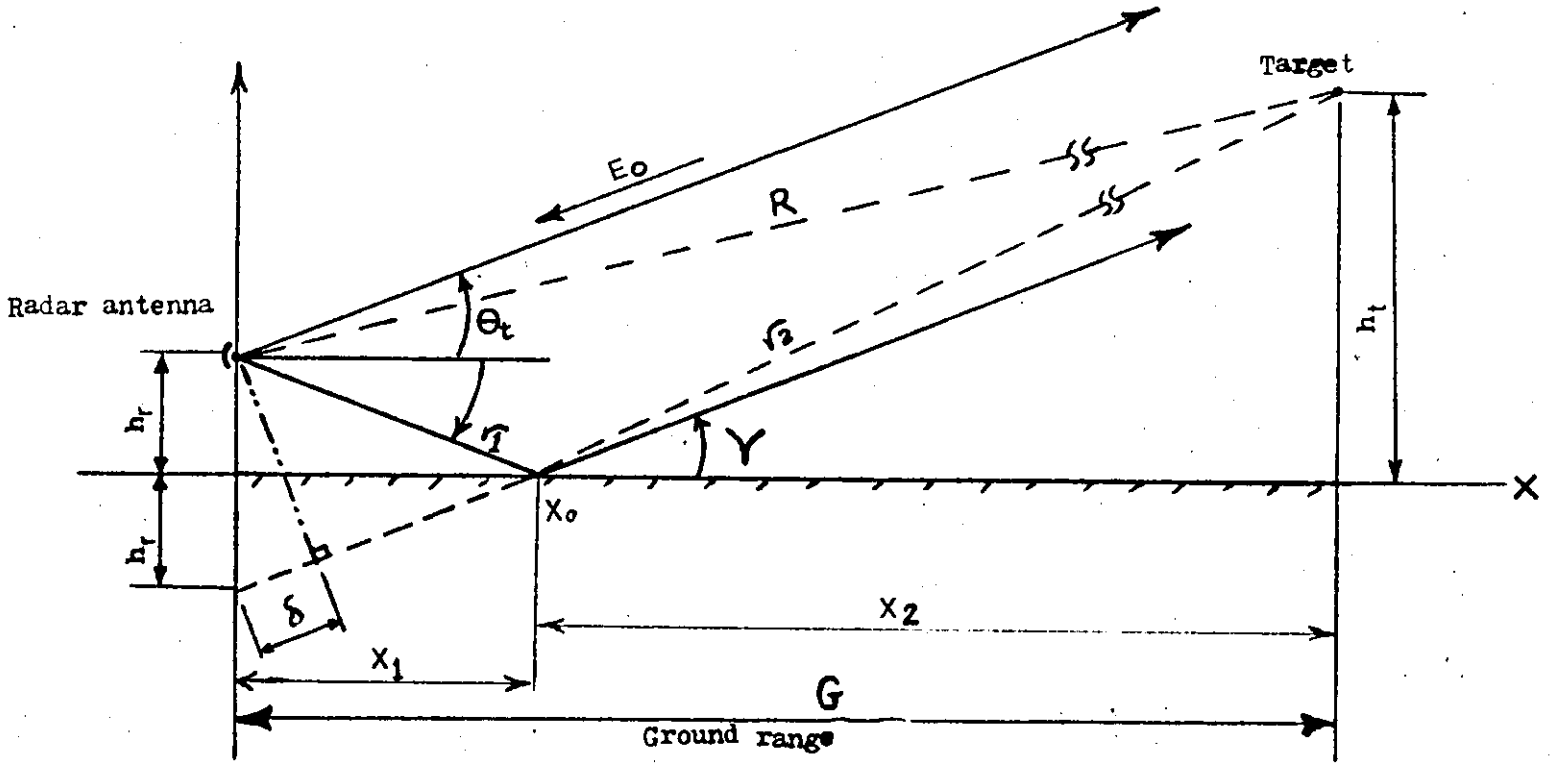

Figure 2-1: Geometry of flat earth reflection

$$Ro^h = \frac{\sin(\gamma) - \sqrt{\varepsilon c}}{\sin(\gamma) + \sqrt{\varepsilon c}} \qquad (2\text{-}5)$$

$$Ro^v = \frac{\sqrt{\varepsilon c \sin(\gamma) - 1}}{\sqrt{\varepsilon c \sin(\gamma) + 1}} \qquad (2\text{-}6)$$

Figures 2-2 and 2-3, show the reflection coefficients for both ground and sea as a function of the grazing angle of the incident wave [2-3]. In figure 2-2 different types of ground (according to soil-water mixture) are shown at a frequency of 8 GHZ, and in figure 2-3 the reflection from the sea surface for frequencies of 100 MHZ, 1 GHZ and 3 GHZ. When the grazing angle is zero the values of Ro^h and Ro^v are equal to -1. The amplitude of Ro^h then decreases gradually with increase of the grazing angle from 0^o to 90^o with its phase staying constant ($\phi = 180^o$). The value of Ro^v is more complicated, where the amplitude value of Ro^v decreases rapidly with increasing value of γ till it reaches a minimum when $\gamma = \sin^{-1}(1/\varepsilon c)$ as shown from (2-6). This grazing angle is called the pseudo-Brewster angle and its value depends on the electrical properties of the surface and it is more pronounced in the case of ground than for sea. When the grazing angle increases beyond the Brewster angle the amplitude of Ro^v increases again till its value becomes equal to Ro^h at $\gamma = 90^o$. The phase of Ro^v changes from 180^o at small grazing angles to zero for large grazing angles with the changeover occuring around the Brewster angle. For a grazing angle in the neighbourhood of one degree, both Ro^h and Ro^v moduli are nearly one and their phases lags are nearly 180^o.

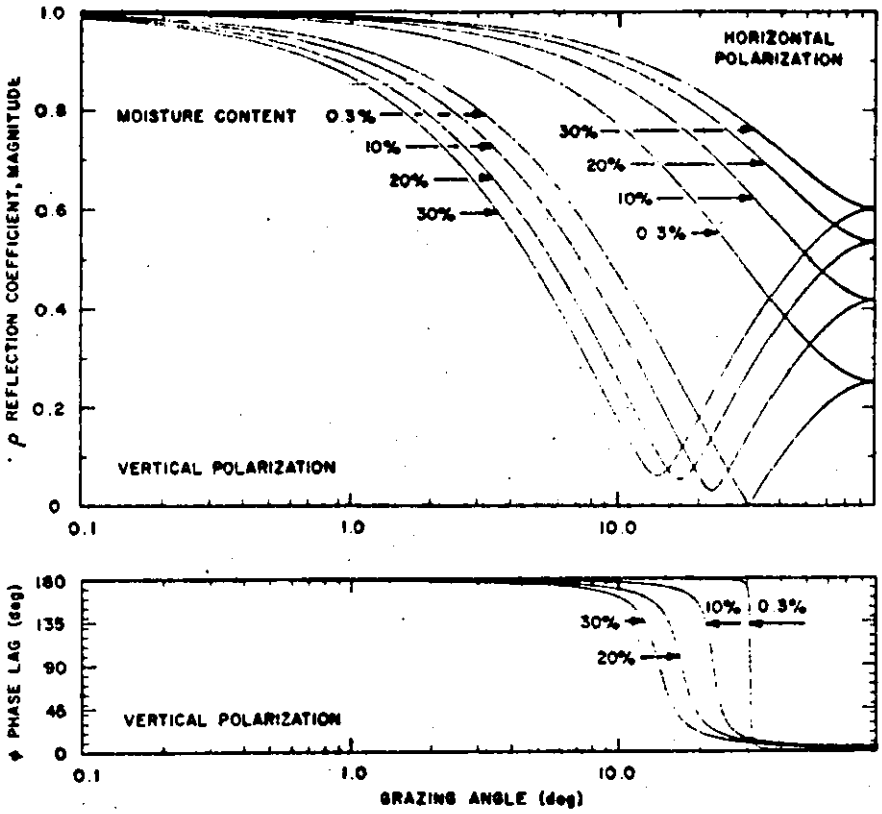

Figure 2-2: The reflection coefficient as a function of grazing angle for four soil-water mixtures at a frequency of 8 GHz [2-3].

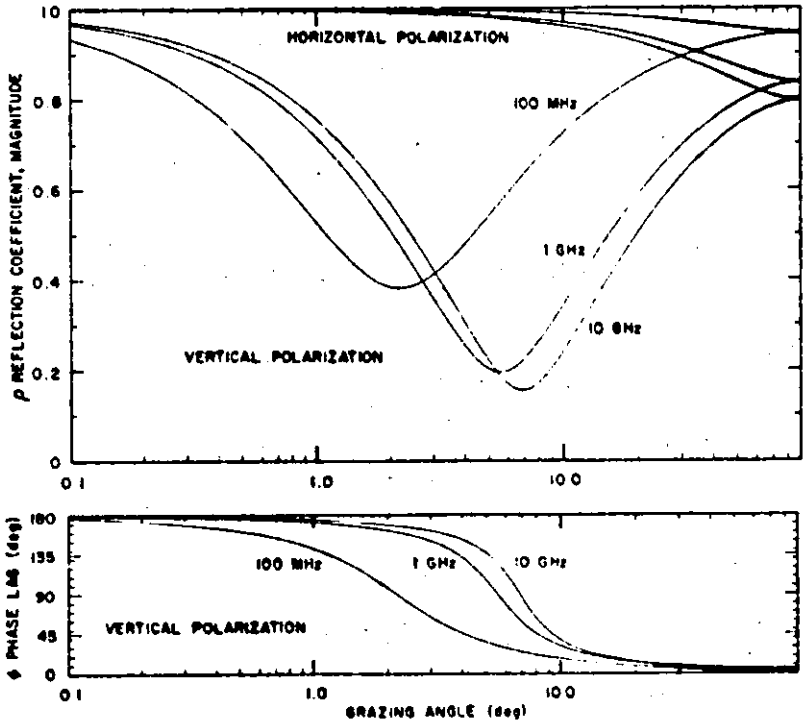

Figure 2-3: The reflection coeffecient as a function of grazing angle for sea water. Curves are shown for frequencies of 100 MHz, 1GHz, and 8GHz. From [2-3]

A circularly polarized wave consists of the sum of a horizontal and vertical component, equal in amplitudes (if not, an elliptically polarized wave occurs), and out of phase by 90 degrees. The reflection of this wave over a smooth surface can be easily calculated from equations (2-1) and (2-2), and given in [2-6] by:

$$Rcs = \frac{1}{2}\left[Ro^{v\,2} + Ro^{h\,2} + 2\,Ro^{v}Ro^{h}\cos(\phi^{h} - \phi^{v})\right]^{1/2} \qquad (2\text{-}7)$$

$$\Phi c = \sin^{-1}\left\{\frac{Ro^{v}}{2\,Rcs}\left[\sin(\phi^{v}) + \frac{Ro^{h}}{Ro^{v}}\sin(\phi^{h})\right]\right\} \qquad (2\text{-}8)$$

where Rcs and Φc are the reflection coefficient and the phase for circular polarization, when the receiving antenna is circularly polarized in the same sense as the transmitting source. The reflection coefficient for opposite sense circular polarization is given [2-6] by:

$$Rco = \frac{1}{2}\left[Ro^{v\,2} + Ro^{h\,2} - 2\,Ro^{v}Ro^{h}\cos(\phi^{h} - \phi^{v})\right]^{1/2} \qquad (2\text{-}9)$$

Figure 2-4 shows the reflection coefficient for circular polarization from a smooth surface as a function of the grazing angle for C-band. Ro^{h} and Ro^{v} are drawn as a dashed line for comparison only.

It is clear from the curves that for low-altitude targets, the character of the received signal will depend strongly on the sense of the receiving antenna polarization circularity with respect to the transmitted one.

The discussion of the specular reflection from a smooth

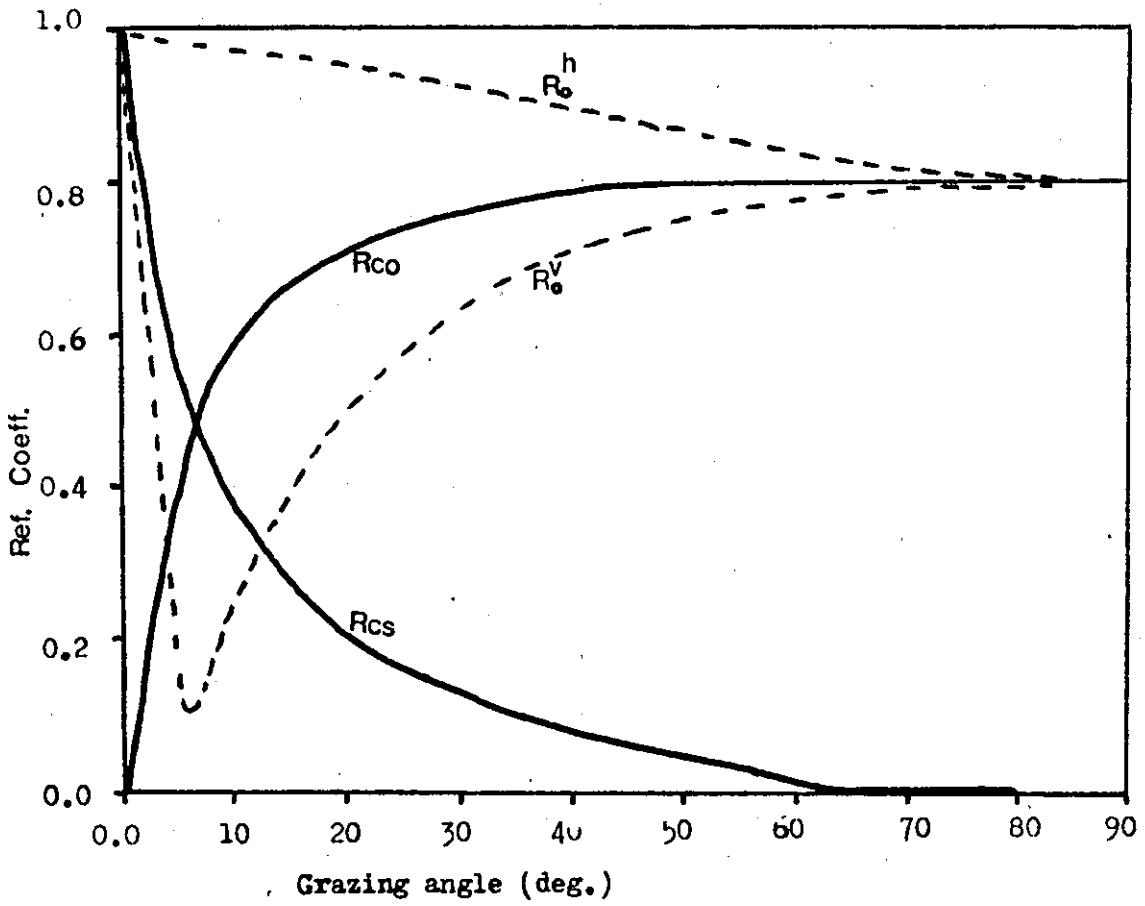

Figure 2-4: Reflection coefficient for circular polarization [2-6].

surface in this section can be used to represent actual surface reflectivities in at least the following areas [2-3]:

a: Flat desert surfaces

b: Flat surface covered by snow

c: Sea or lakes surfaces with negligable wave heights

2.3 The divergence factor

The reflection coefficients in (2-1) and (2-2) are valid only in the case when the smooth surface is plane. In practice they can be used for short range paths, between a target and a radar. If the reflection is occuring from a curved earth (see fig. 2-5), a new factor, the so called divergence factor (D) must be introduced, and the reflection coefficients for both linear polarizations becoms $R^{h,v} = Ro^{h,v} D$. Accepting that the target and antenna heights are very small in comparison with the earth's radius and that the total multipath length is approximately equal to the ground range G, the divergence factor is given by [2-2] as follow:

$$D = \left[1+\frac{2\, r_1\, r_2}{a(r_1 + r_2)\sin(\gamma)}\right]^{-1/2} \left[1+\frac{2\, r_1\, r_2}{b(r_1 + r_2)}\right]^{-1/2} \qquad (2\text{-}10)$$

In practice, the earth is considered to be spherical with (a=b) and if the grazing angle is very small, then D may be given by:

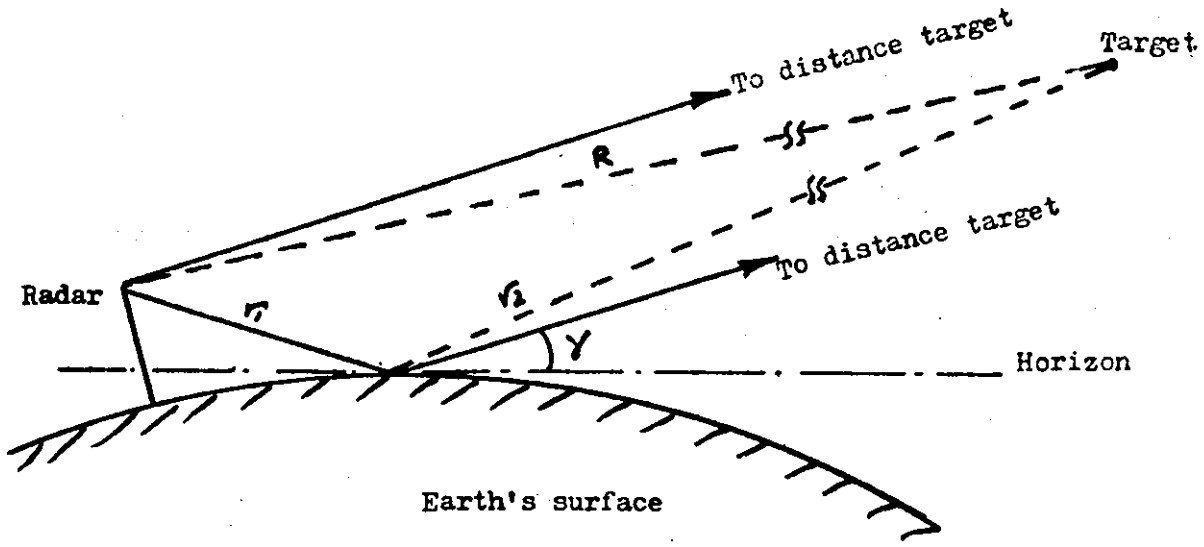

Figure 2-5: Geometry of long-range specular multipath

$$D = \left[1 + \frac{2\, r_1\, r_2}{a(r_1 + r_2)\sin(\gamma)} \right]^{-1/2} \qquad (2\text{-}11)$$

where, r_1 and r_2 are the slant ranges of the receiving antenna and the target from the point of reflection on the surface respectively, a and b are the radii of curvature of the intersections of the surface of the earth and two vertical planes perpendicular to the direction of propagation.

2.4 Fresnel zone:

Due to the phase relationships among the reflected field vectors from a smooth illuminated surface between the transmitter (target) and receiver (radar), most of the indirect or reflected energy will cancel, except that from a comparatively small elliptical patch of the surface which combines with the direct field energy at the receiving point. This elliptical reflection area is called the Fresnel zone. The dimensions of these zones and their locations are very important in the radar siting problem. A simplified calculation of the zones are given in [2-1,2] by:

The centre of the ellipses

$$Xon \approx \frac{G}{2} \frac{1 + \dfrac{2\, h_r(h_t + h_r)}{n\, \lambda\, G}}{1 + \dfrac{(h_t + h_r)^2}{n\, \lambda\, G}} \qquad (2\text{-}12)$$

The semimajor axis

$$X1n = \frac{G}{2} \frac{\sqrt{1+\frac{2\,\delta_o}{n\,\lambda}}}{1+\frac{(h_t+h_r)^2}{n\,\lambda\,G}} \qquad (2\text{-}13)$$

The semiminor axis

$$Y1n = \sqrt{\frac{n\,\lambda\,G}{2}} \sqrt{\frac{(1+\frac{2\,\delta_o}{n\,\lambda})}{1+\frac{(h_t+h_r)^2}{n\,\lambda\,G}}} \qquad (2\text{-}14)$$

assuming that h_r, h_t and δ_o are all much smaller than G; h_t and h_r are the heights of the target and the radar respectively, G is the ground range, δ_o is the approximate path difference between the direct and indirect waves at the receiving point given by:

$$\delta_o = \frac{2\,h_t\,h_r}{G} \qquad (2\text{-}15)$$

and the n_th ellipse is determined by:

$$\delta_n = \delta_o + \frac{n\,\lambda}{2} \qquad (2\text{-}16)$$

Equation (2-16) shows that the successive zones are in phase opposition, so the energy from adjacent zones tends to cancel but, because the excitation amplitude decreases from

zone to zone, not completely. This explains the argument behind considering the first Fresnel zone as the main contributer to the reflected energy at the receiving point.

2.5 The Rayleigh Criterion:

In practice a surface may be smooth for some wavelengths and rough for others, or for a given wavelength it may be either smooth or rough for different values of the grazing angle. Thus, the first step in studying the surface scattering is to determine the type of the surface depending on the two given parameters. Rayleigh suggested a simple formula, which depends on measuring the phase difference (Ψ) between two parallel rays encountered on a surface with height difference (h) at grazing angle γ [2-2].

$$\Psi = \frac{4 \pi h}{\lambda} \sin(\gamma) \qquad (2\text{-}17)$$

If $\Psi = 0^{\circ}$ (or very small), the two reflected rays will be in-phase and the surface is smooth. If $\Psi = 180^{\circ}$, the two reflected rays will be in phase opposition and cancel out in this direction. But, according to the law of "energy conservation" they can not be lost and must be scattered in other directions and the surface is rough. By taking the middle value of the phase difference ($\Psi = 90^{\circ}$) between these two extremes, and substituting it in (2-17), the smooth surface condition "Rayleigh Criterion" can be given by:

$$h < \frac{\lambda}{8 \sin(\gamma)} \qquad (2\text{-}18)$$

$$\gamma c = \sin^{-1}\left(\frac{\lambda}{8 h}\right) \qquad (2\text{-}19)$$

The right-hand part of equation (2-19), shows that there are two ways to make the surface appears to be smooth, (a): by making the value h/λ very small ($h/\lambda \rightarrow 0$), (b): by taking a very small grazing angle ($\gamma \rightarrow 0$).

Obviously, most of the real surfaces in nature are neither smooth nor rough. Various theoretical and experimantal investigations show the field scattered by a rough surface to be the sum of specular and diffuse components. Table 2-1, shows the critical angle γc, above which the surface appears rough at different wave length, and sea states. When γ is greater than twice γc, the specular component from the surface becomes negligable and the main source of scattering is the diffuse one [2-5]. When the grazing angle is less than the critical angle, the specular reflection coefficient will be the dominant term.

Table 2-1

Maximum angles for specular reflection at different radar frequencies and sea state [from, 2-5].

Sea State Number	Description of sea	Wave height (m)	Rms Height (m)	Critical Angle, (deg)		
				λ=0.7m	λ=0.1m	λ=0.03m
1	Smooth	0-0.3	0-0.065	>45	>6	>1.8
2	Slight	0.3-1	0.065-0.21	12-45	1.8-6	0.5-1.8
3	Moderate	1-1.5	0.21-0.32	8-12	1.2-1.8	0.3-0.5
4	Rough	1.5-2.5	0.32-0.54	5-8	0.7-1.2	0.2-0.3
5	Very rough	2.5-4	0.54-0.86	3-5	0.4-0.7	0.12-0.2
6	High	4-6	0.86-1.3	2-3	0.3-0.4	0.09-0.12
7		>6	>1.3	<2	<0.3	<0.04

2-6 Multipath interference

The radar antenna receives the reflected wave and the direct wave simultaneously. When the reflection takes place over a smooth, plane surface, and assuming a homogeneous atmosphere, the treatment is simple. From figure 2-1, the amplitude of the total field at the radar antenna is given [2-2], [2-17] by:

$$E = Eo \sqrt{(1+|R^{h,v}|)^2+4\,|R^{h,v}|\cos^2(\emptyset.5\ \Psi)} \qquad (2\text{-}20)$$

where, Ψ is the total phase shift between the two waves given by

$$\Psi = 2\ \Pi \frac{\delta}{\lambda} + \Phi \qquad (2\text{-}21)$$

where, Φ is the phase associated with the reflection coefficient, and δ is the path length diffference between the direct wave and the reflected wave, which can be calculated from figure 2-1 as follow:

$$\delta = 2\ h_r \sin(\gamma) \qquad (2\text{-}22)$$

$$\sin(\gamma) = \frac{h_r + h_t}{G} \quad \text{for small } \gamma \qquad (2\text{-}23)$$

$$\delta = \frac{2\ h_r\ (h_r + h_t)}{G} \simeq \frac{2\ h_r\ h_t}{G} \qquad (2\text{-}24)$$

Assuming in equation (2-24), $h_r << h_t$, Eo is the direct field

strength, $R^{h,v}$ is the amplitude of the reflection coefficient of the surface. From equation (2-20) E can take any value between a maximum and a minimum according to the value of Ψ (when the radar is stationed in the same position , Ψ will be a function of the target position). Assuming $\phi=\pi$, for horizontally or vertically polarized waves at small grazing angle (less than the Brewster angle), the minimum value of E will occur when:

$$\frac{2\ h_t\ h_r}{\lambda\ G} = k \qquad \text{,k is an integer} \qquad (2\text{-}25)$$

and the maximum value at

$$\frac{4\ h_t\ h_r}{\lambda\ G} = 2\ k + 1 \qquad (2\text{-}26)$$

Thus the presence of a specular multipath over a smooth, plane surface causes the continuous elevation coverage of the beam to break up into a lobed structure [2-10], [2-18].

2-7 Rough surfaces:

Various experimental and theoretical investigations of the rough surface have proved that the scattered field (wave) can be represented by the sum of two components, a specular component and a diffuse component[2-2], [2-4], [2-9], [2-12], [2-13]. The corresponding reflection coefficients are designated Rs and Rd respectively. The characteristics of the specular reflection component Rs is the same as that from a smooth surface with the following restriction:

a- The amplitude of the reflection coefficient is smaller than that for a smooth surface.

b- The reflection coefficient fluctuates.

$$Rs = \rho_s \; D \; Ro \qquad (2\text{-}27)$$

where: ρ_s is the specular scattering coefficient from a rough surface given [2-5] by:

$$\rho_s^2 = \exp\left[-\left(\frac{4\,\Pi\,\sigma_h}{\lambda}\sin(\gamma)\right)^2\right] \qquad (2\text{-}28)$$

and σ_h is the rms deviation of the surface heights.

The fluctuation of Rs in any given model of a rough surface can be considered to be the result of adding together a constant field and a zero mean random field whose real and imaginary parts are normally distributed, with different variances in general(for detail,see [2-2]).

The power from the target which reaches the rough surface and is not reflected specularly or absorbed, will be

scattered in other directions. Part of this power will reach the radar from an extended region "glistening surface" from the neighbourhood of the target to the neighbourhood of the radar. This is called the diffuse reflection component. The basic scattering elements are the small facets which overlie the main large-scale wave pattern or swell. The rms slope of the small surface facets is given by $\beta_o = 2\ \sigma_h/d_c$, where d_c is the correlation distance [2-2]. The diffusely scattered power from a rough surface is given [2-2] by:

$$Rd = \rho_d\ D\ Ro \qquad (2\text{-}29)$$

where ρ_d is the rms value of the diffuse scattering coefficient and D is the divergence factor which can be neglected in the case of low-elevation targets because of its small effect on diffuse scattering [2-13]. Common practice among engineers is to express ρ_d as a simple function of $(\sigma_h \mathrm{Sin}(\gamma)/\lambda)$ as shown in figure 2-6, which was drawn from practical data [2-5]. Since γ varies widely over the glistening surface, using figure 2-6 might lead to an error. Besides Barton [2-9], showed that figure 2-6 is not accurate, and the values of ρ_d shown are smaller than the real values. This is because the antenna used in collecting the data was very directive and part of the scattering surface is not accounted for.

For low-flying targets the grazing angle γ is small in comparison with the rms surface slopes β_o (for sea and land β_o is typically 0.05-0.25 rad.). For such cases, the theory

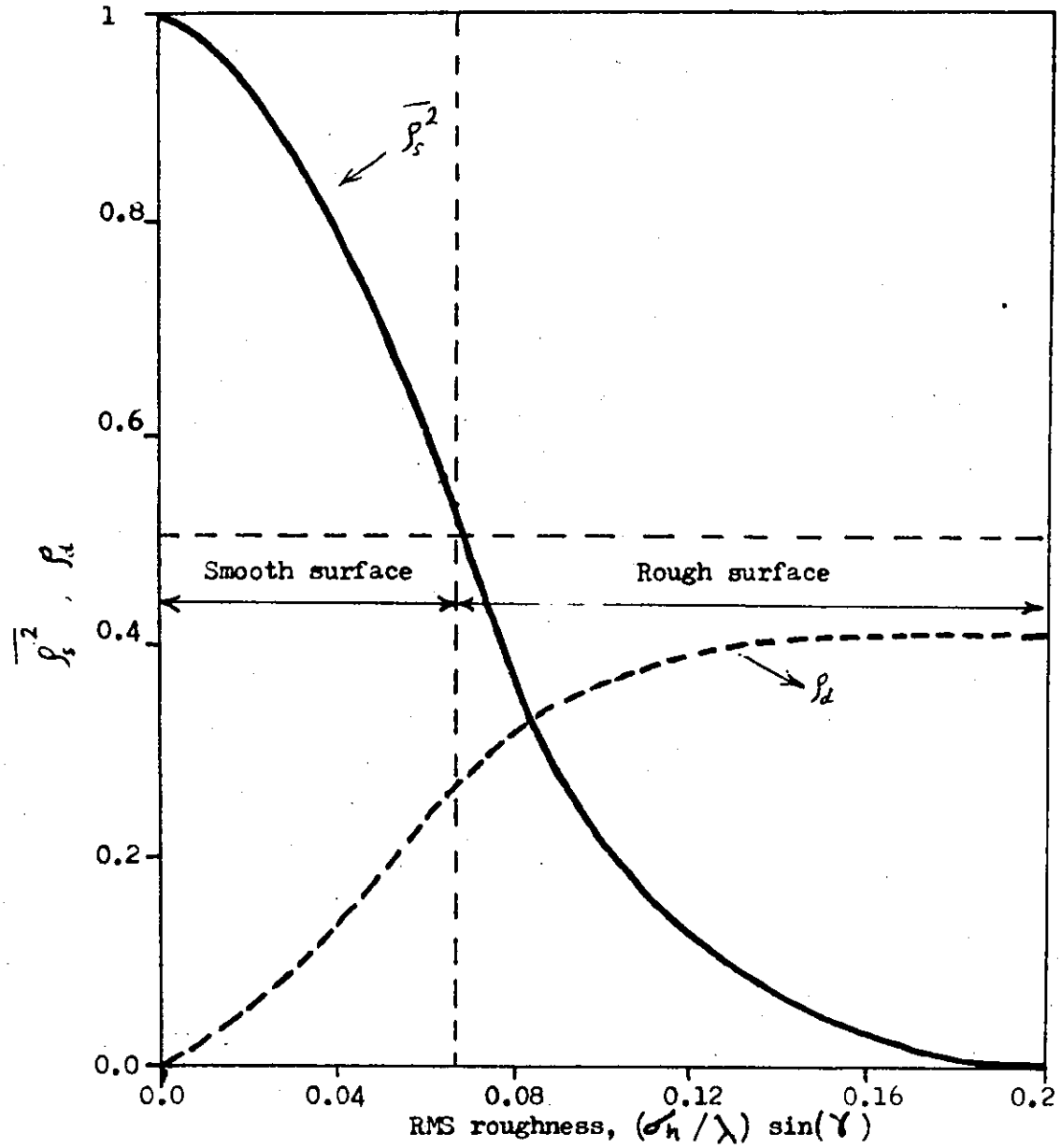

Figure 2-6: Scattering factors Vs roughness (from [2-5]).

by Spizzichino [2-2] predicted that the diffused power will be concentrated near the ends of the glistening surface at A and B as shown in figure 2-7-b. A simple diffuse reflection model has sometimes been used, where the total diffuse power is divided between a foreground component(just in front of the radar antenna at A) and a horizon component (just in front of and below the target, at B). The value of the diffuse and specular component is taken, according to the surface roughness and grazing angle, from figure 2-6. For long range targets the horizon component for this simple diffuse model may lie behind the horizon range with a curved earth. So, this simple model cannot accurately represent the diffuse scattering. In order to get a more accurate model for a low-flying target, and in order to adopt the glistening surface theory to partially rough surfaces, Barton [2-13] introduced a roughness factor (Fd) which would account for removal of reflected diffuse power by specular reflection at either grazing angle γ_1 or γ_2 as shown in figure 2-7-a.

2-7.1 Diffuse reflection model for low-flying target:

In this model, the target is considered to be an active transmitter, with non-directional antenna, illuminating the radar and the surrounding rough surface ($\rho_s=0$). The received power from the direct path (Pr) is given [2-13] by:

$$Pr = \frac{Pt\ Gt\ Gr\ \lambda^2}{(4\ \pi)^2\ R^2} \qquad (2\text{-}30)$$

and the clutter-reflected power Pc is given by

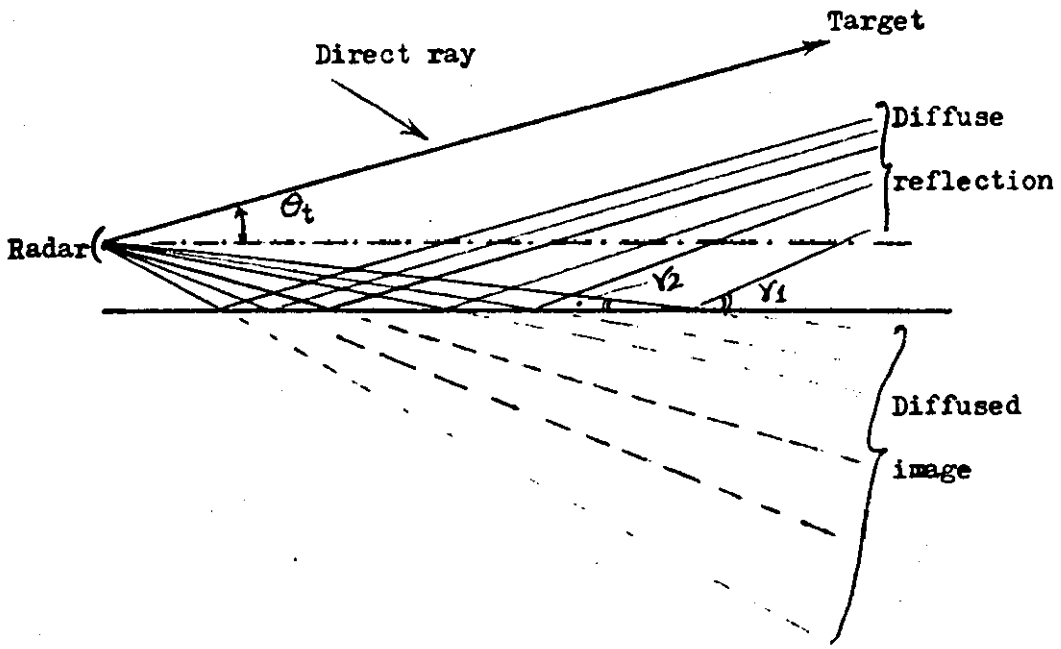

(a)

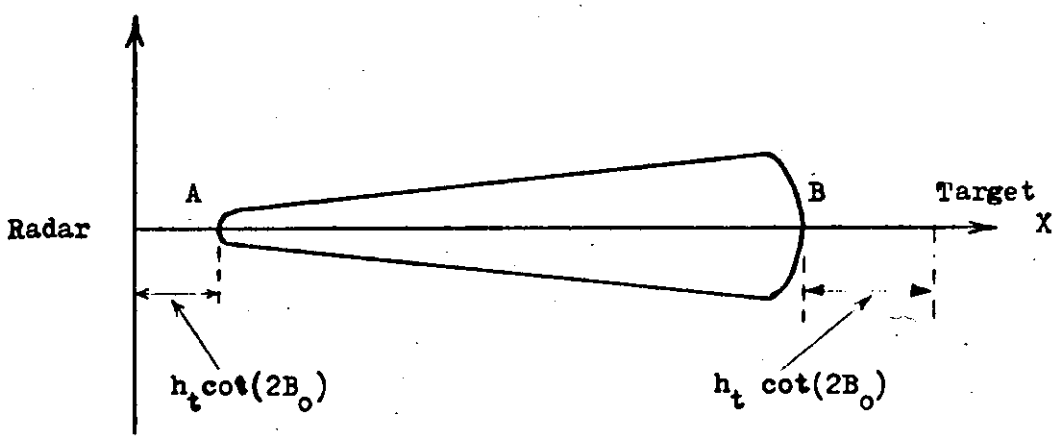

(b)

Figure 2-7: (a) The diffuse reflection from a glistening surface, (b) The glistening surface (top view).

$$Pc=\int dPc = \frac{Pt\ Gt\ Gr\ \lambda^2}{(4\ \pi)^3} \int \frac{\sigma^\circ\, ds}{r_1^2\ r_2^2} \qquad (2\text{-}31)$$

where Gt and Gr are the gains of the transmitting and receiving antennas and σ° is the bistatic scattering coefficient from γ_1 and γ_2. The integration in (2-31) is over the area within the resolution cell formed by the receiving beam and the transmitted waveform, also the gains Gt and Gr are considered to be constant over the 3-dB beamwidth. The contribution of the small area of the surface (where r_1, r_2, σ°, and the antenna gain are constant) is given by:

$$d\rho_d^2=\frac{dPc}{Pr} = \frac{R^2}{(r_1\ r_2)^2} \quad \frac{\sigma^\circ}{4\ \pi}\, ds \qquad (2\text{-}32)$$

Assume that all the diffuse power come from within the glistening surface, with $\sigma^\circ=\cot^2(\beta_o)$, for $\beta<\beta_o$ and zero when $\beta>\beta_o$. Besides, for low-flying target condition assume $\theta_t<\beta_o<<1$, $hr<ht<<R$, $r_1 \approx X_1$, $r_2 \approx X_2$. The coordinate of the glistening surface boundry is then given by the following, from [2-13].

$$Y=\pm\frac{X_1\ X_2}{X_1+X_2}\left(\frac{h_r}{X_1}+\frac{h_t}{X_2}\right)\sqrt{\beta_o^2 - \frac{1}{4}\left(\frac{h_r}{X_1}-\frac{h_t}{X_2}\right)^2} \qquad (2\text{-}33)$$

and it extends from $X_a = h_r/2\beta_o$ to $X_b = R - h_r/2\beta_o$. The total diffuse power is given by:

$$\rho_d^2 = \frac{1}{4\pi\beta_o}\int \frac{R^2\, ds}{X_1^2\, X_2^2} = \frac{1}{2\pi\beta_o^2}\int_{X_a}^{X_b} \frac{R^2\, y\, dx}{(R-X)^2\, X^2} \qquad (2\text{-}34)$$

When the target is at low-altitude and long range, for which the glistening surface extends beyond the horizon range, equation (2-34) becomes as follows [2-13].

$$\rho^2 \simeq \frac{1}{2\pi\beta_o^2}\int_{X_a}^{X_b} \frac{y\, dx}{X^2} \qquad (2\text{-}35)$$

Also, the following approximation can be made: $\theta_t = h_t/R$ and $y \simeq \pm\, \theta_t\, \beta_o$.

In equation (2-34) the surface is considered to be completely rough. In general, a fraction of the power incident on the surface will contribute to the diffuse scattering component but most of it for the specular component (especially when the target is very low over the surface). One method of scaling the diffuse term in (2-34) is by multiplying it by a roughness factor Fd.

$$Fd^2 = 1 - \rho_s^2 = 1 - \exp\left[-\left(\frac{4\pi\sigma_h \sin(\gamma)}{\lambda}\right)^2\right] \qquad (2\text{-}36)$$

Barton [2-13], used separate roughness factors Fd_1 and Fd_2 corresponding to local grazing angles γ_1 and γ_2 associated with each area within the glistening surface.

$$Fd^2 = Fd_1 \; Fd_2 = \sqrt{(1-\rho^2_{s1})(1-\rho^2_{s2})} \qquad (2\text{-}37)$$

Here, ρ_{s1} and ρ_{s2} are the specular reflection coefficient for both paths associated with r_1 and r_2 respectively, see figure 2-1. Fd^2 becomes zero wherever ρ_{s1} or ρ_{s2} equal one (smooth surface case). By including the roughness factor (Fd^2) in equation (2-34), the diffuse scattering coefficient is given [2-13] by:

$$\rho_d^2 \approx \frac{R^2}{2\,\pi\,\beta^2_o} \int_{x_a}^{x_b} \frac{Fd^2\; Y\; dx}{(R-X)^2\; X^2} \qquad (2\text{-}38)$$

This roughness factor accounts for the specular power at low-elevation angles and the horizon effect for a round earth. Also, no shadowing or masking correction factor is required unless very special circumstances exist such as a huge obstacle interupting the path [2-13] .....etc.

In order to meet the law of energy conservation, Barton [2-9] noticed that a geometrical correction factor is needed when $\gamma_1 < 2\beta_o$ to take account of the solid angle of the diffuse reflection being no longer reduced in proportion to γ_1. The effect of the new factor would be to reduce the horizon diffuse power component by one-third to two-thirds for that given in equation (2-34).

Barton [2-13] considered two typical low-angle tracking cases. The glistening surface dimensions were calculated from (2-33), and $\Delta\rho^2_{di}$ values were calculated for ΔX=500m through the region from the specular reflection point to the horizon. Table 2-2 shows complete descriptions for both cases. The diffuse power distribution over the ground range

Table 2-2: Typical paths for evaluation the diffuse reflection, from [2-13].

		Case (A)	Case (B)
Description of path		Short range target	Long range target
Range:	R (km)	10	>>10
Heights:	h_t (m)	105	>>105
	h_r (m)	5	5
Elevation:	θ_t (rad)	0.01	0.01
Surface slope:	β_o (rad)	0.1	0.1
Ground ranges:	X_a (m)	25	25
	X_o (km)	0.5	0.5
	X_h (km)	9.3	9.3
	X_b (km)	9.5	>>10

and the effect of the roughness factor for moderate sea (σ_h=5λ) and rough sea (σ_h=20λ) are shown in figures (2-8-a,b),(2-9-a,b) for short range and long range target respectively. From the curves, the foreground component is slightly affected by the roughness factor but the largest horizon components are gradually reduced. Also, by comparing figure (2-8-a,b) with figure (2-9-a,b), the difference between short ranges and long ones in the horizon region, is small in both roughness cases. In both if the foreground component is excluded, ρ_d will lie between 0.1 and 0.2, and most of this diffused power will originates arround the specular reflection point rather than at horizon.

Figures (2-10-a) and (2-10-b) show the diffuse power distribution in elevation for both short and long range targets for a completely rough surface and for the two roughness factors mentioned earlier. The diffused power from a region at range X will appear at angle ($-h_r/X$) relative to the radar's antenna (for large h_r the modification for curved-earth must be considered). The short range case has a relatively big horizon component for rough surface(ρ_s=0), but the long range case lacks this term. The foreground term for the short range case is somewhat smaller than that for the long range.

Further simulation of this target's diffuse reflection model for different surface roughnesses, rms slopes, elevation angle, and radar-target geometry has been carried out. The results are shown in appendix A2, tables 1 to 7, which will be used in chapter 6 to study the performances of

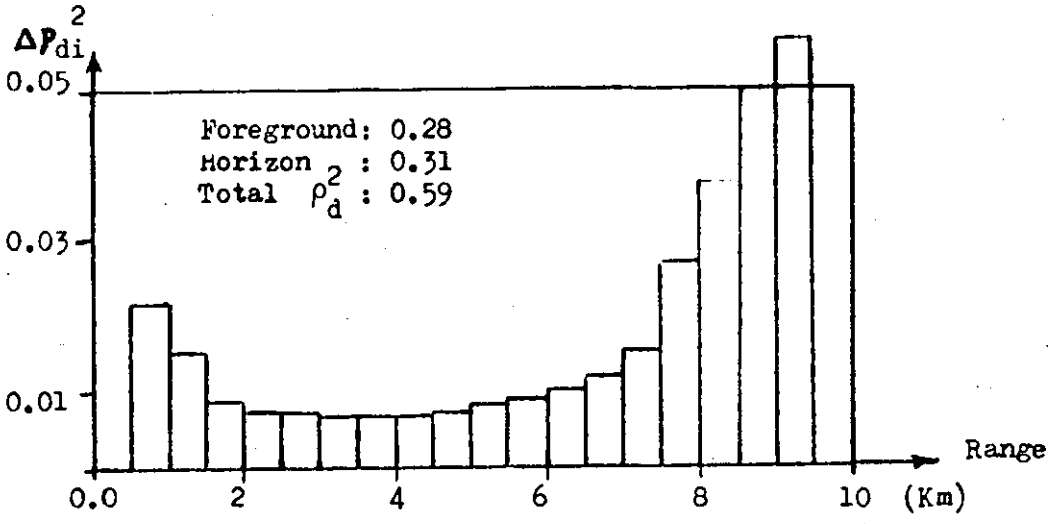

(a)

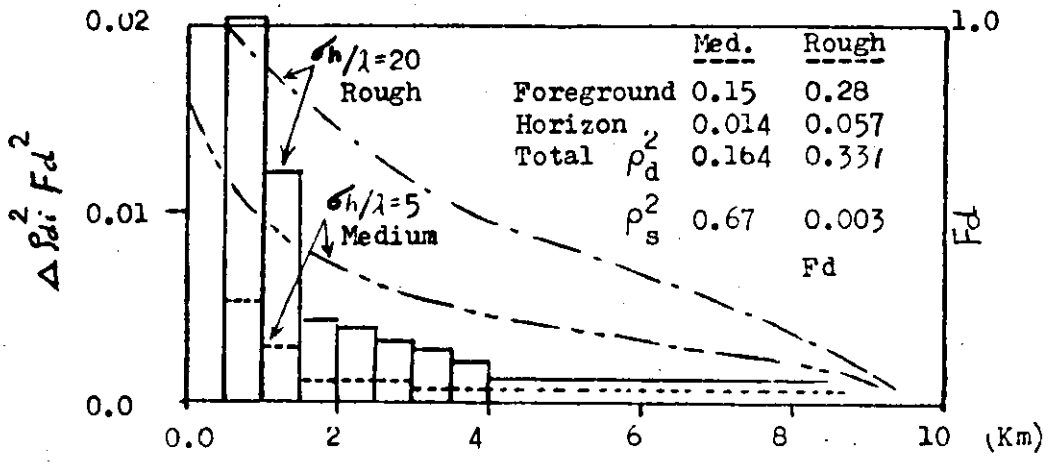

(b)

Figure 2-8: Diffused power distribution over a short ground range

(a): rough surface (ρ_s=0.0).

(b): effect of roughness factor for medium and rough surface (after Barton 2-13).

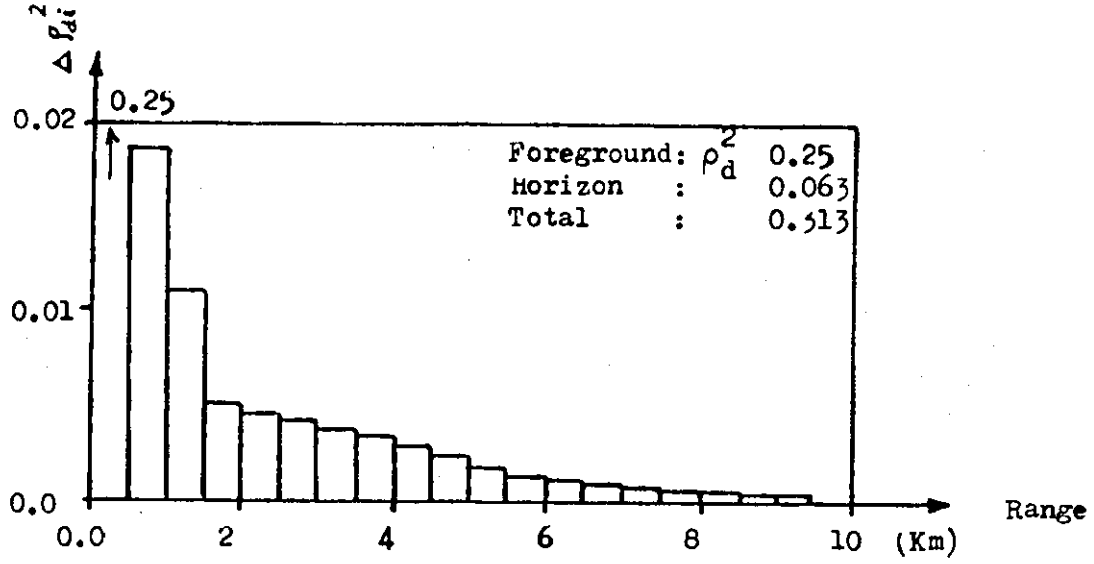

(a)

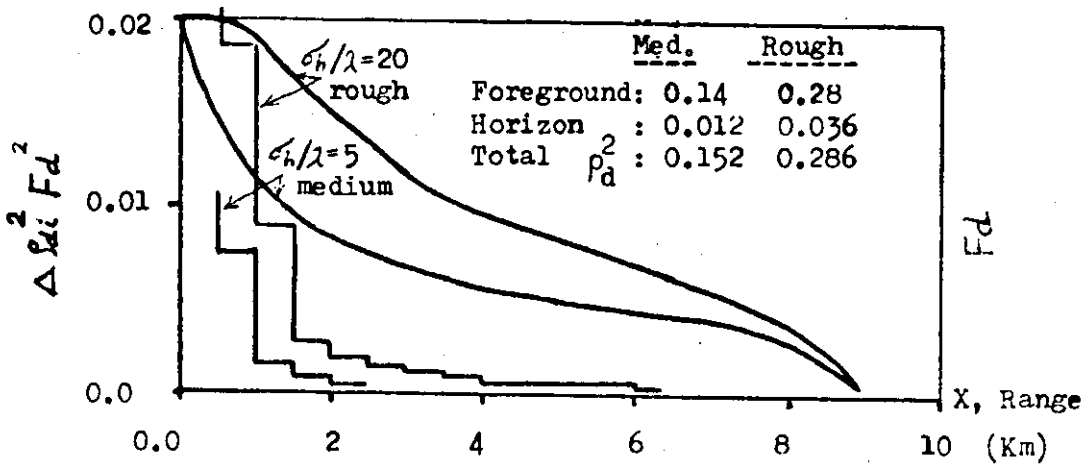

(b)

Figure 2-9: Diffused power distribution over a long ground range

(a): rough surface (ρ_s=0.0)

(b): effect of roughness factors for medium and rough surface (after Barton [2-13]).

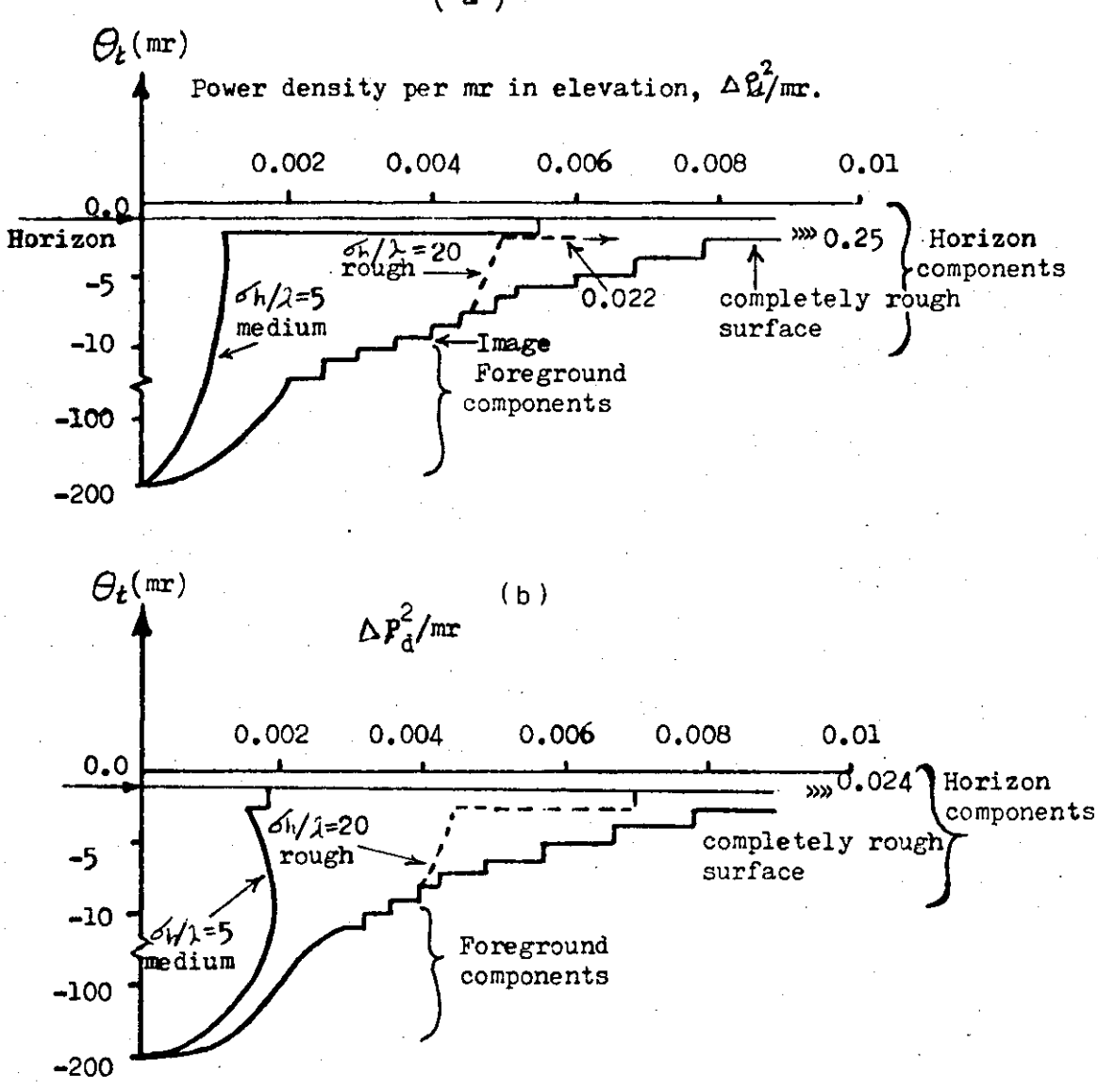

Figure 2-10: Diffused power distribution in elevation for completely rough, medium, and rough surface.

(a): short range target.

(b): long range target.

From [2-13].

some high resolution algorithms in the presence of diffuse and specular multipaths.

2-7.2 The slopes:

The rms slope of the facets overlying the large-scale pattern (β_o) is a very complicated function of the wind speed and direction over the sea. Its reduction would narrow the glistening surface and move its limits farther from the terminals (A & B), as can be seen from equation (2-33), but the net increase in the diffuse power is very small, and vice-versa [2-13].

2-7.3 The elevation angle:

The elevation angle has a big effect on the surface behaviour as shown in equation (2-19). When the elevation angle of the target decreases, the horizon component of Rd which, to some extent depends on the glistening surface widths, decreases and the value of Rs increases making the surface look smoother, and vice versa.

2-8 Depolarization:

Depolarization is the change of the reflected wave polarization from that of the incident one. So far, it is implicitly accepted that the reflected wave polarization is identical to that of the incident. Here we discuss in brief the extent to which this assumption is correct.

On the basis of theoretical work, Beckmann [2-2] proved that , when the incident wave is purely linearly polarized (vertically or horizontally), the reflected wave in the plane of incidence is not depolarized (specular reflection case), and, when the signal is scattered out of the plane of incidence, it is strongly depolarized (diffuse scattering case). Also in [2-4], a description of an experiment over the water surface is given where a pure linear polarization (vertical and horizontal) is transmitted. The received cross polarized scattered field is shown to be on the order of 25 dB below that of the incident field (no mention of the surface roughness is made). Also, the same experiment showed that the signals arriving from directions other than the specular reflection direction (Diffusely scattered field) were highly depolarized.

APPENDIX A2

(includes tables 1 to 7)

Table 1: The range distribution of the diffused power for β_o=0.05, h_r=5m, h_t=205m, R=10km, and σ_h/λ=5.

X_a (m)	X_b (m)	$\Delta\rho_d^2$ σ_h/λ=5	$\Delta\rho_d^2 Fd^2$ σ_h/λ=5	$-h_r/X$ (rad.)
50	250	0.41	0.3700	---------
250	750	0.137	0.0720	-0.010000
750	1250	0.051	0.0146	-0.005000
1250	1750	0.034	0.0067	-0.003333
1750	2250	0.027	0.0041	-0.002500
2250	2750	0.024	0.0029	-0.002000
2750	3250	0.022	0.0023	-0.001666
3250	3750	0.022	0.0019	-0.001428
3750	4250	0.022	0.0017	-0.001250
4250	4750	0.023	0.0016	-0.001111
4750	5250	0.024	0.0015	-0.001000
5250	5750	0.026	0.0015	-0.000909
5750	6250	0.029	0.0015	-0.000833
6250	6750	0.033	0.0015	-0.000769
6750	7250	0.038	0.0016	-0.000714
7250	7750	0.041	0.0017	-0.000666
7750	8000	0.013	0.0005	-0.000634

Total horizon component: $\Delta\rho_d^2$= 0.56, $\Delta\rho_d^2 Fd^2$= 0.189

Total forground component: $\Delta\rho_d^2$= 0.41, $\Delta\rho_d^2 Fd^2$= 0.37

Table 2: The range distribution of the diffused power for β_o=0.20, h_r=5m, h_t=205m, R=10km, and σ_h/λ=5.

X_a (m)	X_b (m)	$\Delta\rho_d^2$ σ_h/λ=5	$\Delta\rho_d^2 Fd^2$ σ_h/λ=5	$-h_r/X$ (rad.)
12.5	250	0.4490	0.4000	---------
250	750	0.0346	0.0181	-0.010000
750	1250	0.0129	0.0037	-0.005000
1250	1750	0.0087	0.0017	-0.003333
1750	2250	0.0070	0.0010	-0.002500
2250	2750	0.0062	0.0007	-0.002000
2750	3250	0.0058	0.0006	-0.001666
3250	3750	0.0057	0.0005	-0.001428
3750	4250	0.0058	0.0004	-0.001250
4250	4750	0.0061	0.0004	-0.001111
4750	5250	0.0066	0.0004	-0.001000
5250	5750	0.0074	0.0004	-0.000909
5750	6250	0.0085	0.0004	-0.000833
6250	6750	0.0103	0.0005	-0.000769
6750	7250	0.0129	0.0005	-0.000714
7250	7750	0.0172	0.0007	-0.000666
7750	8250	0.0250	0.0009	-0.000634
8250	8750	0.0411	0.0015	-0.000625
8750	9250	0.0826	0.0028	-0.000588

Total horizon component : $\Delta\rho_d^2$= 0.366, $\Delta\rho_d^2 Fd^2$= 0.0373

Total forground component: $\Delta\rho_d^2$= 0.449, $\Delta\rho_d^2 Fd^2$= 0.400

Table 3: The range distribution of the diffused power for β_o=0.1, h_r=5m, h_t=205m, R=10km, and σ_h/λ=5,20.

X_a (m)	X_b (m)	$\Delta\rho_d^2$ σ_h/λ=5	$\Delta\rho_d^2 Fd^2$ σ_h/λ=5	$\Delta\rho_d^2 Fd^2$ σ_h/λ=20	$-h_r/X$ (rad.)
25	250	0.417	0.3700	0.4170	--------
250	750	0.069	0.0362	0.0691	-0.010000
750	1250	0.025	0.0074	0.0230	-0.005000
1250	1750	0.017	0.0034	0.0123	-0.003333
1750	2250	0.014	0.0021	0.0080	-0.002500
2250	2750	0.012	0.0015	0.0058	-0.002000
2750	3250	0.011	0.0012	0.0046	-0.001666
3250	3750	0.011	0.0010	0.0039	-0.001428
3750	4250	0.011	0.0009	0.0035	-0.001250
4250	4750	0.012	0.0008	0.0033	-0.001111
4750	5250	0.013	0.0008	0.0032	-0.001000
5250	5750	0.014	0.0008	0.0032	-0.000909
5750	6250	0.016	0.0008	0.0034	-0.000833
6250	6750	0.019	0.0009	0.0038	-0.000769
6750	7250	0.024	0.0011	0.0044	-0.000714
7250	7750	0.032	0.0013	0.0053	-0.000666
7750	8250	0.044	0.0017	0.0069	-0.000634
8250	8750	0.061	0.0023	0.0094	-0.000625
8750	8975	0.028	0.0010	0.0040	-0.000580

Total horizon component : $\Delta\rho_d^2$= 0.433

Total forground component: $\Delta\rho_d^2$= 0.417

Table 4: The range distribution of the diffused power for β_o=0.05, h_r=5m, h_t=105m, R=10km, and σ_h/λ=5.

X_a (m)	X_b (m)	$\Delta\rho_d^2$ σ_h/λ=5	$\Delta\rho_d^2 Fd^2$ σ_h/λ=5	$-h_r/X$ (rad.)
50	500	0.454	0.2350	---------
500	1000	0.045	0.0116	-0.006666
1000	1500	0.024	0.0039	-0.004000
1500	2000	0.017	0.0021	-0.002857
2000	2500	0.014	0.0014	-0.002222
2500	3000	0.013	0.0011	-0.001818
3000	3500	0.012	0.0009	-0.001538
3500	4000	0.012	0.0008	-0.001333
4000	4500	0.012	0.0008	-0.001176
4500	5000	0.013	0.0008	-0.001052
5000	5500	0.014	0.0008	-0.000952
5500	6000	0.016	0.0008	-0.000869
6000	6500	0.018	0.0009	-0.000800
6500	7000	0.022	0.0010	-0.000740
7000	7500	0.028	0.0012	-0.000689
7500	8000	0.038	0.0015	-0.000645
8000	8500	0.054	0.0020	-0.000606
8500	9000	0.070	0.0025	-0.000570

Total horizon component: $\Delta\rho_d^2$= 0.42, $\Delta\rho_d^2 Fd^2$= 0.034

Total forground component: $\Delta\rho_d^2$= 0.45, $\Delta\rho_d^2 Fd^2$= 0.235

Table 5: The range distribution of the diffused power for β_o=0.20, h_r=5m, h_t=105m, R=10km, and σ_h/λ=5.

X_a (m)	X_b (m)	$\Delta\rho_d^2$ σ_h/λ=5	$\Delta\rho_d^2 Fd^2$ σ_h/λ=5	$-h_r/X$ (rad.)
12.5	500	0.4770	0.2529	---------
500	1000	0.0115	0.0029	-0.006666
1000	1500	0.0060	0.0009	-0.004000
1500	2000	0.0043	0.0005	-0.002857
2000	2500	0.0036	0.0004	-0.002222
2500	3000	0.0032	0.0003	-0.001818
3000	3500	0.0031	0.0002	-0.001538
3500	4000	0.0030	0.0002	-0.001333
4000	4500	0.0032	0.0002	-0.001176
4500	5000	0.0033	0.0002	-0.001052
5000	5500	0.0036	0.0002	-0.000952
5500	6000	0.0041	0.0002	-0.000869
6000	6500	0.0048	0.0002	-0.000800
6500	7000	0.0060	0.0003	-0.000740
7000	7500	0.0077	0.0003	-0.000689
7500	8000	0.0108	0.0004	-0.000645
8000	8500	0.0167	0.0006	-0.000606
8500	9000	0.0311	0.0011	-0.000570
9000	9500	0.0840	0.0028	-0.000540
9500	9740	0.1150	0.0037	-0.000519

Total horizon component : $\Delta\rho_d^2$= 0.323, $\Delta\rho_d^2 Fd^2$= 0.0156

Total forground component: $\Delta\rho_d^2$= 0.477, $\Delta\rho_d^2 Fd^2$= 0.2529

Table 6: The range distribution of the diffused power for β_o=0.1, h_r=5m, h_t=105m, R=10km, and σ_h/λ=5,20.

X_a (m)	X_b (m)	$\Delta\rho_d^2$ σ_h/λ=5	$\Delta\rho_d^2 Fd^2$ σ_h/λ=5	σ_h/λ=20	$-h_r/X$ (rad.)
25	500	0.4678	0.2478	0.4677	--------
500	1000	0.0229	0.0058	0.0222	-0.006666
1000	1500	0.0120	0.0019	0.0095	-0.004000
1500	2000	0.0087	0.0010	0.0055	-0.002857
2000	2500	0.0075	0.0007	0.0037	-0.002222
2500	3000	0.0065	0.0006	0.0028	-0.001818
3000	3500	0.0062	0.0005	0.0023	-0.001538
3500	4000	0.0061	0.0004	0.0020	-0.001333
4000	4500	0.0063	0.0004	0.0018	-0.001176
4500	5000	0.0067	0.0004	0.0017	-0.001052
5000	5500	0.0073	0.0004	0.0017	-0.000952
5500	6000	0.0082	0.0004	0.0017	-0.000869
6000	6500	0.0097	0.0005	0.0019	-0.000800
6500	7000	0.0118	0.0005	0.0022	-0.000740
7000	7500	0.0153	0.0006	0.0026	-0.000689
7500	8000	0.0211	0.0008	0.0034	-0.000645
8000	8500	0.0324	0.0012	0.0049	-0.000606
8500	9000	0.0578	0.0020	0.0082	-0.000570
9000	9500	0.1285	0.0040	0.0173	-0.000542

Total horizon component : $\Delta\rho_d^2$= 0.3732

Total forground component: $\Delta\rho_d^2$= 0.4678

Table 7: The range distribution of the diffused power for β_o=0.1, h_r=5m, h_t=1000m, R=100km, and σ_h/λ=5,20.

X_a (m)	X_b (m)	$\Delta\rho_d^2$ σ_h/λ=5	$\Delta\rho_d^2 Fd^2$ σ_h/λ=5	$\Delta\rho_d^2 Fd^2$ σ_h/λ=20	$-h_r/X$ (rad.)
25	500	0.46030	0.23000	0.45990	--------
500	1000	0.02000	0.00463	0.01947	-0.006666
1000	1500	0.00948	0.00135	0.00755	-0.004000
1500	2000	0.00615	0.00063	0.00390	-0.002857
2000	2500	0.00456	0.00036	0.00235	-0.002222
2500	3000	0.00363	0.00024	0.00157	-0.001818
3000	3500	0.00302	0.00017	0.00112	-0.001538
3500	4000	0.00259	0.00012	0.00084	-0.001333
4000	4500	0.00228	9.94E-5	0.00066	-0.001176
4500	5000	0.00203	7.98E-5	0.00053	-0.001052
5000	5500	0.00184	6.57E-5	0.00043	-0.000952
5500	6000	0.00169	5.51E-5	0.00036	-0.000869
6000	6500	0.00156	4.70E-5	0.00031	-0.000800
6500	7000	0.00145	4.07E-5	0.00027	-0.000740
7000	7500	0.00136	3.56E-5	0.00023	-0.000689
7500	8000	0.00128	3.15E-5	0.00021	-0.000645
8000	8500	0.00121	2.81E-5	0.00018	-0.000606
8500	9000	0.00115	2.53E-5	0.00016	-0.000570
9000	9500	0.00110	2.29E-5	0.00015	-0.000542
9500	10000	0.00105	2.09E-5	0.00013	-0.000512

Chapter 3

The Maximum Likelihood Estimator

3-1 Introduction

The difficulty in tracking low-flying targets using conventional tracking methods arises from the presence of a strong surface reflection (specular multipath). White [3-1] discussed this problem in considerable detail. Starting with a classical maximum likelihood analysis of two closely spaced targets, he developed two techniques which are capable of dealing with this problem. In a more recent paper, Cantrell et al. [3-2] studied the problem by applying a closed form of the maximum likelihood estimator to an array divided equally into three subapertures (3SA-MLE). They have shown that the use of this technique gives a performance for resolution of close coherent sources (targets) very near to the optimum obtainable from the aperture were all the elements sampled individually, the loss mounting to one or two dBs equivalent SNR. The snag with the technique is that this good performance is only obtainable for sources which are close to quadrature at the array centre and the performance deteriorates rapidly if the relative source phases approach 0 or Π. The best solution to this problem is to use four

subapertures but the cost involved in this are considerable since the closed form solution for the 3SA-MLE is excessively complex. Moreover it is desirable to keep the simple processing of [3-2] if at all possible.

The technique which has been evolved to handle this situation is to divide the aperture into four groups but use these subapertures in two sets of three, one at each end of the array. The reason for this is that if the two signals are in-phase or anti-phase at the centre of one of the sets they cannot be so phased at the centre of the other if the source bearings are different and one or other of the sets will give an acceptable performance. To use this technique a method for determining which of the sets has the best chance of resolving the sources must be found and this seemed impossible until, as a result of simulations it was found that if the sources are actually in-phase or anti-phase at the set phase centre and the complex amplitudes of the sources are computed within the Cantrell-type algorithm then the relative phase will be indicated correctly. Thus by processing both of the sets and selecting the one which has the most promising indicated signal phases a good performance might be expected.

The main purpose of this chapter is to explore this possibility in detail, starting with a complete study of the 3SA-MLE for different values of ρ_s, S/N, and angular distance between the two targets. The effect of the target's type and the accuracy in estimating the phase difference between the two signals is presented in detail.

3-2 The maximum likelihood formulation for two target and three subapertures

In order to keep our discussion self-contained, and to make it easier to introduce some new remarks about solving the problem of inphase and anti-phase signals, we briefly review the three subapertures method by Cantrell et al.[3-2]. In this method a 21 element, equally spaced linear array (elements spacing is $\lambda/2$) is divided equally into three subapertures (each of 7 elements). Assuming a uniform amplitude weighting is used, the subaperture pattern can be approximated by:

$$G(\theta-\theta_p)=(d/\lambda)[\sin(\pi\Omega d/\lambda)]/(\pi\Omega d/\lambda) \qquad (3-1)$$

where d is the subaperture spacing as shown in figure 3-1, θ_p is the pointing angle of the beams relative to the horizon, and $\Omega=\sin(\theta)-\sin(\theta_p)$.

In the presence of a coherent multipath (specular reflection) the output signals S_1, S_2 and S_3 from the three subapertures can be represented by:

$$S_1= a_1 G_1 \exp(+jZ_1) + a_2 G_2 \exp(+jZ_2) + n_1$$

$$S_2= a_1 G_1 + a_2 G_2 + n_2 \qquad (3-2)$$

$$S_3= a_1 G_1 \exp(-jZ_1) + a_2 G_2 \exp(-jZ_2) + n_3$$

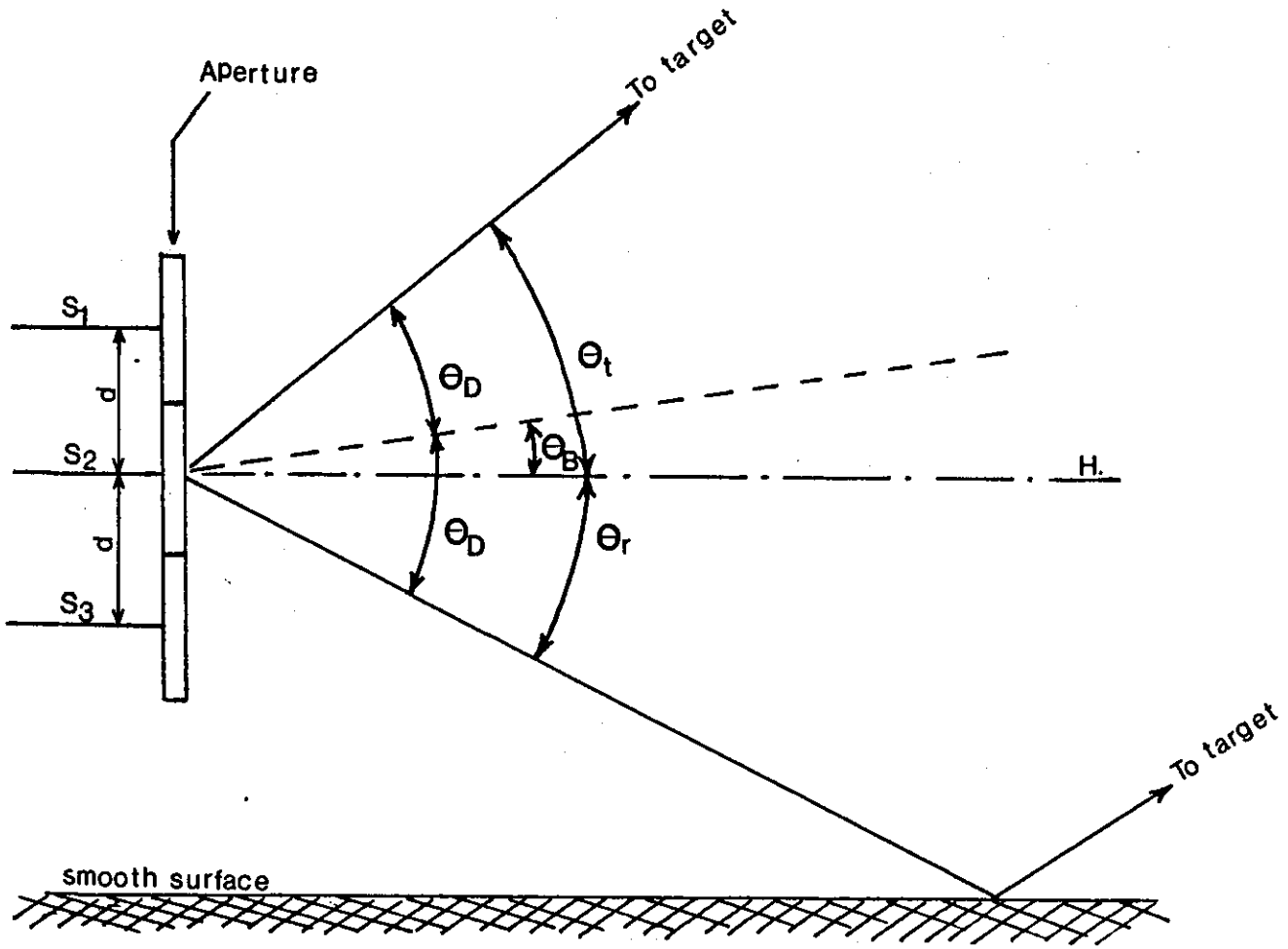

Figure 3-1 : The geometry of the three-subapertures array and two sources (target and its image).

where:

$$G_1 = G(\theta_t - \theta_p) \qquad (3\text{-}3)$$

$$G_2 = G(\theta_r - \theta_p) \qquad (3\text{-}4)$$

$$Z_1 = 2\,\Pi\,d\,\theta_t/\lambda \qquad (3\text{-}5)$$

$$Z_2 = 2\,\Pi\,d\,\theta_r/\lambda \qquad (3\text{-}6)$$

where:

- $\sin(\theta_t) \simeq \theta_t$ and $\sin(\theta_r) \simeq \theta_r$ for small angles is assumed in (3-5) and (3-6) respectively.
- G_1 and G_2 are the subaperture gains in the direction of the target and the specular multipath respectively.
- a_1 and a_2 are the complex amplitudes of the direct signal and its coherent multipath respectively ($a_2=\rho_s\ a_1$).
- θ_t and θ_r are the target and multipath angles measured from the horizon.
- The reference phase center is taken at the centre of the array (at the middle subaperture).
- n_1, n_2 and n_3 are the Gaussian complex noise samples with zero mean and variance of σ^2.

In order to present (3-2) in a vector form we make the following simplification:

$$A_i = a_i\ G_i \quad , \quad \text{where } i=1,2$$

and the vector form

$$S = W A + N$$

$$S = \begin{bmatrix} s_1 \\ s_2 \\ s_3 \end{bmatrix} \quad , \quad W = \begin{bmatrix} w_{11} & w_{12} \\ w_{21} & w_{22} \\ w_{31} & w_{32} \end{bmatrix} \quad , \quad A = \begin{bmatrix} A_1 \\ \\ A_2 \end{bmatrix}$$

$$N^T = \begin{bmatrix} n_1 & n_2 & n_3 \end{bmatrix}$$

Where T represents the transpose, and the coefficients w_{ki} represent the phase progression along the array for each angle of arrival at the center of each subaperture.

$$w_{ki} = \exp [j(2-k) Z_i] \qquad (3\text{-}7)$$

$k = 1,2,3$ and $i=1,2$

where in the matrix W the first column contains the phase progression of the first source (target), and the second column represents the phase progression for the second source (specular multipath).

$$w_1 = \exp (j2 \Pi d \theta_t/\lambda) \qquad (3\text{-}8)$$

$$w_2 = \exp (j2 \Pi d \theta_r/\lambda) \qquad (3\text{-}9)$$

Since θ_t, θ_r, w_1 and w_2 are related to each other through (3-8) and (3-9), then solving for the best estimate of w_1 and w_2 is sufficient.

Knowing that the complex noise vector N is a Gaussian random process, then minimizing the square error is equivalent to maximizing the likelihood function [3-2].

$$L = (S - W A)^* (S - W A) \tag{3-10}$$

where * represents the complex conjugate transpose. If W is known, then the value of A which minimizes (3-10) is given by [3-2] as follow:

$$A = (W^* W)^{-1} W^* S \tag{3-11}$$

by expanding the term in (3-11) we get:

$$A = \begin{bmatrix} A_1 \\ \\ A_2 \end{bmatrix} = 1/G \begin{bmatrix} 2w_1^* - w_1 w_2^{*2} - w_2^* & 2w_2^* - w_2 w_1^{*2} - w_1^* \\ 2 - w_1^* w_2 - w_2^* w_1 & 2 - w_1^* w_2 - w_2^* w_1 \\ 2w_1 - w_1^* w_2^2 - w_2 & 2w_2 - w_1^2 w_2^* - w_1 \end{bmatrix}^T \begin{bmatrix} s_1 \\ \\ s_2 \\ \\ s_3 \end{bmatrix} \tag{3-12}$$

$$G=9-(3+2w_1w_2^*+2w_2w_1^*+w_1^2w_2^{*2}+w_1^{*2}w_2^2) \tag{3-13}$$

L can be written as follow from [3-2].

$$L=(1/\sigma^2)\sum_{k=1}^{3} f_k^2 \tag{3-14}$$

$$f_k= S_k-(w_1^*)^{k-1} A_1 - (w_2^*)^{k-1} A_2 \tag{3-15}$$

by substituting (3-12) into (3-14) and (3-15), then the square error can be reduced to the following simple expression.

$$L=\left|S_1 - (w_1+w_2) S_2 + w_1w_2 S_3\right|^2/(2+\left|w_1+w_2\right|^2) \tag{3-16}$$

Figure 3-2 shows the combining network which produce L and figure 3-3 shows the combined three subaperture beam pattern associated with it. As can be seen from figure 3-3, two nulls are produced in the direction of θ_t and θ_r (this is similar to the normal monopulse performance in case one target is present). Consequently, if the values of w_1 and w_2 which make L small can be determined then two nulls will be produced at both angles of arrival, θ_t and θ_r.

Close examination of L will show that its denominator represents the noise power output from the combining network in the absence of signal, while its numerator represents the signal output power in the absence of noise.

In order to simplify the discussion, let us represent the direct angle θ_t and the multipath one θ_r in terms of a

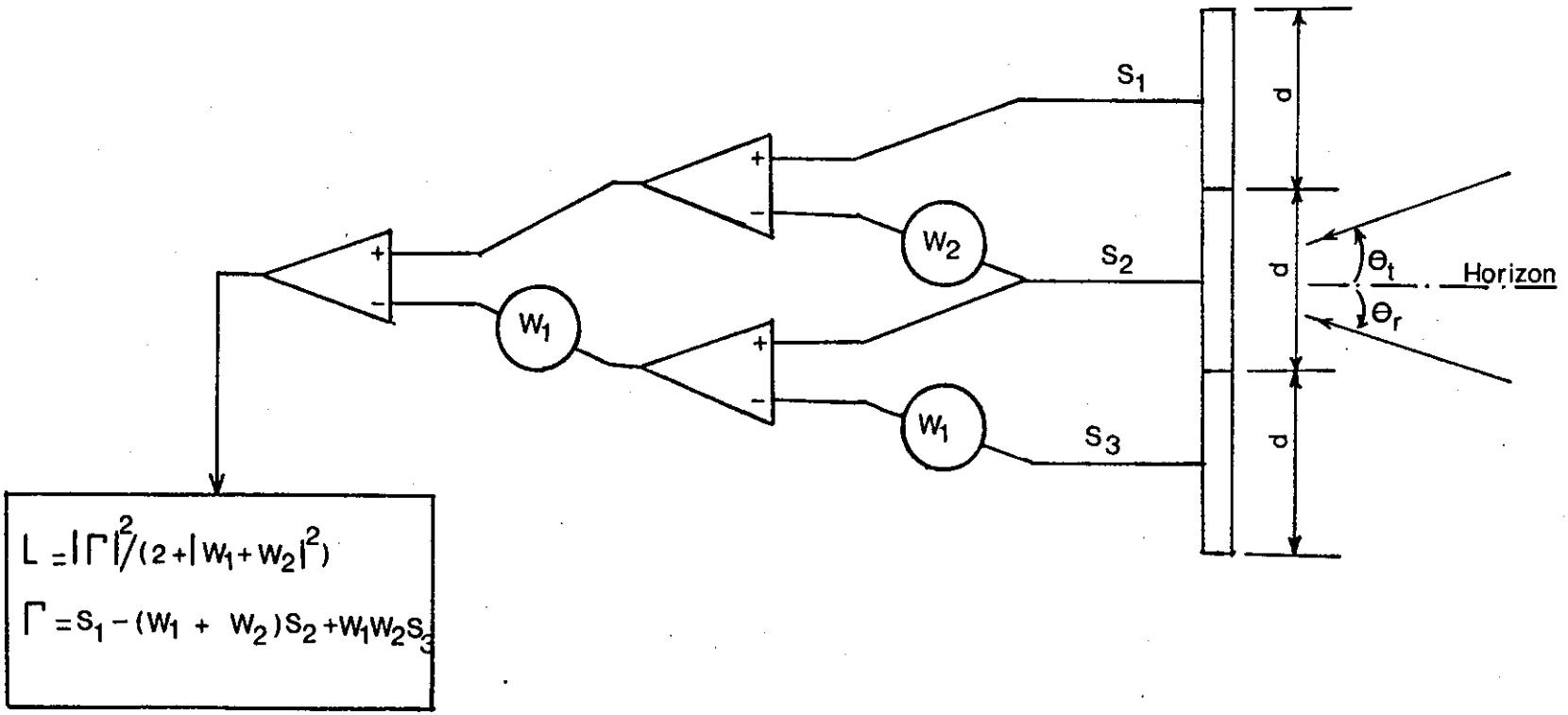

Figure 3-2 : Circuit implementation of the three-subapertures MLE and two sources.

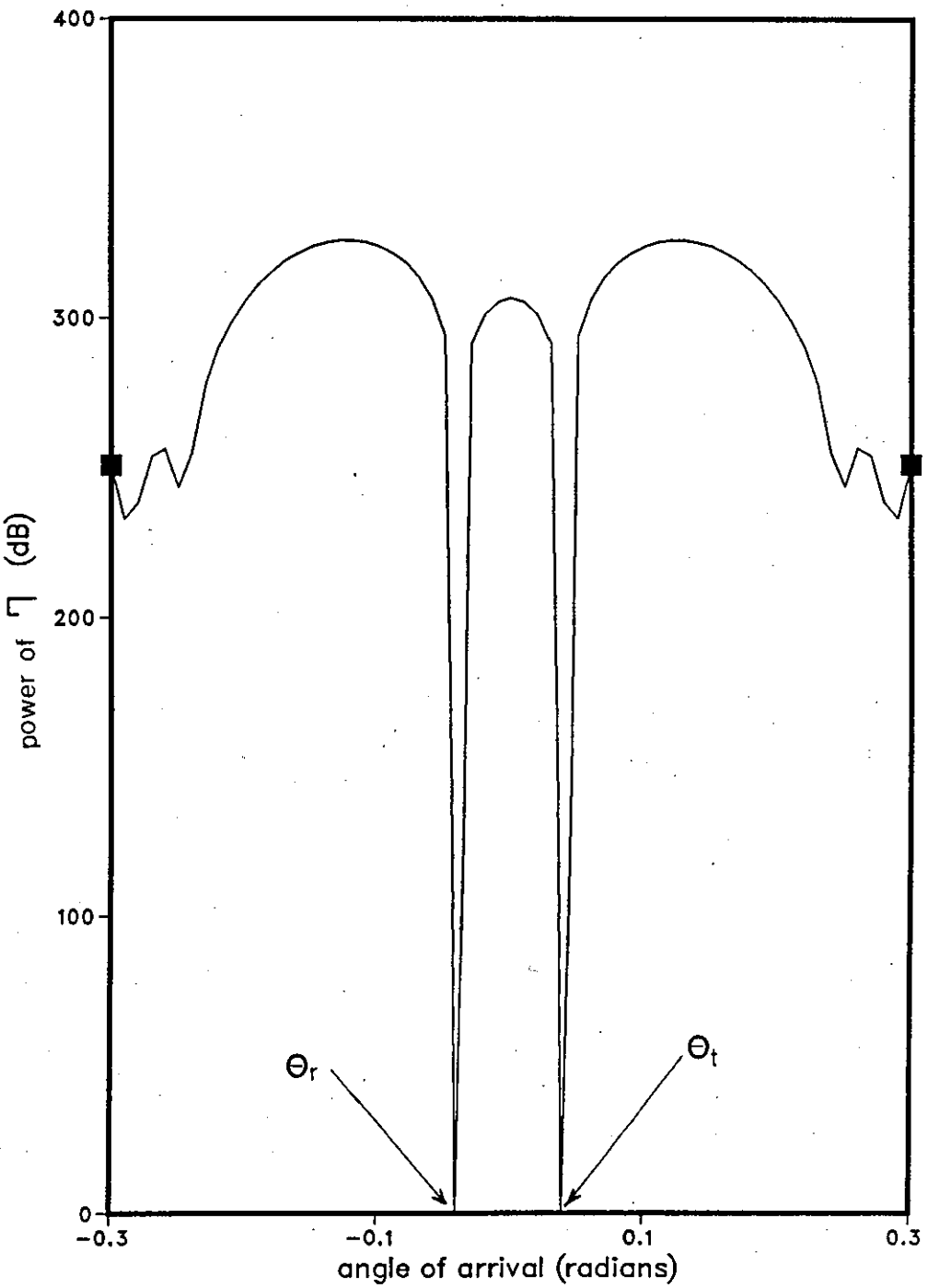

Figure 3−3 : The antenna pattern for the circuit implementation in figure 3−2 of the 3SA−MLE, where the two nulls at ∓ 0.04 radians represent the angular positions of the two sources

bisecting angle (θ_B) and an angular distance angle (θ_D) from the bisector.

$$\theta_t = \theta_B + \theta_D \tag{3-17}$$

$$\theta_r = \theta_B - \theta_D \tag{3-18}$$

consequently

$$w_1 = w_B\, w_D \tag{3-19}$$

$$w_2 = w_B\, w_D^* \tag{3-20}$$

and the square error L becomes as follow:

$$L = \left| S_1 - w_B(w_D + w_D^*) S_2 + w_B^2 S_3 \right|^2 / (2 + \left| w_D + w_D^* \right|^2) \tag{3-21}$$

The problem is to minimize L with respect to the following constraints:

$$w_B w_B^* = 1 \tag{3-22}$$

$$w_D w_D^* = 1 \tag{3-23}$$

Gordon [3-3] introduces additional constraints by considering the reflection coefficient of the surface to be less than one. The purpose of this is to improve the algorithm performance when the two signals are inphase and the signal -to-noise ratio is maximum.

In the following, the MLE solution for the two targets and three subapertures geometry is shown for the symmetric and nonsymmetric cases respectivelly.

3-2.1 Symmetric case solution:

In this case w_B is known a priori and the critical points of w_D (the points of zero slope of L satisfying the condition $w_D w_D^* = 1$) are given by the following from [3-2]:

$$w_D = 1 \tag{3-24}$$

$$w_D = -1 \tag{3-25}$$

$$w_D = V/2 \mp j\sqrt{1 - (V/2)^2} \tag{3-26}$$

where V is any root to the following equation which satisfies the condition

$$V<2$$

$$V^2 + 2[(2-|R_t|^2)/(R_t+R_t^*)]V - 2 = 0 \tag{3-27}$$

and R_t is given by:

$$R_t = (S_1 + w_B^2 S_3)/w_B S_2 \tag{3-28}$$

The value of L must be evaluated for each critical point of w_D and the one providing the absolute minimum value of L gives the best estimate of the angle of arrival.

$$\theta_t = [\lambda/(2\pi d)] \tan^{-1}[\mathrm{Im}(w_D w_B)/\mathrm{Re}(w_D w_B)] \tag{3-29}$$

There are two special cases which occur with probability zero. The first occurs when $S_2=0$ and the

minimum value of L is attained at both values w_D=1 and w_D=-1. The second special case occurs when the imaginary part of R_t is zero, the real part is less than two, S_2 is not zero, and L can be made zero by setting V = R_t. This case occurs when there is no noise added to the received signals. More details of the minimization process for the function L is given in [3-2] and appendix A3.

3-2.2 The nonsymmetric case solution:

In this case w_B and w_D are not known and we have to estimate both of them. The solution is given in [3-2] by:

$$U = (|S_3|^2 - |S_1|^2)/(S_2 S_3^* - S_1 S_2^*) \qquad (3\text{-}30)$$

when the absolute value of U is less than or equal to two, then the values of w_D and w_B which minimize L subject to the constraints $w_D w_D^*$=1 and $w_B w_B^*$=1 are as follow:

$$w_B = |U|/U \qquad (3\text{-}31)$$

$$w_D = (|U|/2) \pm j\sqrt{1-|U|^2/4} \qquad (3\text{-}32)$$

when the absolute value of U is bigger than two then the solution will be:

$$w_D = 1 + j0 \qquad (3\text{-}33)$$

and w_B is one of the following quartic equation roots

$$\alpha w_B^4 - \alpha_g w_B^3 + \alpha_g w_B - \alpha^* = 0 \tag{3-34}$$

where:

$$\alpha_g = S_1^* S_2 + S_2^* S_3 \tag{3-35}$$

$$\alpha = S_1^* S_3 \tag{3-36}$$

A detailed discussion is given in appendix B3 and a simulation result for the symmetric and nonsymmetric cases are shown in a later section to demonstrate the performance of this algorithm (3SA-MLE) according to S/R, reflection coefficient, and the nonsymmetry condition. Also, its performance in the presence of diffuse multipath is simulated according to the theory given in chapter 2; and compared with other algorithms performances in chapter 6.

3-3 The four subapertures technique

Simulation results in figures 3-8, 3-14, and reference [3-2] have shown that the good performance of the 3SA-MLE is only obtainable when the phase difference (Ψ) between the two coherent sources (target and image) at the centre of the aperture is close to quadrature ($\pi/4$ to $3\pi/4$) and declines very rapidly when Ψ approaches 0 or π (only π in the symmetric case). It is shown in figure 3-8 that the performance accuracy is very high when $\Psi=0$ for the symmetric case; however this condition is not always possible and the general case is the nonsymmetric one. One way of improving the performance at Ψ equal zero or π at the array centre is to change these values to others as close as possible to quadrature where the best estimate of the angle occurs. This is done by dividing the array into four subarrays (subapertures) using them in two sets of three, one at each end of the array as shown in figure 3-4. The first set (AP1) outputs are s_1, s_2, and s_3; and the second set (AP2) outputs are s_2, s_3, and s_4. The idea behind dividing the aperture into two separate sets in processing is to enable us to compare between the values of Ψ at the centre of each set and chose the one closer to quadrature. This is done by processing both sets of apertures according to the 3SA-MLE by Cantrell et al.[3-2] in parallel. The worst performance of the four subapertures technique (4SA-MLE) is when Ψ equals 0 or π at the centre of the four subapertures where the phase difference at the centre of both sets is equal. In the

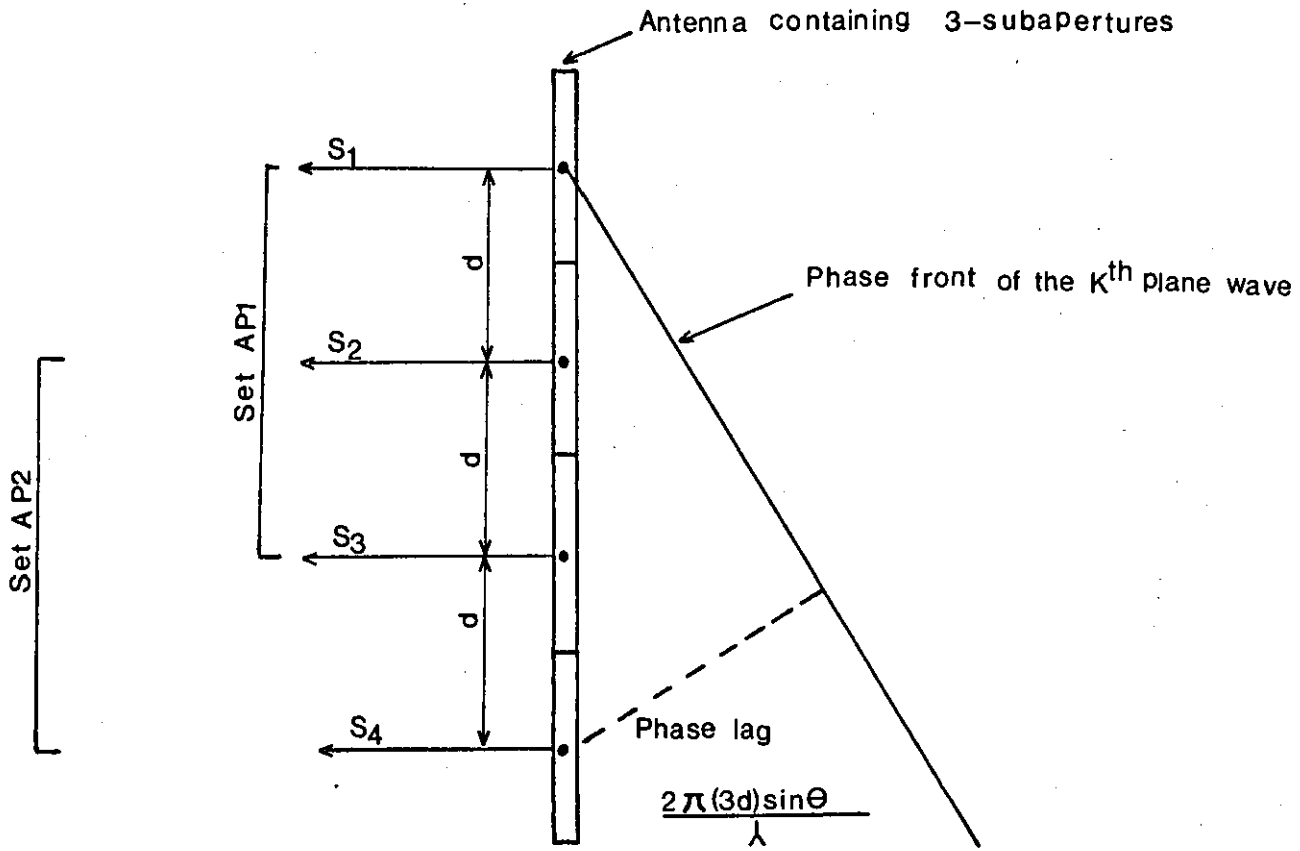

Figure 3-4 : The geometry of four-subapertures array divided into two sets of three (AP1 & AP2).

following, a mathematical and operational analysis for the four subapertures technique is carried out.

Let us assume that the phase centre is at the middle of the four subapertures array. The output of each subaperture is given by the following:

$$s_m = a_1 G_1 \exp[j(5/2 - m)Z_1] + a_2 G_2 \exp[j(5/2 - m)Z_2] \quad (3\text{-}37)$$

where m=1,4

By applying the 3SA-MLE solution in section 3-2 on both of AP1 and AP2 separately we get.

for AP1

$$S = \begin{bmatrix} s_1 \\ s_2 \\ s_3 \end{bmatrix}, \quad A = \begin{bmatrix} A_1 \\ \\ A_2 \end{bmatrix}, \quad W = \begin{bmatrix} (w_1^*)^{3/2} & (w_2^*)^{3/2} \\ (w_1^*)^{1/2} & (w_2^*)^{1/2} \\ w_1^{1/2} & w_2^{1/2} \end{bmatrix}$$

and the cost function L can be calculated according to (3-14) and (3-15) and given by:

$$L = \left| s_1 - w_B(w_D + w_D^*)s_2 + w_B^2 s_3 \right|^2 / (2 + |w_D + w_D^*|^2) \quad (3\text{-}38)$$

and for AP2

$$S = \begin{bmatrix} s_2 \\ s_3 \\ s_4 \end{bmatrix}, \quad A = \begin{bmatrix} A_1 \\ \\ A_2 \end{bmatrix}, \quad W = \begin{bmatrix} (w_1^*)^{1/2} & (w_2^*)^{1/2} \\ w_1^{1/2} & w_2^{1/2} \\ w_1^{3/2} & w_2^{3/2} \end{bmatrix}$$

and the cost function L is as in (3-38) except that s_2, s_3, and s_4 must replace s_1, s_2, and s_3 respectively and is given by:

$$L = \left| s_2 - w_B(w_D + w_D^*)s_3 + w_B^2 s_4 \right|^2 / (2 + |w_D + w_D^*|^2) \qquad (3\text{-}39)$$

where the symmetric and nonsymmetric sources case studies for AP1 and AP2 are the same as in 3-2.1 and 3-2.2 and will not be repeated here. The phase difference Ψ calculation procedure at the centres of AP1 and AP2 can be done as follows:

a- Minimize the cost function L in (3-38) for AP1 and in (3-39) for AP2 independently according to the constraints given in section 3-2 for the case of interest (i.e symmetric or nonsymmetric) and chose the absolute minimum which gives the best angle estimate for each set.

b- The values of w_1 and w_2 can be calculated for each set independently from the corresponding w_B and w_D through (3-19) and (3-20) respectively.

c- The values of a_1 and a_2 for both of AP1 and AP2 can be

easily calculated by substituting the estimated values of w_1 and w_2 in any two of the input equations in (3-37)

d- The calculated values of a_1 and a_2 for both of AP1 and AP2 are complex variables which can be represented by amplitude and phase as follows:

$$a_1=a_{1r}+ja_{1j}=|a_1|\exp(j\Psi_1) \qquad (3-40)$$

$$a_2=a_{2r}+ja_{2j}=|a_2|\exp(j\Psi_2) \qquad (3-41)$$

where the subscripts r and j are to represent the real and imaginary parts of a_1 and a_2 respectively; also Ψ_1 and Ψ_2 are the associated phases. By calculating the phase difference ($\Psi=\Psi_1-\Psi_2$) for both of AP1 and AP2 at their local centres separately and considering the closest one to quadrature (the closest to 0° in the symmetric case), then the corresponding aperture (i.e AP1 or AP2) would give the best angle estimate. Figures 3-5 and 3-6 show illustrating block diagram for these procedures for the symmetric and nonsymmetric cases respectively.

In fact, it is not necessary to go through the previous lengthy processing to the end if the target and its image are symmetric, and a simpler method of solution does exist. For the symmetric case our main concern is when the two coherent signals are in phase opposition at the centre of the aperture where destructive interference takes place and the overall signal amplitude at the central subaperture is very small (especially when the amplitudes of the two signals are close) in comparison with that of the other two subapertures at its

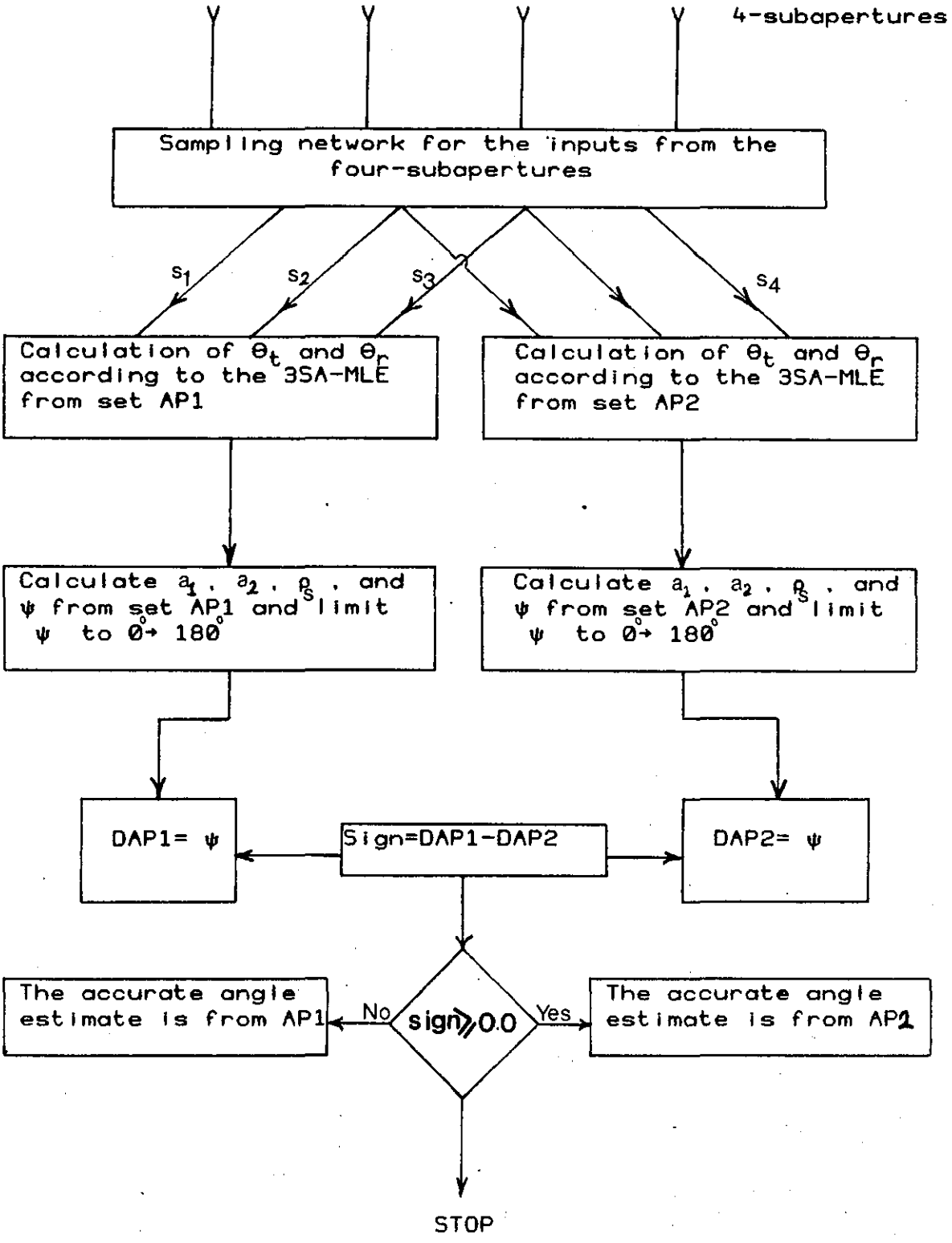

Fig. 3-5 : Block diagram represents the four-subapertures processing technique for the symmetric case.

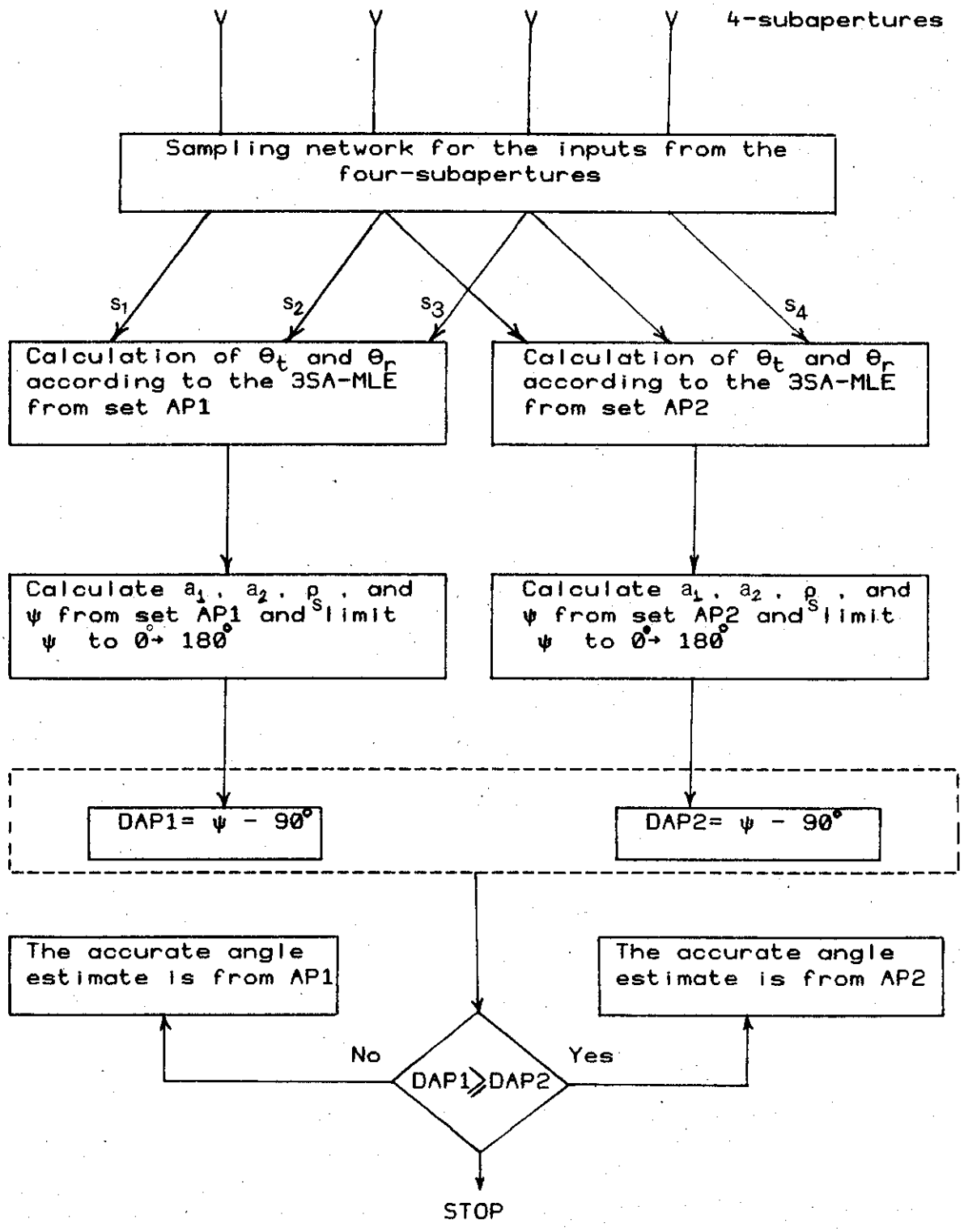

Fig. 3-6 : Block diagram represents the four-subapertures processing technique for the nonsymmetric case.

sides. So, by comparing the amplitude of the central subaperture of AP1 ($|s_2|$) with that of the central subaperture of AP2 ($|s_3|$) and considering the aperture (i.e AP1 or AP2) which gives the higher amplitude then it would be the one which gives better angle estimation too. Figure 3-7 shows a block diagram presentation for this case which saves much unnecessary work load.

A new simple procedure to find out whether the two coherent signals from the target and its image are in-phase or phase opposition is shown in chapter 4 as a part of new simple trigonometric method to solve the multipath problem.

3-3.1 The phase shift formulation

The geometry of a linear array and two sources is shown in figure 3-21. The elements spacing is a half wavelength and the phase reference is taken at the edge element for convenience. By moving along the array the phase difference between the two incident signals (Ψ) will change as a function of θ_t and θ_r and the distance moved (the distance moved is $n\lambda/2$; where n=1,N; and N is the number of elements in the array). The change in Ψ can easily be found by calculating the phase lag for each source as follows:

For the first source:

$$\Psi_{t1}=\Psi_{t\emptyset}+2\pi(n\lambda/2)\sin(\theta_t)/\lambda \qquad (3\text{-}42)$$

For the second source:

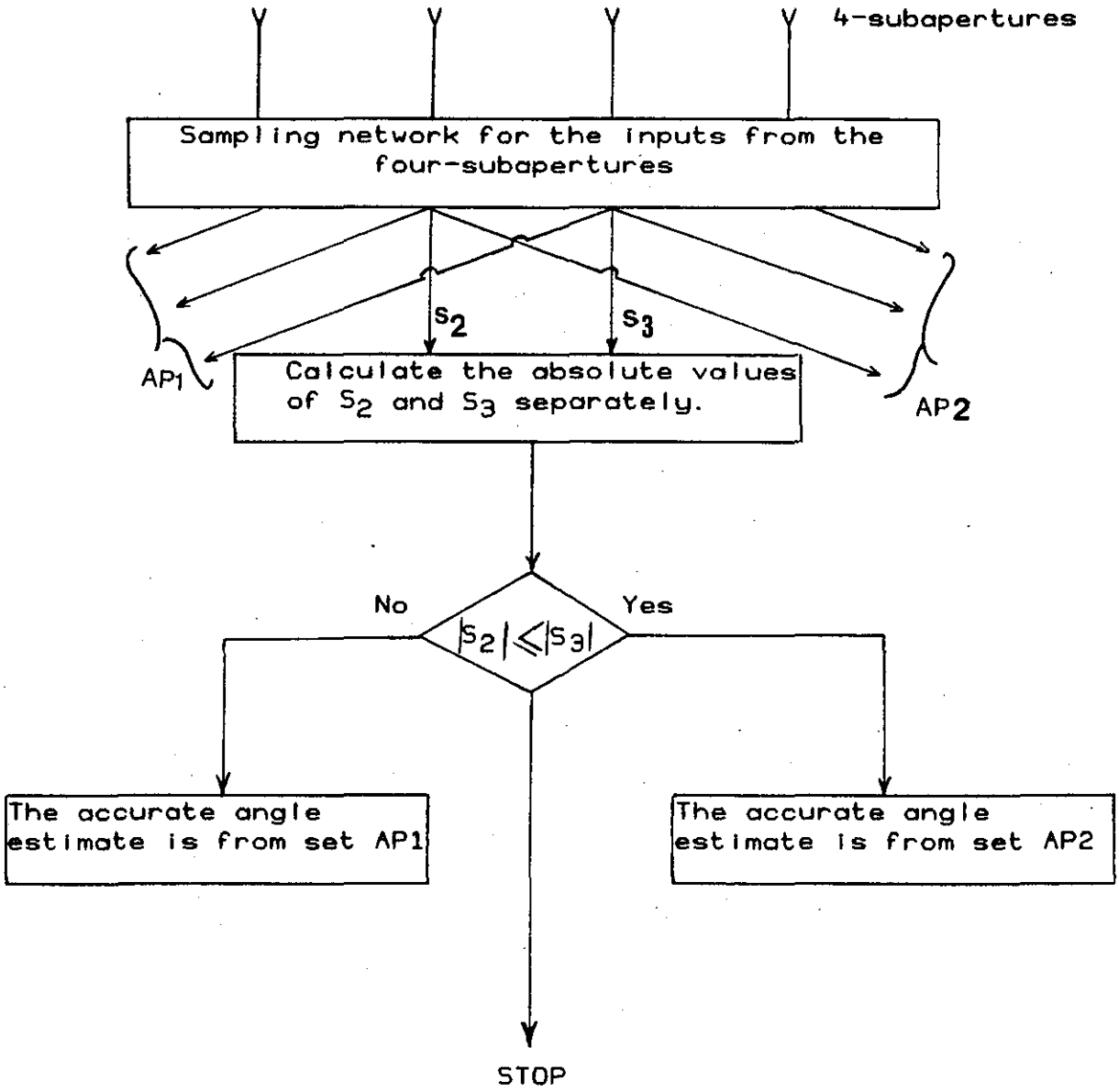

Fig. 3-7 : Block diagram represents the four-subapertures processing technique for the symmetric case using the amplitudes comparison method.

$$\Psi_{r1}=\Psi_{r\emptyset}+2\pi(n\lambda/2)\sin(\theta_r)/\lambda \qquad (3\text{-}43)$$

where $\Psi_{t\emptyset}$ and $\Psi_{r\emptyset}$ are the reference phases for the first and second source respectively and Ψ_{t1}, Ψ_{r1} are the new ones.

By subtracting (3-43) from (3-42) and making the proper cancellations we get the new phase difference.

$$\Psi_{t1}-\Psi_{r1}=\Psi_{t\emptyset}-\Psi_{r\emptyset}+n\pi[\sin(\theta_t)-\sin(\theta_r)] \qquad (3\text{-}44)$$

and the change in the value of Ψ is $\Delta\Psi$

$$\Delta\Psi=\Psi_{t1}-\Psi_{r1}-\Psi_{t\emptyset}+\Psi_{r\emptyset} \qquad (3\text{-}45)$$

$$\Delta\Psi=n\pi(\theta_t-\theta_r) \qquad (3\text{-}46)$$

by replacing the values of θ_t and θ_r by equivelents from (3-17) and (3-18) respectively we get the following.

$$\Delta\Psi=2n\pi\theta_D \qquad (3\text{-}47)$$

where $\sin(\theta_t)=\theta_t$ and $\sin(\theta_r)=\theta_r$ are assumed in (3-46) for small incidence angles.

One can see from (3-47) that $\Delta\Psi$ depends on two factors, the angular distance from the bisector θ_D and the distance moved along the array in terms of the element number. Table 3-1 shows the values of $\Delta\Psi$ as a function of n for different values of θ_D. In this table, the values of θ_D are taken as 0.5, 0.25, 0.125 BW (BW is the three dBs beamwidths of the 21 elements linear array mentioned above).

By closely examining the four subapertures technique for the nonsymmetric sources case (the general case) according to table 3-1, one can see that if Ψ is 0 or Π at the middle of the array then a good resolution can be expected if Θ_D is close to 0.5 BW and deteriorates when Θ_D gets smaller. If Ψ is 0 or Π at the middle of AP1 or AP2 then the resolution is close to optimum when Θ_D is close to 0.5 BW and good when it is 0.25 BW and deteriorates for smaller values of Θ_D. If Ψ is 0 or Π at the center of the external edge subaperture of AP1 or AP2 then the resolution is good for Θ_D close to 0.5 or 0.125 BW and close to optimum when Θ_D is close to 0.25 BW. Similar results can be easily shown for the symmetric case. However, these improvements are obvious in the simulation results in the next section.

Table 3-1

The phase shift relationship as a function of n and Θ_D.

n	$\Delta\Psi$ (radians)		
	Θ_D=0.5BW	Θ_D=0.25BW	Θ_D=0.125BW
3.5	0.9236	0.4618	0.2309
7.0	1.8472	0.9236	0.4618
14	3.6945	1.8472	0.9236

3-4 Simulation results and discussion

All the simulations have been made using three (or four) subapertures of seven elements each, interelement spacing being $\lambda/2$. Gaussian noise of zero mean and σ^2 variance was added to the signals and one thousand trials were made to find the average errors in the angle estimation at each given phase difference. The root mean square (RMS) error was calculated as follows:

$$error_1 = \theta_t - \hat{\theta}_t$$

$$error_2 = \theta_r - \hat{\theta}_r$$

$$\text{RMS angle-of-arrival error} = \sqrt{\frac{\sum (error_1^2 + error_2^2)}{2 \times \text{number of trials}}}$$

where $\hat{\theta}_t$ and $\hat{\theta}_r$ are the estimated angles of arrival for the direct signal and its coherent multipath. The error has also been normalized to the 3dB beamwidth of the whole array calculated as follows [3-4]:

$$\text{3dB beamwidth (BW)} = 102/N \qquad \text{(in degrees)}$$

where, N is the number of elements in the array (interelement spacing is $\lambda/2$). The signal to noise ratio (S/N) is calculated for the direct signal only, as received by the

main beam of the whole array and defined from [3-2] as follows.

For three-subapertures:

$$(S/N)\ dB = 10 \log [(3(G_1|a_1|)^2)/(2\sigma^2)]$$

and for four-subapertures:

$$(S/N)\ dB = 10 \log [(4(G_1|a_1|)^2)/(2\sigma^2)]$$

There are two practical methods for separating the direct angle bearing from the coherent multipath one. The first is by calculating the amplitudes of the two signals, where the angle associated with the higher amplitude represents the direct angle of arrival and the one associated with the smaller amplitude represents the multipath angle of arrival. This method adds extra unnecessary load to the system, also it is very critical when the two signals amplitudes are very close. The other way is to separate the two angles according to their sign, i.e the positive angle represents the direct angle of arrival and the negative angle represents the multipath one (in case of confusion, the most positive one relative to the horizon is taken to be the direct angle and the opposite for the multipath one). This method depends on the fact that the target is always above the surface and has the higher angle above the horizon. In the simulation performed for this study of a low-flying target over a smooth surface, the second method was chosen, since it is more likely to be used in a practical system.

The target model used in this simulation is Swerling case 5 type (SW.5), where the amplitude of the received signal is constant from pulse to pulse (from snap-shot to snap-shot, in the case that one snap-shot per pulse is taken). For comparison, a signal with a fluctuating amplitude according to Swerling case 2 target type (SW.2) is considered too, where the amplitude of the received signal changes randomly from pulse to pulse. It is generated in simulation by taking the real and imaginary parts of the two signals from a Gaussian sequence with zero mean and given variance [3-5]. A noisy signal is generated using (3-2) for the 3SA-MLE and (3-37) for the 4SA-MLE according to the target's models above, and the solutions were computed for the symmetric and nonsymmetric cases for the three and four subapertures methods. The phase difference (Ψ) is always taken to be multiples of 22.5 degrees in the range from 0° to 180°. From now on the absolute value of the specular reflection will be refered to as ρ_s.

A histogram of simulation results is used to demonstrate the performance of the 3SA-MLE and 4SA-MLE at some cases, where the rms angle-of-arrival (+beamwidth) is divided into 20 zones of accuracy, from 0.0-0.05, ...0.9-0.95, >0.95.

3-4.1 The symmetric case solution

Figure 3-8 shows the simulation results of the 3SA-MLE for a target with Θ_B=0, S/N=30 dB, ρ_s=0.9 , and Θ_D=0.5,0.25,0.125 BW, using SW.5 target type

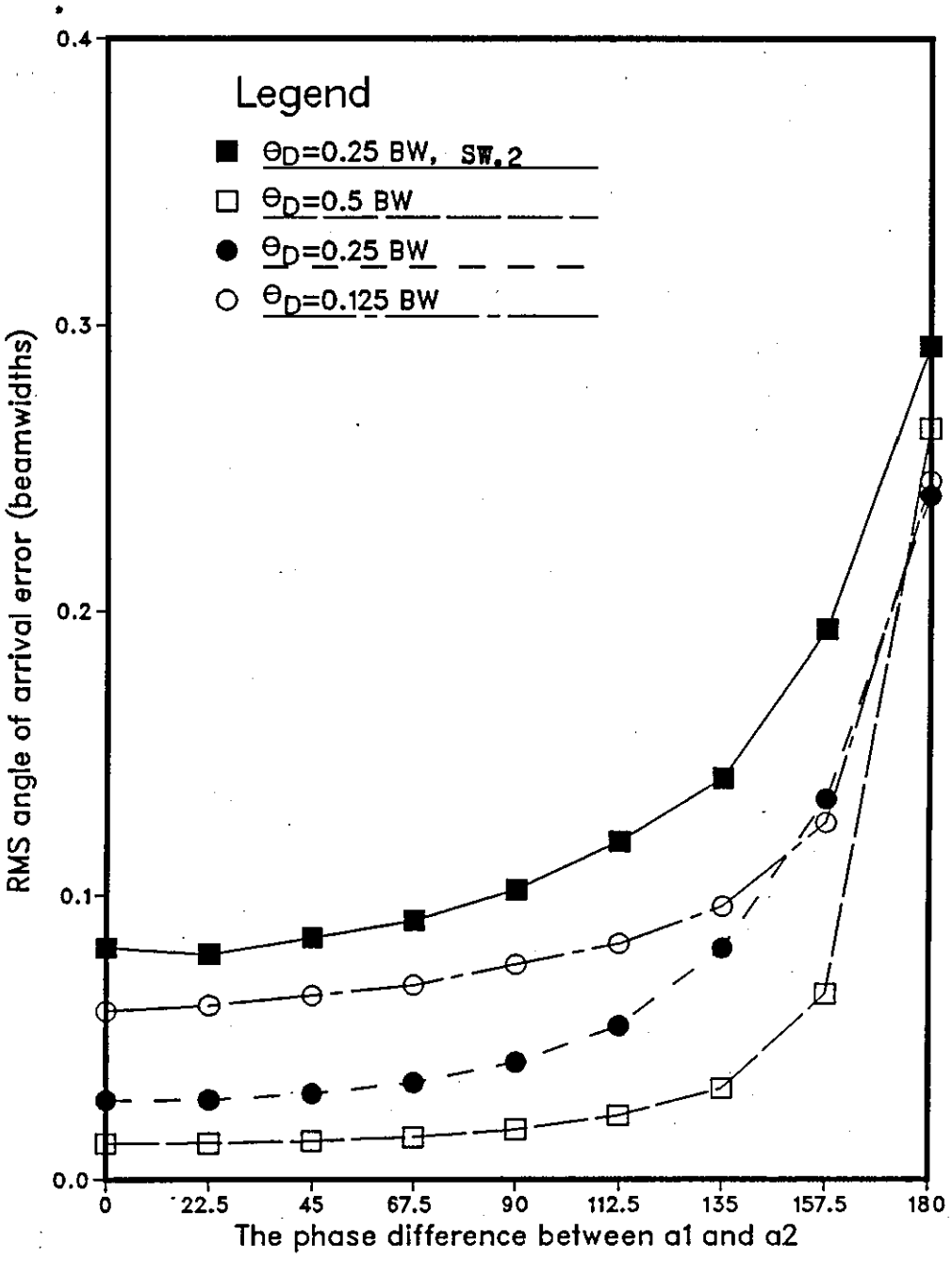

Figure3-8 : RMS error of symmetric 3SA–MLE as a function of phase difference between the two signals for Θ_B=0.0, S/N=30 dB, ρ_s=0.9. For comparison, SW.2 target's type is shown

(nonfluctuating amplitude). For comparison the corresponding result is shown for SW.2 target type (fluctuating amplitude) only for the case θ_D=0.25 BW. In comparing the solution using SW.5 target's type to that using SW.2, we find that the first is much more accurate than the second over all values of Ψ with average rms angle-of-arrival error enhancement of 0.06. The rms error is larger when Ψ=180° and very small when Ψ=0°, also it increases when θ_D decreases. Cantrel et.al. [3-2] show that the resolution obtained is very close to the optimum obtainable from the array were all elements sampled individually and it produces smaller error than the corresponding Cramer-Rao bounds (this is because the MLE is slightly biased). Figure 3-9 presents the S/N performance for SW.5 signal type with θ_B=0, θ_D=0.5 BW, ρ_s=0.9, and S/N= 30,20,10 dB. In general, one concludes that the rms error increases as the S/N decreases. Figure 3-10 presents the performance with different values of ρ_s (i.e with different relative power between the two coherent sources), where θ_B=0, θ_D=0.25 BW, S/N=30 dB, and ρ_s=0.9,0.5,0.1. In general, when ρ_s decreases the performance gets better when the absolute value of Ψ is close to the out of phase case (generally when Ψ>90°, depends on ρ_s) and a little worse elsewhere. The improvement at Ψ=180° is very substantial where the rms error drops from 0.24 to just 0.066 when ρ_s changes from 0.9 to 0.1. he main reason behind this improvement is that when the two signals are in anti-phase (or close) and their relative amplitudes are close (such as when ρ_s=0.9) then destructive interference occurs,

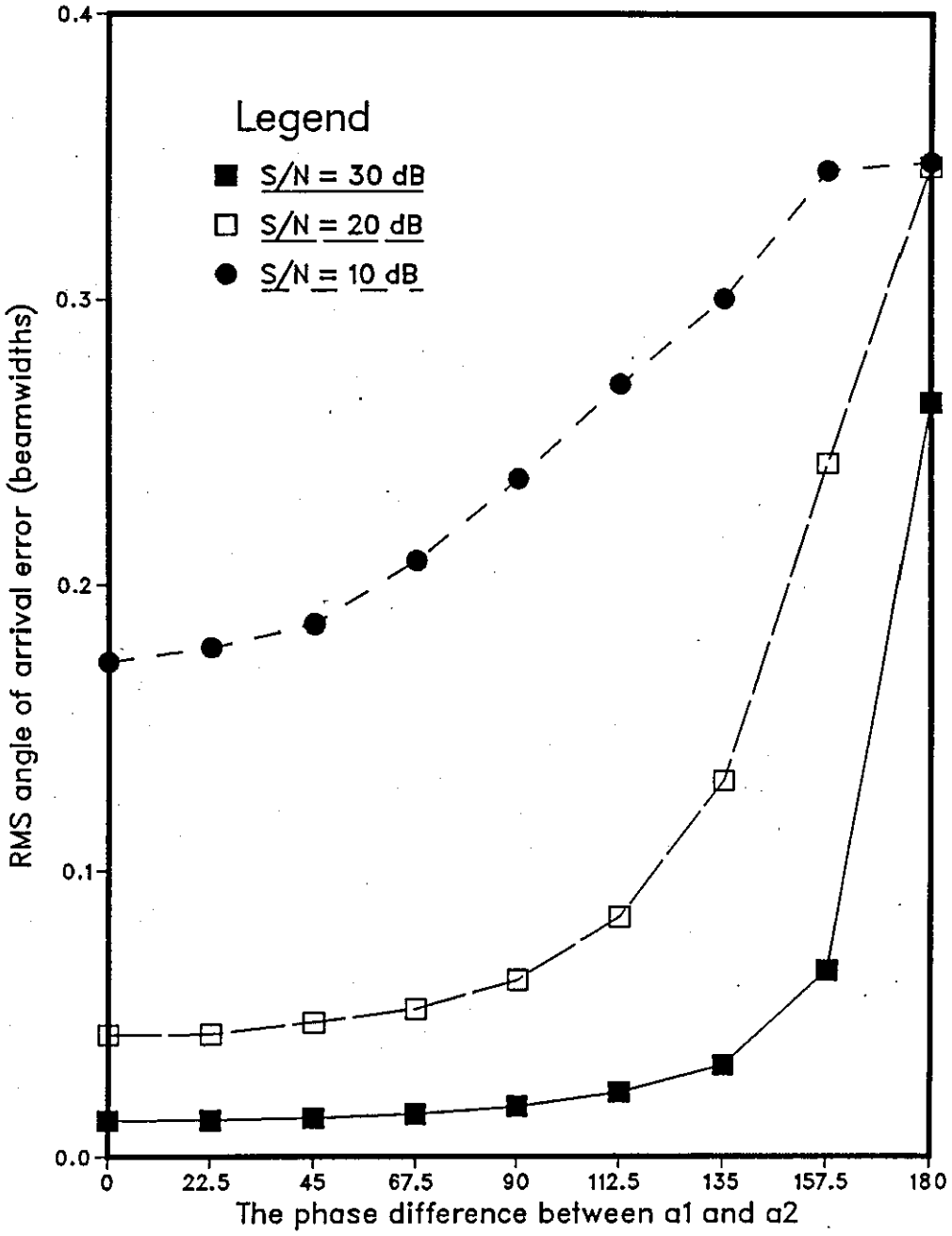

Figure 3–9 : RMS error of symmetric 3SA–MLE as a function of phase difference between the two signals for Θ_B=0.0, Θ_D=0.5 BW, ρ_s=0.9

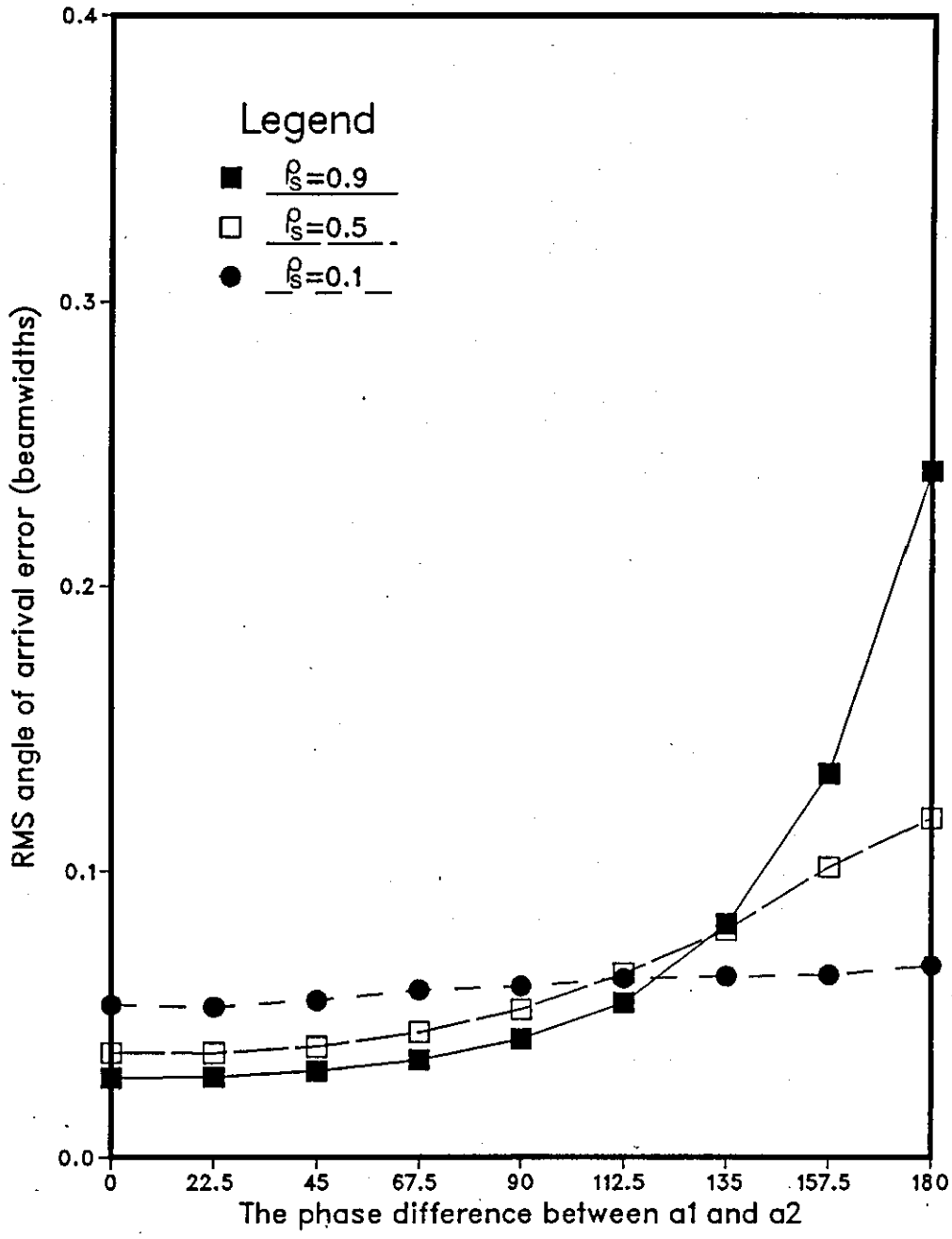

Figure 3-10 : RMS error of symmetric 3SA–MLE as a function of phase difference between the two signals for Θ_B=0.0, S/N=30 dB, Θ_D=0.25 BW

leading to very low S/N. But when the relative amplitudes are not close (such as when ρ_s=0.5 or 0.1) then the destructive interference is less pronounced, leading to higher S/N and in turn to better accuracy. The increase in the rms error at small Ψ when ρ_s=0.5,0.1 is very small where it rises from 0.028 at ρ_s=0.9 to 0.053 at ρ_s=0.1 which is very negligible in comparison with the improvement obtained when Ψ is close to 180° (generally Ψ >90°).

Before discussing the new four-subapertures method results , we examine the case of the imaginary angle [3-3] occurrence (i.e when $\theta_t=\theta_r$) and the accuracy in estimating the phase differene from the estimated angles of arrival of the target and its coherent multipath. Table 3-2 shows computer simulation results for the frequency of occurrences of the imaginary angle (Im-ang) and when the absolute error of the estimated value of Ψ is greater than a given value (assumed here to be 10°) from its true one (ph-div), in 1000 trials for θ_B=0, S/N=30 dB, ρ_s=0.9, and θ_D=0.5,0.25,0.125 BW for SW.5 target's type (and SW.2 target's type just at θ_D=0.25 BW for comparison). The imaginary angle occurrence is zero over all values of Ψ when θ_D=0.5 BW except at Ψ=180° where it occures 203 times which might explains the bad performance at this point. When θ_D decreases the Im-ang occurrence increases over all values of Ψ leading to degradation in the angle estimation accuracy as shown in figure 3-8. The estimated value of Ψ is worst when the two signals are close to phase opposition as can be seen from the table (mainly because of the decrease in the S/N) with one

Table 3-2 The imaginary angle and erroneous estimated phase difference (>10° deviation from the true value) occurrences in the symmetric 3SA-MLE for θ_B=0, S/N=30 dB, ρ_s=0.9, θ_D=0.5,0.25,0.125 BW, for 1000 trials at each phase shown. For comparison the results for SW.2 target's type is shown when θ_D=0.25 BW.

Phase	0.5 BW		0.25 BW				0.125 BW	
	Im-ang.	Ph-div.	IM-ang		Ph-div.		IM-ang.	Ph-div.
	SW.5	SW.5	SW.5	SW.2	SW.5	SW.2	SW.5	SW.5
0.0	0	0	0	45	10	195	122	213
22.5	0	0	0	47	35	269	134	431
45.0	0	0	1	51	120	376	154	638
67.5	0	1	1	61	229	451	184	718
90.0	0	1	1	81	312	522	225	792
112.5	0	5	5	99	366	611	263	813
135.0	0	5	40	172	395	613	296	821
157.5	0	11	179	284	415	649	407	826
180.0	203	0	422	416	18	181	482	112

exception at $\Psi=180^{\circ}$ where the imaginary angle occurs very frequently. The reason behind this exception is that when an imaginary angle occurs, a test is carried out to find whether the two signals are close to in-phase or anti-phase conditions. The test condition is that whenever the two signals are anti-phase at the centre of the array, then $|S_2| < |S_3|$ and $|S_2| < |S_1|$ (the opposite occurs when the two signals are in phase agreement at the array's centre). Thus, depending on the above conditions the value of Ψ is set to either 0° or 180° whenever the imaginary angle occurs, leading to high accuracy in estimating the value of Ψ when the two signals are anti-phase in particular. The frequency of occurrence of ph-div increases as Θ_D decreases, as can be seen from the table. In comparing with the SW.2 target type for $\Theta_D=0.25$ BW, one concludes that the frequency of occurrences of the imaginary angle and the erroneous values of the estimated Ψ is much higher for the second type. This explains the increase in the rms error shown in figure 3-8. In figure 3-11 a histogram is shown for both types where the rms error of the SW.5 target type is shown to be within the range 0-0.05 for 78 % of the time and 0.05-0.1 for 18 % , while for the second target type it drops to 55 % and 24 % respectively. Besides, one can see the frequent occurrence of the imaginary angle in the second case. In conclusion, the bigger the angular seperation, and the smaller the phase difference between the two targets, the better the accuracy in estimating the value of Ψ, and less the occurrence of imaginary angles.

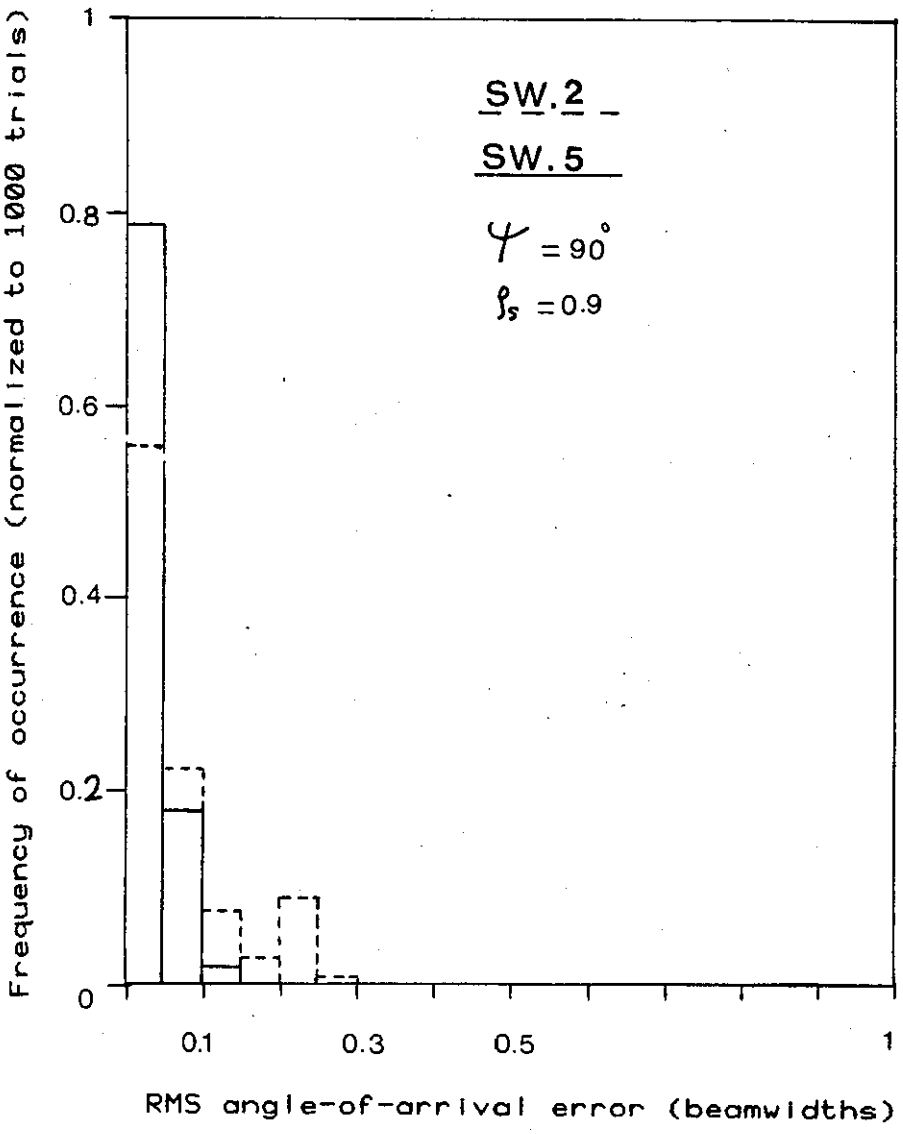

Figure 3- 11 :Histogram shows the performance of the symmetric 3SA-MLE for Swerling cases 2 and 5 target's type Θ_B=0, Θ_D=0.25 BW, S/N=30 dB, ρ_s=0.9, Ψ=90°.

According to the discussion above and the block diagram in figure 3-5 a computer simulation is carried out to determine the effectiveness of the 4SA-MLE in improving the performance of the symmetric case of the 3SA-MLE when the two targets are in (or close to) phase opposition. Figure 3-12 shows the simulation results of the symmetric 4SA-MLE for $\theta_B=0$, $\rho_s=0.9$, S/N=30 dB, and $\theta_D=0.5, 0.25, 0.125$ BW, using SW.5 target's type. For comparison 3SA-MLE is shown only for $\theta_D=0.25$ BW (27 elements are used insted of 28 for the 4SA-MLE to be able to divide into three-equal-subapertures). In comparing each curve with its correspondent in figure 3-8 (keeping in mind that we use just 3/4 of the total array's elements in the four-suabapertures method, while the rms error is normalized to 3dB beamwidth of the whole array) one can see a big reduction in the rms error when Ψ is close to 180° in general and in particular when θ_D is large where the accuracy increases sharply. A little degredation at small values of Ψ is shown mainly related to the normalization method and the lower S/N per subaperture (1.2 dB less), and the deviation of the new chosen value of Ψ from 0°. In comparing the result of 3SA-MLE (using 27 elements) with its correspondent 4SA-MLE ones (using 28 elements) for $\theta_D=0.25$ BW as shown on the same figure, a big improvement is shown when Ψ is close to anti-phase condition and a little degredation elsewhere (rms error increases by 0.018 at $\Psi=0^\circ$). The main reason for this degredation is the higher S/N per subaperture for the 3SA-MLE case (≈1 dB) in comparison with the 4SA-MLE ones. Figure 3-13 shows a histogram of results for $\theta_D=0.25$ BW

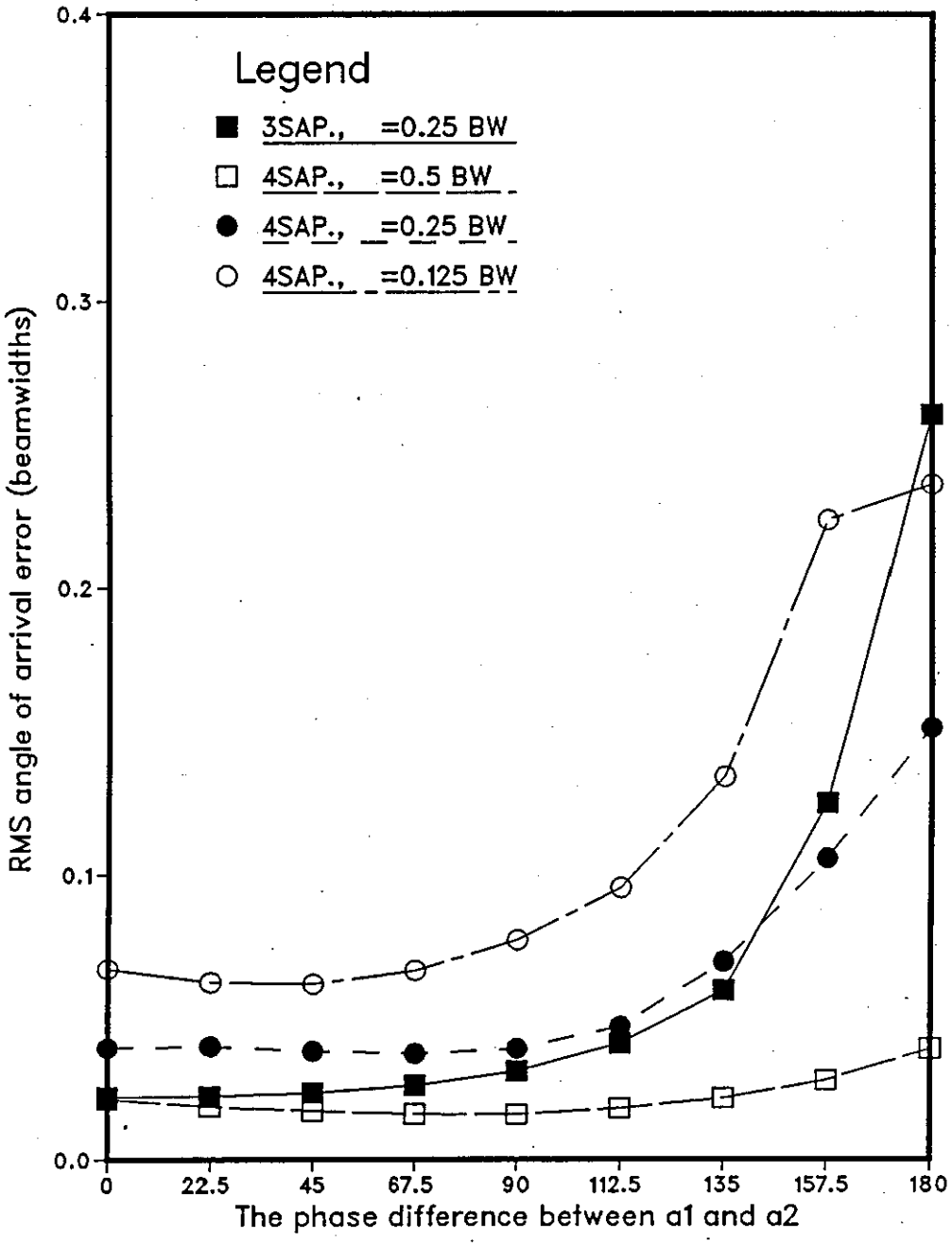

Figure 3-12 : RMS error of symmetric 4SA–MLE as a function of phase difference between the two signals for Θ_B=0.0, S/N= 30 dB, ρ_s=0.9. For comparison, 3SA–MLE is shown for Θ_D=0.25 BW

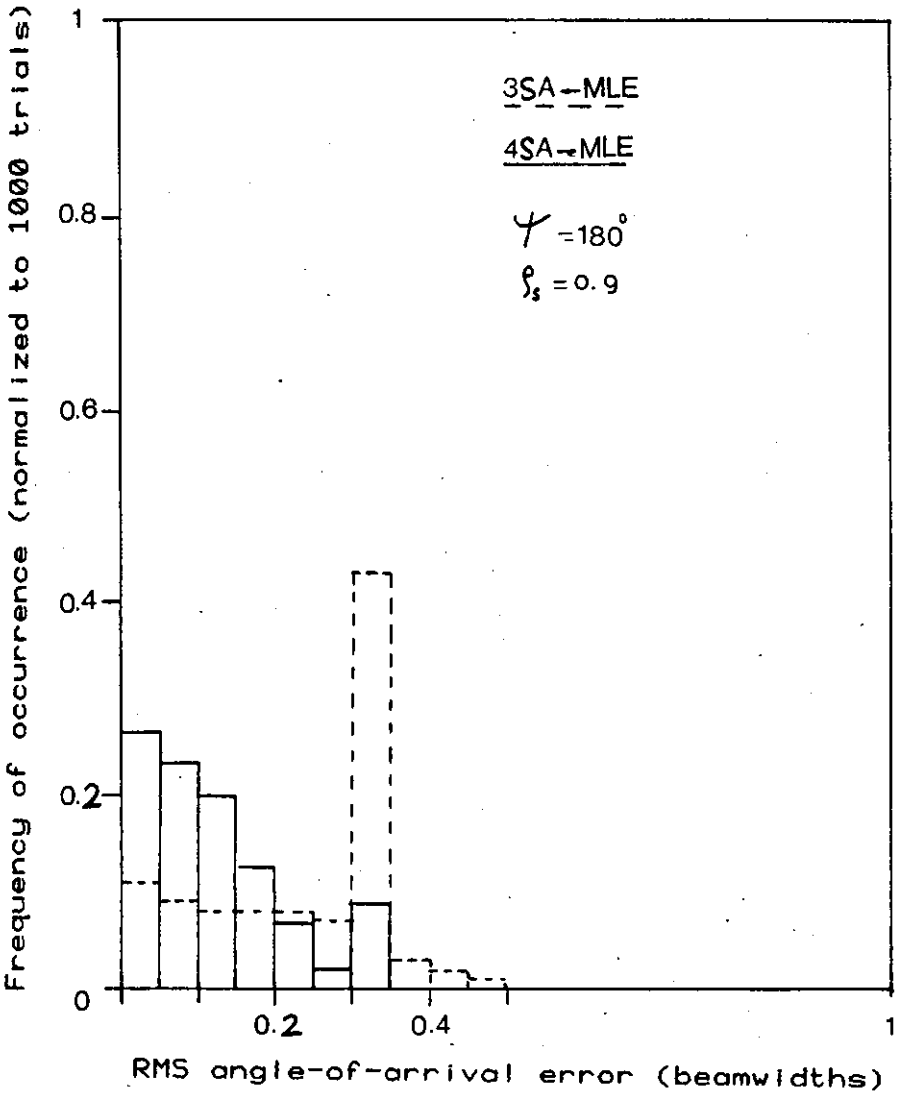

Figure 3- 13 :Histogram shows the performance of the symmetric 3SA-MLE and 4SA-MLE for Swerling cases 5 target type θ_B=0, θ_D=0.25 BW, S/N=30 dB, ρ_s=0.9, Ψ=180.

ρ_s=0.9, S/N=30 dB, θ_B=0, and Ψ=180° for the 3SA-MLE and the 4SA-MLE, where the rms error (÷beamwidth) apears to be within the range 0-0.1 for 52 % of the time for the 4SA-MLE, while it drops to 20 % for the 3SA-MLE. Also, one can see the high occurrence of imaginary and erroneous angles (44 % of time) for the 3SA-MLE in comparison with that of the 4SA-MLE ones (9 % of time)

In the above four-subaperture method we used the estimated phase difference to decide which set gives the best angle estimation. This technique required parallel processing for two sets of three subapertures (AP1 and AP2), which double the processing load and increases the cost of the system as we have seen in section 3-3 where a simpler system which was suggested depending on amplitude comparison of the input signals from the two subapertures in the middle of the four-subapertures' array. Here, figure 3-14 shows the simulation results for the 4SA-MLE (amplitude comparison method) according to the block diagram shown in figure 3-7 for θ_B=0, S/N=30 dB, ρ_s=0.9, and θ_D=0.5,0.25,0.125 BW. In comparing these results with their correspondents in figure 3-12 one can see that the rms error is the same for all values of Ψ when θ_D=0.5,0.25 BW with the exception at Ψ=180° where this method shows very little increase in the rms error (rms error increases by 0.003 for θ_D=0.5 BW and 0.02 for θ_D=0.25 BW). When θ_D=0.125 BW this method appears to work better than the previous one when Ψ >90° and worse when Ψ <90°. Both methods shows the same accuracy when Ψ=0° or 180°.

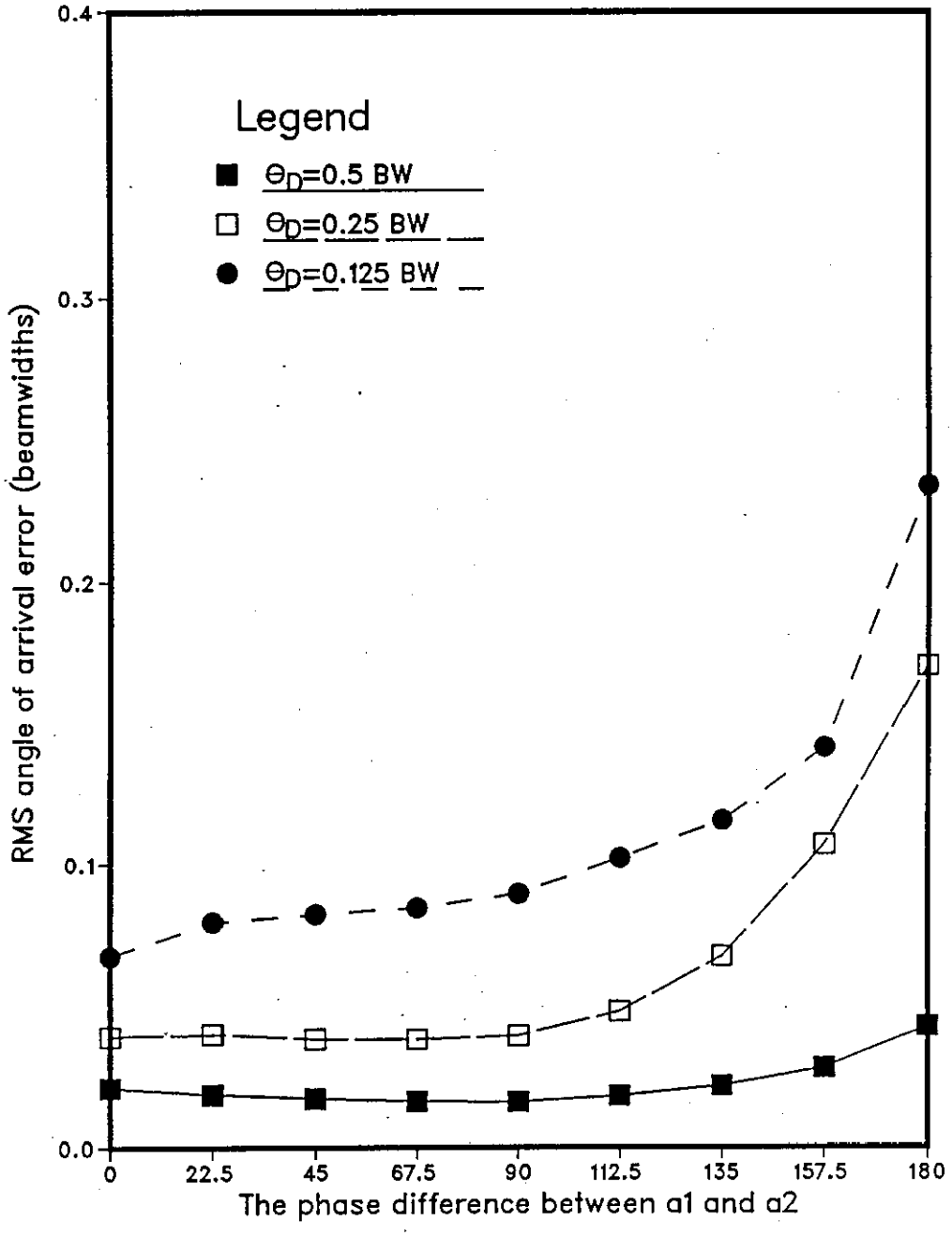

Figure 3-14: RMS error of symmetric 4SA–MLE as a function of phase difference between the two signals for Θ_B=0.0, S/N= 30 dB, ρ_s=0.9, amplitudes comparison method.

3-4.2 The nonsymmetric case solution

Figure 3-15 shows the simulation results of the 3SA-MLE for a target with θ_B=0, ρ_s=0.9, S/N=30 dB, and θ_D=0.5,0.25,0.125 BW, using SW.5 target type (for comparison the corresponding results are shown for the SW.2 target type only when θ_D=0.25 BW). In comparing the solutions, one finds that the rms error increases as θ_D decreases, and the worst estimation occurs when the two sources are in-phase or anti-phase (Ψ=0° or 180°) or close to either as can be seen from the curves. The best accuracy is obtained when the two sources are in phase quadrature for all values of θ_D, except when θ_D=0.125 BW where the optimum accuracy is obtained at Ψ=112°. The accuracy obtained when θ_D=0.25 BW for the SW.5 target type is much higher than that for the SW.2 target type, where the rms error increases by 0.07 for the second at Ψ=90°. Cantrell et.al. [3-2] show that the resolution obtained is very close to the optimum obtainable from the same array were all the elements sampled individually and it produces smaller rms error than that of the corresponding Cramer-Rao bounds [3-6,7]. Figure 3-16 shows the S/N performance of the 3SA-MLE for θ_B=0, θ_D=0.5 BW, ρ_s=0.9, and S/N=30,20,10 dB, where the rms error is shown to increase as the S/N decreases over all values of Ψ. Figure 3-17 presents the performance of the 3SA-MLE for different values of the specular reflection coefficient for θ_B=0, θ_D=0.25 BW, S/N=30 dB, and ρ_s=0.9,0.5,0.1. In general, when ρ_s decreases the rms error increases, especially when ρ_s

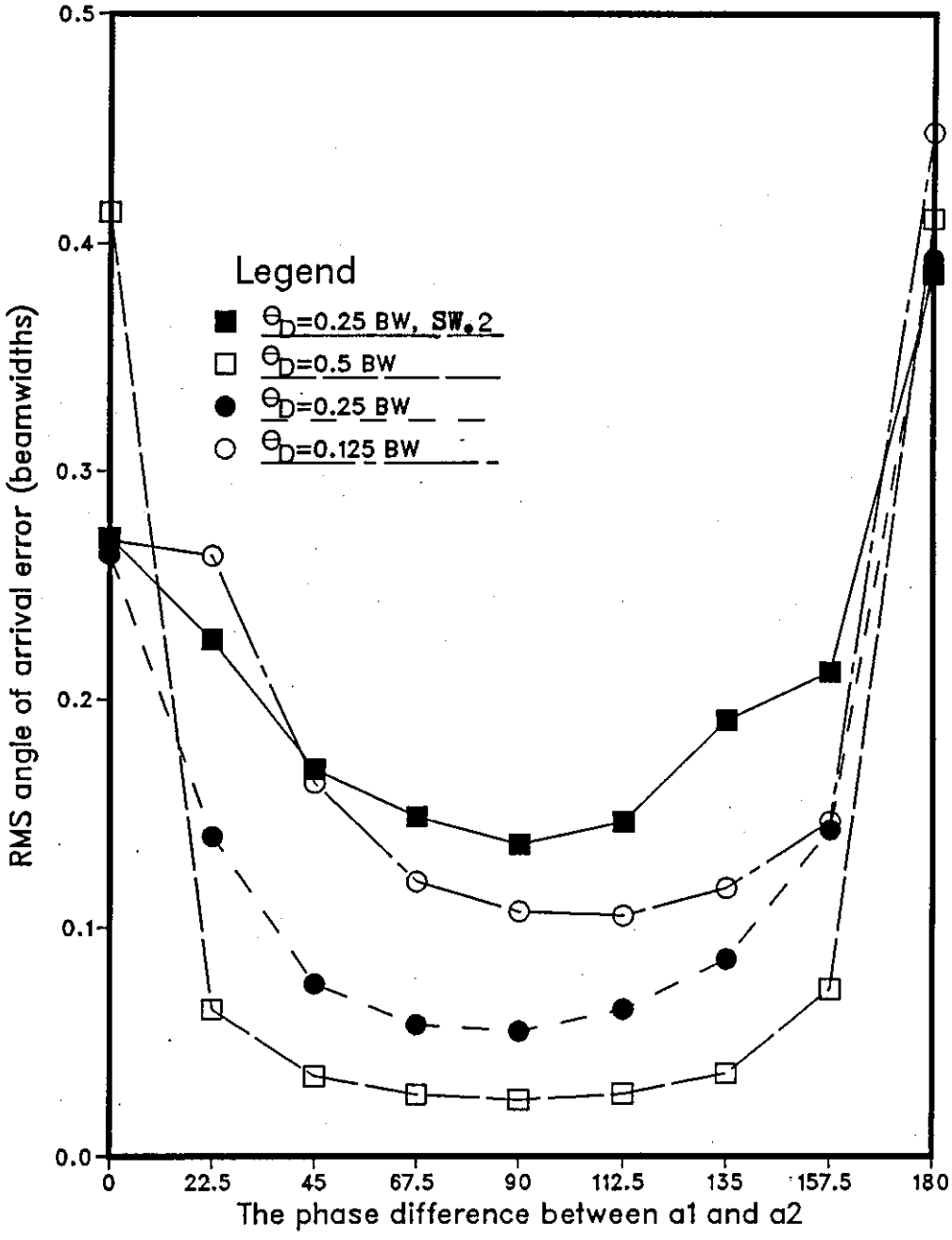

Figure 3-15 : RMS error of nonsymmetric 3SA-MLE as a function of phase difference between the two signals for Θ_B=0.0, S/N=30 dB, ρ_s=0.9. For comparison, SW.2 target's type is shown

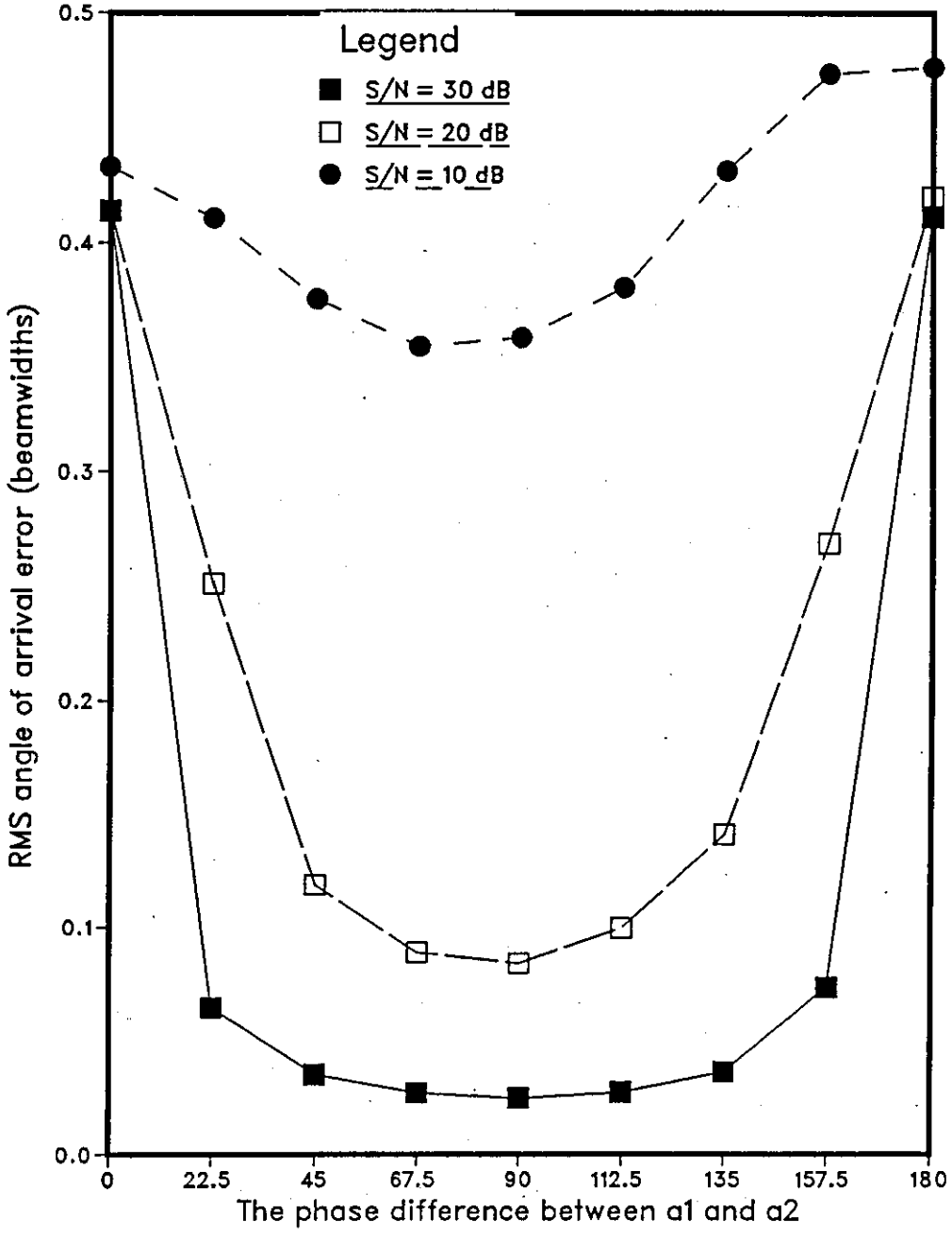

Figure 3-16 : RMS error of nonsymmetric 3SA-MLE as a function of phase difference between the two signals for Θ_B=0.0, Θ_D=0.5 BW, ρ_s=0.9

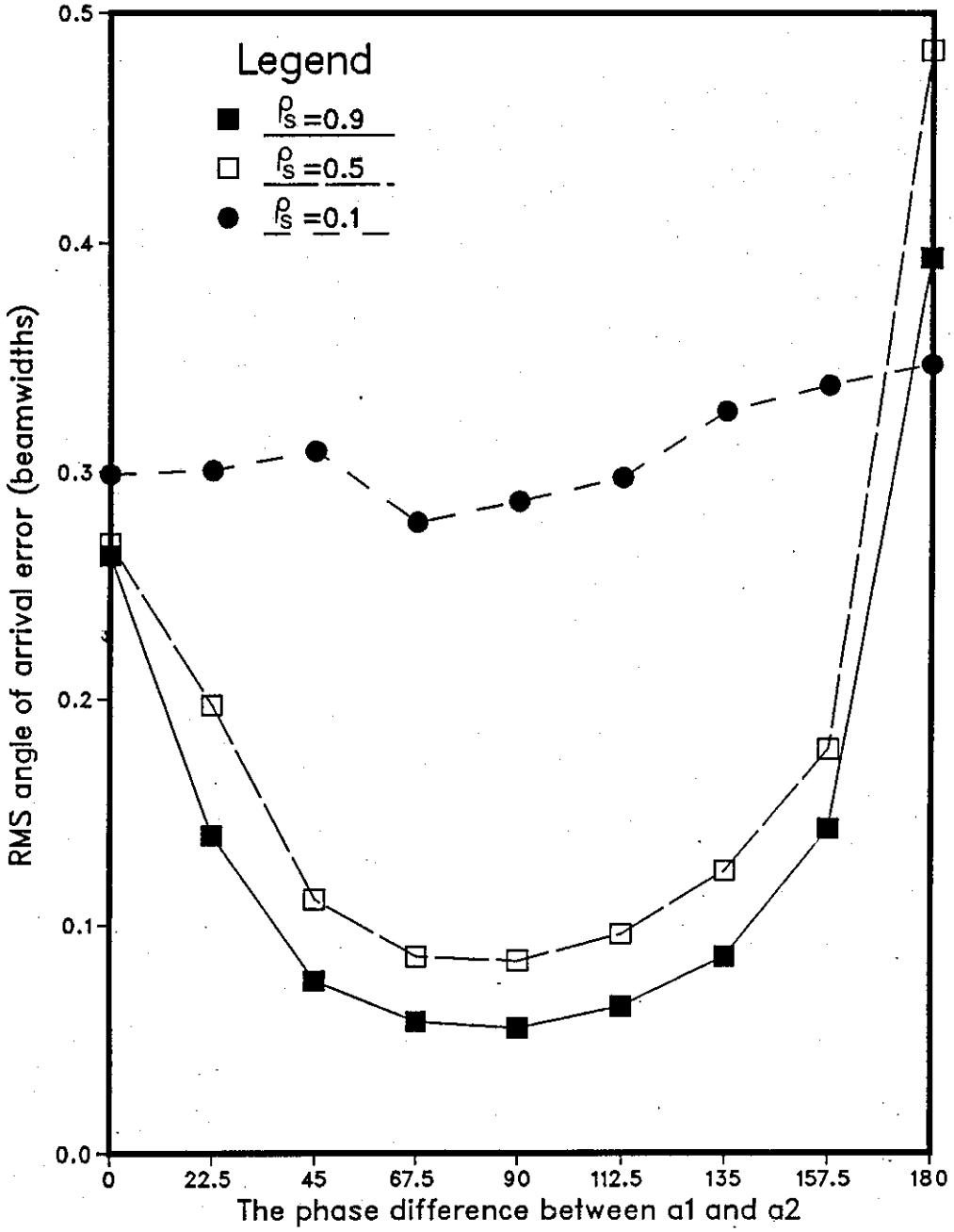

Figure 3-17 : RMS error of nonsymmetric 3SA–MLE as a function of phase difference between the two signals for Θ_B=0.0, Θ_D=0.25 BW, S/N= 30 dB

is very small (0.1). In figure 3-18 the rms error in estimating the direct angle and the multipath one are calculated separately for ρ_s=0.1, S/N=30 dB, θ_D=0.25 BW, θ_B=0, where the rms error for the first is shown to be much less that for the second over all values of Ψ. The average rms error for the first is about o.2 in comparison with 0.38 for the second over all values of Ψ. The reason is the individual S/N of each source which is very high for the first in comparison with the second which provides a shallow null (minimum L) in the pattern leading to higher error.

As we have seen from the results above, the performance of the nonsymmetric 3SA-MLE is very poor when the target and its coherent multipath are in-phase or anti-phase. In section 3-3 a new 4SA-MLE method is introduced to solve this problem and improve the performance in these two regions. Before showing the simulation results for this method we examine the case of the imaginary angle occurrence and the accuracy obtained in estimating the phase difference Ψ from the estimated angles of arrival of the two sources. Table 3-3 shows computer simulation results for the frequency of occurrences of the imaginary angle (Im-ang) and when the absolute error of the estimated value of Ψ is greater than a given value (taken here to be 10°) from its true one (ph-div), for θ_B=0, S/N=30 dB , ρ_s=0.9, and θ_D=0.5,0.25,0.125 BW for SW.5 target's type (and SW.2 target's type just when θ_D=0.25 BW for comparison). The imaginary angle occurrence is zero over all values of Ψ when θ_D=0.5 BW, except at $\Psi=180^{\circ}$ where it occurs 402 times out of 1000, which might explain the bad

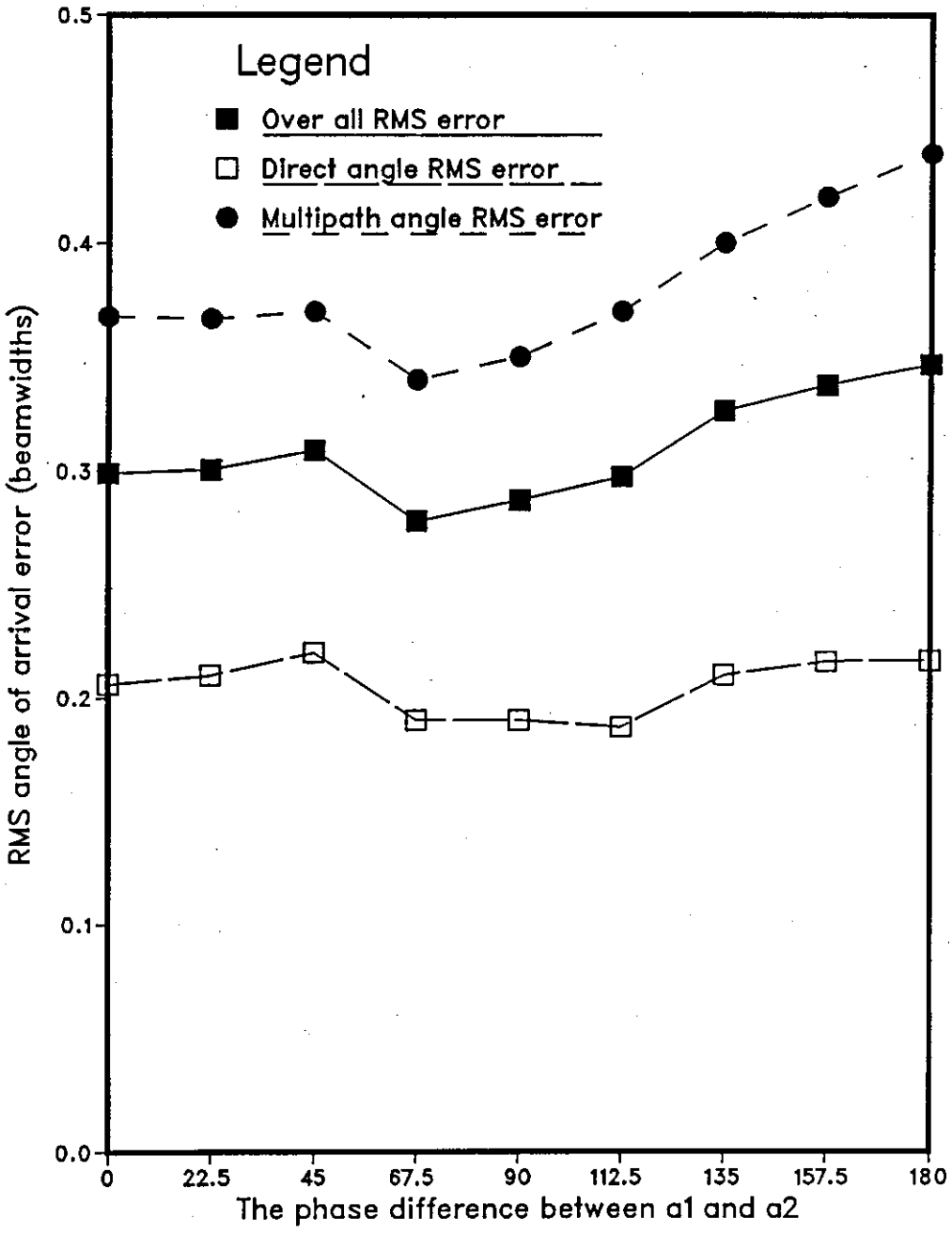

Figure 3-18 : RMS error of nonsymmetric 3SA–MLE as a function of phase difference between the two signals for Θ_B=0.0, Θ_D=0.25 BW, S/N= 30 dB, ρ_s=0.1

Table 3-3 The imaginary angle and erroneous estimated phase difference (>10° deviation from the true value) occurrences in the nonsymmetric 3SA-MLE for θ_B=0, S/N=30 dB, ρ_s=0.9, θ_D=0.5,0.25,0.125 BW, for 1000 trials at each phase shown. For comparison the results for SW.2 target's type is shown when θ_D=0.25 BW.

Phase	0.5 BW		0.25 BW				0.125 BW	
	Im-ang.	Ph-div.	IM-ang		Ph-div.		IM-ang.	Ph-div.
	SW.5	SW.5	SW.5	SW.2	SW.5	SW.2	SW.5	SW.5
0.0	0	753	0	8	741	819	9	886
22.5	0	0	0	9	128	417	33	683
45.0	0	0	0	11	133	399	60	614
67.5	0	1	0	24	221	455	99	667
90.0	0	2	1	45	314	522	157	735
112.5	0	5	9	75	365	572	224	801
135.0	0	11	35	169	438	606	298	842
157.5	0	19	195	287	445	632	402	856
180.0	402	1	397	388	23	164	385	143

performance at this point. When Θ_D decreases the imaginary angle occurrence increases over all values of Ψ as can be seen from the table. The occurrence of the imaginary angle at $\Psi=0^\circ$ is the smallest, but it does not mean that the estimated angle is accurate, in fact it is very erroneous as can be seen from figure 3-15. The estimated value of Ψ is the worst when the two sources are in phase agreement, while it is very accurate when they are in phase opposition as can be seen from table 3-3. The reason beyond this high accuracy (when $\Psi=180^\circ$) is that , when an imaginary angle occurs a test is carried out to find whether the two signals are close to in-phase or anti-phase conditions depending on the same facts explained in section 3-4.1. Also, this explains the poor estimation of the value of Ψ when its true value is zero and where the imaginary angle occurrence is very small. The frequency of occurrence of the imaginary angle and the erroneous values of the estimated Ψ for the SW.2 target type is higher than that for SW.5 type as can be seen from the table for Θ_D=0.25 BW.

According to the above discussion and the block diagram in figure 3-6 a computer simulation is carried out to express the effectiveness of the 4SA-MLE method to improve the nonsymmetric case of the 3SA-MLE performance when $\Psi=0^\circ$ or 180°. Figure 3-19 shows these results for Θ_B=0, S/N=30 dB, ρ_s=0.9, Θ_D= 0.5, 0.25, 0.125 BW, using SW.5 target's type. For comparison 3SA-MLE is shown only for Θ_D=0.25 BW (27 elements are used insted of 28). By comparing each curve with its correspondent in figure 3-15 (keeping in mind that

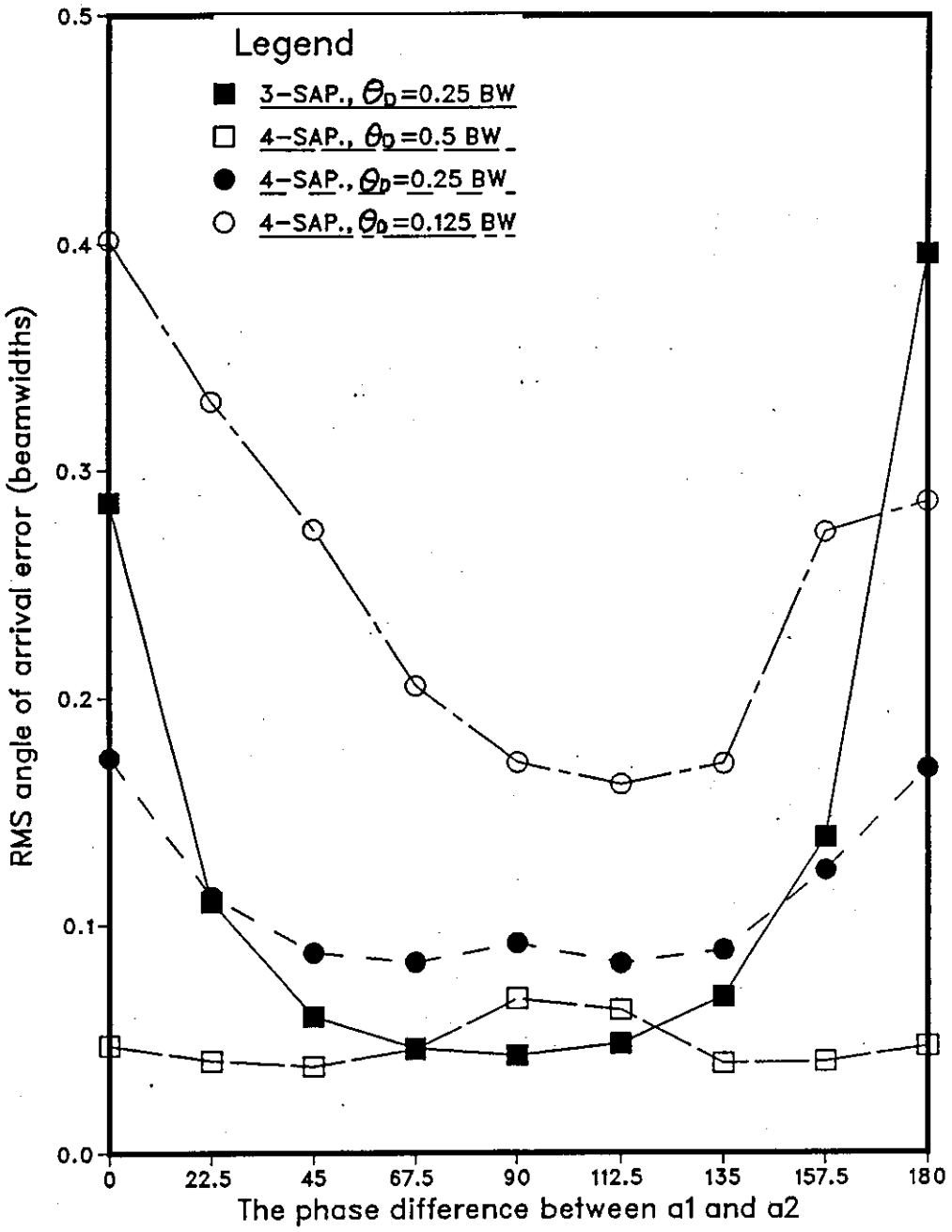

Figure 3-19 : RMS error of nonsymmetric 4SA-MLE as a function of phase difference between the two signals for Θ_B=0.0, S/N= 30 dB, ρ_s=0.9. For comparison, 3SA-MLE is shown for Θ_D=0.25 BW

we use just 3/4 of the total elements of the array for the 4SA-MLE method, while the rms error is normalized to the 3dB beamwidth of the whole array) one can see a large reduction in the rms error for θ_D=0.5, 0.25 BW when Ψ=0° or 180° (or close to any of them) and only a very small increase when Ψ is close to quadrature (mainly related to smaller S/N per subaperture, the 3dB normalization, and the deviation of the new chosen value of Ψ from the quadrature). The rms error appears to be worse for θ_D=0.125 BW, which is mainly related to the inaccurate estimation of the phase difference Ψ which the performance of the new method depends on. In comparing the 3SA-MLE (27 elements) and the 4SA-MLE one for θ_D=0.25 BW a big improvement can be seen when the phase difference between the two sources is close to 0° or 180° and a little degredation when it is close to quadrature for the same reasons explained above. Figure 3-20 shows a histogram of results for θ_D=0.25 BW, θ_B=0, ρ_s=0.9, S/N=30 dB, and Ψ=0°,180° for the three and four subapertures method, where the rms error (+beamwidth) for the first is within the range 0-0.1 for 18 % of the time when Ψ=0° and 8 % when Ψ=180°, while it rises to 45 % and 44 % for the second respectively. Thus, one can conclude that the four-subapertures method for solving the in-phase and anti-phase problem (just the anti-phase for the symmetric case) is very effective, but it does introduce extra work load in the nonsymmetric solution case. Therefore a new way is needed to reduce this work load, if possible, which will be shown as a part of a new algorithm in the next chapter.

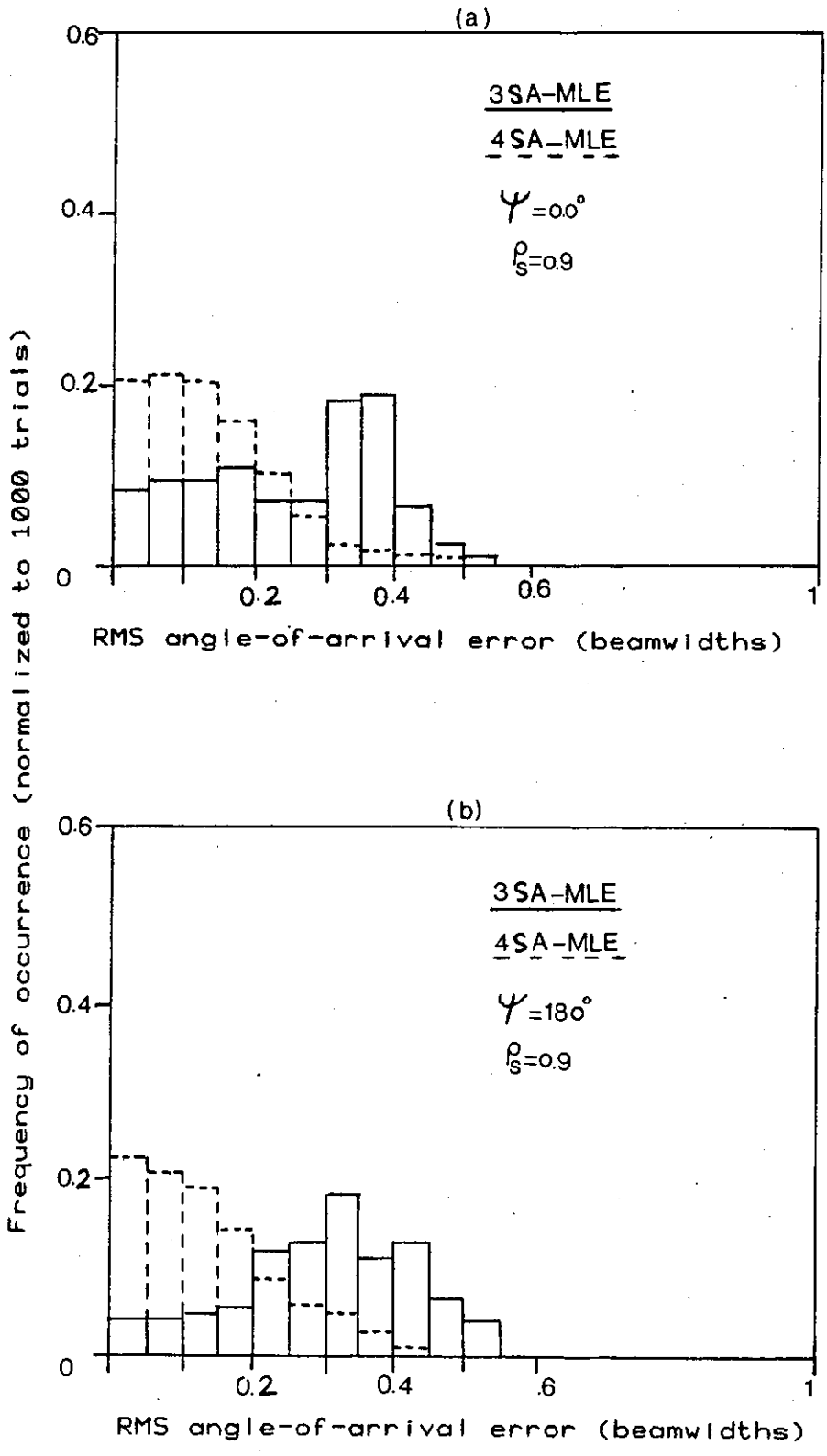

Figure 3- 20 :Histogram shows the performance of the nonsymmetric 3SA-MLE and 4SA-MLE for Swerling case 5 target type θ_B=0, θ_D=0.25 BW, S/N=30 dB, ρ_s=0.9, (a)- for Ψ=0.0°, (b)- for Ψ=180°.

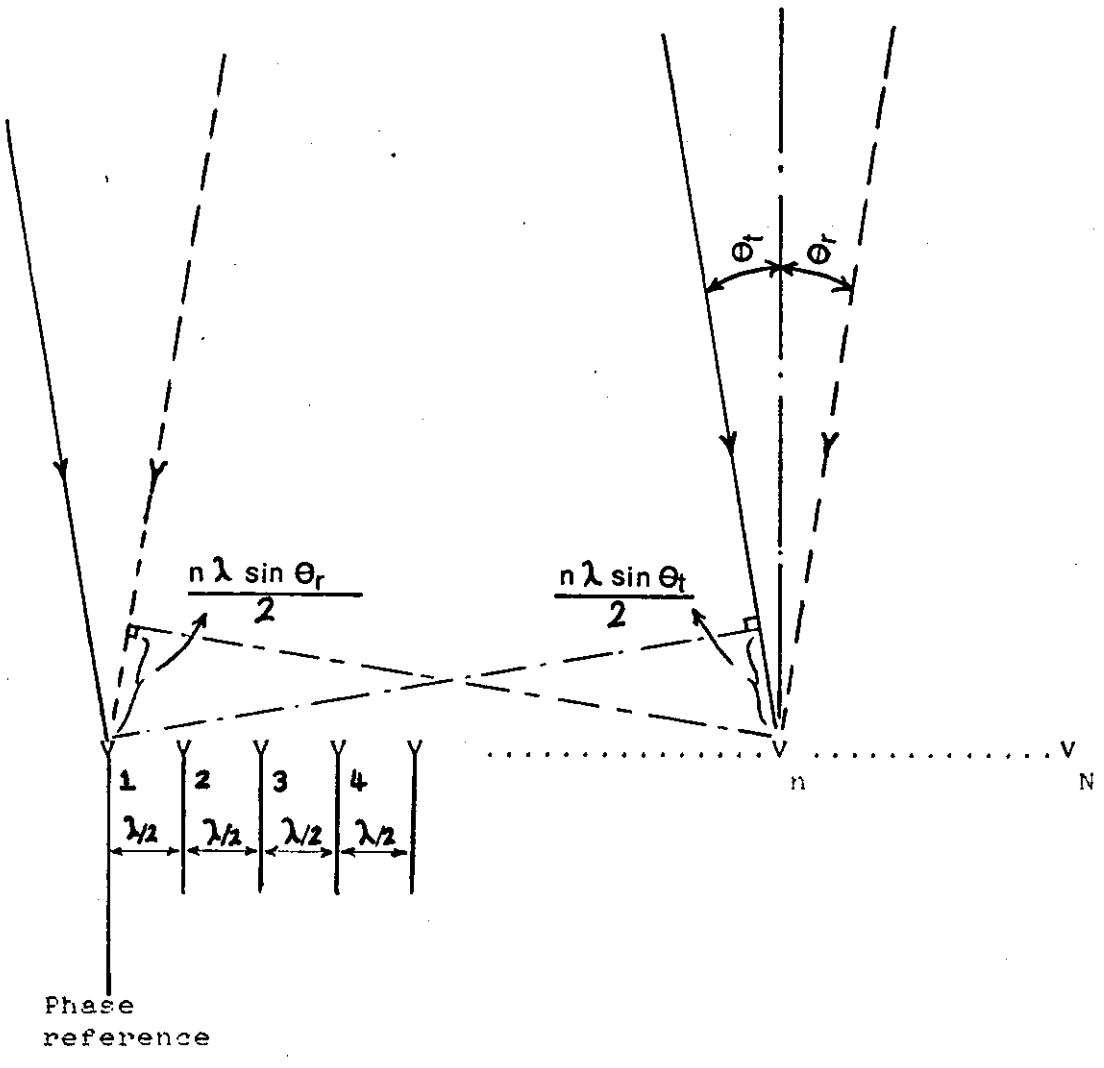

Figure 3-21 : The geometry of a linear array and two sources

APPENDIX A3

The Critical Points For The Symmetric Solution

Let $f(x,y)$ be an analytic function in the two variables x,y and consider finding the extreme values of $f(w_D, w_D^*)$. Where w_D varies subject to the constraint $w_D w_D^* = 1$

$$w_D = \exp(i\theta) \quad , \quad w_D^* = \exp(-i\theta)$$

where θ is a variable.

By taking the derivative of f with respect to θ we get:

$$(d/d\theta) f(w_D, w_D^*) = \partial f/\partial w_D \, (dw_D/d\theta) + (\partial f/\partial w_D^*)(dw_D^*/d\theta)$$

$$= i[w_D \, \partial f/\partial w_D - w_D^* \, \partial f/\partial w_D^*] \qquad \text{(A3-1)}$$

By solving equation (A3-1), the critical points of $f(w_D, w_D^*)$ subject to the constraint $w_D w_D^* = 1$ can be found:

$$w_D \, \partial f/\partial w_D - w_D^* \, \partial f/\partial w_D^* = 0 \qquad \text{(A3-2)}$$

Now, let us apply (A3-2) to the cost function L in (3-21) .

$$w_D \, \partial L/\partial w_D - w_D^* \, \partial L/\partial w_D^* = 0 \qquad \text{(A3-3)}$$

$$(w_D - w_D^*) \, \partial L/\partial V = 0 \ , \text{ where } V = w_D + w_D^* \qquad \text{(A3-4)}$$

and w_B is known for the symmetric case.

From (A3-4) the critical points are given by the values of w_D, w_D^* which obey the following two relations

$$w_D = w_D^* \qquad \text{(A3-5)}$$

or $$\partial L/\partial V = 0 \qquad \text{(A3-6)}$$

The relation in (A3-5) is possible only in case $w_D=w_D^*=\mp 1$ and by proceeding in (A3-6) we find.

$$\partial L/\partial V = V + 2V\Delta - 2 = 0$$

where:

$$\Delta = (2 - |R_f|^2)/(R_f + R_f^*)$$

$$R_f = (S_1 + w_B^2 S_3)/w_B S_2$$

By solving $V = w_D + w_D^* = w_D + 1/w_D$ for w_D we get

$$w_D = V/2 \mp j\sqrt{1-(V/2)^2} \qquad \text{(A3-7)}$$

APPENDIX B3

The Critical Points For The Nonsymmetric Solution

The cost function L to be minimized is given by the following:

$$L=|S_1-q_1|^2+|S_2-q_2|^2+|S_3-q_3|^2 \qquad (B3\text{-}1)$$

where:

$$q_k = A_1(w_1^*)^k+A_2(w_2^*)^k \quad , \quad k=1,2,3 \qquad (B3\text{-}2)$$

Let us consider making the value of L equal zero with real angles, making the following assumptions:

$$\mu=(w_1^*+w_2^*)^{-1} \qquad (B3\text{-}3)$$

if $|w_1| = |w_2| = 1$, we get

$$\mu/\mu^*=(w_1+w_2)/(w_1^*+w_2^*) = w_1w_2 \qquad (B3\text{-}4)$$

From (B3-2) and (B3-4) we find

$$q_2=\mu^*q_1+\mu q_3 \qquad (B3\text{-}5)$$

However, L can be made to vanish to zero by putting $q_1=S_1$, $q_3=S_3$ and

$$q_2=S_2 =\mu^*S_1+\mu S_3 \qquad (B3\text{-}6)$$

to solve (B3-6) for μ, we take its conjugate and the following two equations

$$S_2=\mu^* S_1+\mu S_3 \qquad \text{(B3-7)}$$

$$S_2^*=\mu S_1^*+\mu^* S_3^* \qquad \text{(B3-8)}$$

Equations (B3-7) and (B3-8) represent a linear system in μ and μ^*; solving for μ

$$\mu=(S_2 S_3^*-S_1 S_2^*)/(|S_3|^2-|S_1|^2)=1/U$$

where U is shown in (3-30). On realising that W_1 and w_2 are the roots of the following equation:

$$0=(w-w_1^*)(w-w_2^*)= w^2-(1/\mu)w+\mu^*/\mu \qquad \text{(B3-9)}$$

the values of w_1 and w_2 can be calculated from μ by solving (B3-9)

$$w_1^* = (1+j\sqrt{4|\mu|^2-1})/2\mu \qquad \text{(B3-10)}$$

$$w_2^* = (1-j\sqrt{4|\mu|^2-1})/2\mu \qquad \text{(B3-11)}$$

As one can see from (B3-10) and (B3-11) the absolute values of w_1 and w_2 are equal to one only if $\mu \geq 1/2$ (or equivalently, $|U| \geq 2$).

The values of w_B and w_D can be obtained easily from the next two equations:

$$w_B^2=w_1w_2 \quad , \quad w_D^2=w_1w_2^*$$

Now, let us look at the case when $\mu<1/2$. The proof for finding the values of w_1 and w_2 which minimize the cost function L is too lengthy and the result are given in [3-2]. The value of L is minimized when $w_1=w_2$ or equivalently when $w_D=1$. In this case the cost function is reduced to

$$L=1/6\ |S_1-2w_BS_2+w_B^2S_3|^2$$

and the explicit presentation of L as a function of w_B and w_B^* is given by:

$$L=1/6\,(S_1-2w_BS_2+w_B^2S_3)(S_1^*-2w_B^*S_2^*+w_B^{*2}S_3^*)$$

and according to appendix A3 the critical values of w_B subject to the given constraints are the solution to the following equation

$$w_B(\partial L/\partial w_B)-w_B^*(\partial L/\partial w_B^*)=0 \qquad \text{(B3-12)}$$

straightforward calculation shows that (B3-12) reduces to the form given in (3-34).

Chapter 4

The Trigonometric High Resolution Method

4-1 Introduction

The tracking of a low-flying target in the presence of strong reflection from the underlying smooth surface is a problem area of considerable interest in radar. The simplest closed-form solution so far is the three-subaperture maximum likelihood method discussed in the previous chapter, which it involves the solution of a quartic equation for the nonsymmetric case and a quadratic equation for the symmetric case. Also, a new four-subapertures technique (which depends on estimating the value of the phase difference between the two sources at the array centre) to improve the performance accuracy when the two sources are close to an in-phase or anti-phase condition is presented with extensive discussion and simulation results.

In this chapter a new simple three-subapertures trigonometric method (3SA-TRM) to solve the coherent multipath problem is presented. It has a similar performance to the 3SA-MLE in general and is simpler in practical implementation. A simple new procedure to find out whether the two coherent signals are close to an in-phase or

anti-phase condition is derived and applied to the four-subapertures technique discussed in the previous chapter. The advantages of this procedure in saving time and reducing work load are discussed and simulation results are shown. Additionally, new three and four subapertures techniques (symm. and nonsymm., 3&4SA-TRM) improve the performance of this algorithm when $\Psi=0^{\circ}$ or 180°. These preserve the accuracy obtainable when using the full aperture, divided into three-subapertures only, both when Ψ is close to quadrature and when Ψ is close to zero for the nonsymmetric and symmetric cases respectivly. Simulation results are shown.

The overall emphasis will be mainly on comparing the performance of this new method (3SA-TRM) with the 3SA-MLE method and showing its advantages.

4-2 Trigonometric solution formulation

Assume the same linear array, divided into three-subapertures, used in the previous chapter (section 3-2) with the same radar-target geometry and its associated angular relations shown in figure 3-1. The outputs of the three-subapertures will be the same as those shown in equation (3-2) and are repeated here for convenience as follows:

$$S_1 = a_1 G_1 \exp(+jZ_1) + a_2 G_2 \exp(+jZ_2) + n_1 \qquad (4\text{-}1)$$

$$S_2 = a_1 G_1 + a_2 G_2 + n_2 \qquad (4\text{-}2)$$

$$S_3 = a_1 G_1 \exp(-jZ_1) + a_2 G_2 \exp(-jZ_2) + n_3 \qquad (4\text{-}3)$$

The description of each term in the above equations is shown in chapter 3 and will not be repeated here.

The noise terms (n_1, n_2, n_3) in the above equations will now be neglected and a solution for θ_B and θ_D found. Taking the sum of equation (4-1) and (4-3) and dividing by equation (4-2) gives:

$$\frac{S_1+S_3}{S_2} = 2[a_1G_1 \cos(Z_1)+a_2G_2 \cos(Z_2)]/(a_1G_1+a_2G_2) \qquad (4-4)$$

Then by subtracting equation (4-3) from (4-1) and dividing by (4-2) we get the following:

$$\frac{S_1-S_3}{S_2} = j2[a_1G_1 \sin(Z_1)+a_2G_2 \sin(Z_2)]/(a_1G_1+a_2G_2) \qquad (4-5)$$

By substituting the values of Z_1 and Z_2 into equations (4-4) and (4-5) by their equivalents in terms of θ_B and θ_D (see, equations (3-5), (3-6), (3-17), (3-18) in chap.3) and after simplification we get:

$$\frac{S_1+S_3}{S_2} = 2\cos(w\theta_B) \cos(w\theta_D)-2\sin(w\theta_B) \sin(w\theta_D)\left[\frac{(a_1G_1-a_2G_2)}{(a_1G_1+a_2G_2)}\right] \qquad (4-6)$$

$$\frac{S_1-S_3}{S_2} = j2\{\sin(w\theta_B) \cos(w\theta_D)+\cos(w\theta_B) \sin(w\theta_D)\left[\frac{(a_1G_1-a_2G_2)}{(a_1G_1+a_2G_2)}\right]\} \qquad (4-7)$$

where $w=2\pi d/\lambda$

In equations (4-6) and (4-7) there is an identical underlined term which simplifies as follows:

$$Tre= (a_1G_1-a_2G_2)/(a_1G_1+a_2G_2)$$

$$=\{[1-|a_2|\,G_2\,\exp(\Psi_2-\Psi_1)/|a_1|\,G_1]/$$

$$[1+|a_2|\,G_2\,\exp(\Psi_2-\Psi_1)/|a_1|\,G_1]\} \qquad (4-8)$$

letting the phase difference $\Psi=\Psi_2-\Psi_1$, and $K=(|a_2|G_2/|a_1|G_1)$ gives:

$$Ter=[(1-K^2)-j2K\,\sin(\Psi)]/[1+K^2+2K\,\cos(\Psi)] \qquad (4-9)$$

Now substitute equation (4-9) into equations (4-6) and (4-7) and find the real and imaginary parts.

$$\frac{S_1+S_3}{S_2} = 2\,\cos(w\Theta_B)\,\cos(w\Theta_D)-2\,\sin(w\Theta_B)\,\sin(w\Theta_D)\{[(1-K^2)$$
$$-j2K\,\sin(\Psi)]/(1+K^2+2K\,\cos(\Psi))\} \qquad (4-10)$$

$$\text{Real}\left(\frac{S_1+S_3}{S_2}\right)=2\,\cos(w\Theta_B)\,\cos(w\Theta_D)-2\,\sin(w\Theta_B)\,\sin(w\Theta_D)[(1-K^2)$$
$$/(1+K^2+2K\,\cos(\Psi))] \qquad (4-11)$$

$$\text{Imag}\left(\frac{S_1+S_3}{S_2}\right)= 4K\,\sin(\Psi)\,[\sin(w\Theta_B)\,\sin(w\Theta_D)]/[1+K^2+2K\,\cos(\Psi)] \qquad (4-12)$$

$$\frac{S_1-S_3}{S_2} = j2\,\sin(w\Theta_B)\,\cos(w\Theta_D)+j2\,\cos(w\Theta_B)\,\sin(w\Theta_D)\{[(1-K^2)$$
$$-j2K\,\sin(\Psi)]/[1+K^2+2K\,\cos(\Psi)]\} \qquad (4-13)$$

$$\text{real}\left(\frac{S_1-S_3}{S_2}\right) = 4K\sin(\Psi)\,[\cos(w\Theta_B)\sin(w\Theta_D)]/[1+K^2+2K\cos(\Psi)] \qquad (4\text{-}14)$$

$$\text{Imag}\left(\frac{S_1-S_3}{S_2}\right) = 2\sin(w\Theta_B)\cos(w\Theta_D)+2(1-K^2)[\cos(w\Theta_B)\sin(w\Theta_D)]/$$

$$[1+K^2+2K\cos(\Psi)] \qquad (4\text{-}15)$$

Carefully examining equations (4-12) and (4-14) it is seen that there is only one difference: in equation (4-12) we have $\sin(w\Theta_B)$ insted of $\cos(w\Theta_B)$ in (4-14). Dividing these two equations gives:

$$\Theta_B = (1/w)\tan^{-1}\{\text{Imag}\,[(S_1+S_3)/S_2]/\text{Real}\,[(S_1-S_3)/S_2]\} \qquad (4\text{-}16)$$

From equation (4-16) it can be seen that the calculation of Θ_B is independent of the phase difference (Ψ) between the direct signal and its coherent multipath except at $\Psi=0.0^\circ$ or 180° where the undetermined solution occurs ($\Theta_B=\tan^{-1}(0/0)$, in case no noise exist).

Inspecting the second term of equation (4-11), it is seen to involve the multiplication of two sines for small angles (Θ_B, Θ_D) and the value of ($1-K^2$) which is very small when the specular reflection coefficient of the smooth surface is large. Therefore, its effect on the equation is very small and (4-11) can be approximated by:

$$\text{Real}\,[(S_1+S_3)/S_2] = 2\cos(w\Theta_B)\cos(w\Theta_D) \qquad (4\text{-}17)$$

On substituting the value of θ_B from equation (4-16) in equation (4-17) the angle θ_D can be calculated easily and in turn θ_t & θ_r the angles of arrival in the elevation plane for the direct signal and its coherent multipath.

$$\theta_D = (1/w)\ \cos^{-1}\{\text{Real}\ [(S_1+S_3)/S_2]\ /2\ \cos(w\theta_B)\} \qquad (4\text{-}18)$$

When noise is present the solutions are perturbed but if the signals can, as is normally the case, still be represented as the sum of two plane waves then the preceding solution continues to give the best maximum likelihood bearing estimates as will be shown from the simulation results in the coming section.

Now, let us investigate the solutions for the symmetric and nonsymmetric cases separately according to their definitions in chapter 3. The phase difference (Ψ) status indicator and the four-subapertures technique will be discussed too.

4-2.1 The symmetric case solution

In this case the target and its image are symmetrically located about the centre of the elevation pattern of the antenna and θ_B is Known (for a broad-side beam from a vertical array $\theta_B=0$). To calculate θ_D, substitute the known value of θ_B in equation (4-18). When $\theta_B=0$ then $\theta_t = \theta_D$ and $\theta_r=-\theta_D$ and from equation (4-18) we get:

$$\theta_D = (1/w)\cos^{-1}\{\text{Real}\,[S_1+S_3)/S_2]\} \qquad (4\text{-}19)$$

In comparing this simple equation, where θ_D can be easily calculated from a look-up table, with its equivalent of the 3SA-MLE method (in chap.3) in which a quadratic equation is required to be solved , one concludes that this method is simpler to implement in practical system and it is faster in calculation.

4-2.2 The nonsymmetric case solution

In this case θ_B is not known a priori unlike the symmetric case above and it has to be estimated from equation (4-16). It can be seen that the value of θ_B does not depend on the reflection coefficient of the surface except when ρ_s=0.0, where the undetermined solution of (0/0) occurs. Also, θ_B does not theoretically depend on the phase difference between the two signals (no noise being added to the signals) except when the phase difference is either zero or 180 degrees when the undetermined solution of (0/0) occurs again. Besides, the calculation of θ_D from (4-18) shows that it depends on θ_B and by looking at the second term of equation (4-11) one finds that θ_D depends on the reflection coefficient of the surface through K and the estimate of θ_D becomes biased when the absolute value of ρ_s gets very small.

In comparing this simple nonsymmetric solution, which involves finding the values of θ_B and θ_D from a look-up

table, with its equivalent of the 3SA-MLE method which involves the solution of a quartic equation, one easily concludes that this method is simpler to implement in a real system and it is faster in execution. The performance accuracy of this method (symmetric and nonsymmetric cases) is found to be similar to that of the 3SA-MLE in general with some extra advantages as will be seen in the next section.

4-2.3 The phase difference status indicator

When the direct signal and its coherent multipath are in-phase ($\Psi=0^{\circ}$) or anti-phase ($\Psi=180^{\circ}$) at the centre of the array the accuracy in estimating the elevation angle is found to be poor (just when $\Psi=180^{\circ}$ for the symmetric case) as will be shown from the simulation results in the next section. Therefore, it is very useful to be able to decide if the two signals are actually in-phase or anti-phase in order to detect gross error in estimating the angle and if all possible to avoid it. A simple technique can be used from equation (4-14) by looking at the value of the real part of $[(S_1-S_3)/S_2]$. This value approaches zero whenever $\Psi=0^{\circ}$ or 180° (the same can be seen from equation (4-12) but its use is limited to the non-zero values of Θ_B). In practice, the absolute value of the numerator of equation (4-14) must be used only to avoid the effect of cos(Ψ) in the denominator, where its change of sign leads to undesirable changes in the denominator overall value. The absolute value of the denominator is largest when $\Psi=0^{\circ}$ (or multiples of 360°) and

smallest when $\Psi=180^{\circ}$ (or 180° + multiples of 360°), for a given values of ρ_B, θ_B, and θ_D, while the absolute value of the numerator the largest when $\Psi=90^{\circ}$ (or 90° + multiples of 180°) and smallest whenever $\Psi=0^{\circ}$ or 180° (or multiples of 180°).

This method will be used in a four-subaperture technique (4SA-TRM) similar to that discussed in chapter 3 and in a new mutual three and four-subapertures technique (3&4SA-TRM) to get the optimum possible estimation accuracy.

4-2.4 The four-subapertures techniques

In the previous chapter we discussed the four-subapertures technique to solve the in-phase and anti-phase estimation accuracy problem with the 3SA-MLE. This technique depends on estimating the phase difference value (Ψ) from the estimated angles of arrivals (see,section 3-3). The procedure was lengthy in processing and costly in terms of practical implementation, also it sacrifices some accuracy when Ψ is close to quadrature (close to zero for the symmetric case) by not using all of the available elements in the array. This method can be equally applied here by following the same steps shown in section 3-3, the only difference is that the estimation of θ_t and θ_r must be done by using 3SA-TRM insted 3SA-MLE.

In the above sub-section a new method is shown which allow us to choose the best aperture set (AP1 or AP2, see figure 3-4 in chap.3) right from the start and before the

bearing estimation process begins. Figure 4-1 shows a block diagram of the four-subapertures processing technique using the new in-phase and anti-phase procedure (4SA-TRM) which can be sumarized by the following steps:

a- Calculate the absolute values (sys1 and sys2) of the numerators of the real parts of $(S_1-S_3)/S_2$ and $(S_2-S_4)/S_3$ respectively.

b- Compare sys1 with sys2 and choose the aperture (AP1 or AP2) associated with the higher in value.

c- Continue estimation of the values of θ_t and θ_r by using the 3SA-TRM method with samples input from the chosen aperture in step b.

The choice in step b above leads to degredation in the performance of the symmetric case (for $\Psi<90^{\circ}$) where the best estimate is obtainable when $\Psi=0^{\circ}$. This price is needed in order to get better performance when $\Psi=180^{\circ}$ by using this technique unless others are available. In fact another technique is already discussed in chapter 3 which depends on the amplitudes comparison principles and it is not going to be repeated here.

However, a new mutual three and four subapertures technique (3&4SA-TRM) is found to improve the performance of all types of four-subapertures discussed so far. This technique depends on dividing the linear array into three and four-subapertures in parallel with instantaneous sampling as shown in figure 4-2. The samples from the four-subapertures arrangement are stored for possible use within the processing cycle if the in-phase or anti-phase condition occurs (just

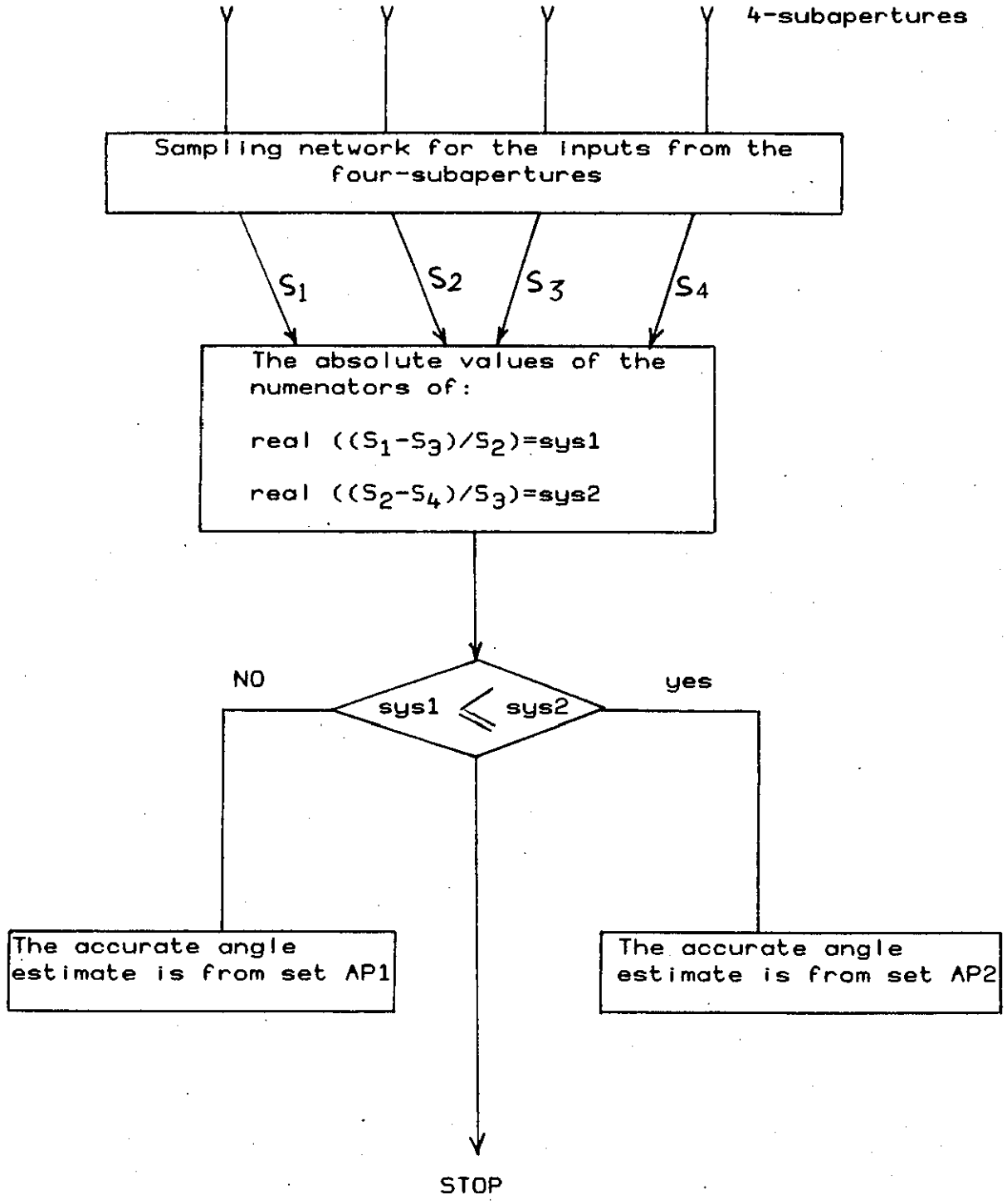

Fig. 4-1 : Block diagram represents the four-subapertures processing technique for the nonsymmetric and symmetric cases.

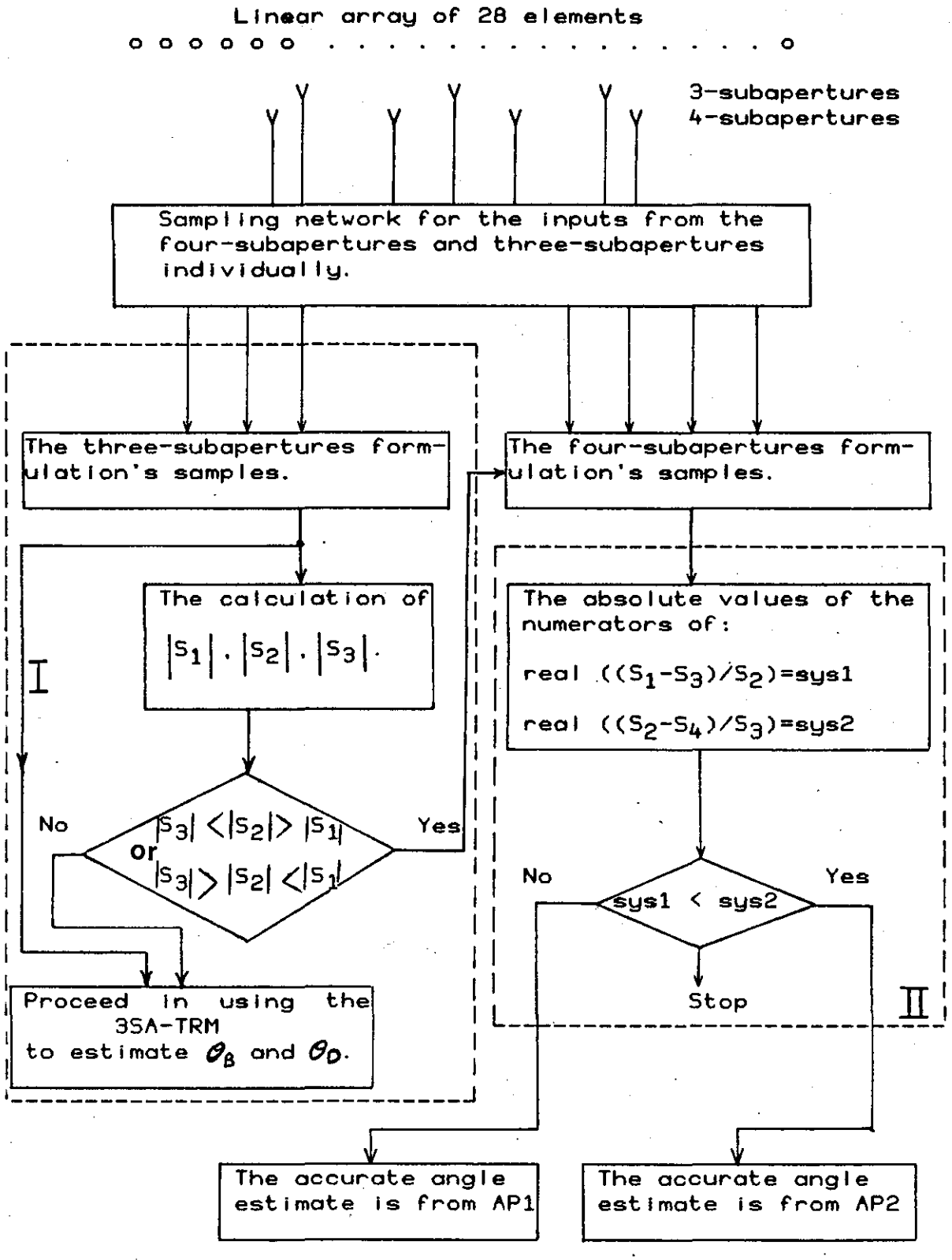

Fig. 4-2 : Block diagram represents the combined three and four subapertures processing technique for the nonsymmetric and symmetric cases.

anti-phase for the symmetric case). The absolute values of S_1, S_2, and S_3 from the three-subapertures arrangement (inside the doted box I, not to be mixed with the ones inside the doted box II for the four-subapertures) are calculated and checked for possible in-phase or anti-phase occurrence (just anti-phase for the symmetic case), depending on the fact that when the two received signals are in-phase at the array centre then $|S_1| < |S_2| > |S_3|$, and the opposite for anti-phase signals. If it is found that the two signals are not close to in-phase or anti-phase (just anti-phase for the symmetric case) then the solution will continue using the 3SA-TRM method with full array capacity as shown in figure 4-2, otherwise the stored samples from the four-subapertures arrangement will be enabled and the four-subapertures processing technique (4SA-TRM) proceeds according to steps a, b, and c listed earlier in this subsection, and as shown inside the doted box II in figure 4-2.

In fact there is easier way to implement the 3&4SA-TRM technique for the symmetric case solution by using amplitude comparison only. This can be done easily by replacing the dotted box II in figure 4-2 by the dotted one in figure 4-3 (keeping in mind that S_1, S_2, and S_3 in box I are different from those in box II). The four-subapertures amplitudes comparison for the symmetric case is discussed in the previous chapter and not going to be repeated here. All the techniques using four-subapertures are equally applied to the 3SA-MLE method discussed in chapter 3 and vis versa. The next section presents the simulation results for the 3SA-TRM, 4SA-TRM, and 3&4SA-TRM with extended descussion.

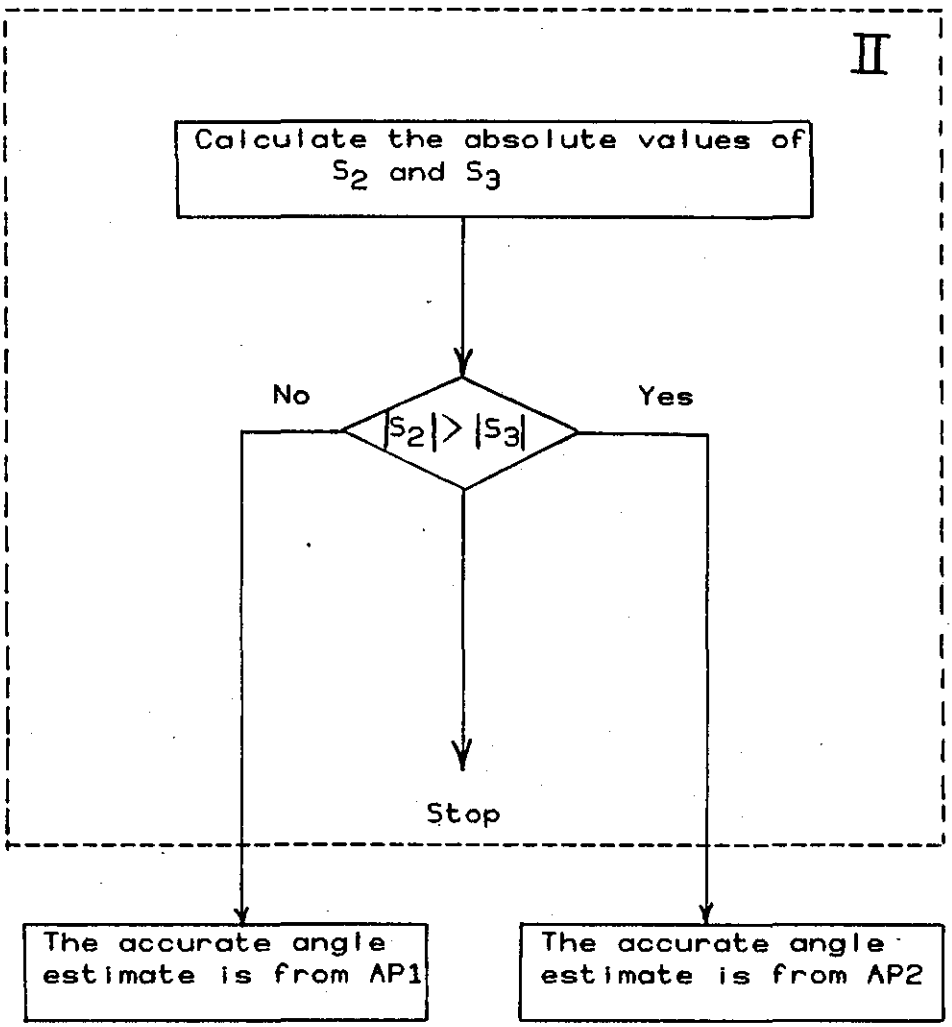

Fig. 4-3 : Block diagram represents the combined three and four subapertures processing technique for the symmetric case (amplitude comparison only).

4-3 Simulation results and discussion

All the simulations have been made using three (or four) subapertures of seven elements each, except for the mutual 3&4SA-TRM technique where the number of elements in each subaperture for the three-subapertures arrangement is nine insted of seven. Interelement spacing is $\lambda/2$. Gaussian noise of zero mean and σ^2 variance was added to the signals and one thousand trials were made to find the average errors in the angle estimation at each given phase difference. The rms error, 3dB beamwidth, and S/N were calculated as shown in chapter 3 (sec. 3-4).

The target model used in this simulation is Swerling case 5 type (SW.5), and for comparison purposes Swerling case 2 (SW.2) target type is used too. A noisy signal is generated for the 3SA-TRM and 4SA-TRM according to the target models above and in the same way used for the 3SA-MLE and 4SA-MLE shown in chapter 3. The solutions were computed for the symmetric and nonsymmetric cases for all the techniques discussed so far in this chapter. The phase difference (Ψ) is always taken to be multiples of 22.5 degrees in the range from 0° to 180°. A histogram of simulation results is used to demonstrate the performance of the 3SA-TRM and 4SA-TRM at some cases, where the rms angle-of-arrival (+beamwidth) is divided into 20 zones of accuracy, from 0.0-0.05, ...0.9-0.95, >0.95.

4-3.1 The symmetric case solution

Figure 4-4 shows the simulation results of the 3SA-TRM for a target with θ_B=0, S/N=30 dB, ρ_s=0.9 , and θ_D=0.5,0.25,0.125 BW, using SW.5 target type. For comparison the corresponding result is shown for SW.2 target type only for the case θ_D=0.25 BW. In comparing the solution using SW.5 target type to that using SW.2, we find that the first is much more accurate than the second over all values of Ψ with average rms angle-of-arrival error enhancement of 0.06. The rms error is large when Ψ=180° and very small when Ψ=0°, also it increases when θ_D decreases. In comparing these curves with their correspondents in the 3SA-MLE in figure 3-8 (chap.3) one concludes that the estimation accuracy obtainable is very much alike over all values of Ψ and θ_D with very small deviations when Ψ is close to the antiphase condition (this is more obvious for SW.2 target's type). Besides, figure 4-5 shows a histogram of simulation results for the symmetric 3SA-TRM for the above two target's types, when θ_D=0.25 BW, θ_B=0, S/N=30 dB, ρ_s=0.9, Ψ=90 degrees, where the rms error of the SW.5 type is shown to be within the range 0.0-0.05 for 78 % of the time and 0.05-0.1 for 18 %, while for the second target type it drops to 63 % , and 31 % respectively. In comparing these results with their correspondents in figure 3-11 (chap.3) one can see that the performance is very much the same for the first while some improvement in accuracy is shown for the second. Figure 4-6 presents the S/N performance for SW.5

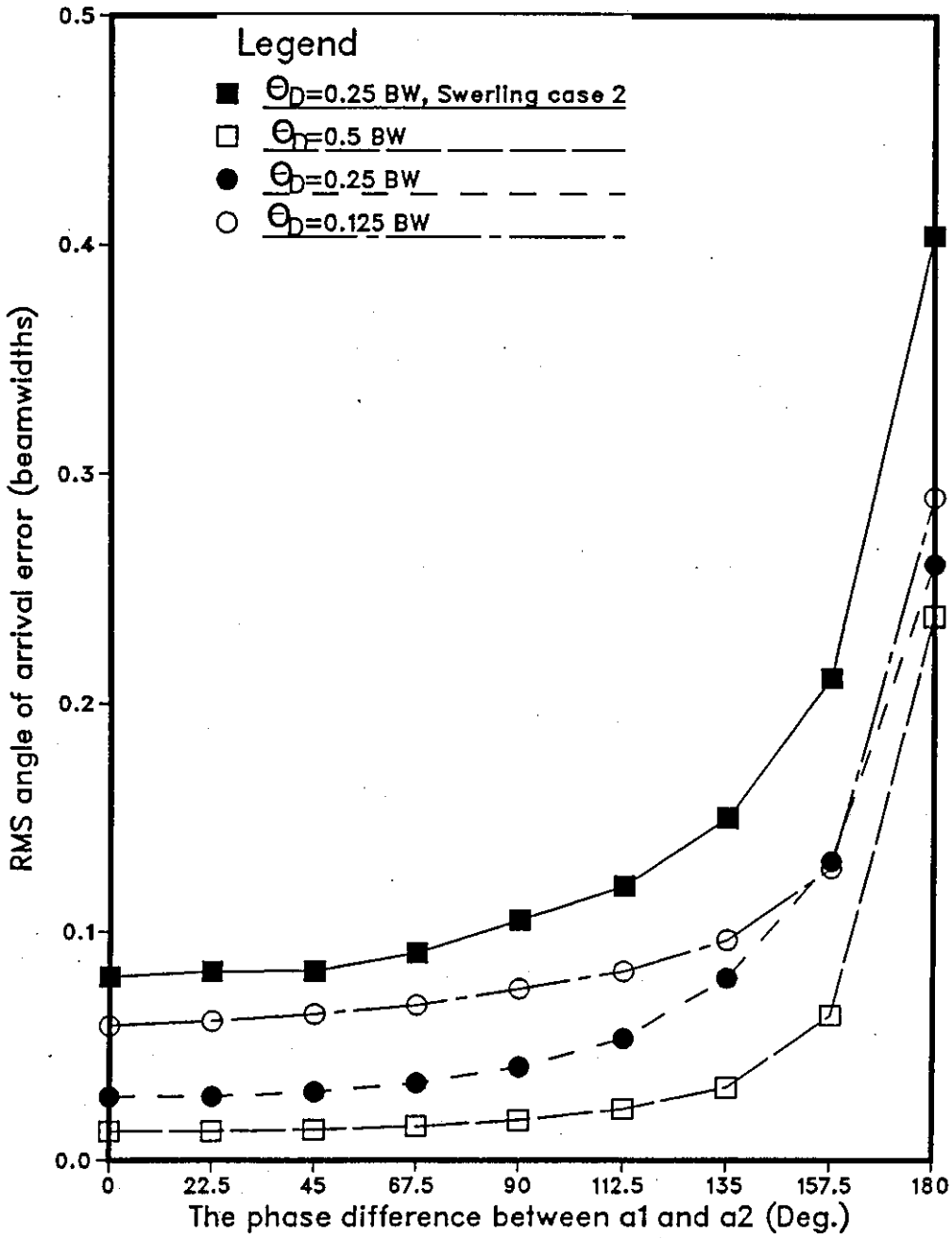

Figure 4–4 :RMS error of symmetric 3SA–TRM as a function of phase difference between the two signals for Θ_B=0.0, S/N=30 dB, ρ_s=0.9. For comparison, SW.2 target's type is shown

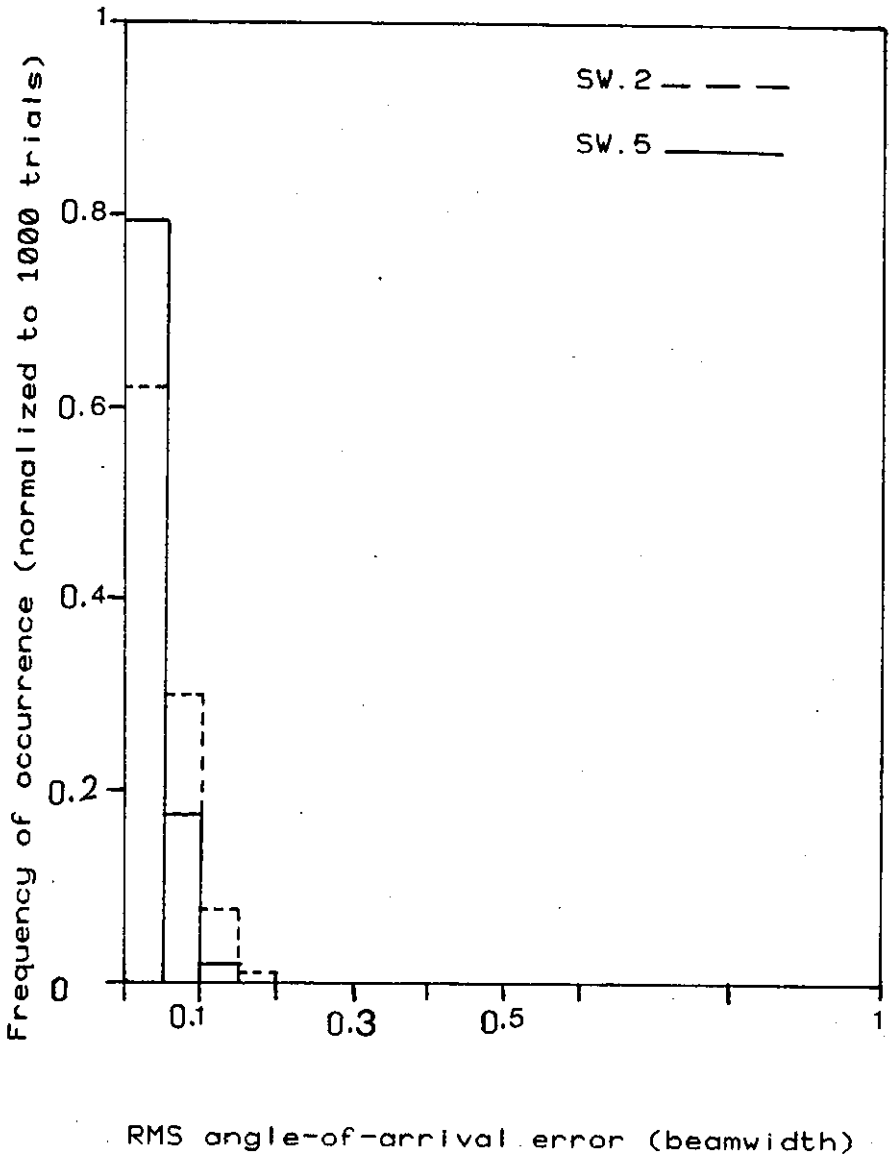

Figur 4-5 :Histogram shows the performance of the symmetric 3SA-TRM for Swerling cases 2 and 5 target types θ_B=0, θ_D=0.25 BW, S/N=30 dB, ρ_s=0.9, Ψ=90°.

target's type with θ_B=0, θ_D=0.5 BW, ρ_s=0.9, and S/N= 30,20,10 dB. In general, one concludes that the rms error increases as the S/N decreases. In comparing these curves with those of figure 3-9 (chap.3) one can see similar accuracy over all values of Ψ except when Ψ=180° where some deviations occurs. Figure 4-7 presents the performance with different values of ρ_s where θ_B=0, θ_D=0.25 BW, S/N=30 dB, and ρ_s=0.9,0.5,0.1. In general, when ρ_s decreases the performance gets better when the absolute value of Ψ is close to the out of phase case (generally when Ψ>90°, depends on ρ_s) and a little worse elsewhere. The improvement at Ψ=180° is very substantial where the rms error drops from 0.26 to just 0.065 when ρ_s changes from 0.9 to 0.1. In comparing these curves with those in figure 3-10 (chap.3) one can see very much similar results. The main reason beyond this improvement when Ψ=180° is the same in both methods (3SA-TRM, 3SA-MLE) and is not going to be repeated here (see sec.3-4.1 in chap.3).

Before discussing the new four-subapertures method results, let us examine the case of the imaginary angle occurrence (i.e when $\theta_t=\theta_r$) and the accuracy in estimating the phase difference from the estimated angles of arrival of the target and its coherent multipath. Table 4-1 shows computer simulation results for the frequency of occurrences of the imaginary angle (Im-ang) and when the absolute error of the estimated value of Ψ is greater than a given value (assumed here to be 10°) from its true one (ph-div), in 1000 trials for θ_B=0, S/N=30 dB, ρ_s=0.9, and θ_D=0.5,0.25,0.125 BW for SW.5 target's type (and SW.2 target's type just at

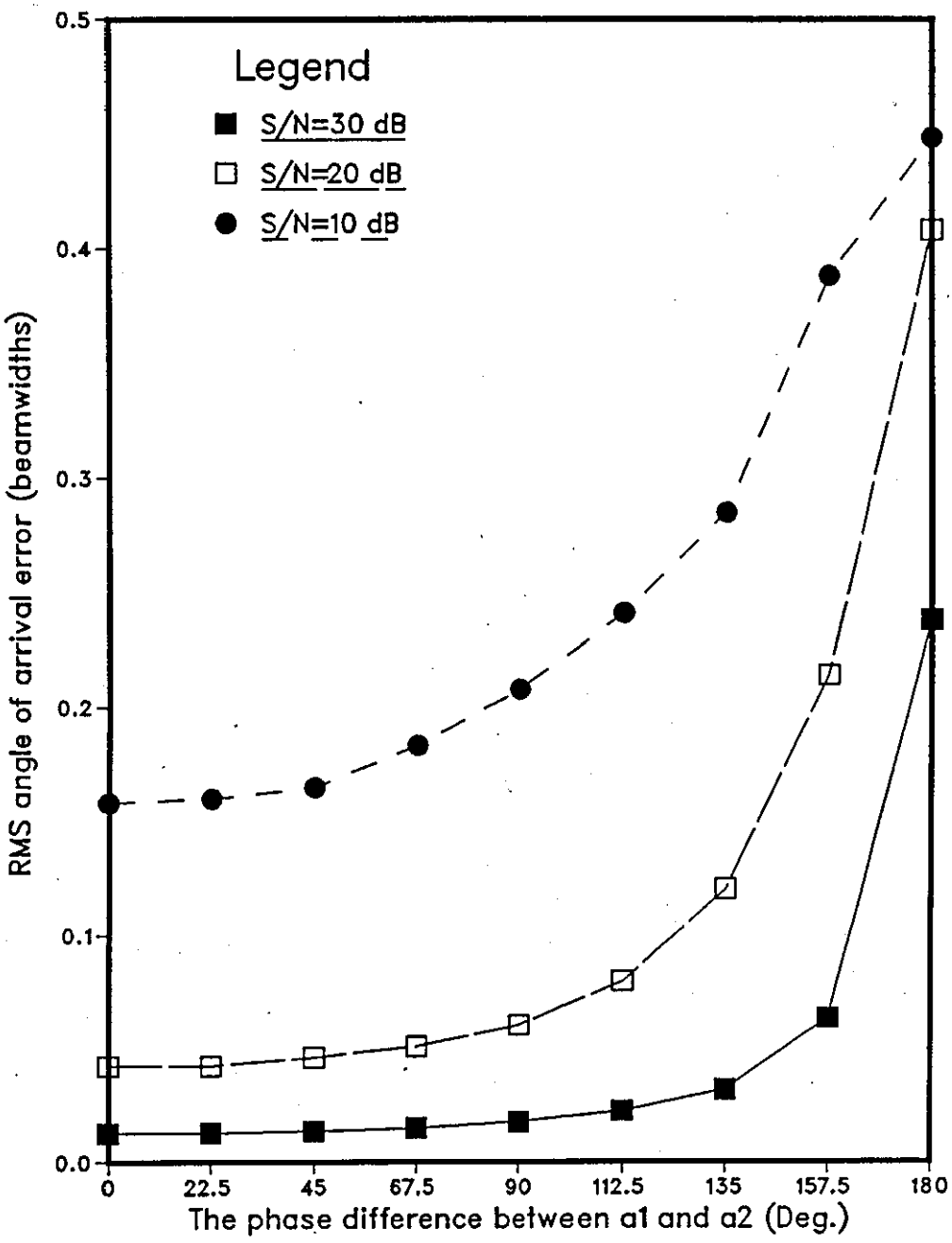

Figure 4–6 :RMS error of symmetric 3SA–TRM as a function of phase difference between the two signals for Θ_B=0.0, Θ_D=0.5 BW, ρ_s=0.9

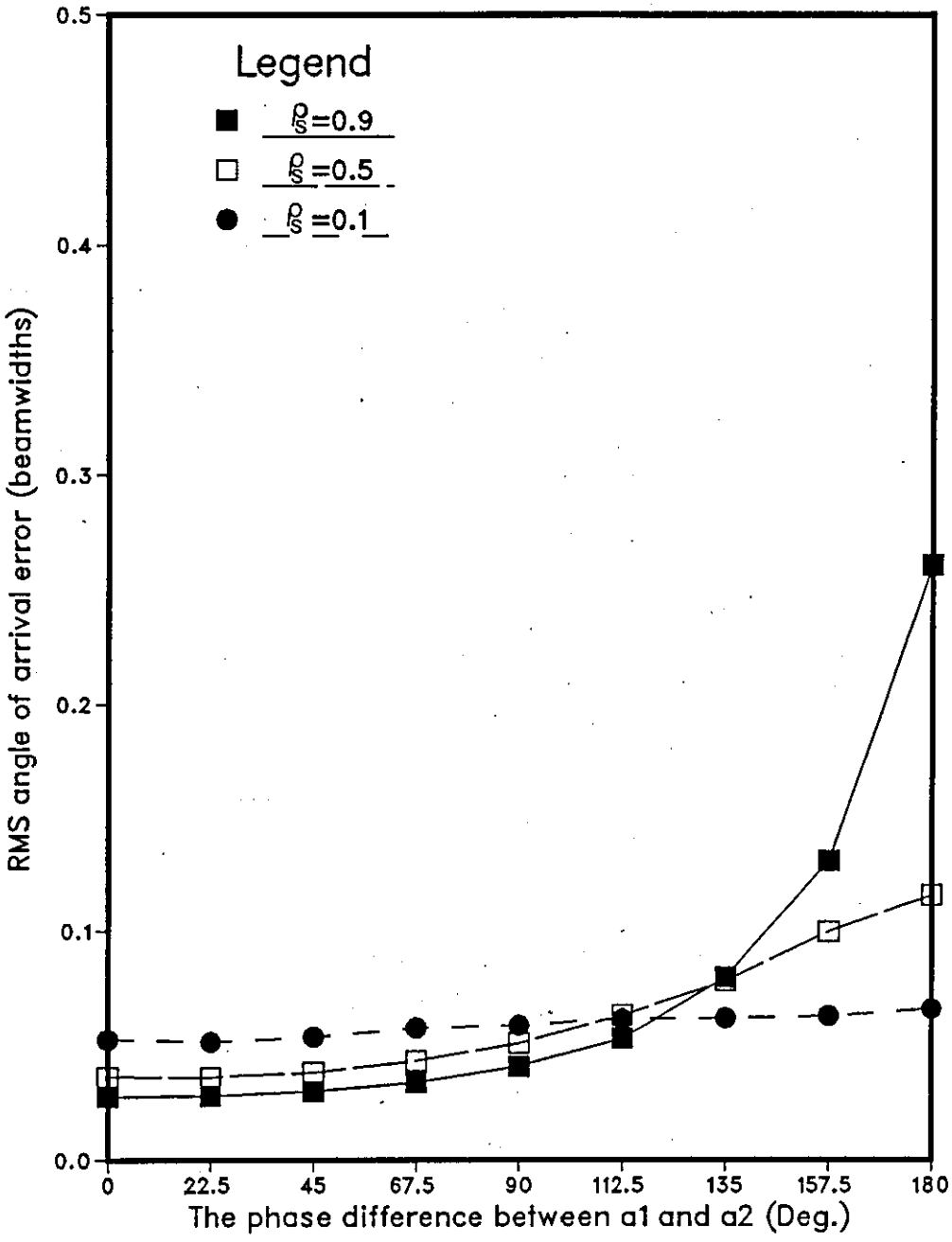

Figure 4–7 :RMS error of symmetric 3SA–TRM as a function of phase difference between the two signals for Θ_B=0.0, S/N =30 dB, Θ_D=0.25 BW.

Table 4-1 The imaginary angle and erroneous estimated phase difference (>10° deviation from the true value) occurrences in the symmetric 3SA-TRM for θ_B=0, S/N=30 dB, ρ_s=0.9, θ_D=0.5,0.25,0.125 BW, for 1000 trials at each phase shown. For comparison the results for SW.2 target's type is shown when θ_D=0.25 BW.

Phase	0.5 BW		0.25 BW				0.125 BW	
	Im-ang.	Ph-div.	IM-ang		Ph-div.		IM-ang.	Ph-div.
	SW.5	SW.5	SW.5	SW.2	SW.5	SW.2	SW.5	SW.5
0.0	0	0	0	38	9	203	120	212
22.5	0	0	0	40	36	258	132	425
45.0	0	0	1	41	120	373	147	635
67.5	0	1	1	58	227	445	179	715
90.0	0	1	1	67	310	525	217	787
112.5	0	5	4	86	366	605	253	810
135.0	0	5	37	148	386	616	287	818
157.5	0	6	156	227	402	641	375	822
180.0	107	0	284	239	31	235	339	164

Θ_D=0.25 BW for comparison). The imaginary angle occurrence is zero over all values of Ψ when Θ_D=0.5 BW except at Ψ=180° where it occurs 107 times which might explains the bad performance at this point. When Θ_D decreases the Im-ang occurrence increases over all values of Ψ leading to degredation in the angle estimation accuracy as shown in figure 4-4. The estimated value of Ψ is worst when the two signals are close to phase opposition as can be seen from the table (mainly because of the decrease in the S/N) with one exception at Ψ=180° where the imaginary angle occurs very frequently. The reason behind this exception is that when an imaginary angle occurs a test is carried out to find whether the two signals are close to in-phase or anti-phase conditions depending on the fact that whenever the two signals are anti-phase at the centre of the array then $|S_3|>|S_2|<|S_1|$ and the opposite occurs when the two signals are in phase agreement at the array's centre. Thus, depending on the above conditions the value of Ψ is set to either 0° or 180° whenever the imaginary angle occurs leading to high accuracy in estimating the value of Ψ when the two signals are anti-phase in particular and elsewhere in general. The frequency of occurrence of ph-div increases as Θ_D decreases as can be seen from the table. In comparing with the SW.2 target ⊐ type for Θ_D=0.25 BW one concludes that the frequency of occurrences of the imaginary angle and the erroneous values of the estimated Ψ is much higher for the second type which explains the increase in the rms error shown in figure 4-5, where a histogram is shown for both types. In comparing

these results with those in table 3-2 (chap.3) one finds that the imaginary angle occurrences using this method is slightly less than that of using the 3SA-MLE, except at $\Psi=180^{\circ}$ where it becomes much less. The phase estimation is very much alike in both methods over all values of θ_D and Ψ. Thus, one concludes that using the four-subapertures techniques discussed in chapter 3 (by following the same steps in figure 3-5 after replacing the 3SA-MLE by 3SA-TRM) will leads to very much similar results and is not going to be repeated here with the new trigonometric solution. In conclusion, the bigger the angular seperation, and the smaller the phase difference between the two targets, the better the accuracy in estimating the value of Ψ, and the less the occurrence of imaginary angles.

According to the discussion in section 4-2 above and the block diagram in figure 4-1 a computer simulation is carried out to determine the effectiveness of the 4SA-TRM in improving the performance of the symmetric case of the 3SA-TRM when the two targets are in (or close to) phase opposition. Figure 4-8 shows the simulation results of the symmetric 4SA-TRM for $\theta_B=0$, $\rho_s=0.9$, S/N=30 dB, and $\theta_D=0.5,0.25,0.125$ BW, using SW.5 target type. For comparison 3SA-TRM is shown only for $\theta_D=0.25$ BW (27 elements are used insted of 28 for the 4SA-TRM to be able to divide into three-equal-subapertures). In comparing each curve with its correspondent in figure 4-4, keeping in mind that we use just 3/4 of the total array's elements in the four-suabapertures method, while the rms error is normalized to 3dB beamwidth of

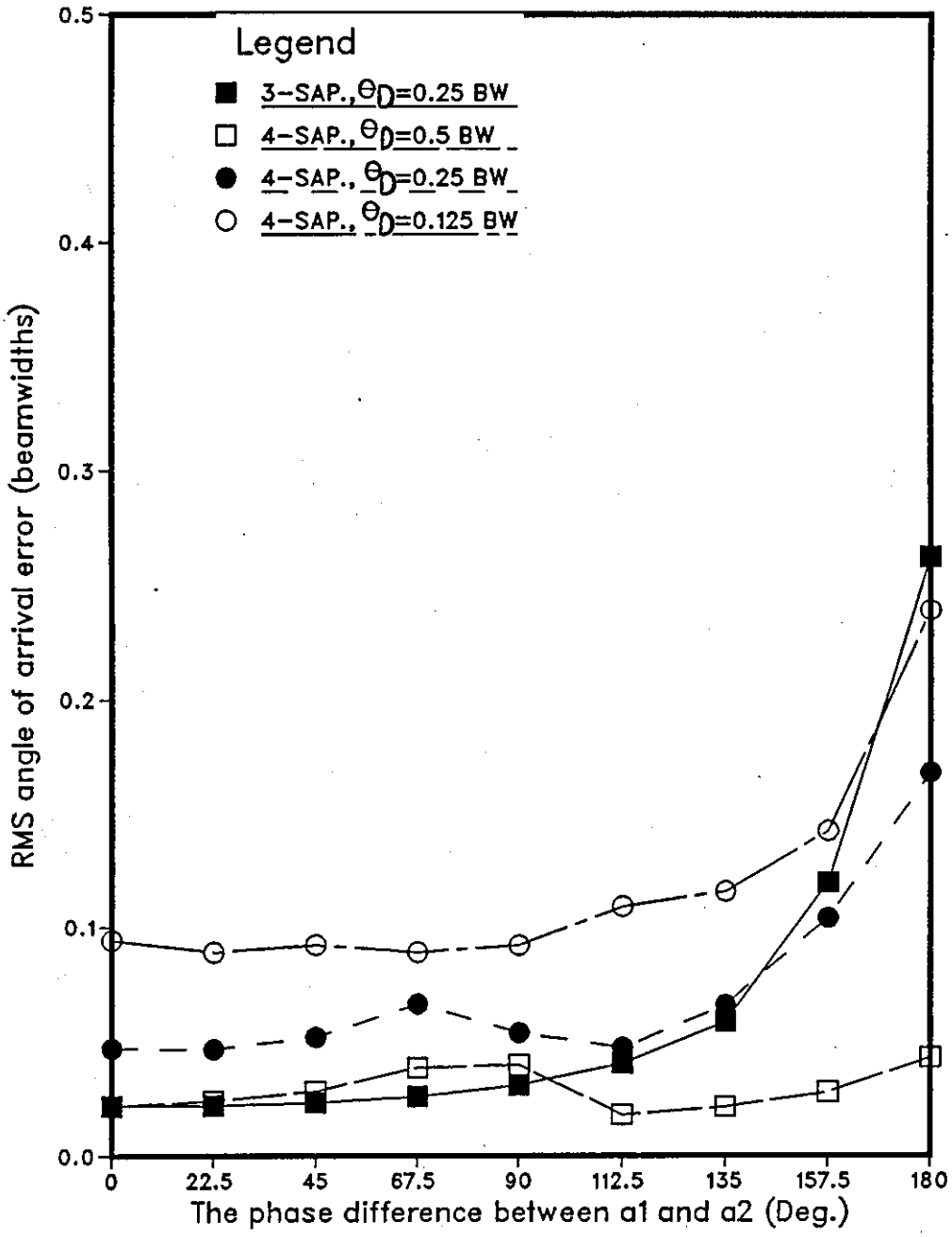

Figure 4-8 :RMS error of symmetric 4SA-TRM as a function of phase difference between the two signals for Θ_B=0.0, S/N=30 dB, ρ_s=0.9. For comparison, 3SA-TRM is shown for Θ_D =0.25 BW

the whole array, one can see a big reduction in the rms error when Ψ is close to 180° in general and in particular the accuracy increases sharply when θ_D is large. A little degredation at small values of Ψ is shown to be mainly related to the normalization method and the lower S/N per subaperture (1.2 dB less), and the comparison method used where the best solution is assumed to be at phase quadrature and not at zero phase where the actual best solution occurs (see, sec. 4-2.3). In comparing the result of 3SA-TRM (using 27 elements) with its correspondent 4SA-TRM ones (using 28 elements) for θ_D=0.25 BW as shown on the same figure, a big improvement is shown when Ψ is close to anti-phase condition and a little degredation elsewhere. Rms error increases by 0.02 at $\Psi=0^{\circ}$ and is worst at $\Psi=67.5^{\circ}$ where it increases by 0.031. The main reason for this degredation is the higher S/N per subaperture for the 3SA-TRM case (~1 dB) in comparison with the 4SA-TRM ones and the used comparison method. By comparing these results with those in figure 3-12 (chap.3) one can see that the performance of the 3SA-MLE is slightly better for all values of Ψ except when θ_D=0.125 BW where this method shows slightly higher accuracy when $\Psi>90^{\circ}$ in general. Figure 4-9 shows a histogram results for θ_D=0.25 BW, ρ_s=0.9, S/N=30 dB, θ_B=0, and $\Psi=180^{\circ}$ for the 3SA-MLE and the 4SA-TRM, where the rms error (+beamwidth) appears to be within the range 0-0.1 for 55 % of the time for the 4SA-TRM, while it drops to 20 % for the 3SA-TRM. Also, one can see the high occurrence of imaginary and erroneous angles (44 % of the time) for the 3SA-TRM in comparison with that of the

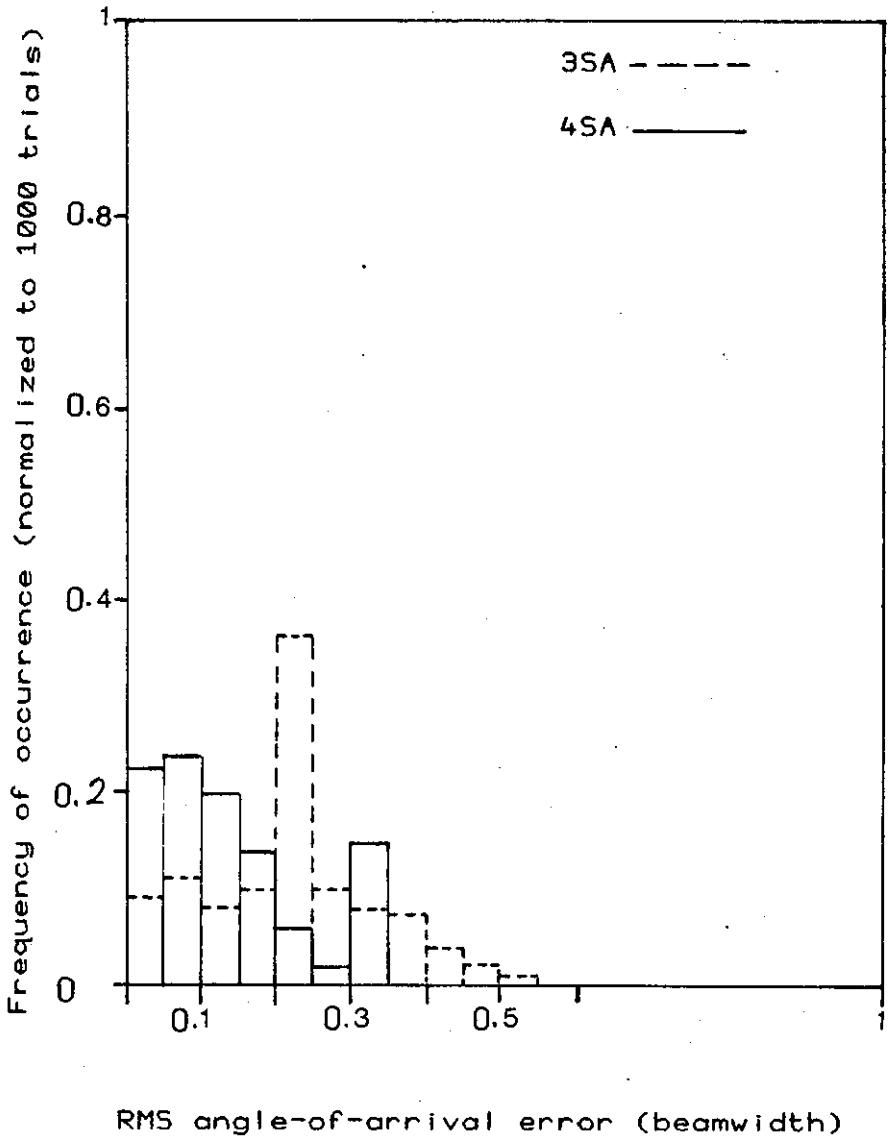

Figur 4-9 :Histogram shows the performance of the symmetric 3SA-TRM and 4SA-TRM for Swerling case 5 target type θ_B=0, θ_D=0.25 BW, S/N=30 dB, ρ_s=0.9, Ψ=180°.

4SA-TRM ones (20 % of the times).

In the above four-subapertures technique we used the comparison procedure, between sys1 and sys2, to decide which set gives the best angle estimation. In fact the amplitude comparison technique discussed in the previous chapter is more accurate and efficient for the symmetric case solution. However it is still not efficient enough for some accuracy is lost when the two signals are far from being antiphase, by not being able to use all the available elements of the array. As discussed in section 4-2.4 a new 3&4SA-TRM technique is possible which makes optimum solution obtainable over all values of Ψ by making use of the full array whenever possible. Figure 4-10 shows simulation results for the symmetric 3&4SA-TRM according to the block diagram in figure 4-2 (in the dotted box I, just the second comparison inquality must be used which represent the anti-phase condition) for Θ_B=0, S/N=30 dB, ρ_s=0.9, and Θ_D=0.5,0.25,0.125 BW, using SW.5 target's type. For comparison 3SA-TRM performance is shown only for Θ_D=0.25 BW (27 elements are used insted of 28). In comparing each curve with its correspondent in figure 4-8, where the 4SA-TRM technique is used only, one can see that the rms error is the same when Ψ close to anti-phase condition (4SA-TRM tech. mainly chosen) while a big improvement occurs for low values of Ψ where the choice of the 3SA-TRM is mainly occurs. By comparing the 3SA-TRM and the 3&4SA-TRM performance for Θ_D=0.25 BW, one can see a negligible variation in accuracy when the value of Ψ is far from the anti-phase condition (mainly related to the missing

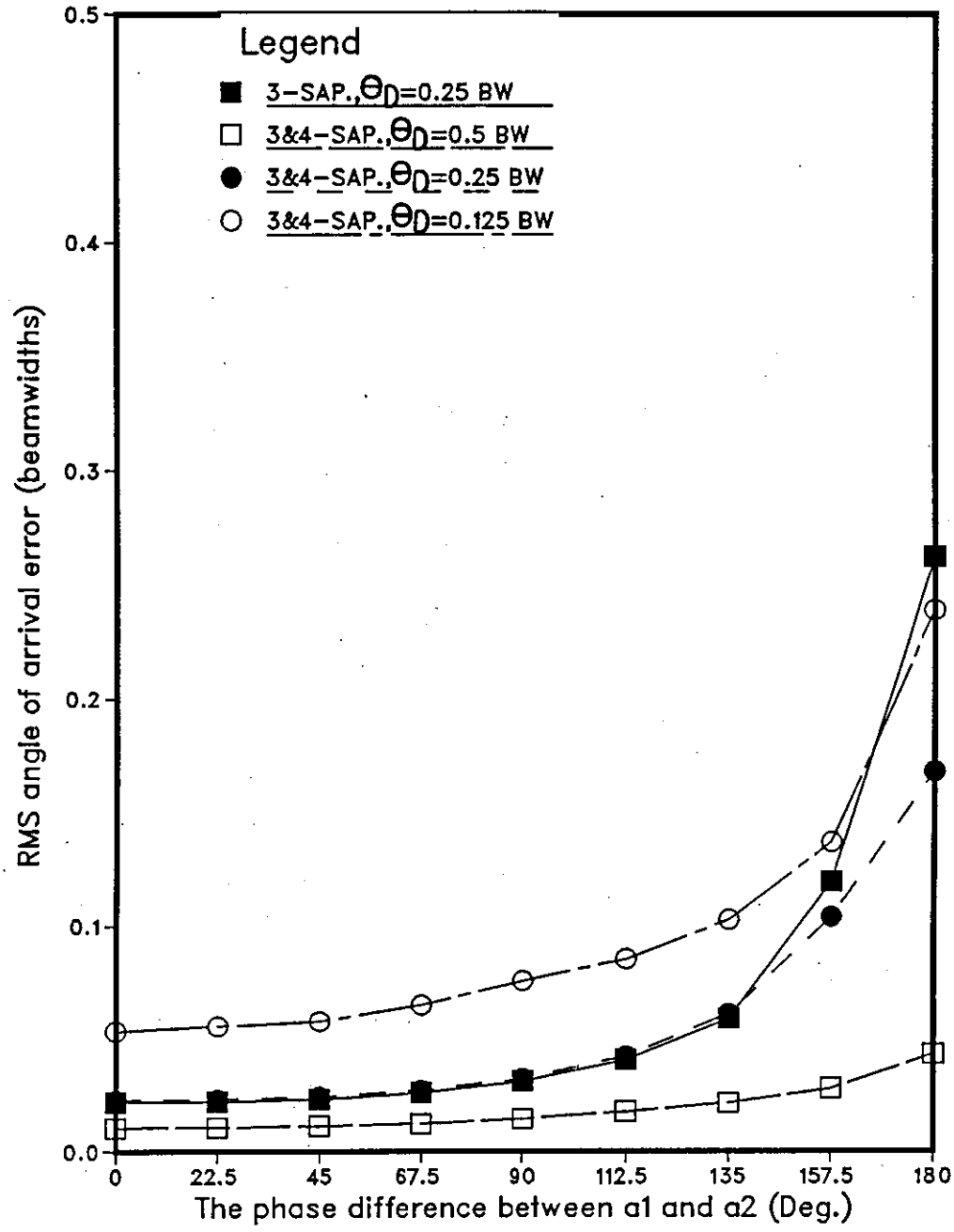

Figure 4-10 :RMS error of symmetric 3&4SA-TRM as a function of phase difference between the two signals for Θ_B=0.0, S/N=30 dB, ρ_s=0.9. For comparison, 3SA-TRM is shown for Θ_D=0.25 BW

element) and a great improvement in accuracy for the 3&4SA-TRM over the 3SA-TRM when Ψ is close to 180 degrees. Thus, by using this method one always can get the best possible solution in estimating the targets positions. However another 3&4SA-TRM technique using a fully amplitude comparison procedure is discussed in section 4-2.4, where its block diagram can be easily obtained by replacing the doted box II in figure 4-2 by the one in figure 4-3. Simulation results for this technique are shown in figure 4-11 for Θ_B=0, S/N=30 dB, ρ_s=0.9, Θ_D=0.5,0.25,0.125 BW. For comparison the symmetric 3SA-TRM results are shown for Θ_D=0.25 BW only. In comparing each curve with its correspondent in figure 4-10 one can see identical performance for both techniques over all values of Ψ and Θ_D.

In conclusion, by using the 3&4SA-TRM technique an optimum use of the array's elements can be used by having the ability to choose between three or four subapertures performance according to the status of the phase difference between the two received signals. The same can be easily applied to the 3SA-MLE discussed in chap.3 and similar results are expected.

4-3.2 The nonsymmetric case solution

Figure 4-12 shows the simulation results of the 3SA-TRM for a target with Θ_B=0, ρ_s=0.9, S/N=30 dB, and Θ_D=0.5,0.25,0.125 BW, using SW.5 target type (for comparison the corresponding results is shown for the SW.2

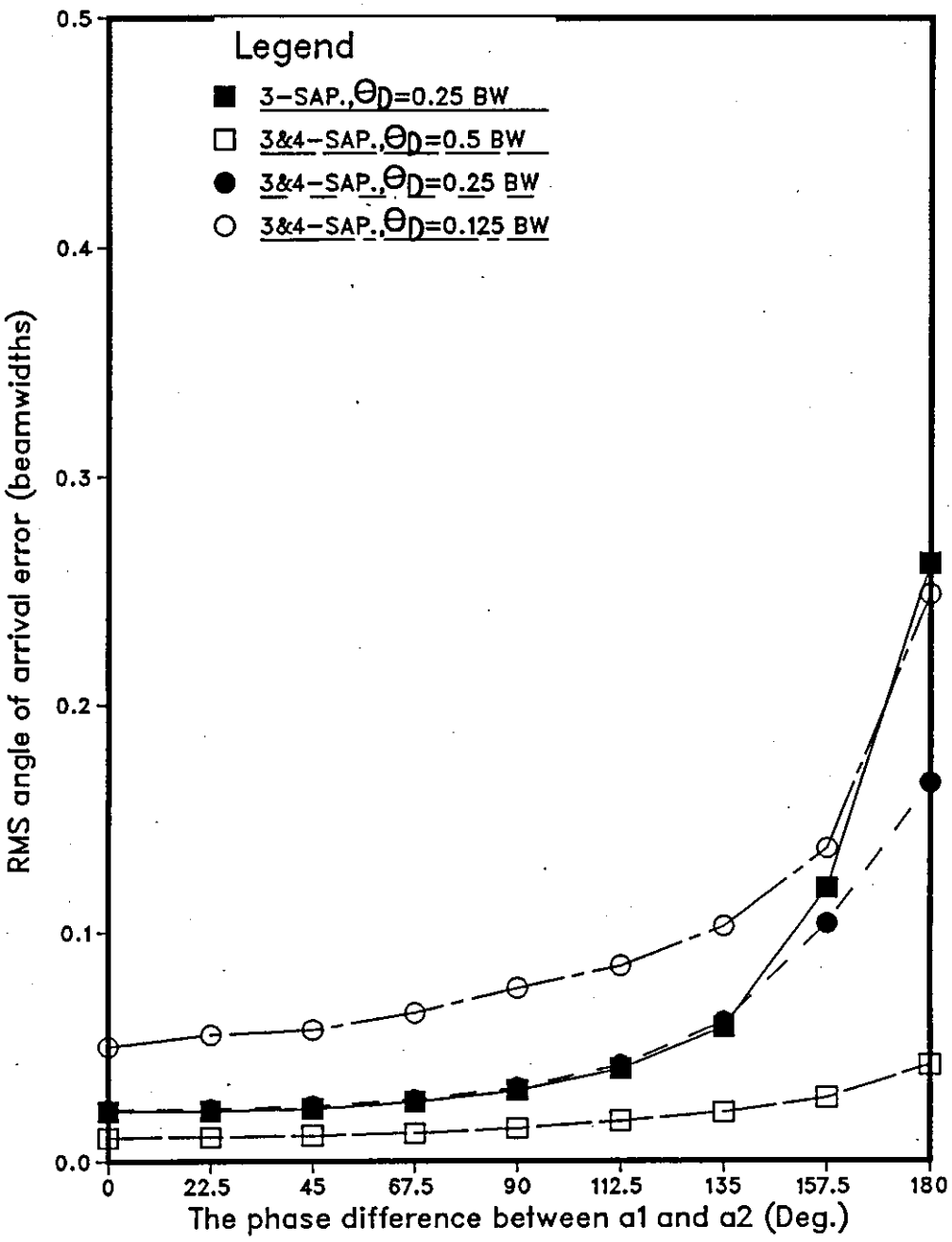

Figure 4-11 :RMS error of symmetric 3&4SA-TRM as a function of phase difference between the two signals for Θ_B=0.0, S/N=30 dB, ρ_s=0.9. For comparison, 3SA-TRM is shown for Θ_D=0.25 BW.

target's type only when θ_D=0.25 BW). In comparing the solutions, one finds that the rms error increases as θ_D decreases, and the worst estimation occurs when the two sources are in-phase or anti-phase (Ψ=0° or 180°) or close to any of them as can be seen from the curves. The best accuracy is obtained when the two sources are in phase quadrature for all values of θ_D, except when θ_D=0.125 BW where the optimum accuracy is obtained at Ψ=112°. The accuracy obtained when θ_D=0.25 BW for the SW.5 target type is much higher than that for the SW.2 target type, where the rms error increases by 0.07 for the second at Ψ=90. In comparing these curves with their correspondents in the nonsymmetric 3SA-MLE in figure 3-15 (chap.3) one can see that this method shows better performance when Ψ=180°, while the 3SA-MLE is better when Ψ=0°, and both methods shows the same accuracy when Ψ is close to quadrature. This method shows better accuracy with SW.2 target's type over all values of Ψ except at Ψ=0° or 180° where the 3SA-MLE is better. Figur 4-13 shows the S/N performance of the 3SA-TRM for θ_B=0, θ_D=0.5 BW, ρ_s=0.9, and S/N=30,20,10 dB, where the rms error is shown to increase as the S/N decreases over all values of Ψ. In comparing these curves with the correspondents of the nonsymmetric 3SA-MLE in figure 3-16 (chap.3) one concludes that this method works better with low S/N (but not when Ψ=0° or 180°), where the rms error reduction ranges to 0.055 at S/N=10 dB and Ψ=90° as can be seen from the curves. Figure 4-14 presents the performance of the 3SA-TRM for different values of the specular reflection coefficient for θ_B=0,

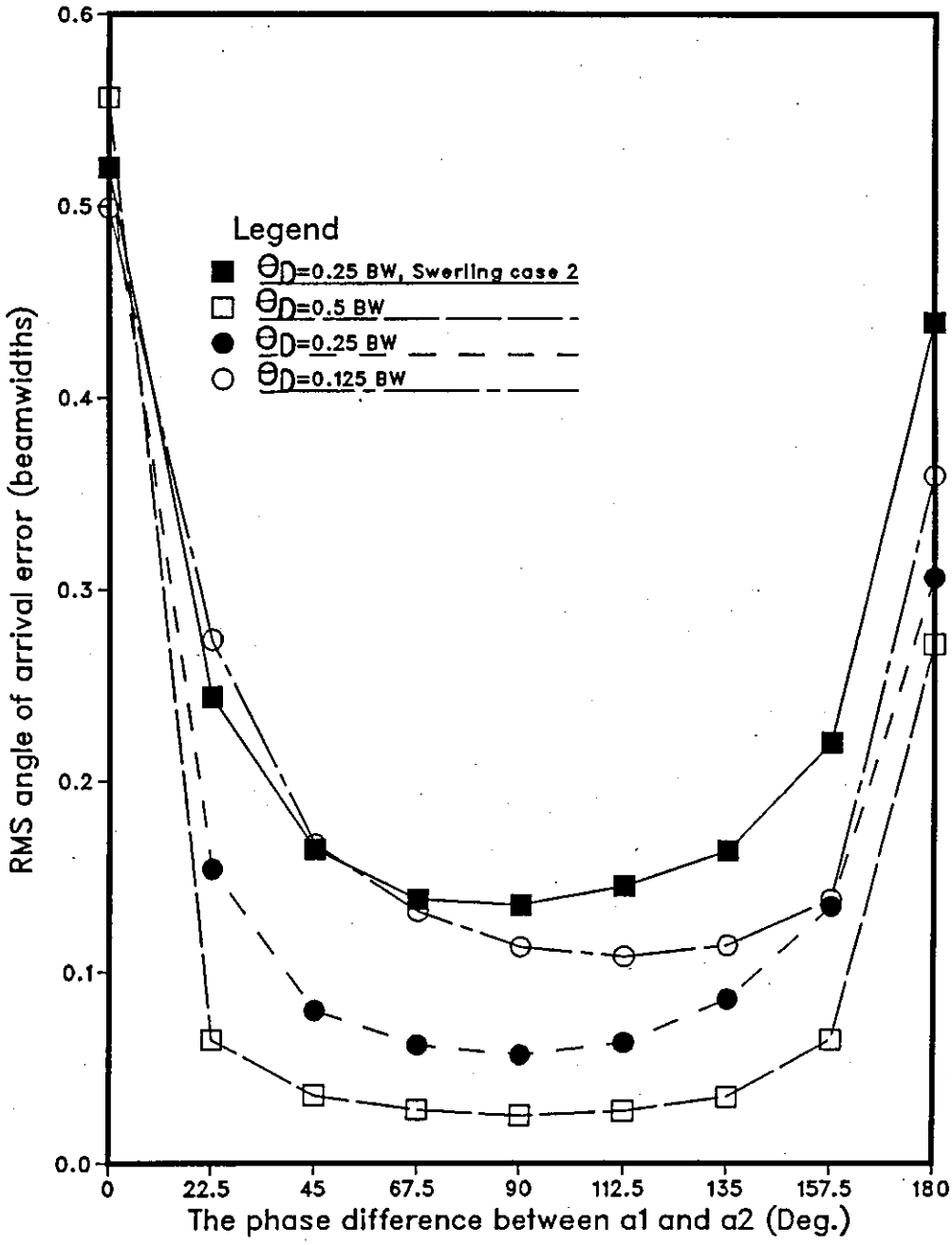

Figure 4–12 :RMS error of nonsymmetric 3SA–TRM as a function of phase difference between the two signals for Θ_B=0.0, S/N= 30 dB, ρ_s=0.9. For comparison, SW.2 target's type is shown

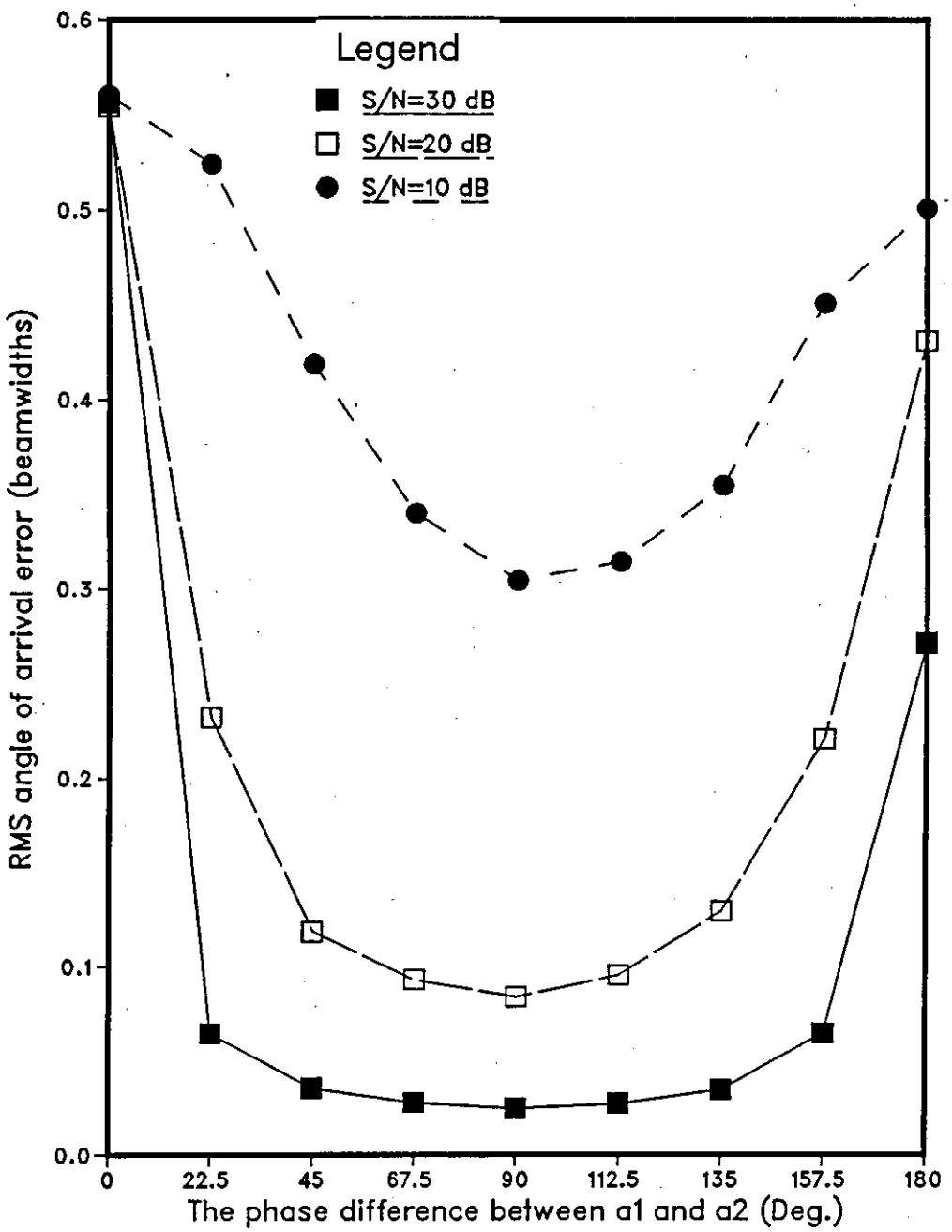

Figure 4–13:RMS error of nonsymmetric 3SA–TRM as a function of phase difference between the two signals for Θ_B=0.0, Θ_D=0.5 BW, ρ_s=0.9

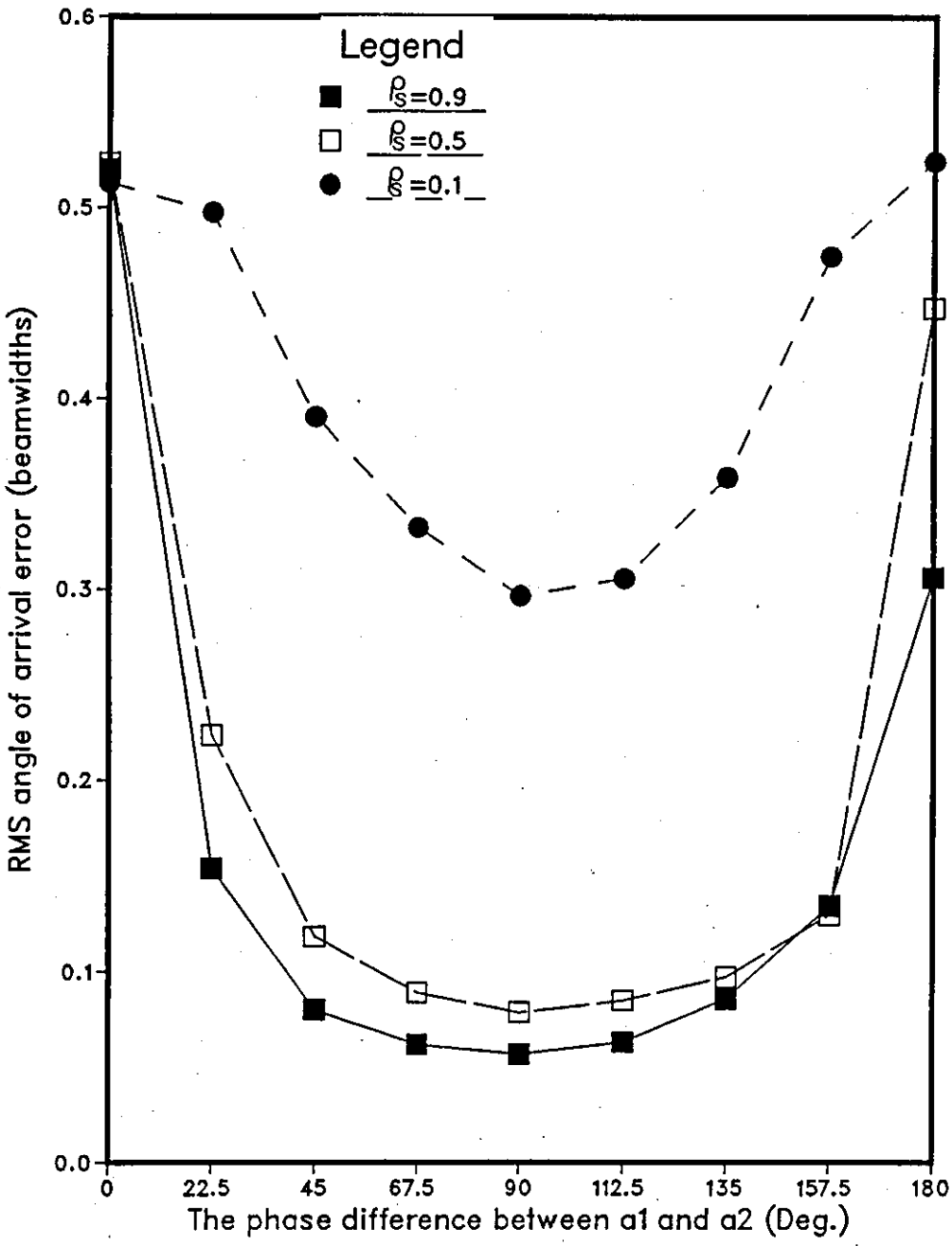

Figure 4–14 :RMS error of nonsymmetric 3SA–TRM as a function of phase difference between the two signals for Θ_B=0.0, Θ_D=0.25 BW, S/N=30 dB

θ_D=0.25 BW, S/N=30 dB, and ρ_s=0.9,0.5,0.1. In general, when ρ_s decreases the rms error increases especially when ρ_s is very small (0.1). In comparing these curves with the correspondents of the nonsymmetric 3SA-MLE in figure 3-17 (chap.3) one can see that both methods shows bad performance in general when ρ_s is small and this method is worse when $\Psi=0^{\circ}$. Further investigations show the method works slightly better than the 3SA-MLE method when θ_D=0.5 BW. Figure 4-15 shows the performance of the nonsymmetric 3SA-TRM with different values of the bisecting angle (the non symmetry performance), for θ_D=0.5 BW, S/N=30 dB, ρ_s=0.9, and θ_B=0.0,0.25,0.5 BW. In comparing with the 3SA-MLE (the solid line) we see that the 3SA-MLE method fails when θ_B=0.34 BW while this method still works with very good accuracy untill θ_B=0.5 BW. Further studies did show that this algorithm (3SA-TRM) will continue to work until one of the received signals reaches the subaperture beam pattern at point below the 3 dB point, while the 3SA-MLE method works with very good accuracy until θ_B=0.3 BW.

As we have seen from the results above, the performance of the nonsymmetric 3SA-TRM is very poor when the target and its coherent multipath are in-phase or anti-phase. In section 4-2.4 a new 4SA-TRM method is introduced to solve this problem and improve the performance in these two regions. Before showing the simulation results for this method we examine the case of the imaginary angle occurrence and the accuracy obtained in estimating the phase difference Ψ from the estimated angles of arrival of the two sources.

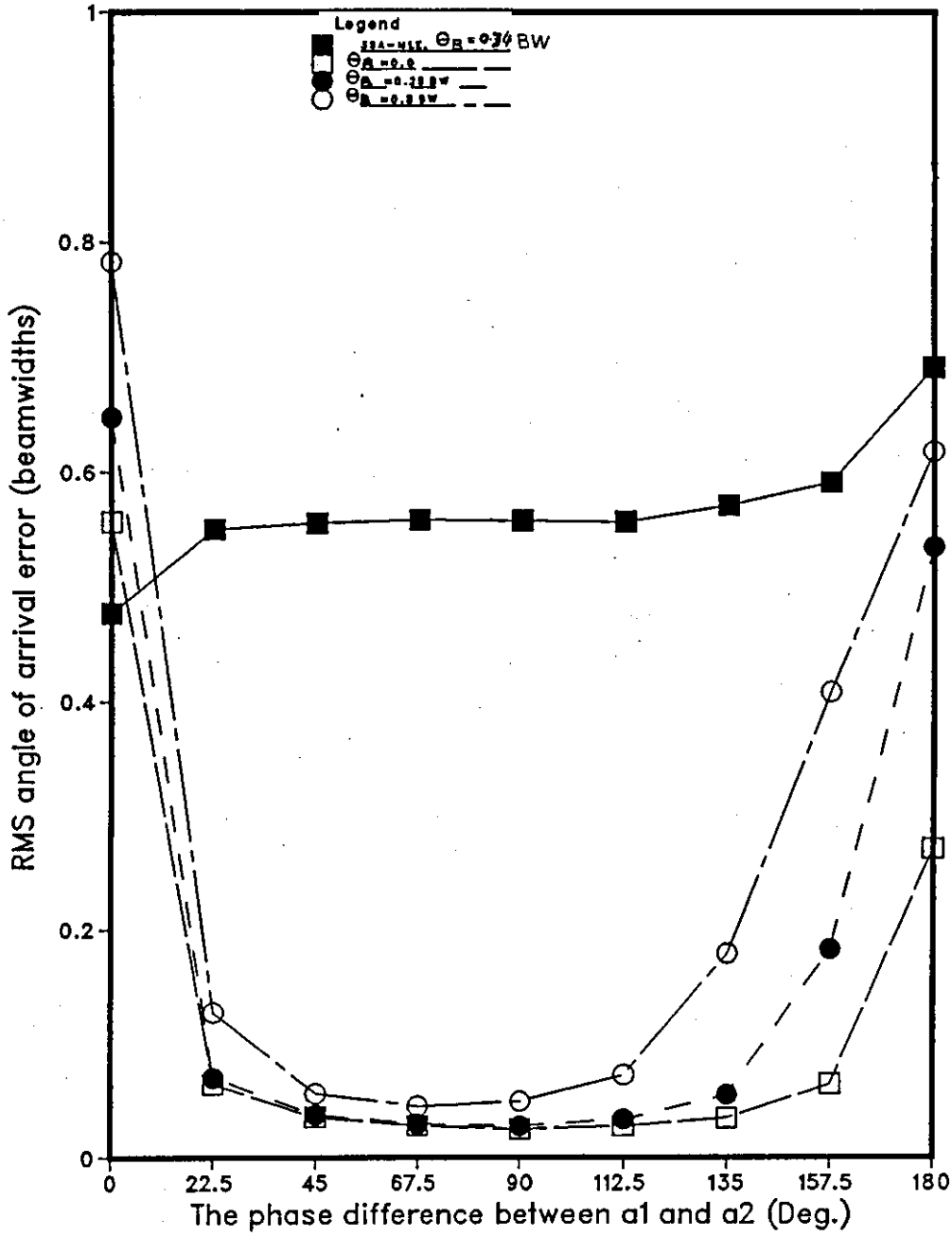

Figure 4–15 :RMS error of nonsymmetric 3SA–TRM as a function of phase difference between the two signals for Θ_D=0.5 BW, ρ_s=0.9, S/N=30 dB. For comparison the performance of the 3SA–MLE is shown

Table 4-2 shows computer simulation results for the frequency of occurrences of the imaginary angle (Im-ang) and when the absolute error of the estimated value of Ψ is greater than a given value (taken here to be 10°) from its true one (ph-div), for Θ_B=0, S/N=30 dB , ρ_s=0.9, and Θ_D=0.5,0.25,0.125 BW for SW.5 target's type (and SW.2 target's type just when Θ_D=0.25 BW for comparison). The imaginary angle occurrence is zero over all values of Ψ when Θ_D=0.5 BW, except at $\Psi=180^{\circ}$ and 0° where it occurs 128 and 378 times out of 1000 respectively, which might explain the bad performance at these two points. When Θ_D decreases the imaginary angle occurrence increases over all values of Ψ as can be seen from the table. The estimated value of Ψ is the worst when the two sources are in phase agreament, while it is very accurate when they are in phase opposition for Θ_D=0.5 BW as can be seen from table 4-2. The reason behind this high accuracy (when $\Psi=180^{\circ}$) is that when an imaginary angle occurs a test is carried out to find whether the two signals are close to in-phase or anti-phase conditions depending on the same facts explained in chapter 3 (section 3-4.1). The frequency of occurrence of the imaginary angle and the erroneous values of the estimated Ψ for the SW.2 target type is higher than that for SW.5 type in general as can be seen from the table for Θ_D=0.25 BW. In comparing these results with those of the nonsymmetric 3SA-MLE in table 3-3 (chap.3) one can see similar results with some exception at $\Psi=0^{\circ}$ and 180° which can be read on the tables. Thus, from the above discussion one concludes that the phase comparison

Table 4-2 The imaginary angle and erroneous estimated phase difference (>10° deviation from the true value) occurrences in the nonsymmetric 3SA-TRM for θ_B=0, S/N=30 dB, ρ_s=0.9, θ_D=0.5,0.25,0.125 BW, for 1000 trials at each phase shown. For comparison the results for SW.2 target's type is shown when θ_D=0.25 BW.

Phase	0.5 BW		0.25 BW				0.125 BW	
	Im-ang.	Ph-div.	IM-ang		Ph-div.		IM-ang.	Ph-div.
	SW.5	SW.5	SW.5	SW.2	SW.5	SW.2	SW.5	SW.5
0.0	378	258	613	623	83	164	713	147
22.5	0	3	55	208	326	537	676	873
45.0	0	0	2	102	200	508	479	835
67.5	0	1	1	94	263	493	371	809
90.0	0	1	1	87	326	533	335	816
112.5	0	3	5	99	367	605	313	842
135.0	0	6	39	158	392	615	323	827
157.5	0	6	162	228	405	641	391	833
180.0	128	0	324	286	28	263	425	191

four-subapertures technique discuused in chapter 3 can be equally applied here by following the steps shown in figure 3-6 and replacing the 3SA-MLE by 3SA-TRM. Similar results are expected as long as the three-subapertures performance of both methods is very much the same as we have already seen from comparing so far.

According to the block diagram in figure 4-1 a computer simulation is carried out to express the effectiveness of the new 4SA-TRM method (by comparing sys1 with sys2) to improve the nonsymmetric case of the 3SA-TRM performance when $\Psi=0^{\circ}$ or 180°. Figure 4-16 shows these results for $\Theta_B=0$, S/N=30 dB, $\rho_s=0.9$, $\Theta_D=0.5, 0.25, 0.125$ BW, using SW.5 target type. For comparison 3SA-TRM is shown only for $\Theta_D=0.25$ BW (27 elements are used insted of 28). By comparing each curve with its correspondent in figure 4-12 (keeping in mind that we use just 3/4 of the total elements of the array for the 4SA-MLE method, while the rms error is normalized to the 3dB beamwidth of the whole array) one can see a large reduction in the rms error for $\Theta_D=0.5, 0.25$ BW when $\Psi=0^{\circ}$ or 180° (or close) and only a very small increase when Ψ is close to quadrature. This is mainly related to smaller S/N per subaperture, the 3dB beamwidth normalization, and the deviation of the new chosen value of Ψ from the quadrature in terms of the new comparing method between sys1 and sys2 and its accuracy. In comparing the 4SA-TRM with the 3SA-TRM (27 elements) for $\Theta_D=0.25$ BW a big improvement can be seen when the phase difference between the two sources is close to 0° or 180° and a little degredation when it is close to quadrature

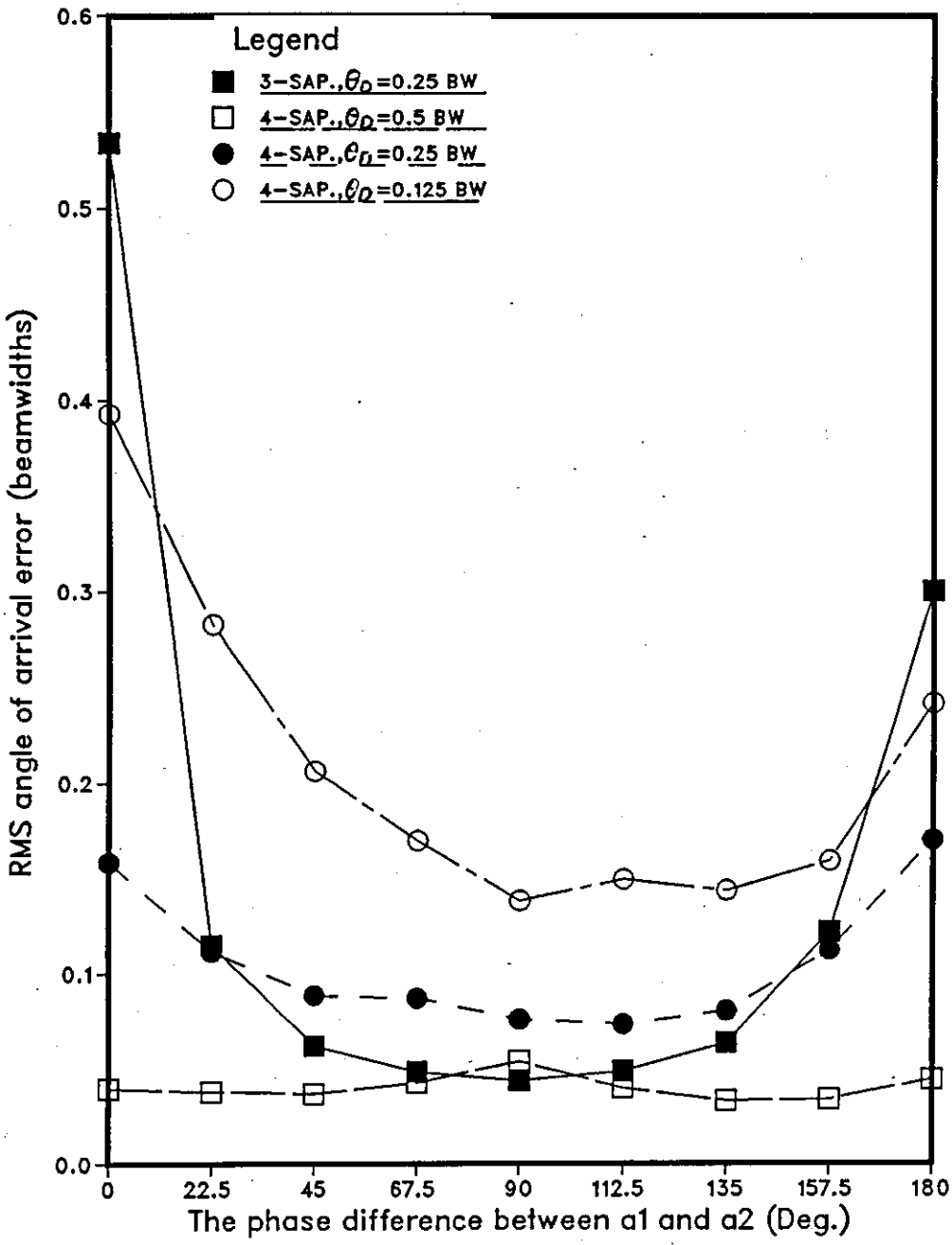

Figure 4–16 :RMS error of nonsymmetric 4SA–TRM as a function of phase difference between the two signals for Θ_B=0.0, S/N=30 dB, ρ_s=0.9. For comparison, 3SA–TRM is shown for Θ_D =0.25 BW

for the same reason explained above. Figure 4-17 shows a histogram of results for Θ_D=0.25 BW, Θ_B=0, ρ_s=0.9, S/N=30 dB, and Ψ=0°,180° for the 3SA-TRM and 4SA-TRM methods, where the rms error (+beamwidth) for the first is within the range 0-0.1 for 38 % of the time when Ψ=0° and 20 % when Ψ=180°, while it rises to 66 % and 48 % for the second respectively. Thus one can conclude that the new four-subapertures method for solving the in-phase and anti-phase problem by comparing between sys1 and sys2 (just the anti-phase for the symmetric case) is very effective, and it reduces the needed work load and hardware in comparison with the phase comparison four-subapertures technique discussed in chapter 3 (the 4SA-MLE) but it is slightly worse for the symmetric case and better for the nonsymmetric one.

Whatever improvement obtained by using the four-subapertures techniques (4SA-TRM) for the in-phase and anti-phase signal conditions, further improvement is obtainable by using the nonsymmetric 3&4SA-TRM method. Figure 4-2 shows the block diagram of this method and figure 4-18 shows the simulation results accordingly for Θ_B=0, S/N=30 dB, ρ_s=0.9, Θ_D=0.5, 0.25, 0.125 BW (the 3SA-TRM method is shown using 27 elements on the same figure for Θ_D=0.25 BW only for comparison purposes). In comparing these curves with those of the 4SA-TRM in figure 4-16 one can see a great improvement in performance when Ψ is close to the quadrature condition (30°<Ψ<140°) and also for Θ_D=0.125 BW in particular over all values of Ψ except at Ψ=0° and 180°. Also, by comparing the 3SA-TRM and 3&4SA-TRM for Θ_D=0.25 BW on figure 4-18 one can see that the two curves are very similar with

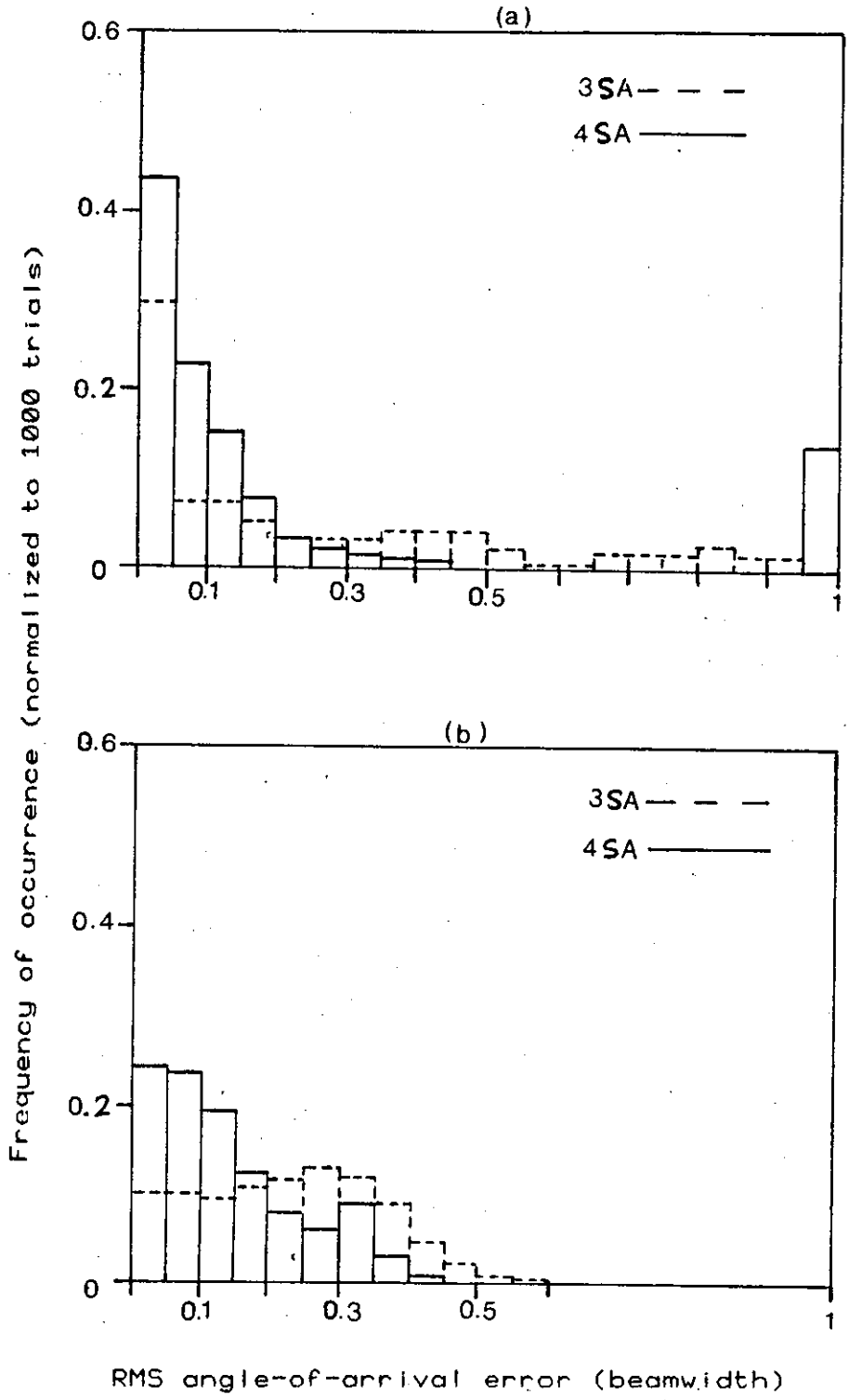

Figur 4-17 :Histogram shows the performance of the nonsymmetric 3SA-TRM and 4SA-TRM for Swerling case 5 target type $\theta_B=0$, $\theta_D=0.25$ BW, S/N=30 dB, $\rho_s=0.9$.
(a)- for $\Psi=0.0^\circ$, (b)- for $\Psi=180^\circ$.

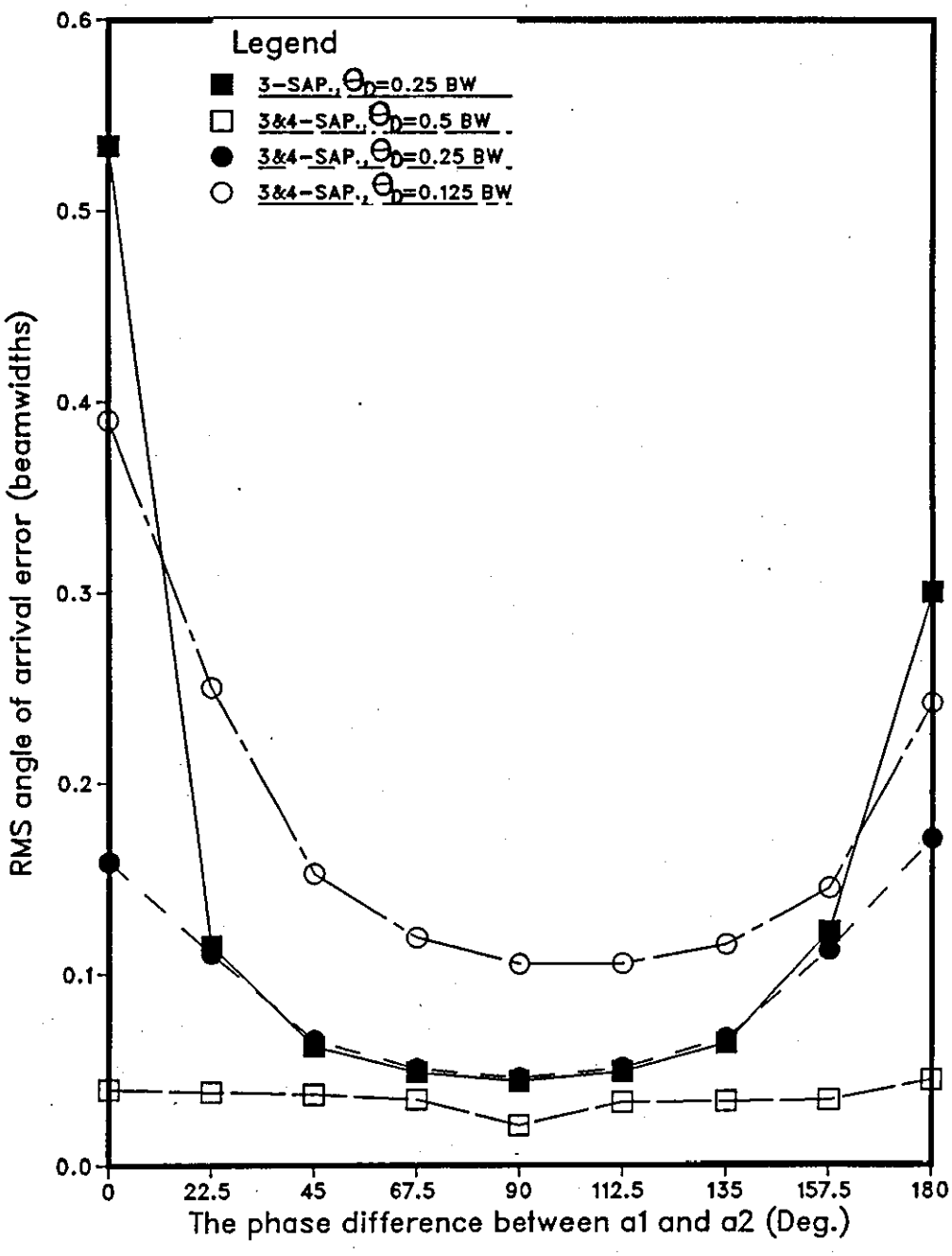

Figure 4–18:RMS error of nonsymmetric 3&4SA–TRM as a function of phase difference between the two signals for θ_B=0.0, S/N=30 dB, ρ_s=0.9. For comparison, 3SA–TRM is shown for θ_D =0.25 BW

negligible differences (mainly related to the missing element, 27 instead of 28) over all values of Ψ except when $30^{\circ}>\Psi>140^{\circ}$, and a big improvement occurs when $30^{\circ}>\Psi>140^{\circ}$. The main reason beyond this improvement is as explained for the symmetric case of the 3&4SA-TRM above.

The lessons learned from this chapter can be summarised by the following points:

a- this trigonometric solution (3SA-TRM) gives very much the same results obtained by the 3SA-MLE for both symmetric and nonsymmetric cases.

b- The 3SA-TRM is faster in processing and simpler to implement in a practical system.

c- The new four-subapertures technique is simpler than the one presented in chapter 3 and saves much time in processing while it gives similar results with few exceptions.

d- The new 3&4SA-TRM technique for the symmetric and nonsymmetric cases is the most promising technique for reducing the rms error in estimating the angles very significantly at $\Psi=0^{\circ}$ or 180° and preserving the accuracy obtainable by using 3SA-TRM elsewhere.

e- The 3&4SA-TRM amplitude comparison technique for the symmetric case is the most efficient one of all presented techniques and very viable for practical implementation.

f- All the techniques used with the new method to solve the in-phase and anti-phase problems are applicable to the method mentioned in chapter 3 and vise-versa.

Chapter 5

The Maximum Entropy Method And Monopulse Radar

5-1 Introduction

Modern spectral estimation techniques for time-series as documented by Childers [5-1], and the maximum entropy method (MEM) in particular, have recently received much attention in the literature because of their ability to resolve closely-spaced spectral elements. The MEM was first suggested by Burg [5-2] and later extensively investigated and discussed in many papers and text books [5-3,5-4,5-5]. Van de Bos [5-6] shows that the MEM is equivalent to least-squares fitting of an all-pole (autoregressive) model to the available data. Haykin and Kesler [5-7] show the complex form of the MEM and Andersen [5-8] gives a fast and simple procedure to calculate the filter coefficients of equal spaced data according to the Burg method in [5-1]. A discussion about how to choose the order of the filter and its effect on the resulting performance is shown in Kay et al. [5-9] and Childers [5-1]. McDonough [5-10] shows that the MEM spectral analysis used in the processing of time-series data is equally applicable to the wavenumber

analysis of signals received by a spatially distributed linear array of sensors. Kesler and Haykin [5-11] show that the MEM provides a rather useful method for obtaining a short-term estimate of the spectral density of radar clutter. The advantages and disadvantages of this method are investigated in the above references and many others and will not be discussed here again.

In general, time-series estimation techniques are only applicable when the underlying proces is stationary. If it is not, such as in the case of a low-flying target over a smooth surface where the direct and reflected signals are coherent, then the resulting wavenumber spectral estimate will not be meaningful unless the two signals are in phase quadrature [5-12]. Because this is not the case one can conclude that these sorts of algorithms are inappropriate for solving such problems. However Evans [5-13, 5-14] shows results from a field test on the performance of the MEM, where it worked very well over an irregular surface, but he did not discuss the scale of irregularities.

The purpose of this chapter is to introduce the MEM in general and to show its performance in solving the specular multipath problem by using the same three-subapertures linear array presented in the previous two chapters. Also, a brief look at the principles and performance of the phase-comparison monopulse radar will be given. The effect of the surface roughness on the performances of the three-subapertures MLE, TRM, MEM, and the phase-comparison monopulse radar will be discussed and compared in chapter 6.

5-2 The maximum entropy formulation

The MEM spectrum estimate for wavenumber spectral estimation can be given by the following equation [5-4].

$$P(\Theta)=\sigma_w^2 \Big/ \Big| 1+\sum_{m=1}^{M} C_{M,m}\, Z^{-m} \Big|^2 \qquad (5\text{-}1)$$

where, $Z=\exp\{j2\pi d \sin(\Theta)/\lambda$, $C_{M,m}$ is the m-th parameter of the all-pole filter, M is the numbers of poles, σ_w^2 is the variance of the white noise input, $p(\Theta)$ is the power density in the angular direction Θ, and d is the subaperture spacing as shown in figure 3-1 (in chap.3), or the interelement spacing in case that individual elements are considered. Using the three subapertures technique mentioned in the previous two chapters, the above equation can be rewritten as follows for the two pole-filter case.

$$P(\Theta)=\sigma_w^2 \Big/ \Big| 1+C_{2,1}\, Z^{-1} + C_{2,2}\, Z^{-2} \Big|^2 \qquad (5\text{-}2)$$

There are two practical methods for locating the peak position in the spectrum. The first is by calculating the roots of the characteristic equation of the prediction error filter (the quadrature equation in the denominator of the equation above for the three subaperture case), then finding the angles of the roots which correspond to each incident plane waves. This method becomes very lengthy and difficult to solve when the number of poles is high. The other method is to find the wavenumber spectrum and search for its peaks.

In the simulation performed for this study of a low-flying target over asmooth surface (rough surface in the next chapter), the second method was chosen, since it is more likely to be used in practical system.

5-2.1 Burg method [5-7]

To use the MEM spectral estimate above we need a procedure to estimate its parameters ($C_{M,1}$, $C_{M,2}$, ..., $C_{M,M}$) and there are several procedures to estimate these from N data samples [5-5,5-9]. The most popular procedure is known as the Burg method. This method depends on minimizing the sum of the forward and backward prediction error power of an all-pole filter (see figure 5-1), subject to the constraint that all the parameters (from 1 to M) satisfy the Levinson recursion (5-10) to ensure the stability of the filter (the poles inside the unit circle) [5-9].

Assuming a wide sense stationary process and starting with M=0, then the power P_1 is the autocorrelation for zero lag, and given by,

$$P_1 = (1/N)\sum_{i=1}^{N} |S_1|^2 \qquad (5\text{-}3)$$

where S_i is the i-th sample from the i-th element (or subaperture) and N is the total number of elements or subapertures. For M=1, then the length of the prediction error filter is two and the error power P_2 defined by the average sum of the resulting powers of the forward and

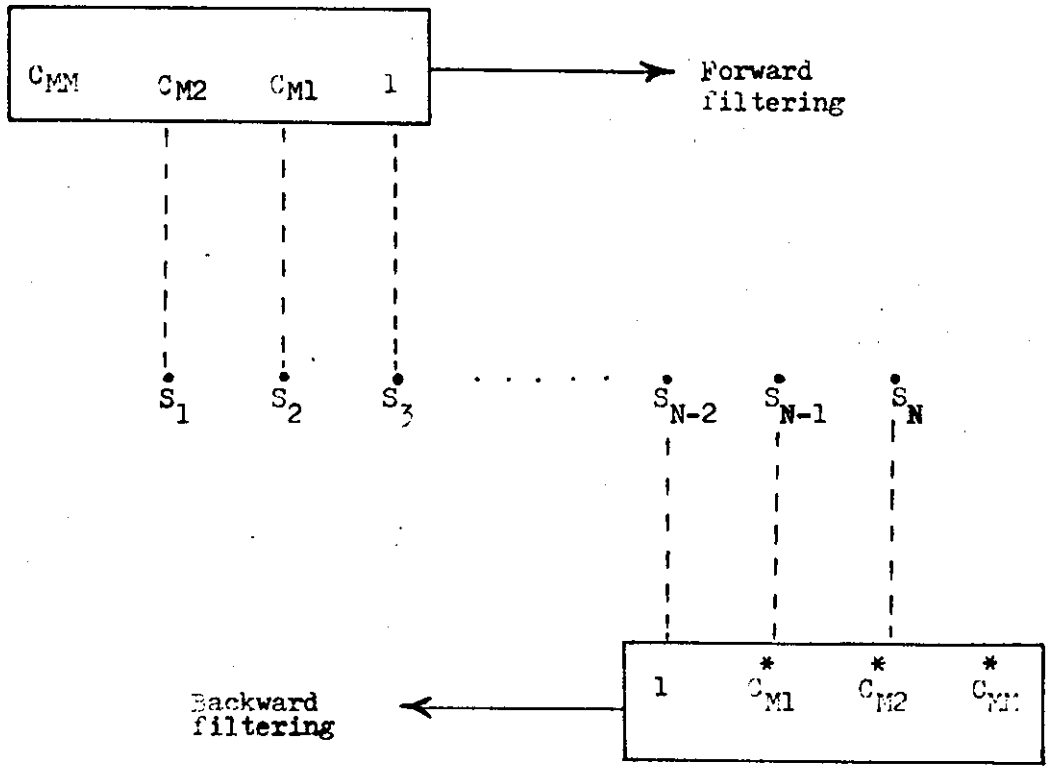

Figure 5-1: The forward and backward filtering of N samples from N subarray or N elements array.

backward filtering (P_2', and P_2'') respectively.

$$P_2 = (1/2)(P_2' + P_2'') \tag{5-4}$$

$$P_2' = [1/(N-1)] \sum_{i=1}^{N-1} \left| S_{i+1} + C_{11}^{*} S_i \right|^2 \tag{5-6}$$

$$P_2'' = [1/(N-1)] \sum_{i=1}^{N-1} \left| S_i + C_{11}^{*} S_{i+1} \right|^2 \tag{5-7}$$

If the mean power P_2 is minimised by taking its partial derivative with respect to C_{11} and setting it to zero, $(\partial P_2/\partial C_{11})=0$, then the power at the output is minimized whenever C_{11} takes the following value.

$$C_{11} = \frac{-2 \sum_{i=1}^{N-1} S_i^{*} S_{i+1}}{\sum_{i=1}^{N-1} \left(|S_i|^2 + |S_{i+1}|^2 \right)} \tag{5-8}$$

and the real value of P_2 is given by the following, from its equivalent correlation matrix.

$$P_2 = (1 - |C_{11}|^2) P_1 \tag{5-9}$$

The above procedure can be extended to higher order filters, where the parameter C_{Mm} for a filter of order M+1 can be defined by the following general equation:

$$C_{Mm} = C_{M-1,m} + C_{MM} C^{*}_{M-1,M-m} \qquad (5\text{-}10)$$

where, m=1,2,.....,M.

and the corresponding output power is given by:

$$P_{M+1} = P_M (1 - |C_{MM}|^2) \qquad (5\text{-}11)$$

From the above equation and since $C_{MM} < 1$, one can conclude that $0.0 \leqslant P_{M+1} \leqslant P_M$, which means that the error decreases by increasing the order of the filter. This is controlled by many factors which compromise between high resolution and fewer spurious peaks and there are many approaches and suggestions in the literature for estimating the filter order. One intuitive approach is to increase the order until the calculated power of the prediction error reaches a minimum. Ulrych et. al. in [5-9] suggested an order choice within the range N/3 to N/2 for the case of a short data sequence. For the three-subapertures arrangement of a linear array with two incident plane waves (direct and reflected signals) the minimum numbers of poles must be two which represent the maximum order of the filter.

5-3 The phase-comparison monopulse

Various methods of precision single target tracking have been developed and used in the past. These methods are mainly based on either simultaneous or sequential lobing

techniques which require a minimum number of echo pulses (at least three pulses) to extract the error signals which are normally used to actuate a servo-control system to position the antenna. During the measurement time, the amplitudes of the received echos must stay constant (non-fluctuating amplitude) otherwise a severe degredation in the tracking accuracy might occur [5-15, 5-16].

The amplitude fluctuations of the received echo pulses will have no effect on the accuracy of the tracking system if the angular measurement procedure depends on the basis of extracting the error signals from one pulse rather than many. One of the most popular method is monopulse tracking which is mainly divided into the following two types: first, the amplitude-comparison monopulse which employs two overlapping antenna beams to obtain the angular error signal in one plane, and the second is the phase-comparison monopulse (or interferometer radar) which employs two parallel antenna beams to obtain the signal error in one plane (in both cases the minimum number of beams required for elevation and azimuth angle tracking are three, but normally four beams are used). Also, the phase and amplitude comparison monopulse features can be used jointly in one system to provide angular tracking in azimuth and elevation by using only two beams rather than minimum of three required for each type individualy [5-15].

The failure of the monopulse radar in tracking a low-flying target over a smooth surface is very widely studied in the literature (see chapter 1). In a comparison

study between phase and amplitude processors for amplitude monopulse systems. Sinsky and Lew [5-17] have shown that when the S/N is high the obtainable performance accuracies are comparable for both processors except for target angles very close to boresight where the second outperforms the first by 3dB signal to noise ratio equivalent. Also they expect the phase processor monopulse to operate with higher accuracy than the amplitude processor one in a noncoherent multipath environment.

In figure 5-2 the geometry of two plane waves (i.e direct signal and its coherent multipath) and two subapertures of a linear array are shown, where the separation between the centres of the two subapertures and the distance from the array centre to the target are given by d and R respectively (R>>d). The complex signal outputs of the two subapertures can be given by:

$$S_1 = a_1 G_1 \exp(jZ_1/2) + a_2 G_2 \exp(jZ_2/2) + n_1 \qquad (5\text{-}12)$$

$$S_2 = a_1 G_1 \exp(-jZ_1/2) + a_2 G_2 \exp(-jZ_2/2) + n_2 \qquad (5\text{-}13)$$

where the description of each term in the above two equations is given in chapter 3. The phase reference is taken at the middle of the array. However, when the target is high over the surface i.e the multipath components are zero in the above two equations, then the change in the phase of the signal (the phase lag) is given by $\Delta PL = Z_1$ or by its equivalent from [5-15]:

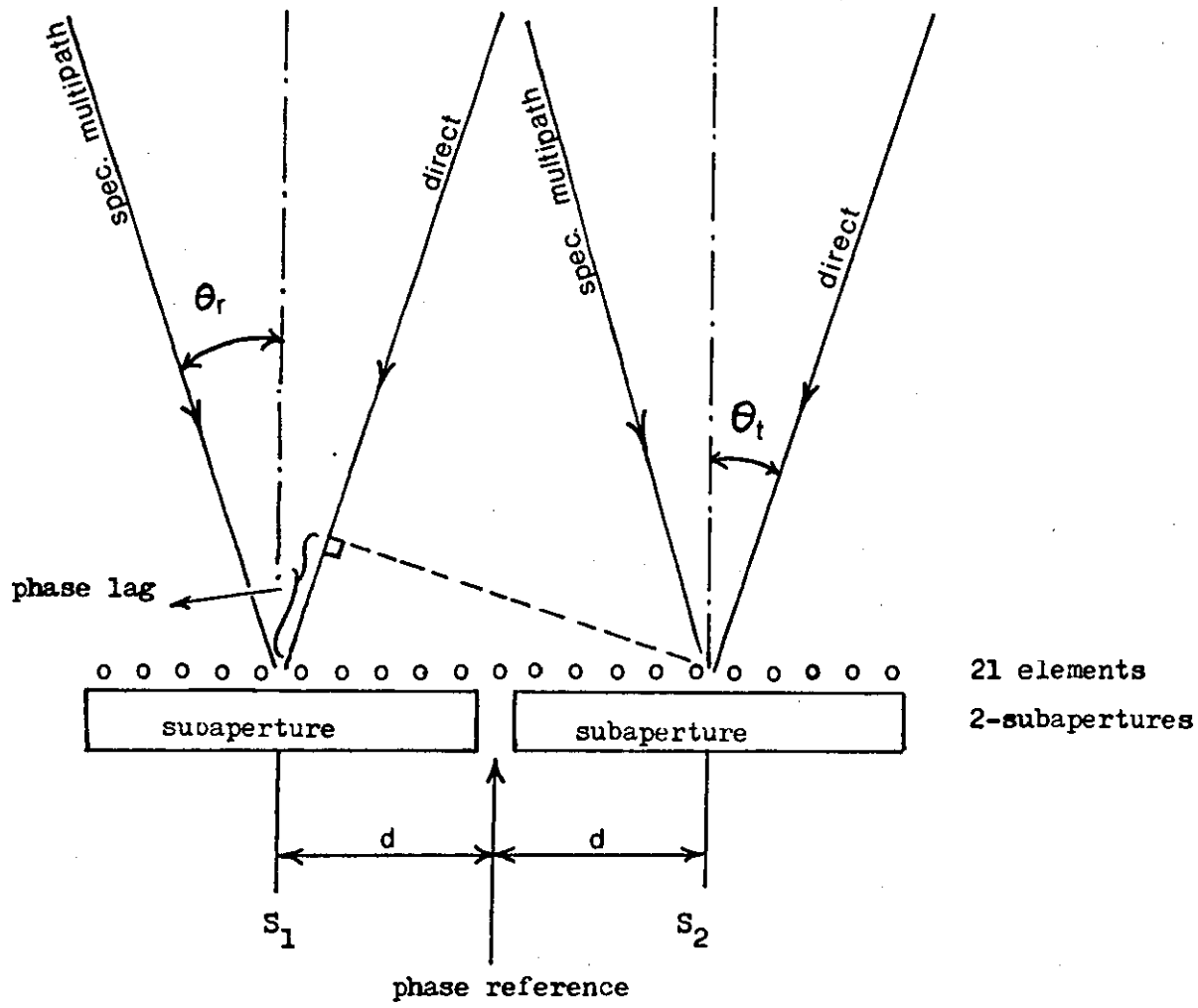

Figure 5-2 :The geometery of two plane waves and two-subapertures of a linear array.

$$\Delta PL = 2\pi d \sin(\theta_t)/\lambda \qquad (5\text{-}14)$$

and the elevation angle is given by:

$$\theta_t = \sin^{-1}[\Delta PL\ \lambda/(2\pi d)] \qquad (5\text{-}15)$$

where the Gaussian noise components are excluded from the calculations above. For small values of the elevation angle $\sin(\theta_t) \approx \theta_t$.

When specular multipath exists the above calculation of the elevation angle will be disturbed . The extent of the disturbance depends on Ψ and the specular reflection coefficient (ρ_s). where high values of ρ_s lead to a complete failure in estimating θ_t. This problem can be better understood by finding the general equation of the phase lag as a function of Ψ and a_s, where a_s as a function of ρ_s and the angular positions (through G_1 and G_2) is given by:

$$a_s = [\ |(a_2G_2)/(a_1G_1)|\ ,\ \angle\Psi\ ] \qquad (5\text{-}16)$$

The associated phases with S_1 and S_2 above can be given by PL1 and PL2 respectively.

$$PL1 = \tan^{-1}\{[\sin(Z_1/2)+a_s\sin(\Psi+ Z_2/2]/ [\cos(Z_1/2)+a_s\cos(\Psi+ Z_2/2]\} \qquad (5\text{-}17)$$

$$PL2 = \tan^{-1}\{[-\sin(Z_1/2)+a_s\sin(\Psi- Z_2/2)]/ [\cos(Z_1/2)+a_s\cos(\Psi- Z_2/2)]\} \qquad (5\text{-}18)$$

where the total phase lag is given by $\Delta PL=PL1-PL2$. One concludes that when $\Psi=0^{\circ}$ the values of PL1 and PL2 are equal with opposite sign. For a symmetric target-image case and $a_s=1$ the values of PL1 and PL2 are zero when $\Psi=0^{\circ}$ and infinity when $\Psi=180^{\circ}$ (PL1 and PL2 are very much noise dependent in these cases). The value of Ψ where the best angle estimation occurs is a function of the angular spacing between the two sources and a_s (for further detail, see [5-20]). A small value of ρ_s leads to an improvement in accuracy over all values of Ψ in general and the nonsymmetric targe-image case would effect the target tracking accuracy in positive or negative sense by decreasing or increasing the value of a_s respectively. An approximate general equation of the angular error ($\Delta\theta_t$) normalized to the angular spacing between the target and its image as a function of Ψ and a_s for a tracking radar is given in Skolnik [5-15] as follows:

$$\Delta\theta_t(\div\text{angular spacing})=[a_s^2+a_s\cos(\Psi)]/[1+a_s^2+2\,a_s\cos(\Psi)]$$

However one method to improve the performance is to tilt the beam up (the off-axis monopulse) in order to reduce the reflected signal strength which in turn reduces its damaging effect [5-19]. The best beam tilt value is the one which directs the first null of the subaperture toward the incoming specular multipath signal reducing its value to zero. But, because we do not know the multipath direction, this method is approximate and it does not always lead to satisfactory results.

Simulation results for a low-flying target over a smooth surface are shown in the next section and its performances over different types of rough surfaces are shown and compared with other methods in chap.6.

5-4 Simulation results and discussion

Simulations for the MEM method and the phase-comparison monopulse (in breif, phase monopulse) have been made using the same 21 element linear array described in chapter 3. This linear array is divided into three equal subapertures for the MEM and two equal subapertures of ten elements each (the element at the middle of the array is neglected) for the phase monopulse. The S/N is always taken to be 30 dB calculated for the direct signal only, as received by the main beam of the whole array. The noisy signal for the phase monopulse is generated according to equations (5-12) and (5-13) above, and for the MEM according to equations (4-1), (4-2), and (4,3) in chapter 4.

5-4.1 The MEM results

These results are calculated for direct and specular multipath signals at elevation angles of 0.25 BW and -0.25 BW respectively. A three-point filter (two poles) is always used and the parameters are calculated according to the Burg method above. Figure 5-3 shows the power spectrum for ρ_s=0.9 and different values of Ψ. When Ψ=0° the two signal components coalesce into one peak (when ρ_s=1, then

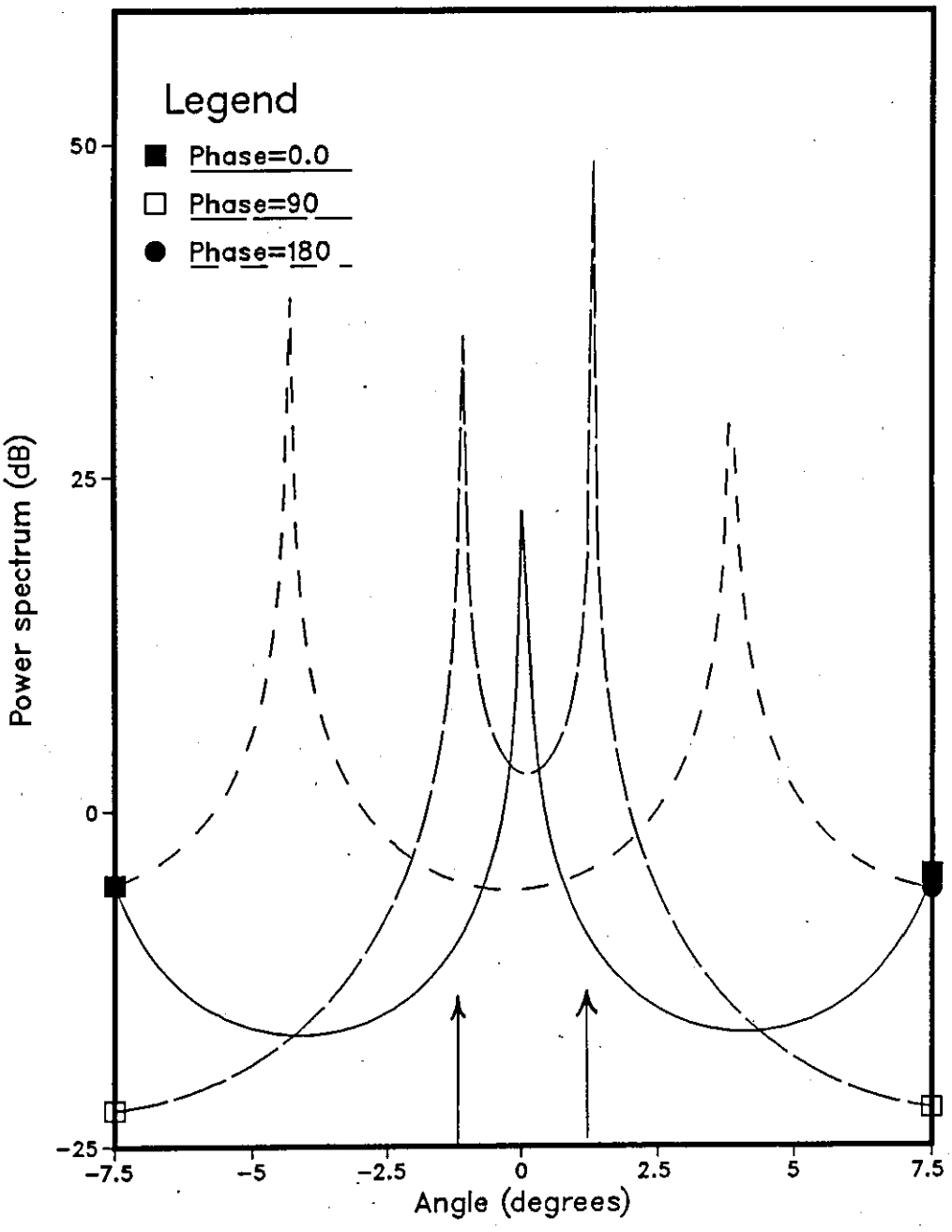

Figure 5–3 :The MEM power spectrum for specular multipath for angle separation of 0.5 BW, S/N=30 dB, ρ_s =0.9 and varying phase difference.

theoretically the peak will be shown half-way between the two signals). When $\Psi=180^{\circ}$, two peaks are shown but their positions are highly biased from the real ones. The best solution is when $\Psi=90^{\circ}$ where the nonstationary process becomes stationary [5-5], and two sharp peaks are shown which locate the angular positions of the two signals with high accuracy. Figure 5-4 shows the power spectrum for $\rho_s=0.42$. The only peak when $\Psi=0^{\circ}$ is biased toward the real position of the direct angle of arrival, also a bias toward the real position of the direct angle is shown when $\Psi=180^{\circ}$. Figure 5-6 shows the power spectrum for $\rho_s=0.1$, where the angular position of the direct signal is located more accurately than for $\rho_s=0.45$ (see fig. 5-4) when $\Psi=0^{\circ}$ or 180°. The specular multipath direction is biased, with wide peaks, as a direct result of its low signal power. Thus, smaller values of ρ_s give better accuracy in locating the direct angle of arrival. Further studies show that these results are very similar to those for sampling the 21 elements individually retaining the the second order filter, despite the large reduction in processing time. The only disadvantage here is the grating lobes which can be avoided in practice. The problems concerning the line splitting, due to phase and noise sensitivity, and the inaccurate indication of the source powers still exist here. Figures 5-7 and 5-8 show the power spectrum for $\rho_s=0.9$ and five different snapshots to find the effect of the Gaussian noise on the peak positions at $\Psi=90^{\circ}$ for SW.5 and SW.2 target types respectively. It can be seen that the peaks are sharper and more accurate for the first than the second.

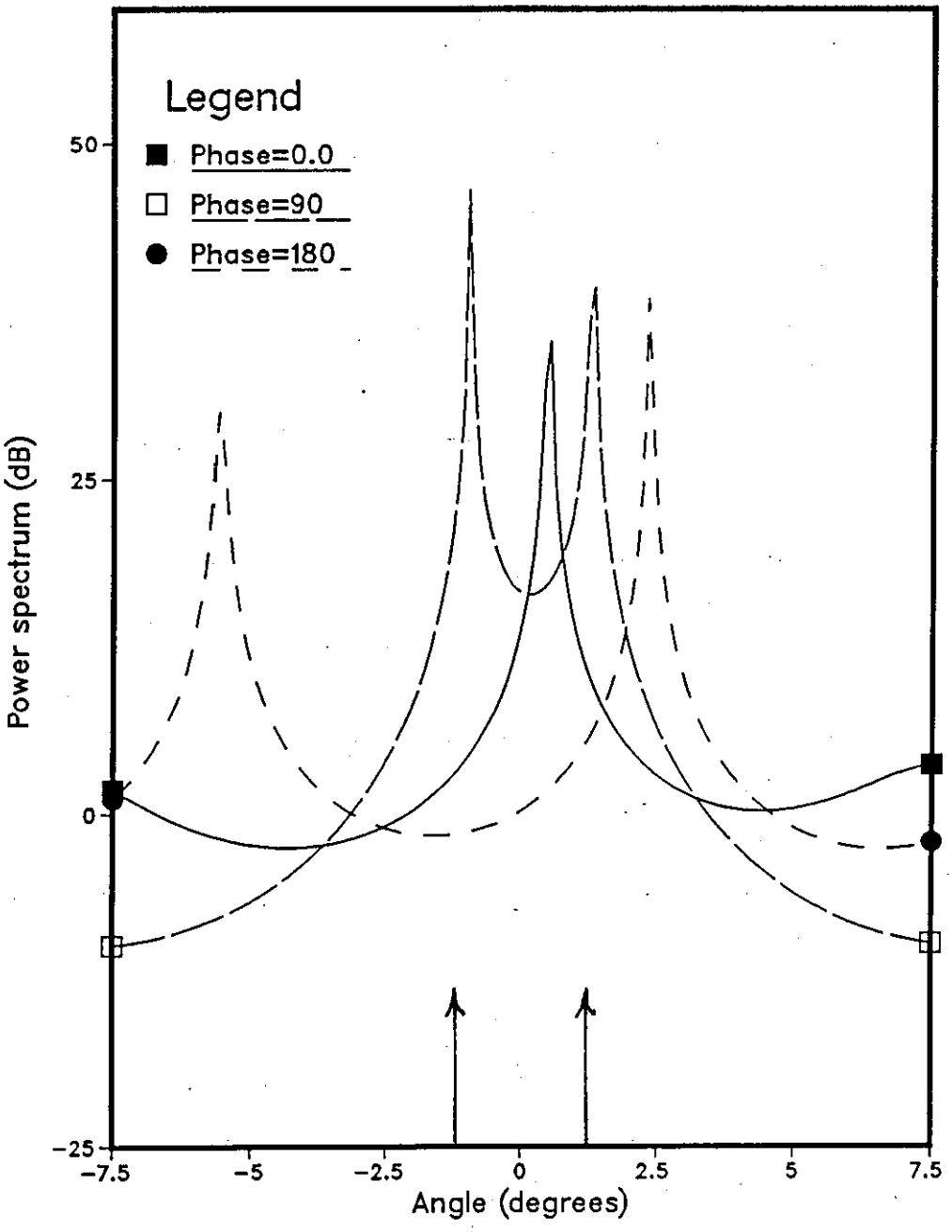

Figure 5–4 :The MEM power spectrum for specular multipath for angle separation of 0.5 BW, S/N=30 dB, ρ_s =0.42 and varying phase difference.

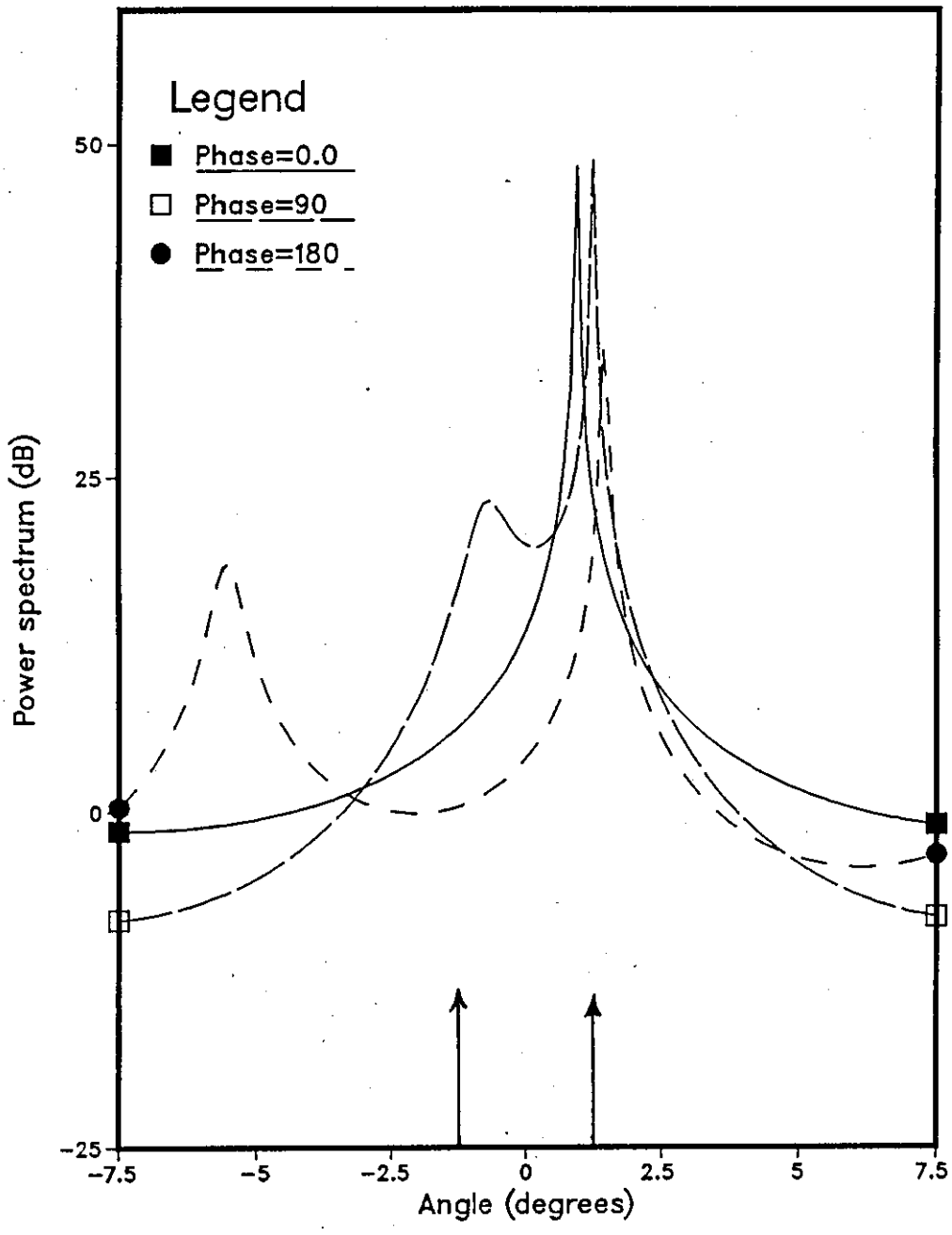

Figure 5–6 :The MEM power spectrum for specular multipath for angle separation of 0.5 BW, S/N=30 dB, ρ_s =0.1 and varying phase difference.

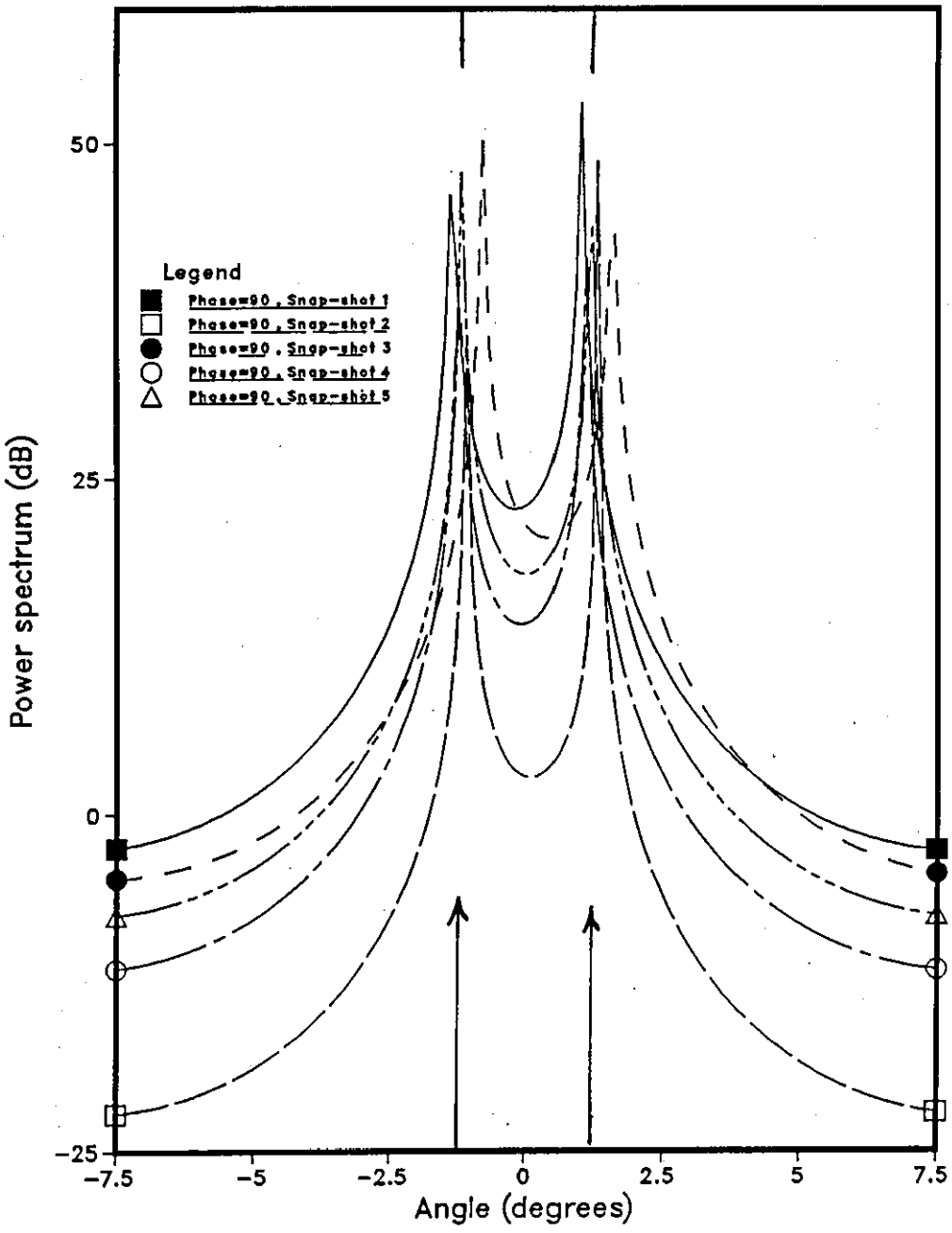

Figure 5–7 :The MEM power spectrum for specular multipath for angle separation of 0.5 BW, S/N=30 dB, ρ_s =0.9 and 5 different snap–shotse. SW.5 target's type

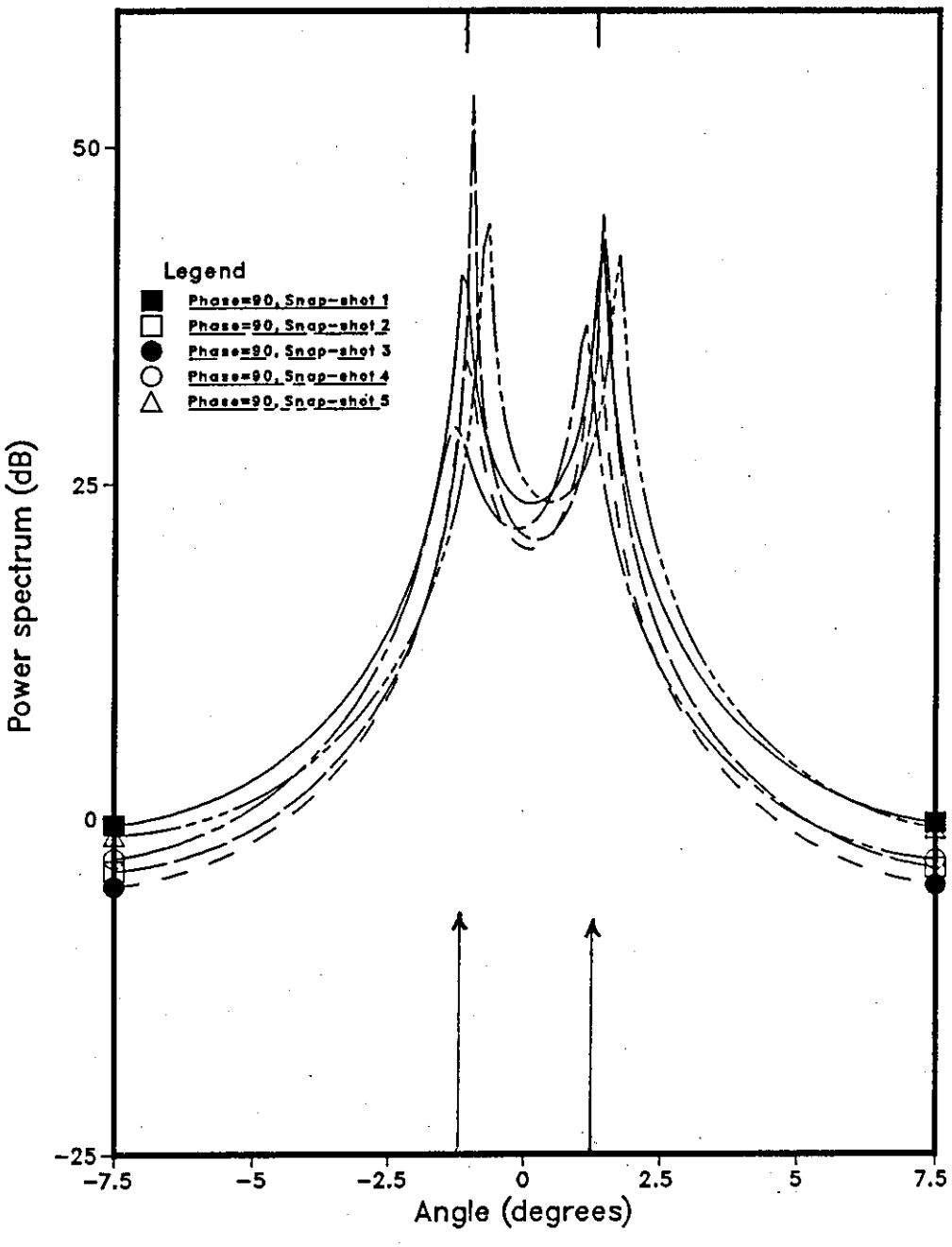

Figure 5–8 :The MEM power spectrum for specular multipath for angle separation of 0.5 BW, S/N=30 dB, ρ_s =0.9 and 5 different snap–shotse. SW.2 target's type.

From these results one can expect the method to work well over a rough surface where the specular reflection is very weak and widely diffused multipath dominates. Interesting simulation results for performance over various rough surfaces are presented in a coming chapter.

5-4.2 The phase monopulse results

The results are computed for a direct signal from a target and its coherent specular multipath at elevation angles of 0.5 BW and -0.5 Bw respectively. The rms error (÷beamwidth) is computed from 1000 trials for every value of Ψ shown. The phase difference (Ψ) is taken in steps of 10° degrees between 0° and 180°. A SW.5 target type is considered unless otherwise indicated.

Figure 5-9 shows the rms error in estimating the angle of arrival using phase monopulse as a function of Ψ for ρ_s=0, 0.1, 0.42, 0.9. For comparison the performance is shown for a SW.2 target type at ρ_s=0.0 only (the solid line) where the increase in the rms error is shown to be very significant over all values of Ψ. The error increases as a non-linear function of ρ_s, where it rises from 0.016 over all values of Ψ for ρ_s=0 to a minimum of 0.26 when $\Psi=90^{\circ}$ for ρ_s=0.9. The smaller rms error when $\Psi=90^{\circ}$ for all values of a_s tested (except when a_s=0.0) can be related to the discusion in the previous section and noise effects. Figure 5-10 shows the off-axis performance for ρ_s=0.9, and different values of the tilt angle. In general, the rms error decreases as the tilt angle increases. For an angle tilt of 1.5 BW

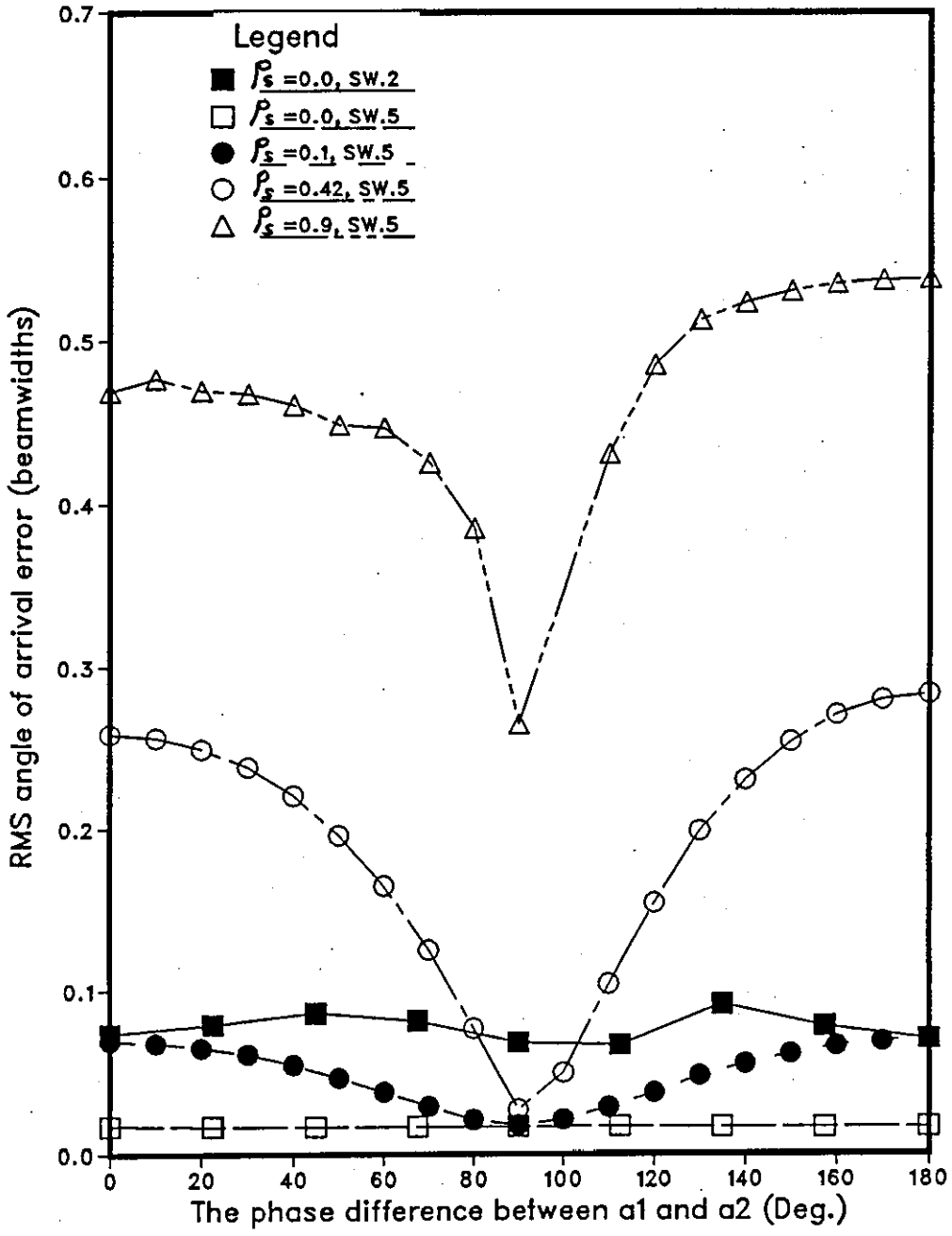

Figure 5-9 :RMS error of Phase monopulse as a function of phase difference between the two coherent signals for angle separation of 1 BW,S/N=30dB, and different values of specular multipath.

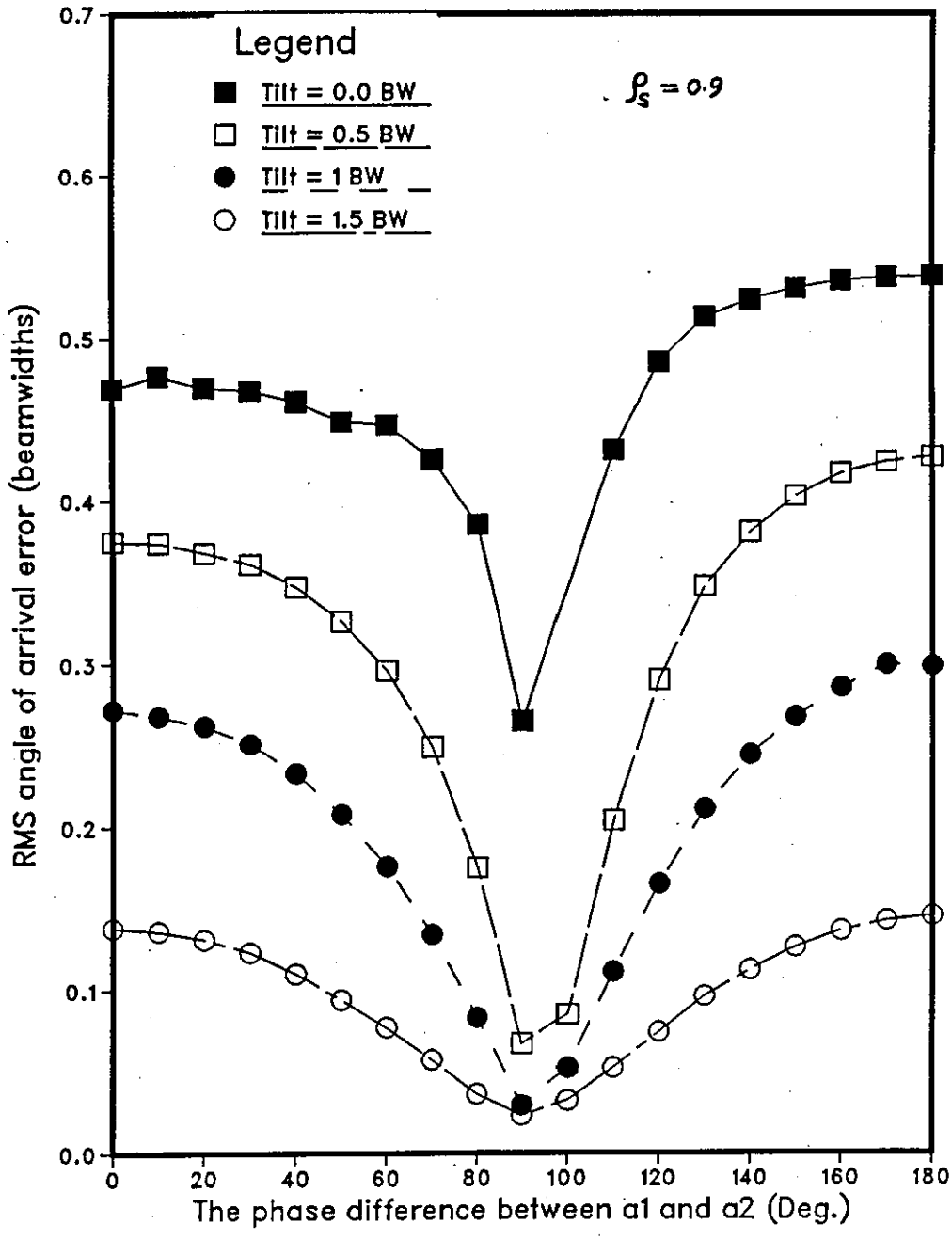

Figure 5–10 : RMS error of Phase monopulse as a function of phase difference between the two coherent signals for angle separation of 1 BW,S/N=30dB, and different values of beam tilt.

(equivalent to 0.75 of the 3dB beamwidth of each subaperture) the lowest rms error is about 0.023 at $\Psi=90^{\circ}$ and highest when $\Psi=0^{\circ}$ or 180° where the rms error rises to about 0.13.

The performance of phase-monopulse over different rough surfaces, where diffuse as well as specular multipath exists, will be studied and compared with related methods in chapter 6.

Chapter 6

Effect of Surface Roughness on Elevation Angle Estimation in Multipath

6-1 Introduction

Much of the past work [6-1,5] on improved radar algorithms for low-flying targets has focused on the case of a single specular reflection from a nominally smooth flat reflecting surface. However in practice, when the reflected signal from a low-flying target propagates over the surface (sea or land) toward a low sited radar, the field incident on the receiving array is composed of a free space component and a component due to the reflection and diffraction from the surface. The latter consists of a coherent part (specular multipath) and noncoherent part (diffuse multipath) as was shown in chapter 2. Barton [6-9] developed a detailed model which describes the diffused multipath power distribution in the four radar cordinates for a low-flying target and shows that most of the diffuse power from a homogeneous, Gaussian wave-height distributed, surface will reach the receiving array from the region within a glistening area (see chap.2).

Cantrell et al.[6-1] have discussed a three subaperture maximum likelihood estimator (3SA-MLE) using a linear array to solve the coherent multipath problem for both symmetric

and nonsymmetric cases as was shown in chapter 3. A new three-subapertures trigonometric solution (3SA-TRM) was found and discussed in chapter 4. Also, the performances of the maximum entropy method (using three-subapertures) and the phase monopulse were discussed in the previous chapter for the specular multipath case and are expected to operate well over a rough surface [6-6], [6-7].

In this chapter the performance of the 3SA-MLE, 3SA-TRM, MEM, and the phase monopulse radar are tested and compared in the presence of diffuse and specular reflection environments. The diffused power model was discussed and simulated in chapter 2. The same simulation results for different surface slopes and roughness have been used. In general the results show, that the accuracy depends on three factors: first, the slopes of the surface, where higher slope values means less degredation of the angle estimation accuracy; second, the surface roughness, where the higher the roughness the worst the accuracy; and third, the beamwidth of the array, where the narrower the beam the better the angle estimation accuracy. When the surface is rough the best obtainable accuracy is shown to be from the maximum entropy method and phase monopulse.

6-2 The composite multipath signal model

The composite output of the m^{th} subaperture in the presence of specular and diffuse multipath over a rough surface is given by Taha and Hudson [6-8] by the following general equation:

$$S_m = a_1 G_1 \exp[(m-2) Z_1] + a_2 G_2 \exp[(m-2) Z_2] + \sum_{j=1}^{N_S} a(j) G(j) \exp[(m-2) Z(j)] + n_m \qquad (6\text{-}1)$$

The subscript m takes the values from 1 to 3 for the three subapertures arrangement.

The first term in the equation represents, at the m^{th} element, the direct signal, the second is the specular multipath, the third represents the sum of the diffuse reflection scatterers, and the last one represents the complex Gaussian noise with zero mean and variance σ^2. Also, a(j) is the complex amplitude (drawn from a Gaussian distribution) of the j^{th} diffuse reflection scatterer and Z(j) its associated grazing angle with respect to the horizon. Ns is the number of the diffuse scatterers assumed within the glistening surface. G(j) is the subaperture pattern response in the j^{th} angular direction which is approximated as in equation (3-1) in chapter 3. The remaining symbols are also as described in chapter 3. For the case of the phase monopulse two subaperture arrangement equation (6-1) becomes as follows:

$$S_m = a_1 G_1 \exp[(m-1.5) Z_1] + a_2 G_2 \exp[(m-1.5) Z_2] + \sum_{j=1}^{N_S} a(j) G(j) \exp[(m-1.5) Z(j)] + n_m \qquad (6\text{-}2)$$

where the subscript m takes the values 1 and 2 only. The descriptions of the terms used are as for equation (6-1). In

the above two equations the phase centre is taken at the middle element of the array. The number of the diffuse reflection scatterers and their angular positions and powers are computed in chapter 2 for different surfaces (appendix A2, tables 1-7). Figure 6-1 shows a detailed radar target geometry over a plane, rough surface where the dashed lines represent some of the diffused power scatterers.

6-3 Simulation results and discussion:

This section presents the results of a computer simulation used to study and compare the performances of the above mentioned methods in different multipath environments. A linear array of 21 elements equally spaced by a half wave-length is used. This array is equally divided into three subapertures of 7 elements (or just two subapertures of 10 elements for the phase monopulse) unless otherwise specified. The signal to noise ratio used is always 30dB, calculated as in chapter 3. The bisecting angle (θ_B) and the angular distance (θ_D) are taken to be 0 and 0.25 BW (BW is the 3dB beamwidth of the whole array), unless otherwise stated. The noisy signal model used is the one shown in equation (6-1) for all the methods except the phase monopulse where equation (6-2) is used insted. The number, and values, of the diffuse scatterers' powers and angular positions are calculated in chapter 2 (Appendix A2, tables 1 to 7) for different surfaces and radar-target geometries and strip lengths. The foreground component of the diffuse power is divided among three scatterers where the power and angular

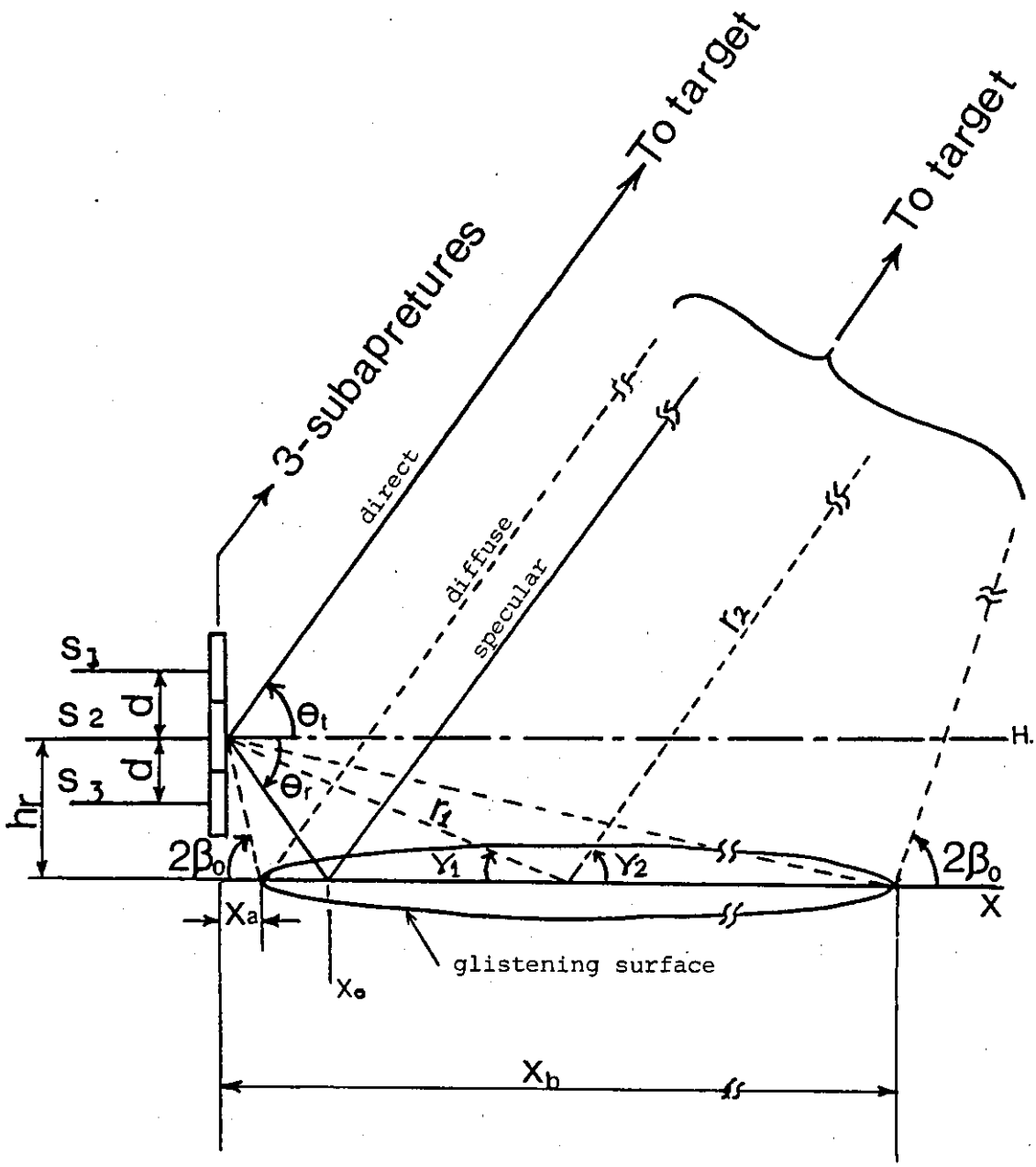

Figure 6-1 The radar target geometry over a rough surface where the dashed lines represent some of the diffuse reflection scatterers.

position of each is computed for every value of β_o and σ_h/λ given in table 6-1. The values of the specular reflection coefficient can easily be found for each surface roughness from equation (2-28) in chapter 2. The phase difference between the direct and specularly reflected signals (Ψ) is taken in steps of 22.5^o (10^o for the phase monopulse case) from 0^o to 180^o. The direct angle of arrival rms errors are averaged over 1000 trials for each value of Ψ and normalized to the 3dB beamwidth.

6-3.1 The maximum likelihood method:

Figures 6-2 and 6-3 demonstrate the performances of the symmetric and nonsymmetric 3SA-MLE respectively over a surface with β_o=0.1 and surface roughness parameter (σ_h/λ) of 0.0, 5, 20 . When σ_h/λ=20 the direct angle estimation accuracy is almost the same at all values of Ψ, showing large degredation in accuracy for all phases in comparison with the smooth surface (σ_h/λ=0, ρ_s=0.9), except at $\Psi=0^o$ or 180^o (just 180^o for the symmetric case) where improvement occurs. When σ_h/λ=5, the rough surface accuracy degrades at all values of Ψ in comparison with the the smooth one except at $\Psi=0^o$ where a little improvement occurs, for the nonsymmetric case only, as can be seen from figure 6-3. Thus, in general, the 3SA-MLE performance degrades as the surface roughness increases. Figures 6-4 and 6-5, present the symmetric and nonsymmetric 3SA-MLE performances of a medium surface roughness σ_h/λ=5 and three different values of β_0 (β_o=0.05, 0.1, 0.2). The direct angle estimation accuracy

Table 6-1: The range distribution of the foreground component of the diffused power for a target radar geometry with h_r=5m, h_t=205m, R=10km and different surface roughness.

σ_h/λ=5				σ_h/λ=20			
β_o=0.2		β_o=0.1		β_o=0.05		β_o=0.1	
Power	Angle	Power	Angle	Power	Angle	Power	Angle
0.18	-0.4	0.2	-0.2	0.18	-0.1	0.2	-0.2
0.16	-0.2	0.1	-0.1	0.12	-0.05	0.14	-0.1
0.06	-0.05	0.07	-0.025	0.07	-0.025	0.07	-0.025

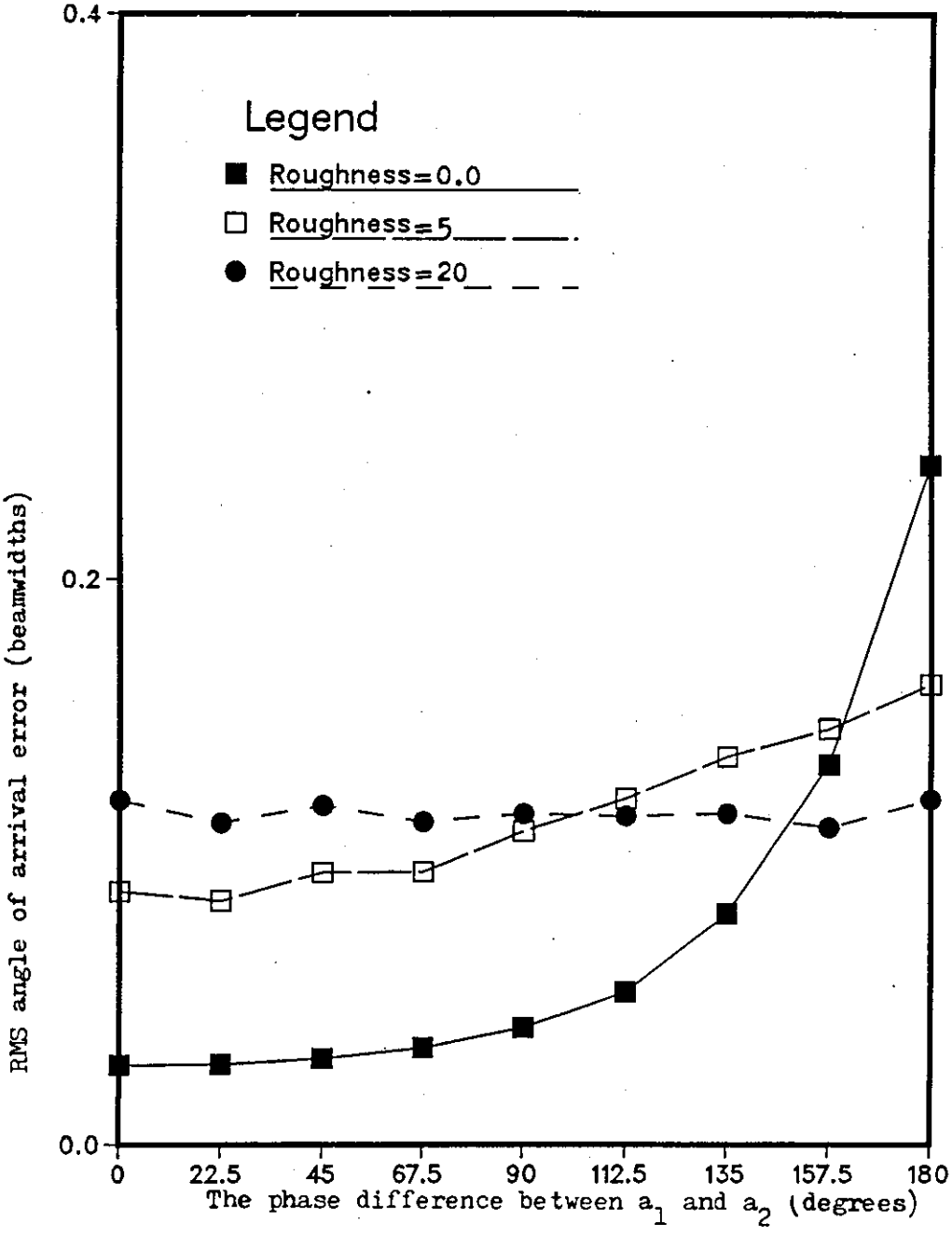

Figure 6-2 :RMS error of symmetric 3SA-MLE as a function of phase difference between the two coherent signals for θ_B=0.0 S/N-30 dB, θ_0 =0.25 BW, β_o =0.1, and $\sigma h/\lambda$=0, 5, 20 (when 0, ρ_s=0.9).

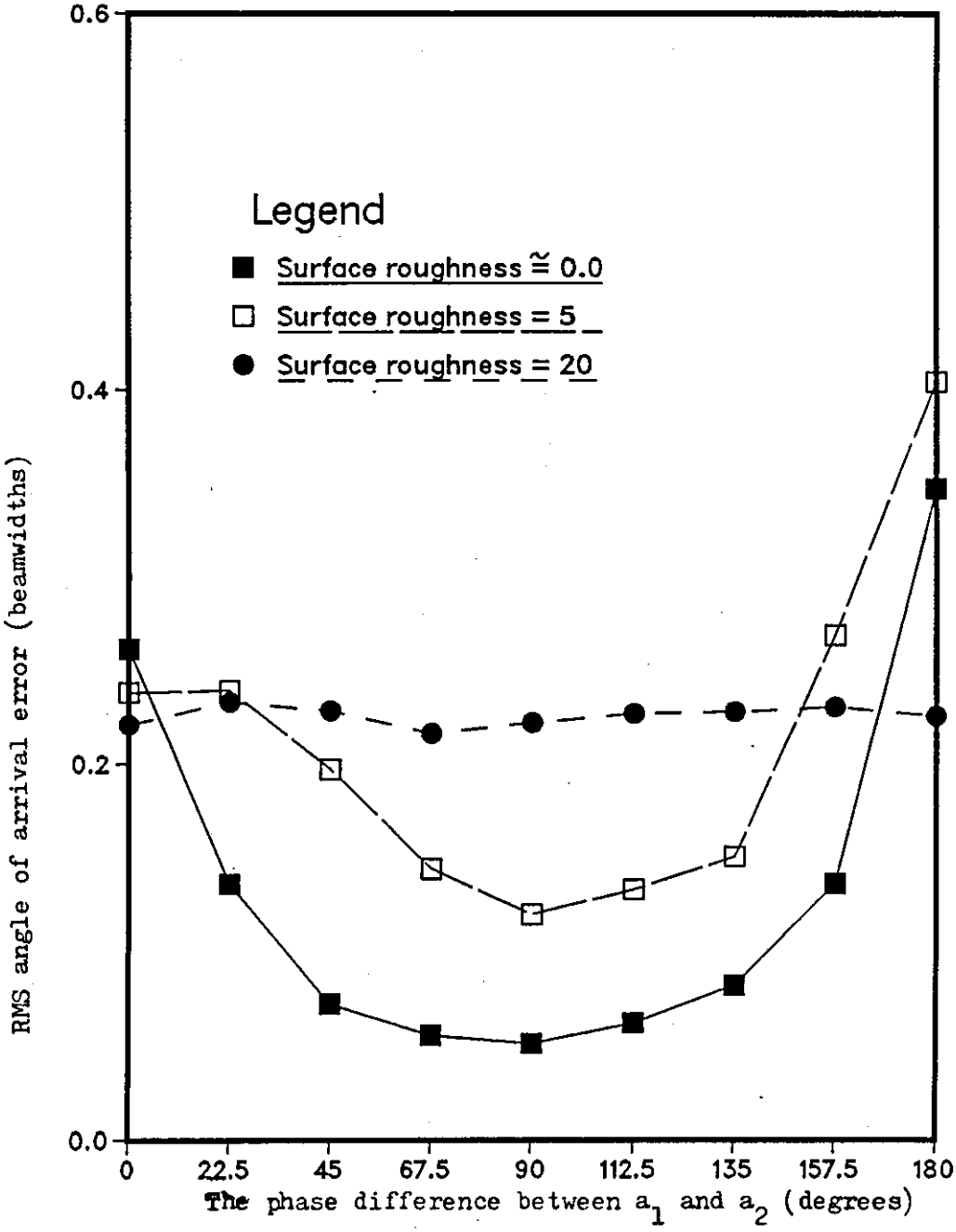

Figure 6-3 :RMS error of nonsymmetric 3SA-MLE as a function of phase difference between the two coherent signals for θ_B=0.0, S/N-30 dB, θ_D=0.25 BW, β=0.1, and $\sigma h/\lambda$=0.0, 5, 20 (when $\sigma h/\lambda$ = 0.0, ρ_s = 0.9).

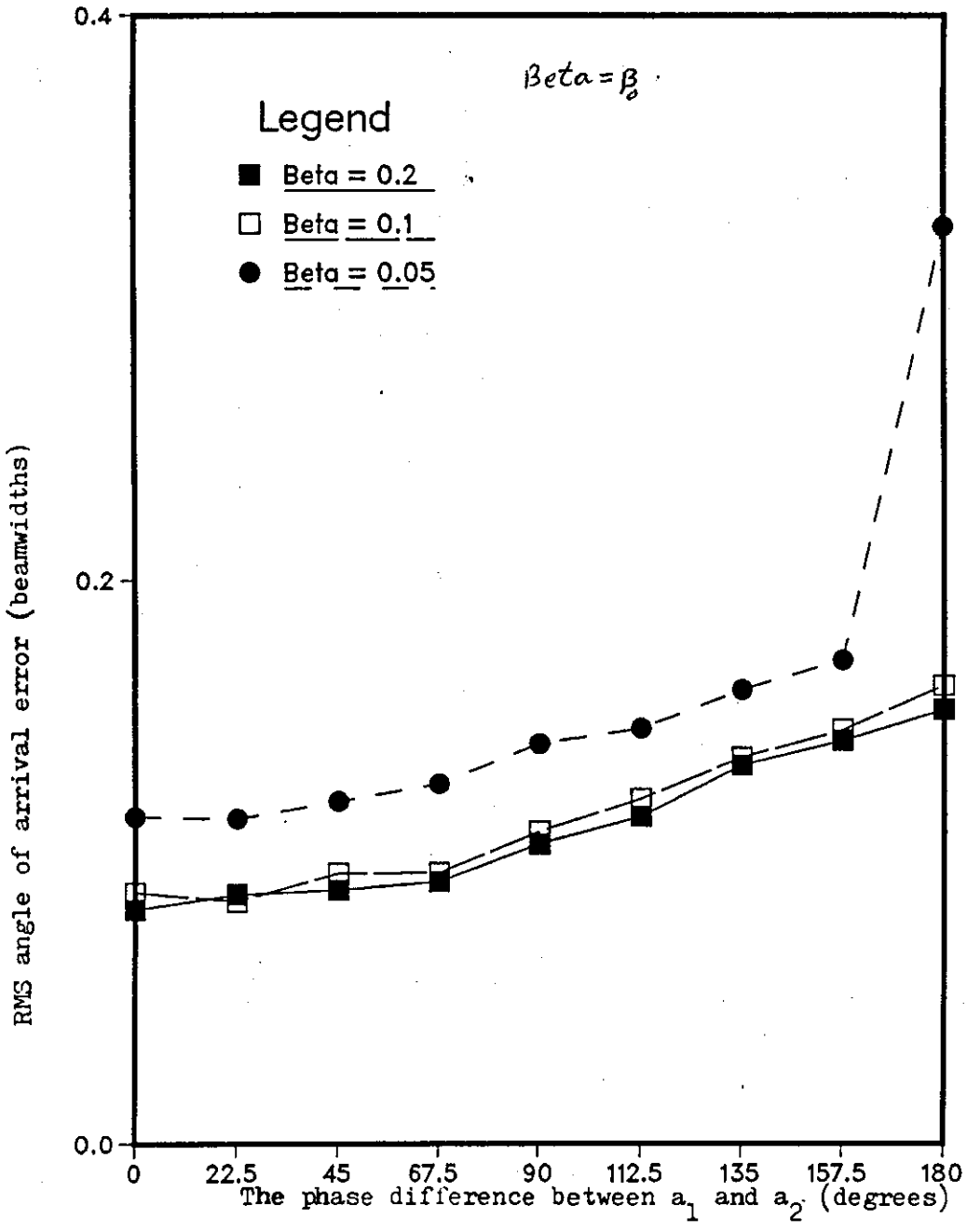

Figure 6-4 :RMS error of symmetric 3SA-MLE as a function of phase difference between the two coherent signals for θ_B=0.0 S/N-30 dB, θ_D=0.25 BW, σ_h/λ=5, and β_o=0.2, 0.1, 0.05.

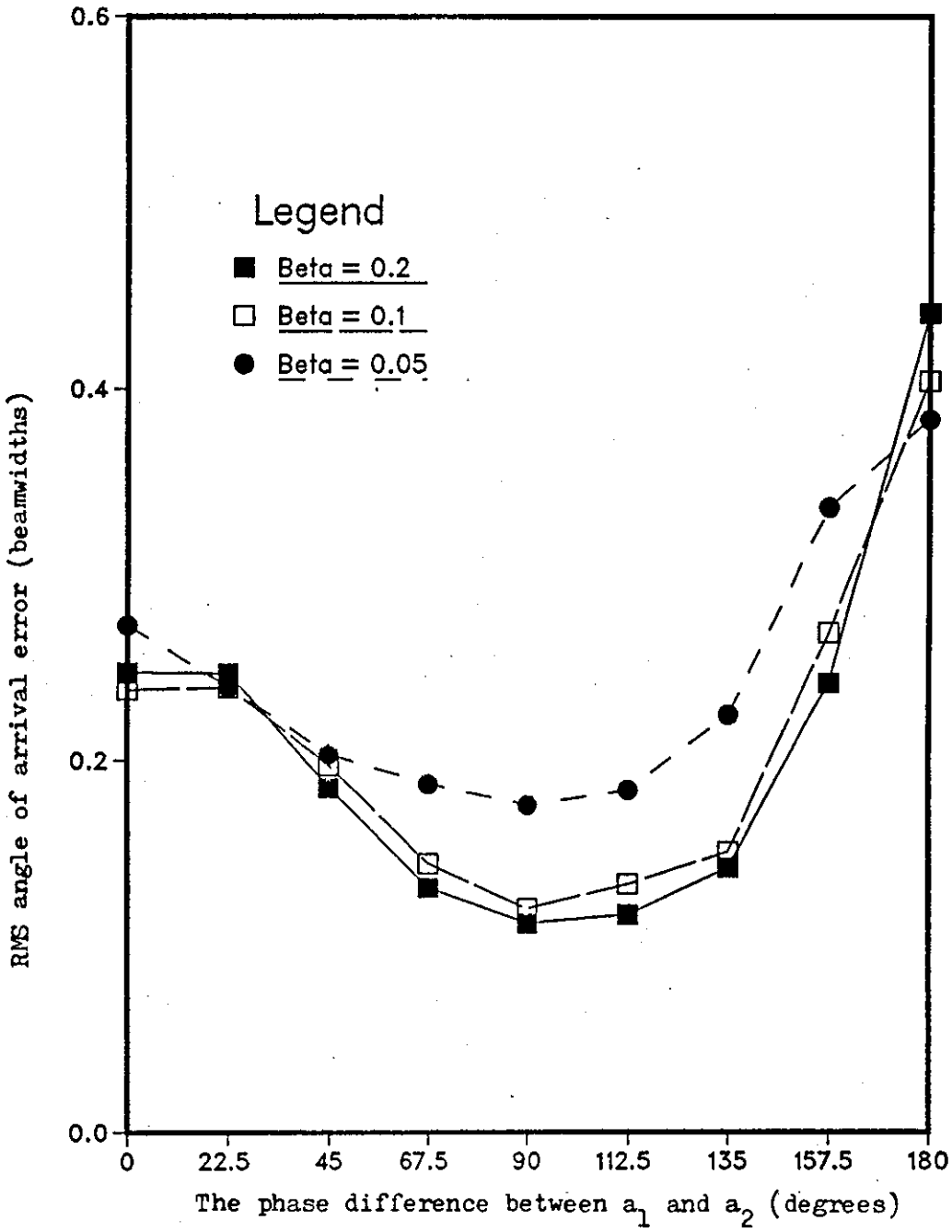

Figure 6-5 :RMS error of nonsymmetric 3SA-MLE as a function of phase difference between the two coherent signals for θ_B =0.0 S/N-30 dB, θ_D =0.25 BW, $\sigma h/\lambda$ =5, and β =0.2, 0.1, 0.05.

decreases as β_o decreases over all values of Ψ, except at $\Psi=180^\circ$ where the opposite occurs for the nonsymmetric case and at $\Psi=0^\circ$ where the accuracy is slightly better for $\beta_o=0.1$ than for $\beta_o=0.2$. Figures 6-6 and 6-7 present the effect of the aperture beamwidth used on the accuracy of the direct angle estimation over a rough surface with $\sigma_h/\lambda=5$, $\beta_o=0.05$. Here a linear array of 42 elements ($\lambda/2$ spacing), equally divided into three subaperture, is used in the simulation in order to reduce the BW by half (from 0.084 to 0.042 radians). One can see from the curves, that the narrower the beam the better the performance over all values of Ψ except at $\Psi=180^\circ$ for the nonsymmetric case where a little decrease in accuracy is shown. The average improvement in rms error at $\Psi=90^\circ$ is about 0.13 of a beamwidths for the nonsymmetric case and less than 0.1 for the symmetric case over all values of Ψ which is very substantial. This improvement can be related to two facts; first the 3SA-MLE works better at higher angular separation between the two coherent sources (the angular distance is 0.5BW insted of 0.25BW for the 21 element array), and the second, and more important, is that the main foreground component of the diffuse reflection is getting closer to the first null of the subaperture beam pattern, greatly reducing its effect.

6-3.2 The trigonometric solution method:

Figures 6-8 and 6-9 show the performances of the symmetric and nonsymmetric 3SA-TRM respectively over a surfaces with $\beta_o=0.1$ and surface roughness of 0.0, 5, and 20.

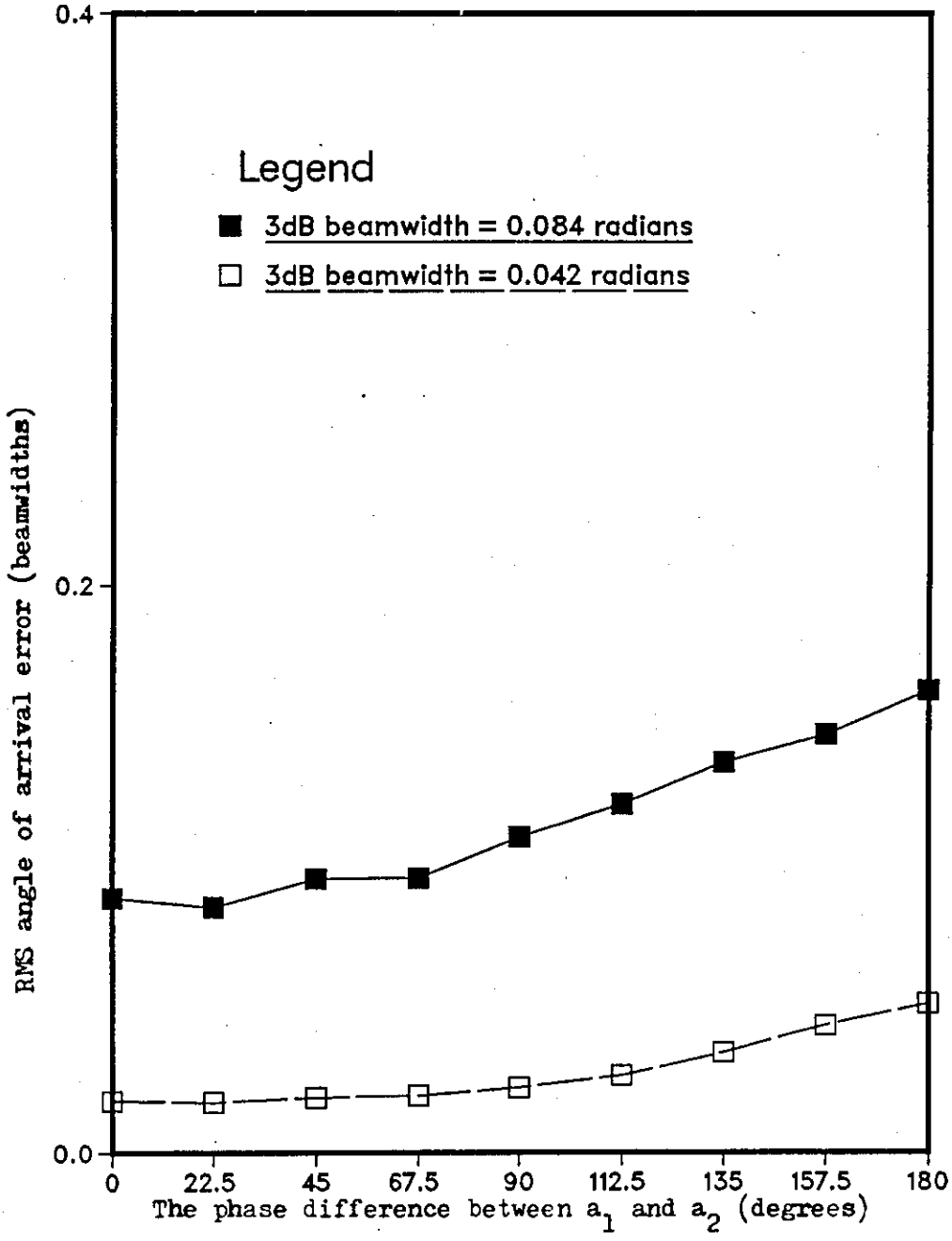

Figure 6-6 :RMS error of symmetric 3SA-MLE as a function of phase difference between the two coherent signals for θ_B =0.0 S/N=30 dB, θ_D =0.25 BW, β_o =0.05, $\delta h/\lambda$ =5, (beamwidth effect comparison).

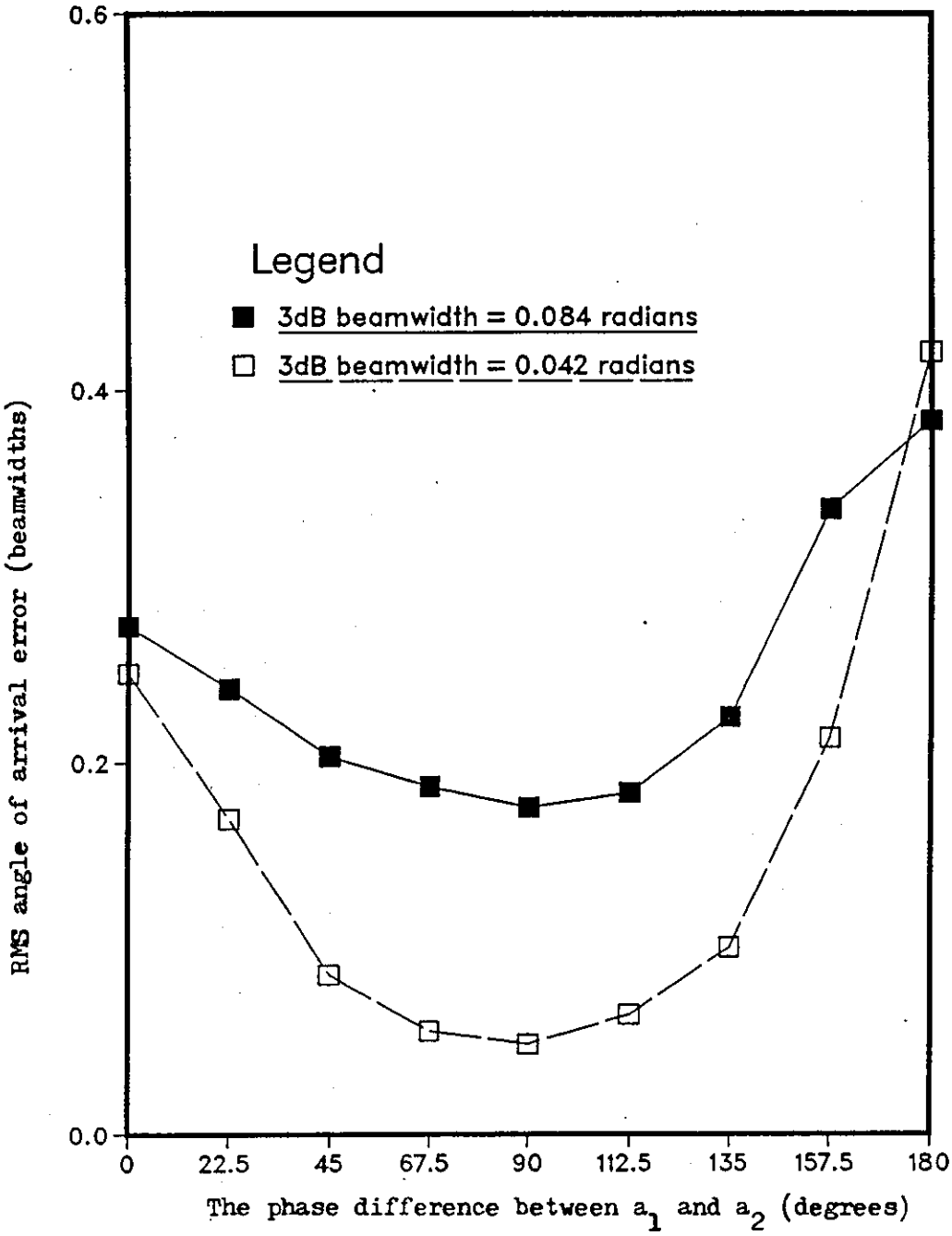

Figure 6-7 :RMS error of nonsymmetric 3SA-MLE as a function of phase difference between the two coherent signals for θ_B=0.0, S/N=30 dB, θ_D=0.25 BW, β =0.05, and $6h/\lambda$ =5 (beamwidth effect comparison).

When $\sigma_h/\lambda=20$ the angle estimation accuracy is almost the same at all values of Ψ, showing large degredation in accuracy for all phases in comparison with the smooth surface ($\sigma_h/\lambda=0$, $\rho_s=0.9$). When $\sigma_h/\lambda=5$, the rough surface accuracy degrades at all values of Ψ in comparison with the the smooth one, except at $\Psi=180^\circ$ where an improvement occurs for the symmetric case only, as can be seen from figure 6-8. Thus, the 3SA-TRM performance degrades as the surface roughness increases. In general, its performance is worst than that of the 3SA-MLE method discussed in the above subsection, especially for $\sigma_h/\lambda=20$, which can be related to nature of the way each method operates. Figures 6-10 and 6-11, present the symmetric and nonsymmetric 3SA-TRM performances of a medium surface roughness $\sigma_h/\lambda=5$ and three different values of β_0 ($\beta_o=0.05, 0.1, 0.2$). The angle estimation accuracy decreases as β_o decreases over all values of Ψ, except at $\Psi=180^\circ$ and nonsymmetric performance where the accuracy is slightly better for $\beta_o=0.05$ than for $\beta_o=0.1$. The performance of the symmetric case of this method is much better than that of the 3SA-MLE above for $\Psi=180^\circ$ and $\beta_o=0.05$. Figures 6-12 and 6-13 present the effect of the aperture beamwidth used on the accuracy of angle estimation over a rough surface with $\sigma_h/\lambda=5$, $\beta_o=0.05$. Here a linear array of 42 elements, as above, is used in the simulation. One can see from the curves, that the narrower the beam the better the performance over all values of Ψ. The average improvement in rms error at $\Psi=90^\circ$ is about 0.18 of a beamwidth for the nonsymmetric case and slightly less than 0.1 for the symmetric case over all

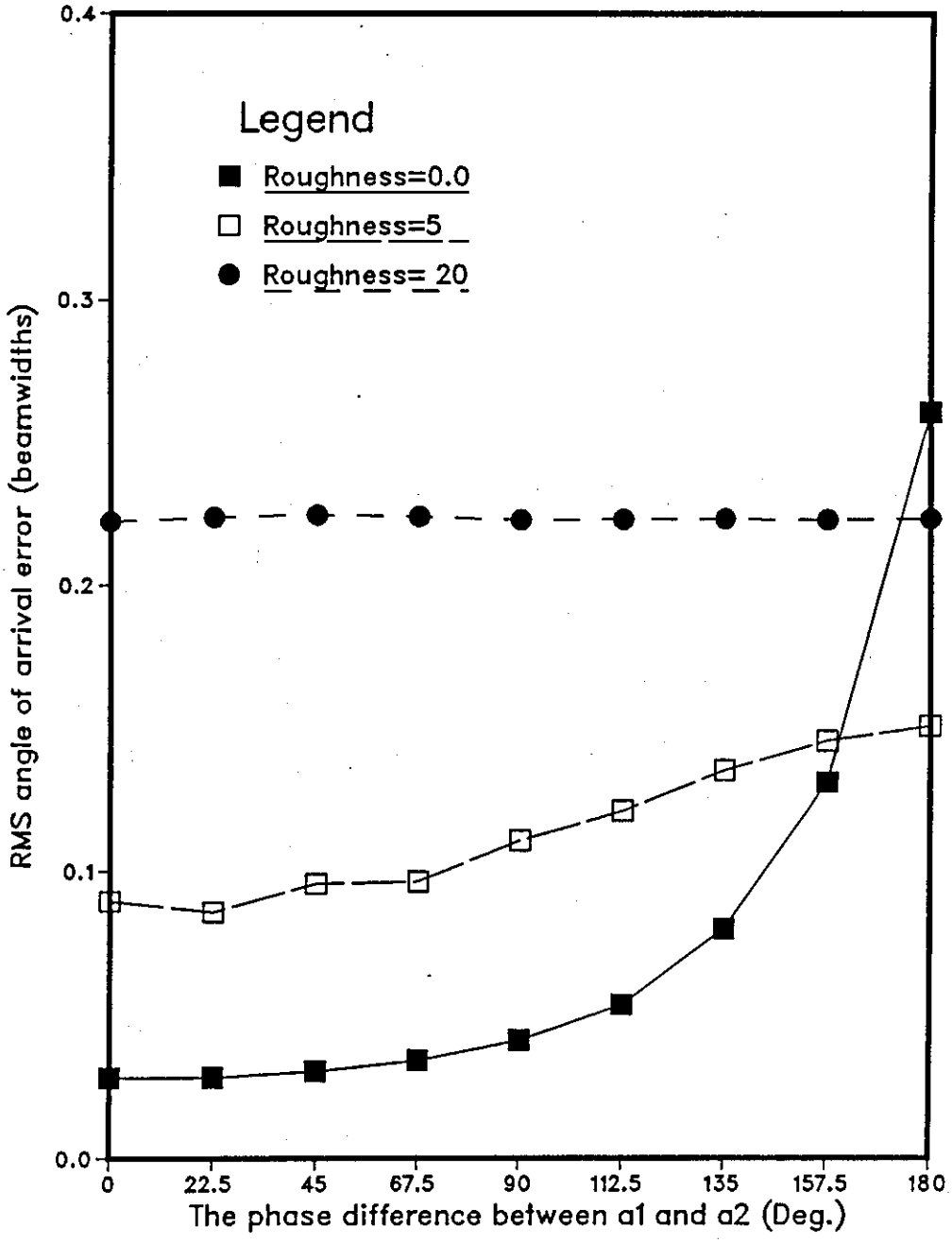

Figure 6–8 :RMS error of symmetric 3SA–TRM as a function of phase difference between the two coherent signals for θ_B =0.0, S/N= 30 dB, θ_D =0.25 BW, β_o =0.1 and σ_h/λ=0, 5, 20.

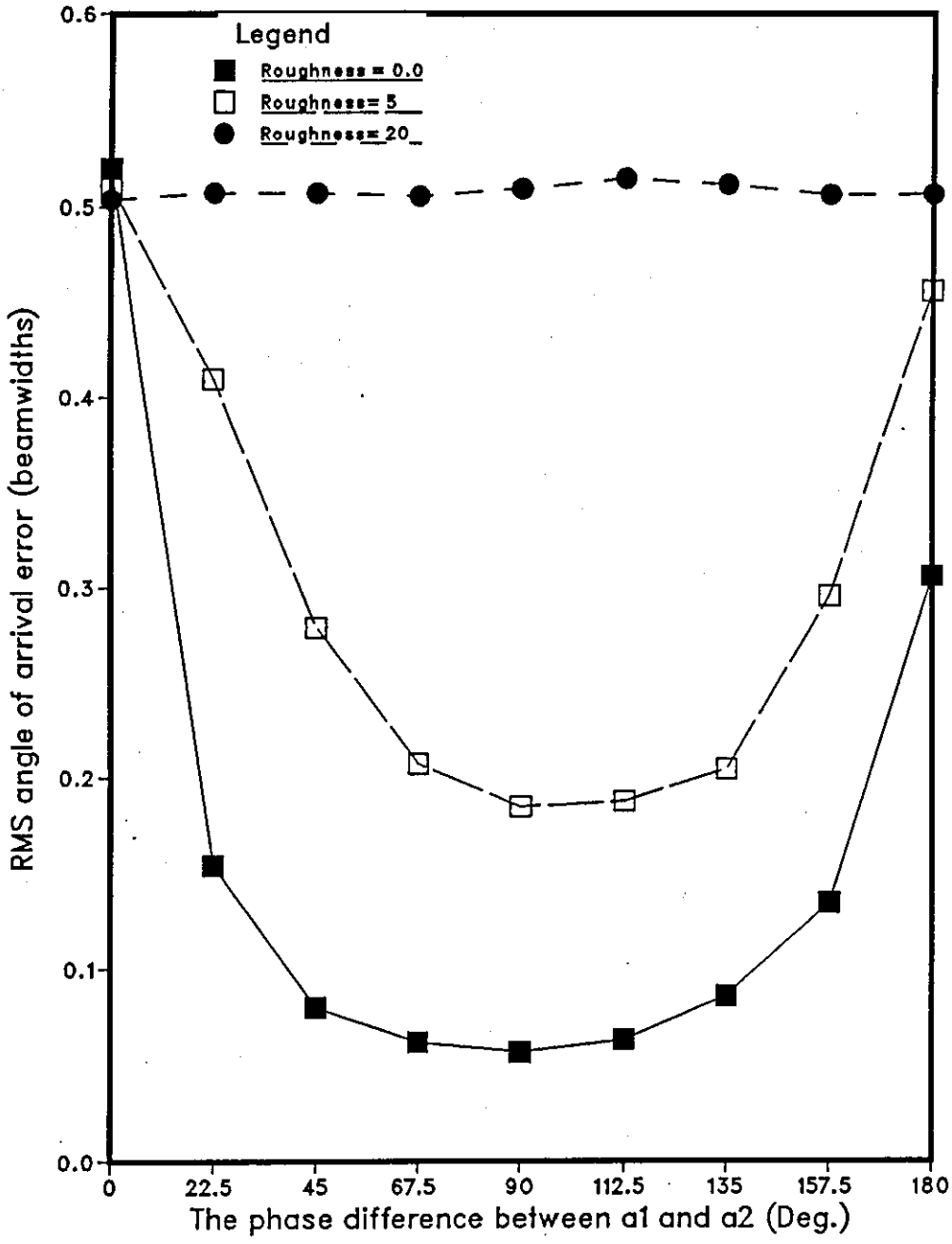

Figure 6– 9 :RMS error of nonsymmetric 3SA–TRM as a function of phase difference between the two coherent signals for θ_B=0.0, S/N= 30 dB, θ_D=0.25 BW, β_0 =0.1, and σ_h/λ =0.0, 5, 20 (when σ_h/λ=0, ρ_s=0.9).

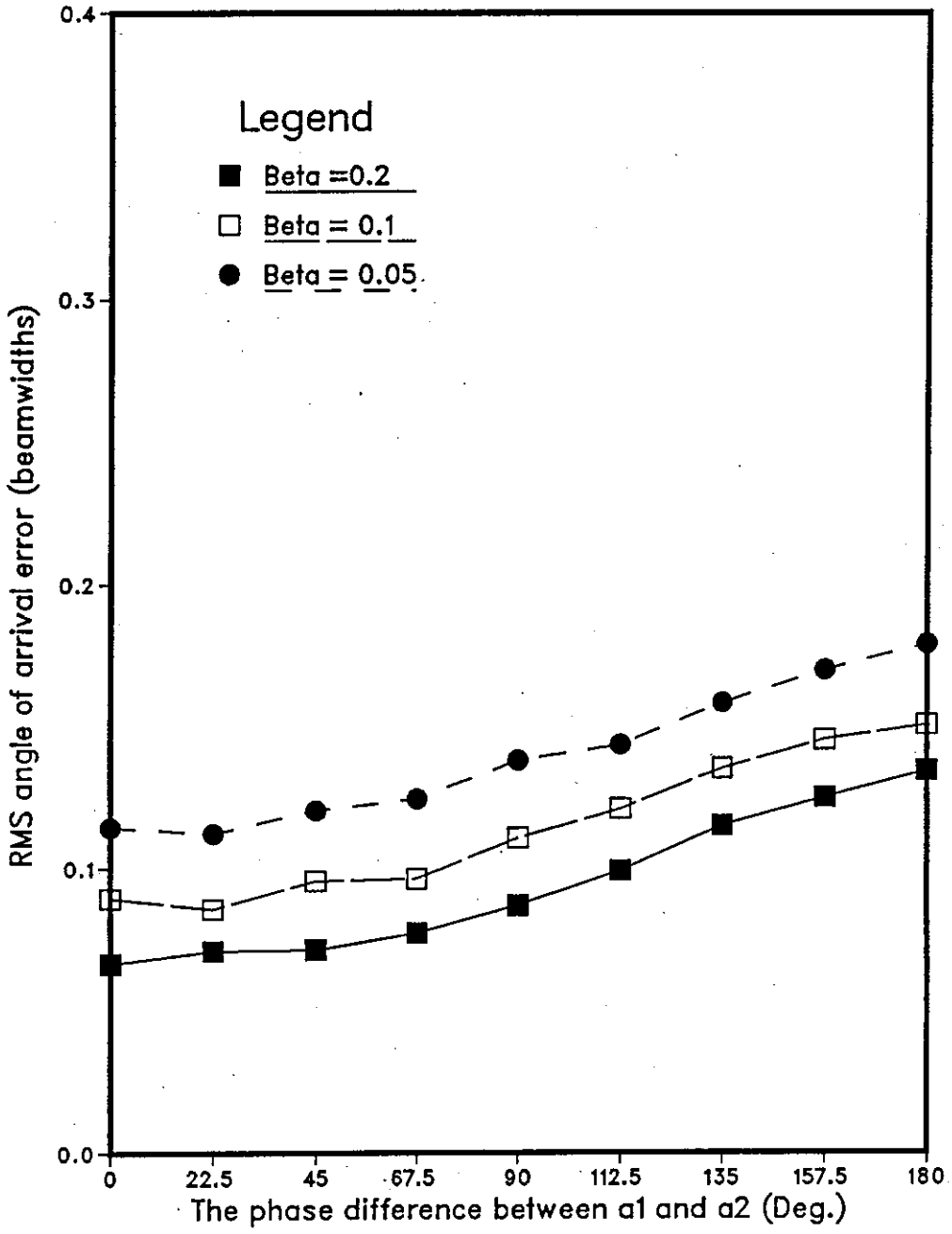

Figure 6-10 :RMS error of symmetric 3SA–TRM as a function of phase difference between the two coherent signals for θ_B =0.0, S/N= 30 dB, θ_D =0.25 BW, d/λ =5 and β =0.2, 0.1, 0.05

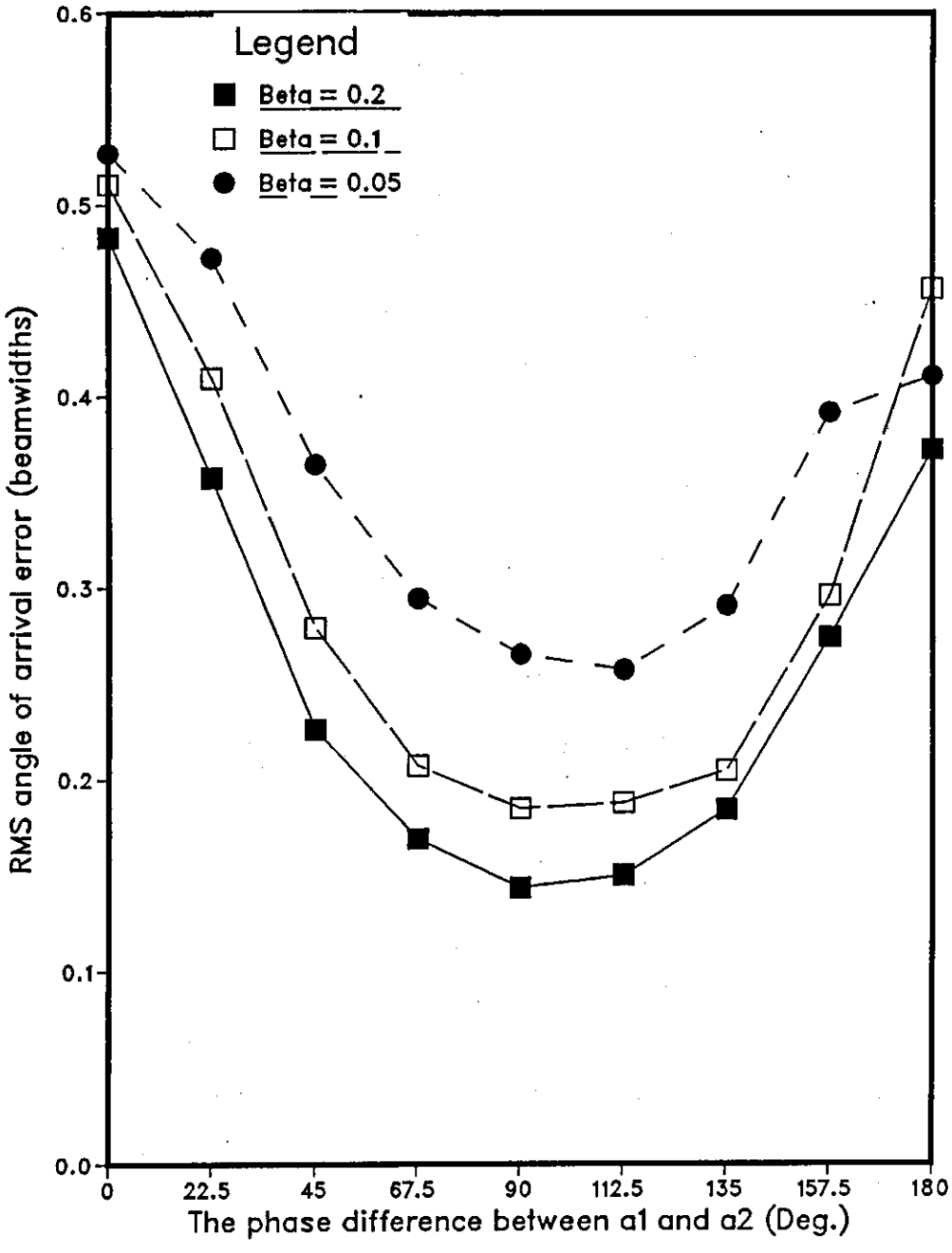

Figure 6–11:RMS error of nonsymmetric 3SA–TRM as a function of phase difference between the two coherent signals for θ_B =0.0, S/N= 30 dB, θ_D =0.25 BW, $6h/\lambda$=5 and β =0.2, 0.1, 0.05

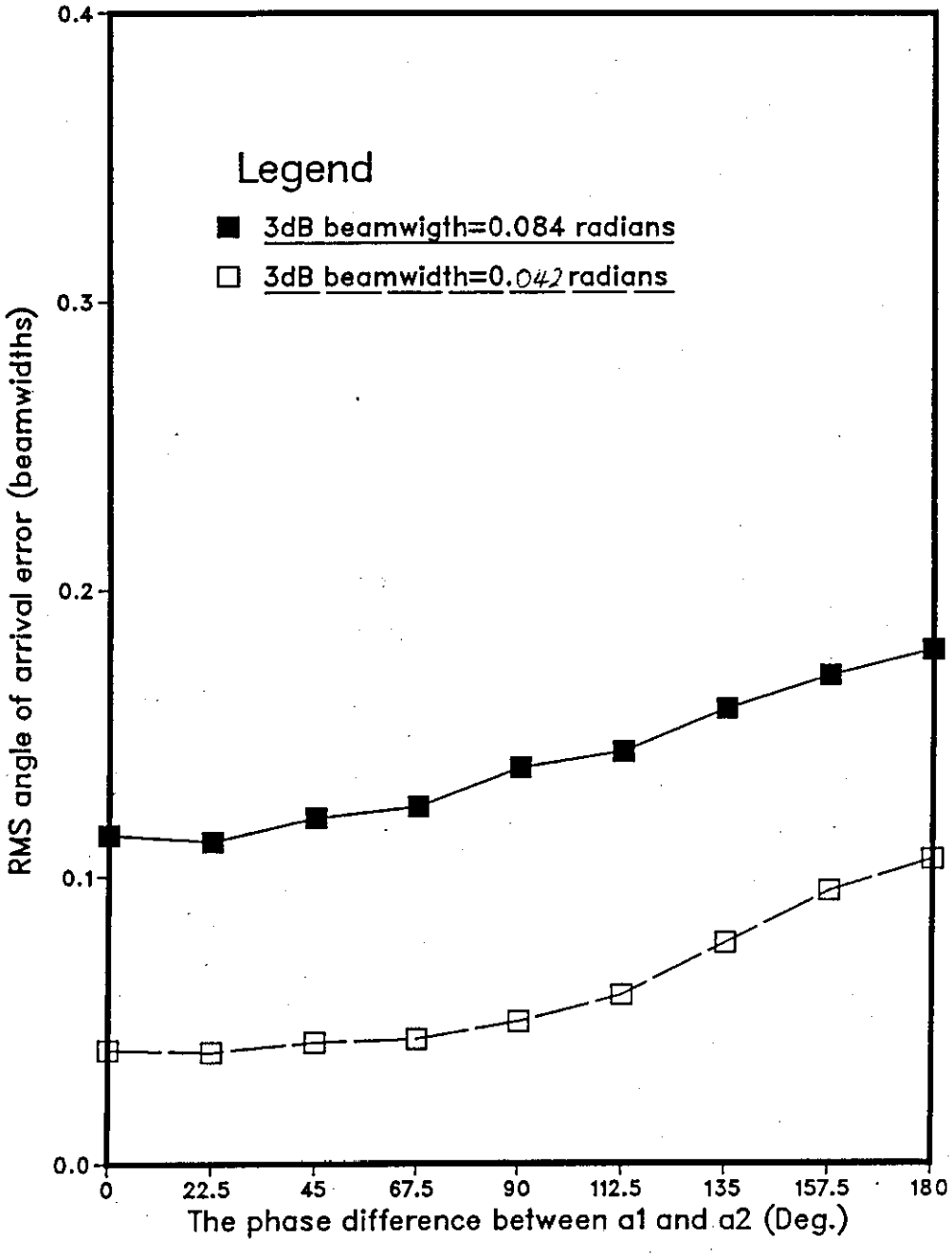

Figure 6-12: RMS error of symmetric 3SA-TRM as a function of phase difference between the two coherent signals for θ_B =0.0, S/N= 30 dB, θ_D =0.25 BW, β_o =0.05 σ_h/λ =5, (beamwidth effect comparison).

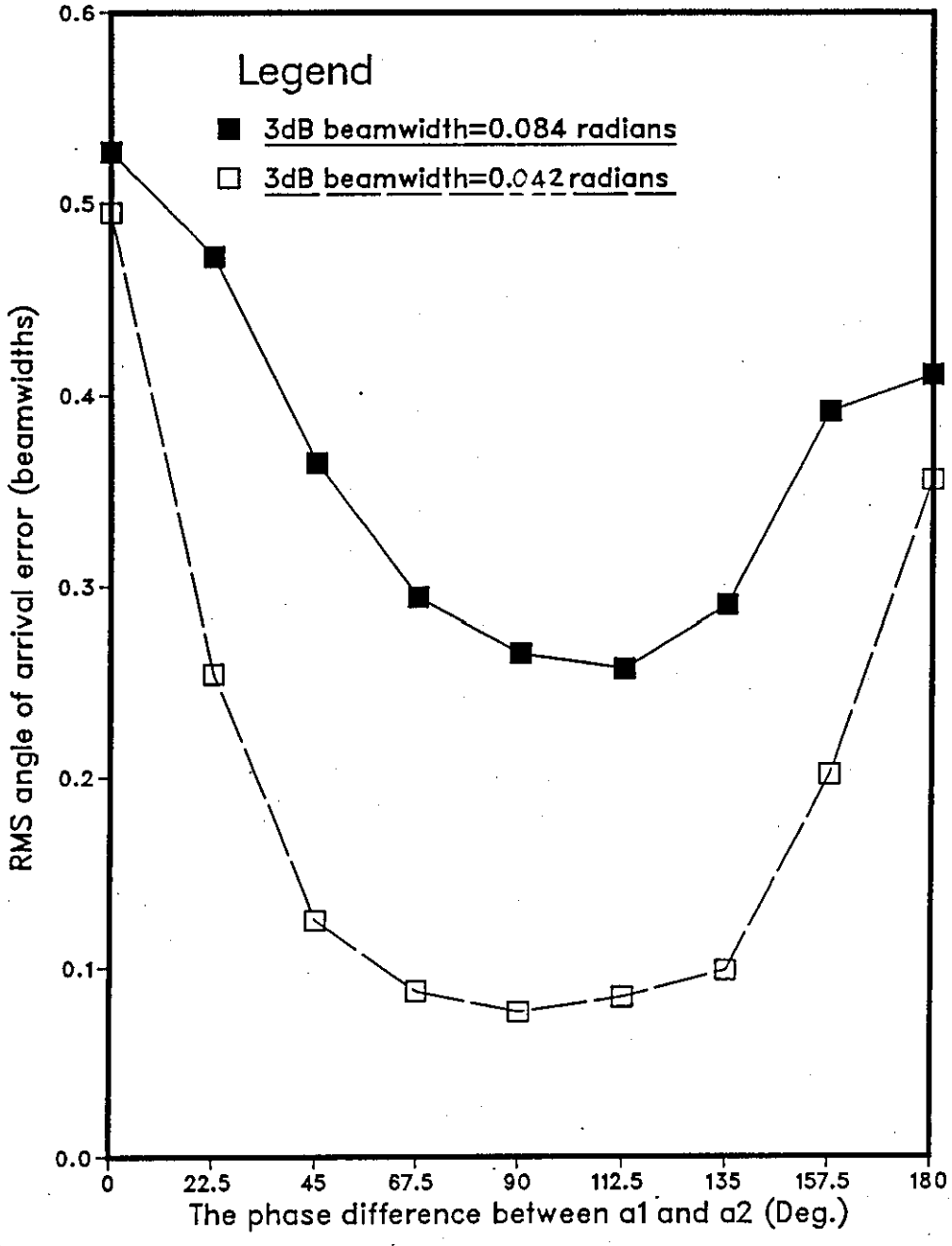

Figure 6-13:RMS error of nonsymmetric 3SA-TRM as a function of phase difference between the two coherent signals for Θ_β=0.0, S/N= 30 dB, Θ_b=0.25 BW, β_o =0.05, and σ_h/λ =5, (beamwidth effect comparison)

values of Ψ which is very substantial. This improvement can be related to the same reasons mentioned in the above subsection.

6-3.3 The phase-comparison monopulse

Figure 6-14 shows the performance of the phase monopulse radar over a rough surface with β_o=0.1 and σ_h/λ=0.0, 5, 20. For a surface roughness of 20 (where ρ_s=0.9X10^{-6}) the obtainable accuracy seems to be very good over all values of Ψ where the rms error rises to about 0.035 only. This can be related to the weak specular multipath component and the randomness of the diffuse one. For σ_h/λ=0.0 or 5, the lowest rms error is shown to be at Ψ=130° and 110° respectively. This displacement is due to the effect of the diffuse multipath component which behaves like a Gaussian noise. For a smooth or moderate surface case, the worst performance is shown to be at Ψ=0° and 180°. The rms error at Ψ=180° worst than that at Ψ=0.0° which generally is a consequence of the constructive and destructive interference between the two coherent signals. Figure 6-15 shows the performance over a moderate surface (σ_h/λ=5) for β_o=0.2, 0.1, 0.05. The rms error increases as the surface slope decreases where the best estimate is shown to be around Ψ=110°. Figure 6-16 demonstrates the off-axis performance over a moderate surface roughness (σ_h/λ=5) for tilt angle=0.0, 0.5, 1.0, 1.5 BW. The rms error decreases as the tilt angle increases where the effect of the specular

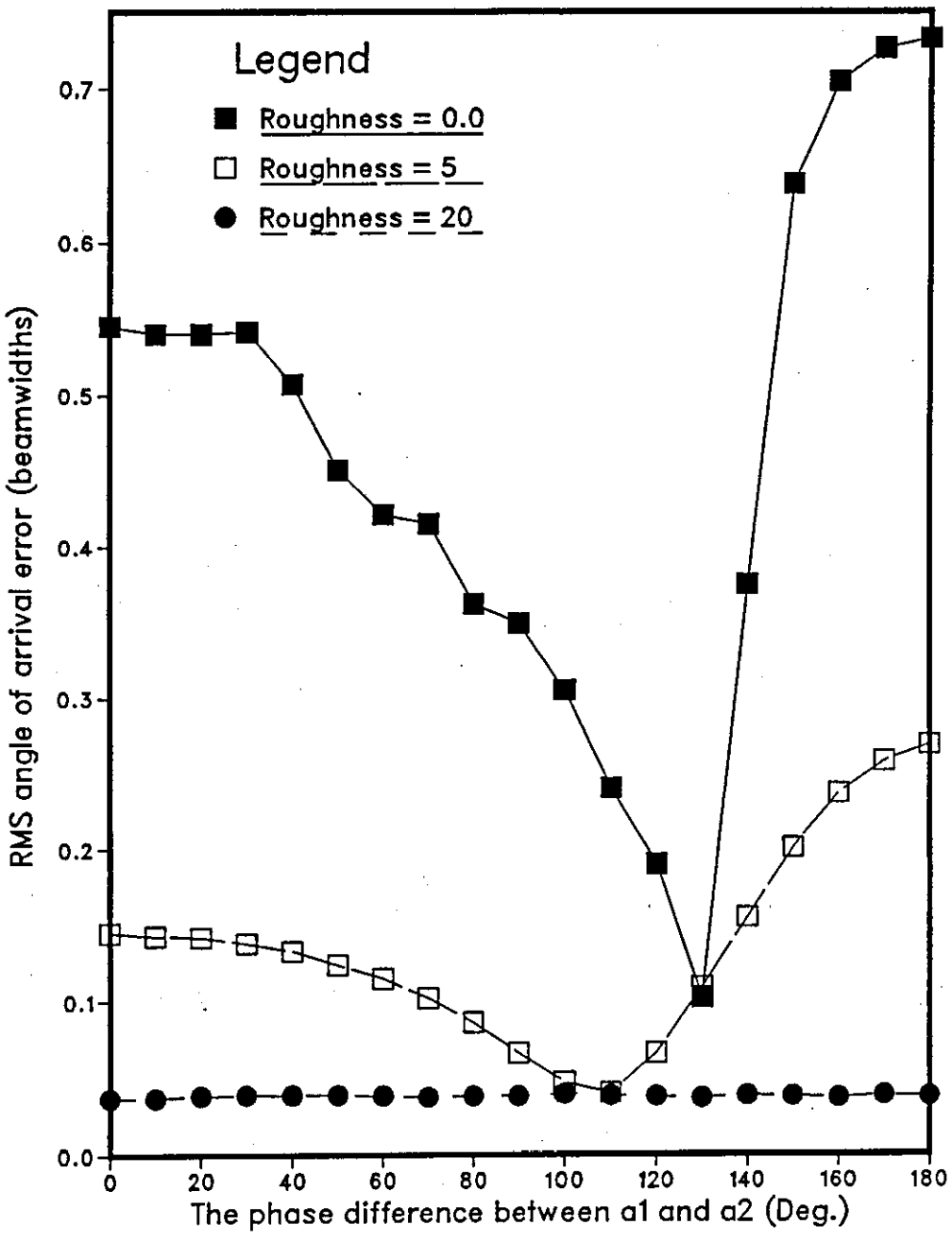

Figure 6-14 :RMS error of Phase monopulse as a function of phase difference between the two coherent signals for angle separation of 0.5 BW, S/N=30 dB, β_o =0.1, $\frac{\sigma_h}{\lambda}$=0.0, 5, 20 (when $\frac{\sigma_h}{\lambda}$ =0, ρ_s=0.9).

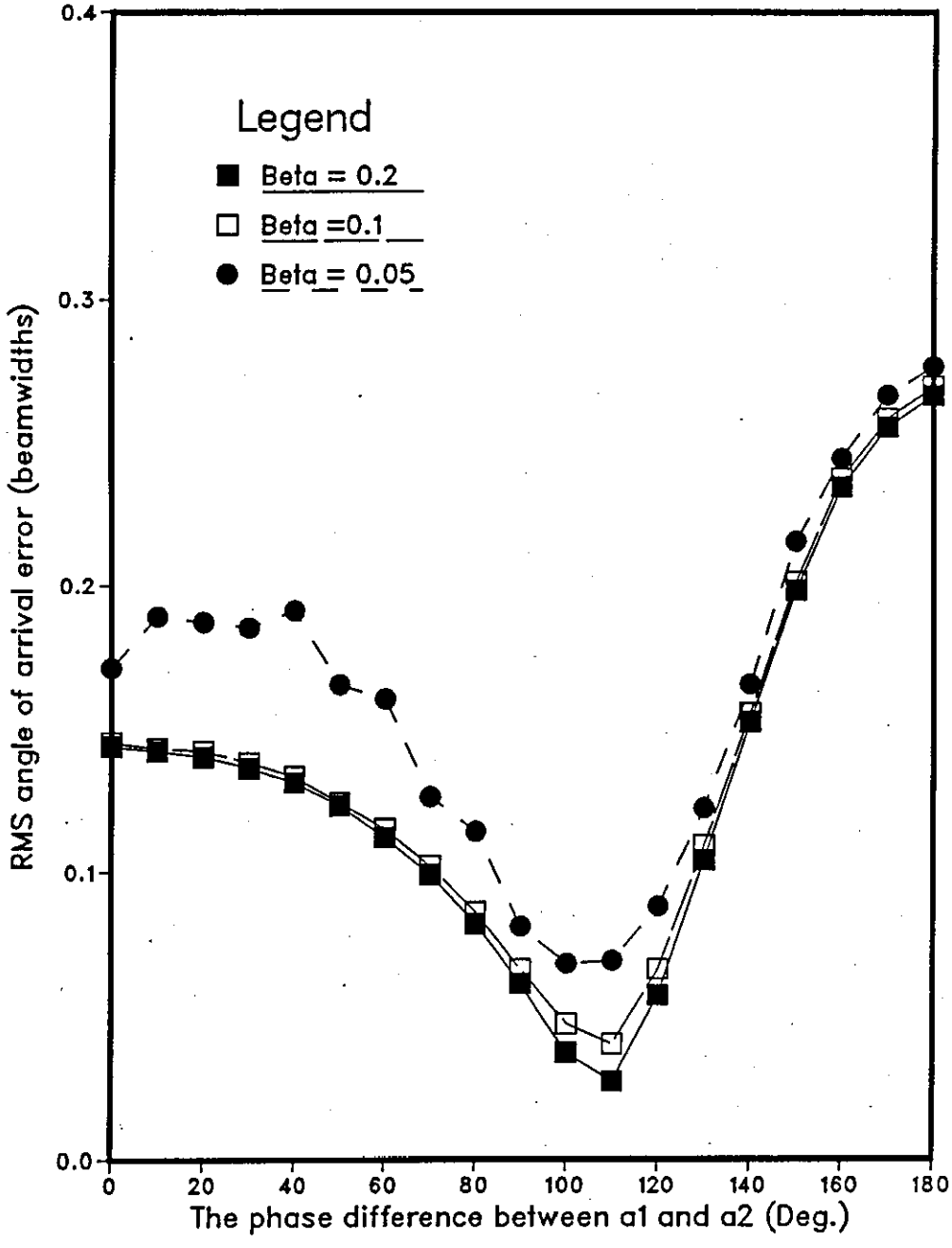

Figure 6-15 :RMS error of Phase monopulse as a function of phase difference between the two coherent signals for angle separation of 0.5 BW, S/N=30 dB, $\frac{\sigma_h}{\lambda}$=5, β_o=0.2, 0.1, 0.05.

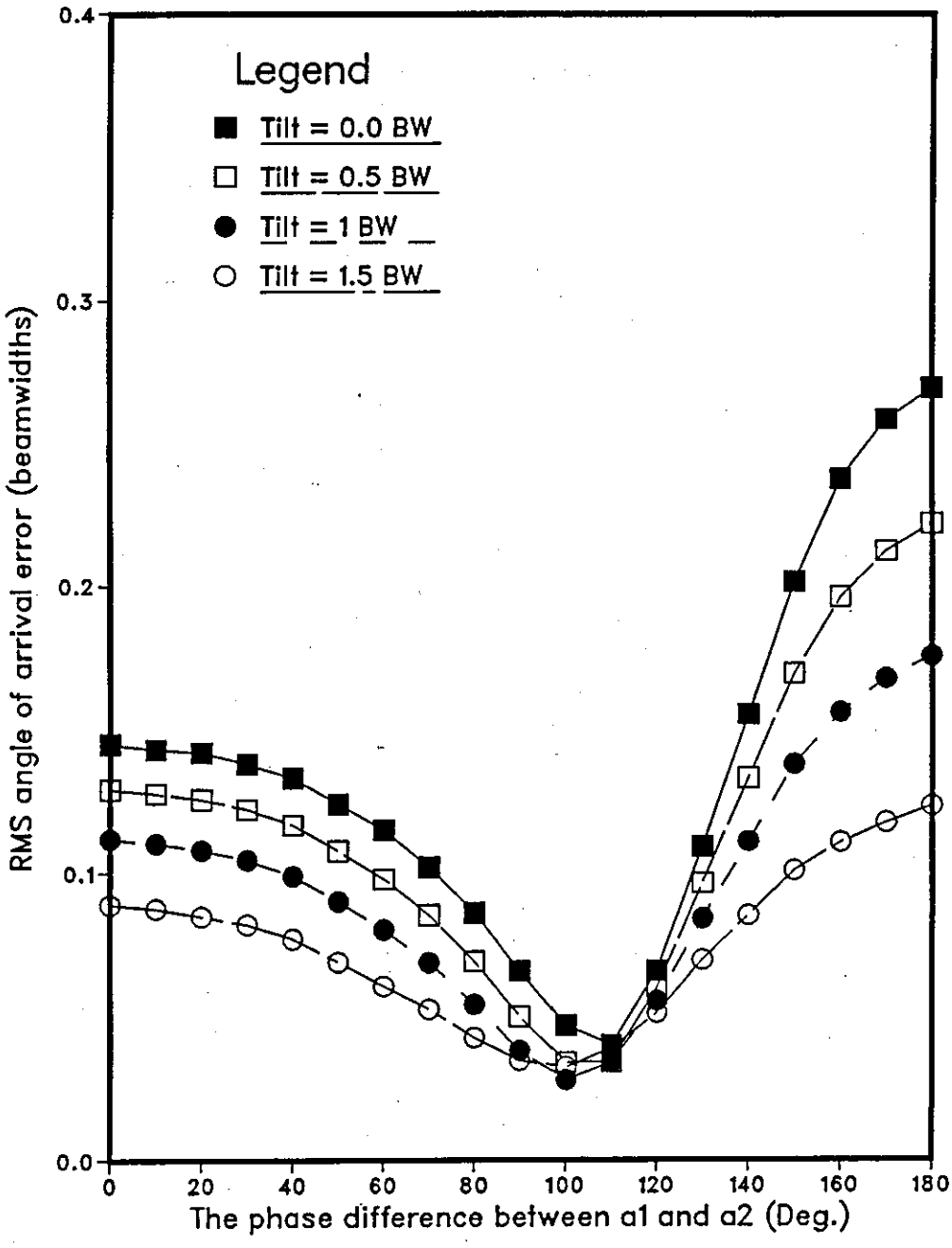

Figure 6-16 :RMS error of Phase monopulse as a function of phase difference between the two coherent signals for angle separation of 0.5 BW, S/N=30 dB, $\frac{\sigma_h}{\lambda}=5$, $\beta_0=0.1$, and different beam tilts.

multipath component and the foreground component of the diffuse multipath are reduced (through the antenna directivity). The chosen value of the tilt angle must be a compromise between the need to reduce the effect of the multipath and the required S/N to get a good accuracy. This depends on the angular spacing between the target and its image where small spacing makes the available accuracy less.

6-3.4 The maximum entropy method:

A histogram is used to demonstrate the performance of the three subapertures maximum entropy method (3SA-MEM) over a rough surface, where the angle of arrival is located by searching for the peaks in the power spectrum. The rms error of the direct angle of arrival (÷ beamwidth) is divided into 20 zones of accuracy from 0.0-0.05, 0.05-0.1,..... 0.9-0.95, >0.95 . The angle is changed in steps of 0.01° to ensure high accuracy in locating the spectral peaks over all values of Ψ. The three point filter coefficients are calculated according to Burg's method as in the previous chapter. The main concern in here is to show this method's ability to perform properly over a rough surface. Figure 6-17 shows the simulation results for a surface with $\sigma_h/\lambda=20$ and $\beta_o=0.1$ where the 3SA-MEM (solid line) performed perfectly well over all values of Ψ. The rms error of the direct angle estimation in beamwidths is better than 0.05, for 90 % of the times while 9 % of cases fall in the range 0.05-0.1. On the same figure a histogram for the same set of data is shown for the 3SA-MLE

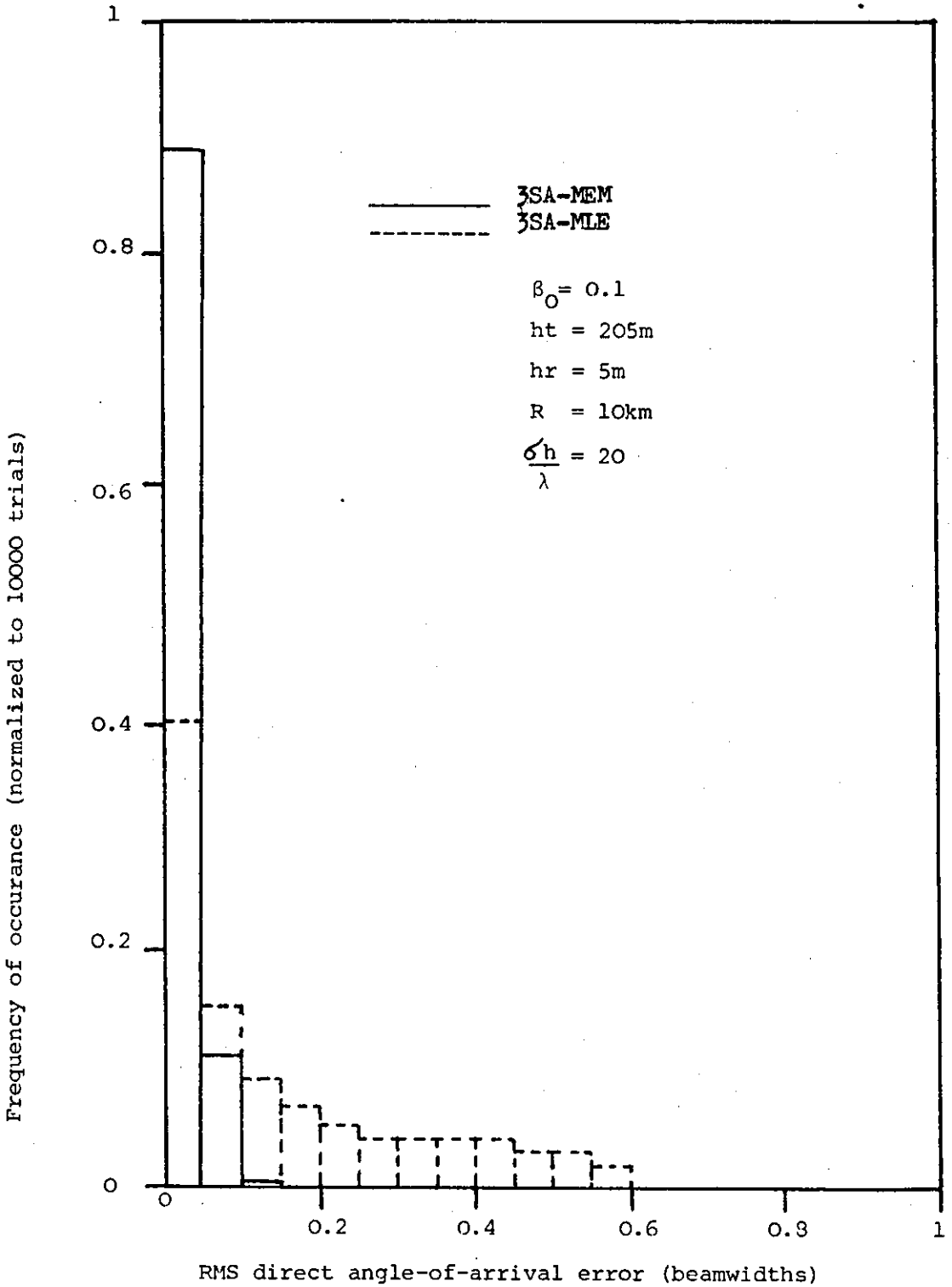

Figure 6-17: Histogram shows the performances of the 3SA-MEM and 3SA-MLE for Θ_B=0.0, Θ_D=0.25 BW, S/N-30 dB, β_o=0.1, and σ_h/λ=20 for all values of phase differenc (Ψ).

(dashed line), where its accuracy is seen to be much less than that for the 3SA-MEM over all values of Ψ. One concludes that the performance of the 3SA-MEM is much better than that of the 3SA-MLE over a rough surface when ρ_s is very small. The main reason for this accuracy is that in this case the input signal will be dominated by a strong directly reflected signal with only very weak coherent multipath plus widely distributed diffuse reflection. These diffuse reflection scatterers will generate poles well inside the unit circle resulting in weak peaks, while the direct signal will generate poles close to the unit circle creating very sharp peaks. Additionally, a histogram of simulation results for a surface with $\sigma_h/\lambda=5$ has been obtained. It shows that the 3SA-MEM works much better than the 3SA-MLE for Ψ close to quadrature and worse when Ψ is far from quadrature. Table 6-2 shows frequency results for this case at different values of Ψ for both methods and figure 6-18 shows its histogram for $\Psi=0^\circ$, 90°, 180° only. Figures 6-19 and 6-20 show the power spectrum for the rough surface case ($\sigma_h/\lambda=20$, $\beta_o=0.1$) where the first shows three spectra for $\Psi=0.0^\circ$, 90°, 180° while the second shows three spectra for $\Psi=180^\circ$ and three different sets of noise, where the peak deviation caused by the noise is obvious.

Thus, in general, one concludes from the above discussion that the phase monopulse is the best for estimating the angle of arrival of a low-flying target over a rough surface. Also, the performance of the maximum entropy over a rough surface is very accurate, but slightly less than

Table 6-2 :Histogram simulation results for the rms angle of arrival error per beamwidths, frequency of occurance out of 1000 trials for each value of Ψ, for medium surface with $\sigma_h/\lambda=5$, $\beta_o=0.1$.

Phase difference (degrees)	Frequency of occurances for the shown rms error bands.					
	0.00-0.05		0.05-0.10		0.10-0.15	
	MLE	MEM	MLE	MEM	MLE	MEM
0.0	119	0.0	132	40	223	626
45.0	290	32	243	274	142	541
90.0	425	701	249	219	142	39
135.0	280	18	253	149	175	487
180.0	43	0.0	64	0.0	92	13

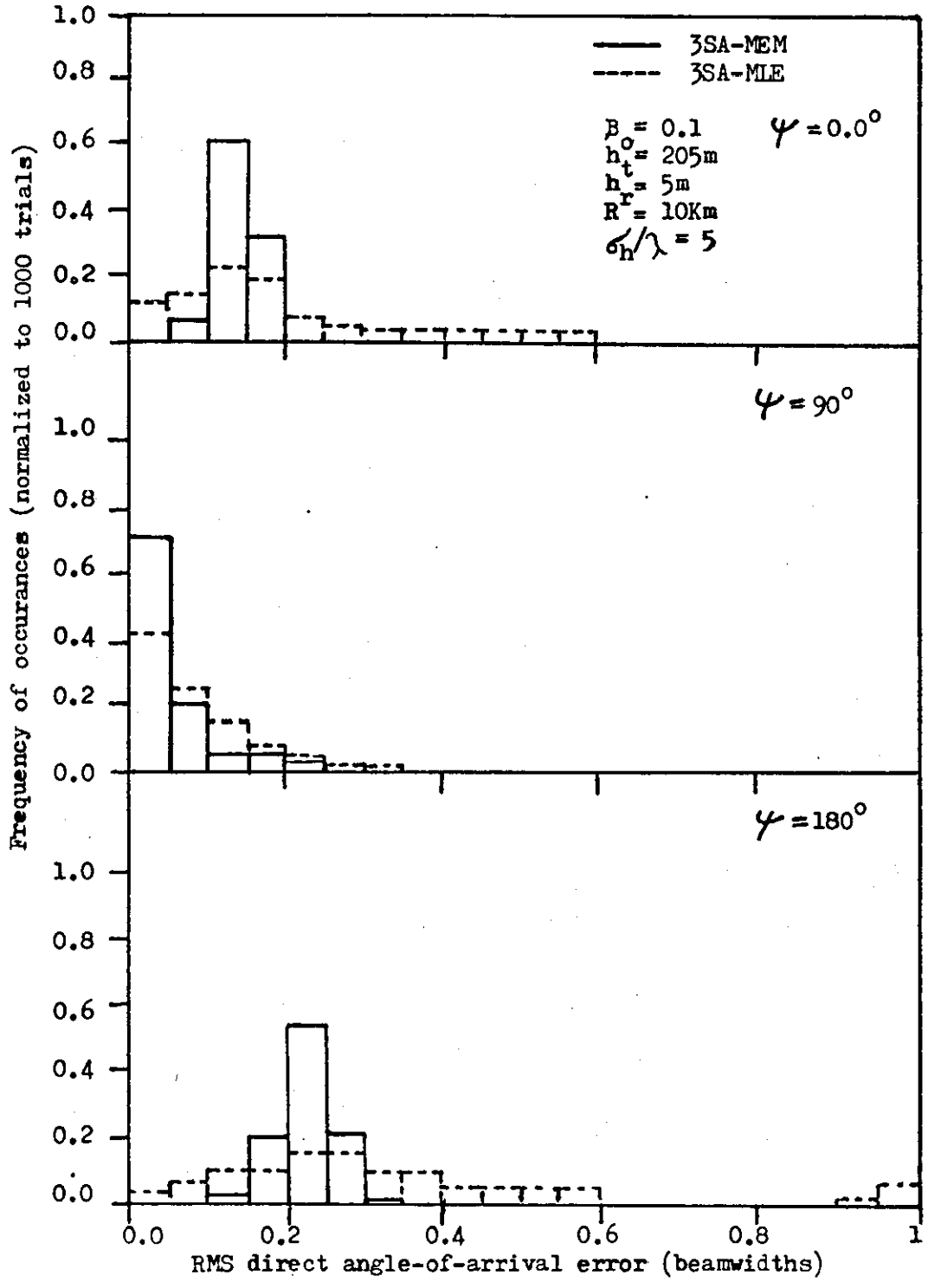

Figure 6-18: Histogram shows the performance of the 3SA-MEM and 3SA-MLE for θ_B=0.0, θ_D=0.25 BW, S/N-30 dB, β_o=0.1, and σ_h/λ=5 at ψ =0.0°, 90°, 180°.

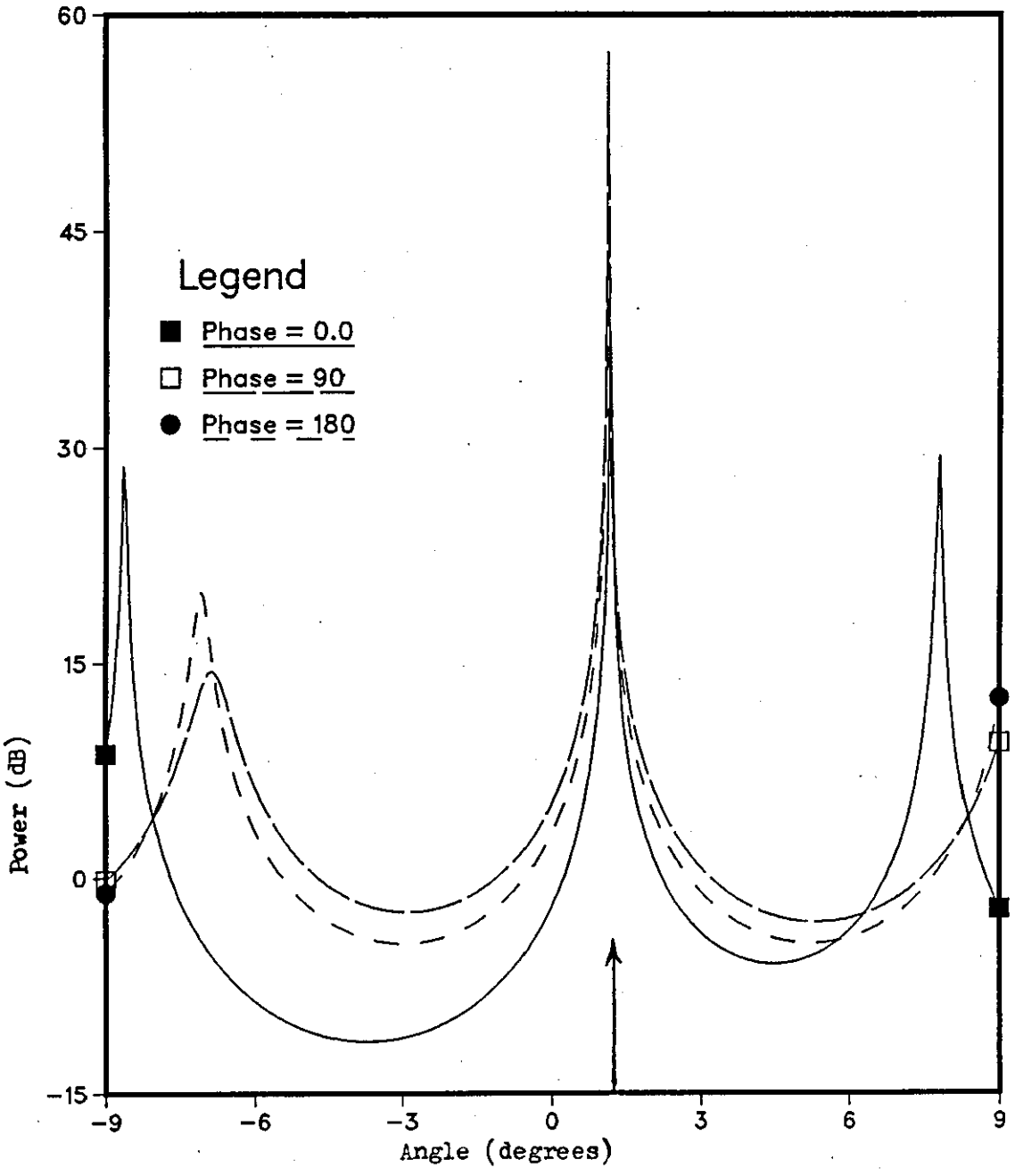

Figure 6-19:The MEM power spectrum for a target flying low over a surface wwith β_o=0.1, σ_h/λ=20, S/N-30 dB, θ_t= 0.25 BW, θ_r=-0.25 BW and different values of phase difference.

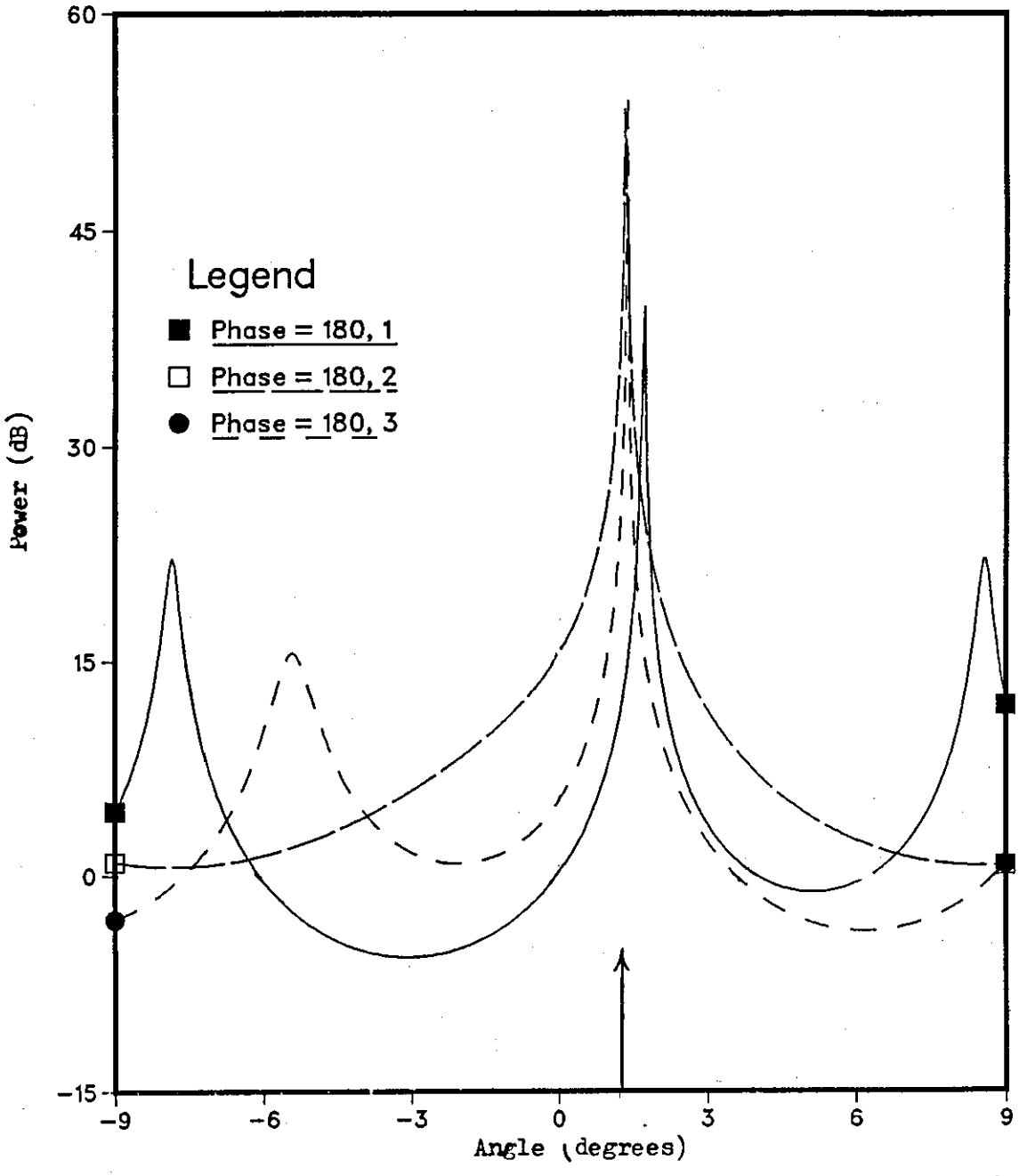

Figure 6-20:The MEM power spectrum for a low-flying target over a surface with β_o=0.1, σ_h/λ=20, S/N=30 dB, θ_t=0.25 BW, θ_r=-0.25 BW φ=180°, and three different snapshots.

that of the phase monopulse. A big degredation in the performance of the 3SA-MLE and 3SA-TRM is shown over a rough surface, even so, they offer the best angle estimate over a smooth surface case.

Chapter 7

Conclusions and Recommendations for Further Work

The thesis has addressed the tracking problem of a low-flying target in multipath environment, with emphasis on coherent multipath effects. The multipath phenomenon and its modelling for smooth and rough surfaces are discussed, and simulation results are obtained for surfaces with different roughness parameters. An investigation of the best known closed-form solution so far, the maximum likelihood estimator which uses a linear array divided equally into three subapertures (3SA-MLE), is carried out. A new trigonometric solution, using the same three subapertures arrangement above (3SA-TRM), to solve the coherent multipath problem,or equivalently two closely spaced targets, is derived and demonstrated by simulation results. A comparison study between the above two algorithms (3SA-MLE, 3SA-TRM) has been carried out too. The snag with both of them is that the good performance is only obtainable for sources which are close to phase quadrature at the array centre and the performance deteriorates rapidly if the relative source phase approaches 0.0° or 180°. Three

techniques are developed to handle this situation in both algorithms. They all depend on dividing the array into four equal subapertures and using them in two set of three, one at each end of the array. The reason for this is that if the two received signals are in-phase or anti-phase at the centre of one of the sets they cannot be so phased at the centre of the other if the sources bearings are different and one or other of the sets will give an acceptable performance. The techniques are different only in the method each one uses to determine the set which has the best chance of solving for the sources. The first technique is based on estimating the phase difference between the two signals at the array centre (chap.3, sec.3-3). The second is only applicable for the symmetric target-image case and based on the fact that when the two signals are in phase opposition at the array centre the overall signal amplitude at the central subaperture is very small in comparison with that of the other subapertures on its sides (especially when the amplitudes of the two received signals are close enough) and vice-versa. The third (explained in detail in chap.4 as a part of new algorithm) is based on measuring the imaginary part of the sum (or the real part of the difference) of the outputs from the two subapertures on both sides of the array divided by the output from the subaperture in the middle. Also, a new combined three and four subaperture techniques (3&4SA-TRM), using the same principles of best set determination explained above, are derived and demonstrated by simulation. Additionally, the performances of the maximum entropy method (MEM) and the

phase-comparison monopulse radar (i.e. the interferometer radar) are tested for the specular multipath problem by using three and two subaperture arrangements of a linear array respectively. The off-axis performance of the phase-comparison monopulse radar is also tested.

The performances of the above four methods are tested and compared for surfaces with different roughness parameters, i.e. when specular and diffuse reflections components exist together.

7-1 Conclusions

As a result of this research, the following conclusions on the tracking problem of a low-flying target can be drawn:

1. The accuracy of the 3SA-MLE and 3SA-TRM are quite comparable when the two received signals are fully coherent (smooth surface case) for both symmetric and nonsymmetric target-image cases.

2. The 3SA-TRM has some advantages over the 3SA-MLE in respect of being easier to implement in a hardware system and being faster in performance, where it only involves finding the arccosine of an angle from a look-up table instead of the quadratic equation solution of the 3SA-MLE.

3. The four subaperture techniques, based on the third method above and introduced in chapter 4 (Sec. 4-2.3), are much

better than the phase estimation based techniques introduced in chapter 3 (Sec. 3-3), in terms of being both faster in processing and cheaper for hardware implementation by allowing the best aperture sub-set to be chosen right from the start, before the bearing estimation process begins.

4. The amplitude comparison based four-subapertures technique to improve the performance of the symmetric cases of the 3SA-TRM and 3SA-MLE when the two received signals are in phase opposition is very efficient in terms of saving times and implementation costs.

5. The composite three and four subaperture techniques i.e. 3&4SA-TRM and 3&4SA-MLE, introduced in chapter 4 (Sec. 4-2.4) are superior to the ones in step 3 and step 4 above in terms of offering higher accuracy when the two coherent signals are far from being in-phase or anti-phase (just anti-phase for the symmetric solution). In general, more complicated combining (subgrouping) and sampling networks are needed.

6. The MEM and the phase-comparison monopulse are very inaccurate when solving the coherent multipath problem unless the specularly reflected signal is very weak in comparison with the direct one, or the two signals are in phase quadrature for the MEM.

7. The phase-comparison monopulse seems to offer the best elevation angle estimation when the underlying surface is rough (specular reflection coefficient is less than 0.1), followed by the maximum entropy method (Burg's method). The performance of the 3SA-MLE is erroneous, while the 3SA-TRM offers the worst performance. For the moderate surface case the available accuracy varies according to the surface roughness parameters, target-radar geometry, and the algorithm in use.

7-2 Recommendations for further work

As with many research problems, new questions always arise during the course of reseach. The following is a list of suggestions for future work which would enhance the understanding of this subject.

1. The effect of mismatch between the subapertures of the array on the performance accuracy of the 3SA-MLE and 3SA-TRM needs to be investigated. In practice, this problem can occur due to many reasons, such as corrosion, dust, connection faults ...etc.

2. This thesis has only considered the case of estimating the angle on the basis of one snapshot (one pulse). However, multiple pulse integration can be used to improve S/N in general and to reduce the effect of the diffuse multipath problem in particular. The integration time, i.e. the

number of pulses to be integrated, depends on the pulse repetition frequency, and the period of time for which changes in the target parameters can be considered to be negligable.

3. A more detailed understanding of the 3SA-MLE and 3SA-TRM methods will be obtained through a hardware implementation and evaluation of their performances in a real environment.

APPENDIX G

This appendix includes the three papers published during the course of this study.

Trigonometric high-resolution method to resolve two close targets

. Taha, MSc
E. Hudson, PhD, MIEE

dexing terms: Radar and radionavigation, Antennas (arrays)

Abstract: Three-subaperture methods for estimating the elevation angles of two targets within the 3 dB beamwidth for the main aperture of a linear array are discussed and applied to the case of a radar target in the presence of multipath over a smooth surface. Simulation results and comparison with the three-subaperture maximum-likelihood estimator by Cantrell *et al.* are presented. A four-subaperture technique to solve the in-phase and antiphase signal cases is suggested.

Introduction

he difficulty of tracking a low-flying target over a ooth surface (like the sea surface) arises from estimatg the elevation angle in the presence of coherent multith. This problem has attracted the attention of many searchers in the field of radar because of its importance -6]. The simplest solution so far is given by Cantrell *et* [2] and Gordon [3], who derived a formula for the aximum-likelihood angle estimator (MLE) which volves the solution of a quartic equation for the nonmmetric case and a quadratic equation for the symetric case (the target and its image located mmetrically about the centre of the aperture pattern in e elevation plane).

In this paper we present a new method which has a nilar performance to the MLE in general and is simpler practical implementation. The emphasis will be on mparing the performance of this method with the aximum-likelihood estimator [2] and showing its vantages. A solution is suggested to solve the in-phase d antiphase signal cases.

Formulation of three-subaperture method

sume we have a linear array of equally spaced ($\lambda/2$) ments and uniform amplitude weights for all elements. dividing this array into three equal subarrays, the n pattern of each subarray (subaperture) can be proximated by the following equation from Reference

$$G(\theta - \theta_p) \simeq (d/\lambda)\{[\sin(\pi du/\lambda)]/[\pi du/\lambda]\} \quad (1)$$

er 5534F (E15), first received 17th September 1986 and in revised n 18th May 1987

authors are with the Department of Electronic & Electrical Engining, University of Technology, Loughborough, Leics. LE11 3TU, ted Kingdom

where d is the subaperture spacing, λ is the wavelength, $u = \sin\theta - \sin\theta_p$ and θ_p is the pointing angle.

Now assume that the subapertures' signal are S_1, S_2 and S_3 as shown in Fig. 1. The elevation angles of arrival

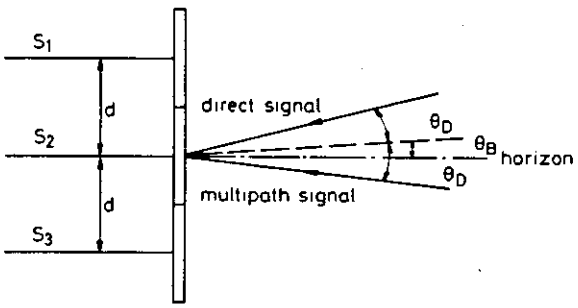

Fig. 1 *Three-subaperture antenna geometry*

for the target and its coherent multipath are θ_1 and θ_2, which can be represented by the bisecting angle θ_B and the angular distance from the bisector θ_D as follows:

$$\theta_1 = \theta_B + \theta_D \quad (2)$$

$$\theta_2 = \theta_B - \theta_D \quad (3)$$

From now on θ_1 and θ_2 will be used instead of $\sin\theta_1$ and $\sin\theta_2$, respectively, for the small angle assumption. Thus

$$S_1 = a_1 G_1 e^{jw\theta_1} + a_2 G_2 e^{jw\theta_2} + n_1 \quad (4)$$

$$S_2 = a_1 G_1 + a_2 G_2 + n_2 \quad (5)$$

$$S_3 = a_1 G_1 e^{-jw\theta_1} + a_2 G_2 e^{-jw\theta_2} + n_3 \quad (6)$$

where $w = 2\pi d/\lambda$, $G_1 = G(\theta_1 - \theta_p)$, $G_2 = G(\theta_2 - \theta_p)$, and $a_1 = A_1 e^{j\phi_1}$ is the complex amplitude of the direct signal; $a_2 = A_2 e^{j\phi_2}$ is the complex amplitude of the multipath signal; and n_1, n_2 and n_3 are complex Gaussian noises with zero mean and σ^2 variance for the real and imaginary parts individually.

The noise terms will now be neglected and a solution for θ_B and θ_D found. Taking the sum of eqns. 4 and 6 and dividing the results by eqn. 5 gives

$$\frac{S_1 + S_3}{S_2} = 2[a_1 G_1 \cos(w\theta_1) + a_2 G_2 \cos(w\theta_2)]/[a_1 G_1 + a_2 G_2] \quad (7)$$

$$= 2\cos(w\theta_B)\cos(w\theta_D) - 2\sin(w\theta_B)\sin(w\theta_D) \times \left[\frac{a_1 G_1 - a_2 G_2}{a_1 G_1 + a_2 G_2}\right] \quad (8)$$

Then, subtracting eqn. 6 from eqn. 4 and dividing by eqn. 5 gives the following:

$$\frac{S_1 - S_3}{S_2} = j2[a_1 G_1 \sin(w\theta_1) + a_2 G_2 \sin(w\theta_2)]/[a_1 G_1 + a_2 G_2] \quad (9)$$

$$= j2\left\{\sin(w\theta_B)\cos(w\theta_D) + \cos(w\theta_B)\sin(w\theta_D) \times \left[\frac{a_1 G_1 - a_2 G_2}{a_1 G_1 + a_2 G_2}\right]\right\} \quad (10)$$

In eqns. 8 and 10 the final bracketed term is identical, and simplifies as follows:

$$L = \frac{a_1 G_1 - a_2 G_2}{a_1 G_1 + a_2 G_2} = \frac{1 - \frac{A_2 G_2}{A_1 G_1} e^{j(\phi_2 - \phi_1)}}{1 + \frac{A_2 G_2}{A_1 G_1} e^{j(\phi_2 - \phi_1)}} \quad (11)$$

Letting the phase difference $\phi = \phi_2 - \phi_1$ and $K = A_2 G_2 / A_1 G_1$ gives

$$L = \frac{(1 - K^2) - j2K \sin\phi}{1 + K^2 + 2K \cos\phi} \quad (12)$$

Now we substitute eqn. 12 into eqns. 8 and 10 and find the real and imaginary parts:

$$\frac{S_1 + S_3}{S_2} = 2\cos(w\theta_B)\cos(w\theta_D) - 2\sin(w\theta_B)\sin(w\theta_D) \times \left[\frac{(1 - K^2) - j2K\sin\phi}{1 + K^2 + 2K\cos\phi}\right] \quad (13)$$

$$\mathrm{Re}\left(\frac{S_1 + S_3}{S_2}\right) = 2\cos(w\theta_B)\cos(w\theta_D) - 2\sin(w\theta_B \sin(w\theta_D) \times \left[\frac{1 - K^2}{1 + K^2 + 2K\cos\phi}\right] \quad (14)$$

$$\mathrm{Im}\left(\frac{S_1 + S_3}{S_2}\right) = \frac{4K\sin\phi}{1 + K^2 + 2K\cos\phi} [\sin(w\theta_B)\sin(w\theta_D)] \quad (15)$$

$$\frac{S_1 - S_3}{S_2} = j2\left\{\sin(w\theta_B)\cos(w\theta_D) + \cos(w\theta_B) \times \sin(w\theta_D)\left[\frac{(1 - K^2) - j2K\sin\phi}{1 + K^2 + 2K\cos\phi}\right]\right\} \quad (16)$$

$$\mathrm{Re}\left(\frac{S_1 - S_3}{S_2}\right) = \frac{4K\sin\phi}{1 + K^2 + 2K\cos\phi} \times [\cos(w\theta_B)\sin(w\theta_D)] \quad (17)$$

$$\mathrm{Im}\left(\frac{S_1 - S_3}{S_2}\right) = 2\sin(w\theta_B)\cos(w\theta_D) + \frac{2(1 - K^2)}{1 + K^2 + 2K\cos\phi}[\cos(w\theta_B)\sin(w\theta_D)] \quad (18)$$

Carefully examining eqns. 15 and 17, it is seen that there is only one difference: in eqn. 15 we have $\sin(w\theta_B)$ instead of $\cos(w\theta_B)$ in eqn. 17. Dividing these two equations gives

$$\theta_B = \frac{1}{w}\tan^{-1}\left[\mathrm{Im}\left(\frac{S_1 + S_3}{S_2}\right) \Big/ \mathrm{Re}\left(\frac{S_1 - S_3}{S_2}\right)\right] \quad (19)$$

From eqn. 19 it can be seen that the calculation of θ_B is independent of the phase difference ϕ between the signal and its coherent multipath, except at $\phi = 0$ and $\phi = 180°$ (we obtain the solution $\theta_B = \tan^{-1}(0/0)$, which is undetermined).

Inspecting the second term of eqn. 14, it is seen to involve the multiplication of two sines for small angles (θ_B, θ_D) and the value $(1 - K^2)$, which is very small when the reflection coefficient of the surface is large. Therefore, its effect on the equation is very small and eqn. 14 can be approximated by

$$\mathrm{Re}\left(\frac{S_1 + S_3}{S_2}\right) \simeq 2\cos(w\theta_B)\cos(w\theta_D) \quad (20)$$

By substituting the value of θ_B from eqn. 19 into eqn. 20, the angle θ_D can be calculated and in turn θ_1 and θ_2, the angles of arrival in the elevation plane for the direct signal and its multipath, respectively:

$$\theta_D \simeq \frac{1}{w}\cos^{-1}\left[\mathrm{Re}\left(\frac{S_1 + S_3}{S_2}\right) \Big/ 2\cos(w\theta_B)\right] \quad (21)$$

When noise is present the solutions are perturbed, but if the signals can, as is normally the case, still be represented as the sum of two plane waves, then the preceding solution continues to give the best maximum-likelihood bearing estimates.

We now investigate the symmetric and nonsymmetric cases separately.

2.1 Symmetric case solution

In this case the target and its image are symmetrically located about the centre of the elevation antenna and θ_B is known (for broadside beam $\theta_B = 0$). To calculate θ_D, substitute the known value of θ_B into eqn. 21. When $\theta_B = 0$ (the beam is looking horizontally) then $\theta_1 = \theta_D$ and $\theta_2 = -\theta_D$, and from eqn. 21 we obtain

$$\theta_D = \frac{1}{w}\cos^{-1}\left[\mathrm{Re}\left(\frac{S_1 + S_3}{S_2}\right)\right] \quad (22)$$

2.2 Nonsymmetric case solution

In this case θ_B is not known *a priori* as in the symmetric case, and has to be estimated from eqn. 19. One can see that θ_B does not depend on the reflection coefficient of the surface except when $|\rho| = 0$, where the undetermined solution of (0/0) occurs. Also, θ_B does not theoretically depend on the phase difference between the two signals (no noise being added to the signals) except when the phase difference is either 0° or 180°, when the undetermined solution of (0/0) occurs again. In addition, the calculation of θ_D from eqn. 21 shows that θ_D depends on θ_B, and by looking at the second term of eqn. 14 one finds that θ_D depends on the reflection coefficient of the surface $|\rho|$ through K, and the estimate of θ_D becomes biased when $|\rho|$ becomes very small.

Now, to show the performance of this method in comparison to the results of Cantrell *et al.* [2], a simulation of the problem has been carried out according to the conditions in Section 3.

3 Simulation

All the simulations have been performed using three subapertures of seven elements each, the interelement

spacing being $\lambda/2$. Gaussian noise of zero mean and σ^2 variance was added to the signals, and 1000 trials were carried out to find the average errors in the angle estimation. The root-mean-square (RMS) error was calculated as follows:

$$\text{error1} = \theta_1 - \hat{\theta}_1$$

$$\text{error2} = \theta_2 - \hat{\theta}_2$$

RMS angle of arrival error

$$= \sqrt{\frac{\sum ((\text{error1})^2 + (\text{error2})^2)}{2 \times \text{number of trials}}}$$

where $\hat{\theta}_1$ and $\hat{\theta}_2$ are the estimated angles of arrival for the direct signal and its coherent multipath, respectively. The error has also been normalised to the 3 dB beamwidth of the array, calculated as follows [7]:

$$3 \text{ dB beamwidth} \simeq \frac{102}{N} \quad \text{degrees}$$

where N is the number of elements in the array (interelement spacing $= \lambda/2$).

The signal/noise (SNR) is defined as follows, from Reference 2:

$$SNR = 10 \log \left[\frac{3(G_1 A_1)^2}{2\sigma^2} \right] \quad \text{dB}$$

Simulation results for the symmetric and nonsymmetric cases are compared with those of Cantrell *et al.* [2] under the same conditions in Section 3.1.

3.1 Symmetric case simulation results

Fig. 2 shows the results for target elevation of $\theta_D = 0.2$ beamwidths and for phase differences from zero to 180° in steps of 22.5°. The signal/noise ratio is 30 dB, $|\rho| = 0.9$ and $\theta_B = 0$. Comparing this curve (solid line) with the one from Reference 2 (broken line) one can see that the performance is almost the same, with only a slight difference in accuracy when the phase difference between the two signals approaches 180°. Fig. 3 shows the low SNR performance of the method (algorithm) when $\theta_D = 0.5$ beamwidths, $\theta_B = 0$, $|\rho| = 0.9$ and SNR = 10 dB were taken. Comparing this curve (solid line) with the one from Reference 2, we see that when the SNR is small the performance of this algorithm is better. The high signal/noise ratio performance for both algorithms is essentially the same.

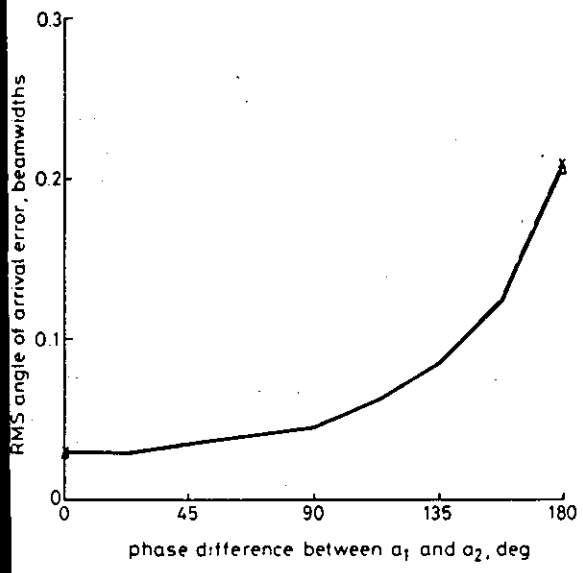

Fig. 2 *RMS error of symmetric case as a function of phase difference between signals*

$|\rho| = 0.9$, $\theta_B = 0$, $\theta_D = 0.2$ beamwidths and SNR = 30 dB
Solid line: new algorithm; broken line: Cantrell *et al.* method [2]

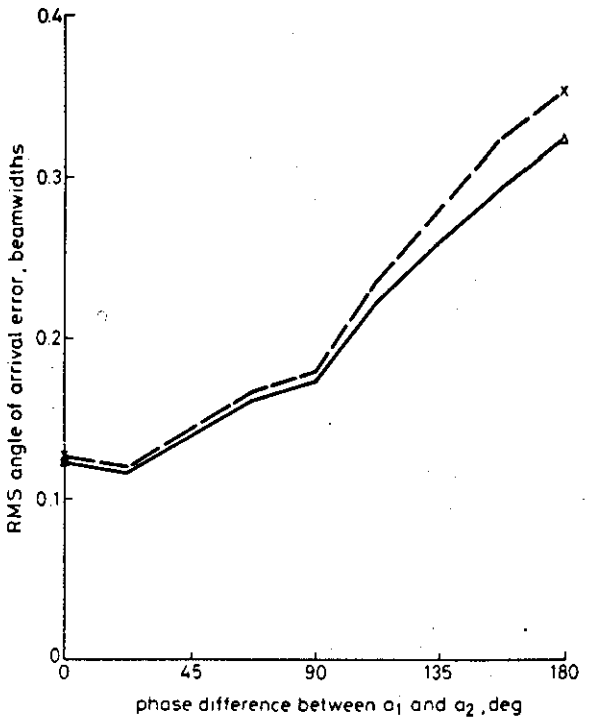

Fig. 3 *RMS error of symmetric case as a function of phase difference between signals*

$|\rho| = 0.9$, $\theta_B = 0$, $\theta_D = 0.5$ beamwidths and SNR = 10 dB
Solid line: new algorithm; broken line: Cantrell *et al.* method [2]

3.2 Nonsymmetric case simulation results

Fig. 4 shows the results for a target elevation of $\theta_D = 0.2$ beamwidths and for phase differences from zero to 180°

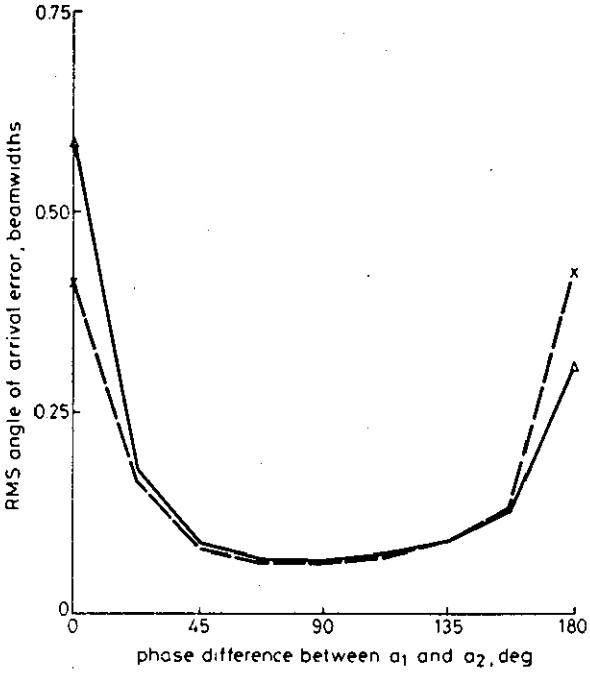

Fig. 4 *RMS error of nonsymmetric case as a function of phase difference between signals*

$|\rho| = 0.9$, $\theta_B = 0$, $\theta_D = 0.2$ beamwidths and SNR = 30 dB
Solid line: new algorithm; broken line = Cantrell *et al.* method [2]

in steps of 22.5°. The SNR is 30 dB, $\theta_B = 0$ and $|\rho| = 0.9$. Comparing this curve with the one from Cantrell *et al.* (MLE) [2] one can see that the performance is essentially the same except when the phase is close to 0°, where the MLE works better, or close to 180°, where this algorithm (method) works better. Fig. 5 shows the performance of

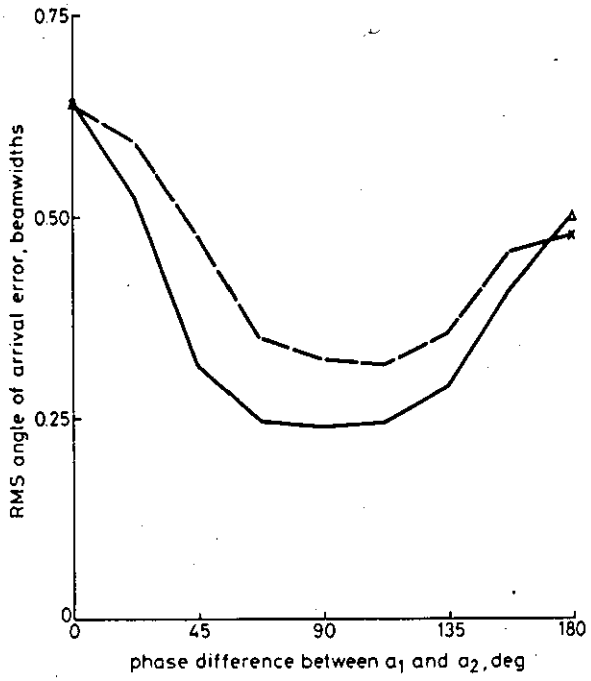

Fig. 5 *RMS error of nonsymmetric case as a function of phase difference between signals*

$|\rho| = 0.9$, $\theta_B = 0$, $\theta_D = 0.5$ beamwidths and SNR = 10 dB
Solid line: new algorithm; broken line: Cantrell *et al.* method [2]

this algorithm for a small signal/noise ratio (10 dB) for an elevation angle of $\theta_D = 0.5$ beamwidths, $\theta_B = 0$ and $|\rho| = 0.9$ as a function of the phase difference ϕ. Comparing this curve with the one from Cantrell *et al.* [2], we see it appears to have a smaller error. The high SNR performance for both algorithms is essentially the same. Fig. 6 shows the performance with small reflection coefficient $|\rho|$ at the surface. The value of the elevation angle of $\theta_D = 0.5$ beamwidths, $\theta_B = 0$, SNR = 30 dB and $|\rho| = 0.1$ were taken. Comparing this curve with the one from Reference 2 we see that this algorithm has smaller error. Fig. 7 shows the performance with relatively large bisecting angle. An elevation angle of $\theta_D = 0.5$ beamwidths, SNR = 30 dB, $|\rho| = 0.9$ and $\theta_B = 0.35$ beamwidths were taken. Comparing with the (MLE) performance of Reference 2, we see that the MLE fails when $\theta_B = 0.35$ beamwidths, where this algorithm still works with very good accuracy. Further studies did show that this algorithm will continue to work until one of the received signals reaches the subaperature beam pattern at a point below the 3 dB point, while the MLE algorithm works with very good accuracy until $\theta_B = 0.3$ beamwidths of the main aperture.

An imaginary angle (i.e. when $\theta_1 = \theta_2$) occurs when the value of θ_D in eqn. 21 is forced to zero, and would arise when the value of

$$\left[\mathrm{Re}\left(\frac{S_1 + S_3}{S_2}\right) \Big/ 2\cos(w\theta_B)\right]$$

is greater than one, basically because of bad estimation of the value of θ_B when $\phi \simeq 0°$ or 180°. Computer simulations have been carried out using the same data set on this method and the MLE in Reference 2. Table 1 shows the frequency of occurence of the imaginary angle (Im (angle)) and $|\rho| > 1$ for $\theta_B = 0$, $\theta_D = 0.5$ beamwidths, $|\rho| = 0.9$ and SNR = 30 dB; $|\rho|$ is calculated by replacing the estimated values of θ_1 and θ_2 in two of the input

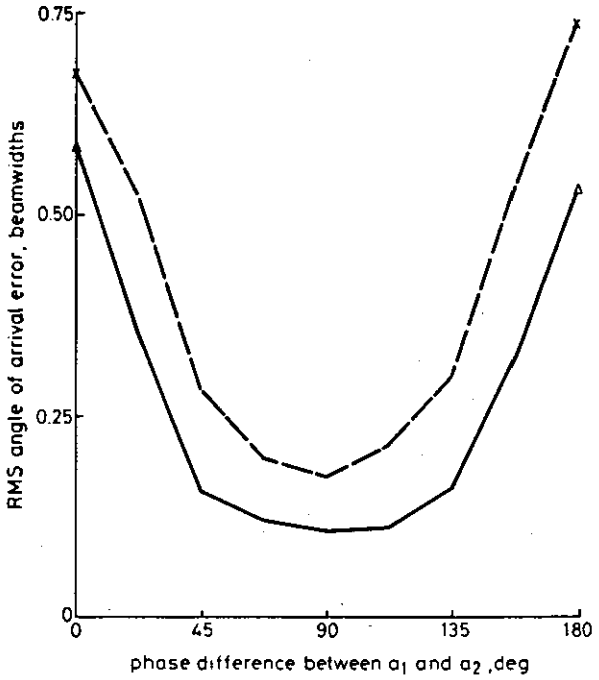

Fig. 6 *RMS error of nonsymmetric case as a function of phase difference between signals*

$|\rho| = 0.1$, $\theta_B = 0$, $\theta_D = 0.5$ beamwidths and SNR = 30 dB
Solid line: new algorithm; broken line: Cantrell *et al.* method [2]

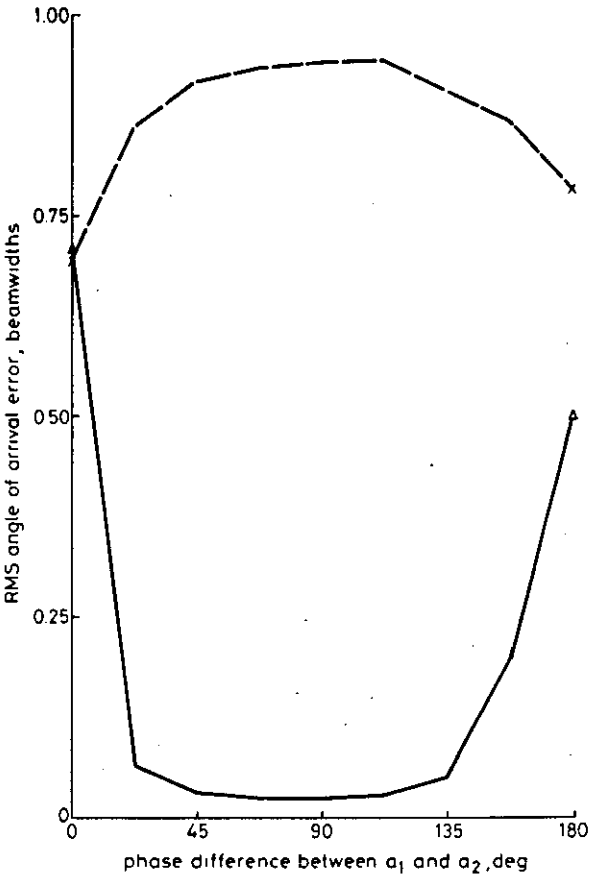

Fig. 7 *RMS error of nonsymmetric case as a function of phase difference between signals*

$|\rho| = 0.9$, $\theta_B = 0.35$ beamwidths, $\theta_D = 0.5$ beamwidths and SNR = 30 dB
Solid line: new algorithm; broken line: Cantrell *et al.* method [2]

Table 1: Frequency of occurrence in 1000 trials for $\theta_s = 0$, $\theta_D = 0.5$ beamwidths and SNR = 30 dB

Phase difference, deg	New method		Cantrell *et al.*, MLE [2]	
	Im (angle)	$\lvert\rho\rvert > 1$	Im (angle)	$\lvert\rho\rvert > 1$
0	399	123	0	492
22.5	0	255	0	255
45	0	59	0	59
67.5	0	10	0	10
90	0	0	0	0
112.5	0	1	0	1
135	0	1	0	1
157.5	0	12	0	12
180	144	16	402	57

equations (eqns. 4 and 5). The significance of showing the number of times $|\rho| > 1$ is to indicate the accuracy increase due to the information that $|\rho| < 1$, used by Gordon [3] to improve the MLE performance at $\phi = 0°$.

From Table 1 it can be concluded that an imaginary angle occurs frequently in the new method at $\phi = 0°$, while for the MLE it does not occur at all. However, its occurence at $\phi = 180°$ is much smaller than that of the MLE. This would explain the better performance of the new method in comparison with the MLE at $\phi = 180°$, which is shown in Fig. 4. The imaginary angle never occurs at $\phi = 0°$ for the MLE, although this does not mean that the estimated angle value is correct. The improved MLE by Gordon [3] actually shows better performance than both methods discussed above when $\phi = 0°$.

For the symmetric case, the imaginary angle occurs when the value of θ_D in eqn. 22 is forced to zero, and would arise when the value of $[\mathrm{Re}\,((S_1 + S_3)/S_2)$ is greater than one, often due to small SNR at $\phi = 180°$.

Simulation results on the same set of data show that the imaginary angle occurs 107 times out of 1000 trials at $\phi = 180°$ for the new method, in comparison with 203 times for the MLE, but never occurs for other ϕ values in either method. The number of times that $|\rho| > 1$ is the same for both methods: about 3.3%.

4 In-phase and antiphase signals

When the signal and its coherent multipath are in phase ($\phi = 0$) or antiphase ($\phi = 180°$) at the centre of the array, the accuracy in estimating the elevation angle is poor in the asymmetric method, so it is very useful to be able to decide if the two signals are actually in-phase or antiphase to detect a gross error in estimating the angle. A simple technique can be used from eqn. 17 by looking at the value of the real part of $(S_1 - S_3)/S_2$. This value approaches zero whenever the phase difference ϕ is close to zero or 180° (the same can be seen from eqn. 15). One solution to this problem is to use a four-subaperature technique (three adjacent subaperatures at a time) so that, when the phase is zero or 180° at the centre of the first three subaperature group, it will not be so at the other three. This technique will be discussed in a separate paper.

5 Discussion

A simple three-subaperture method to solve a coherent multipath resolution problem is presented. Its accuracy is comparable to that of Cantrell *et al.* [2], who applied the maximum-likelihood angle estimator (MLE) to the same three subapertures. The method has comparable performance and appears to show some advantages over the MLE [2] in respect of being easier to implement in a hardware system and being faster in performance, where it involves finding the $(\mathrm{cosine})^{-1}$ of an angle from a look-up table instead of the quadratic equation solution in Reference 2.

A four-subaperture technique is suggested to solve the in-phase and antiphase signal cases.

6 References

1 SHARMAN, S.M.: 'Complex indicated angles applied to unresolved radar targets and multipath', *IEEE Trans.*, 1971, **AES-7**, pp. 160–170

2 CANTRELL, B.H., GORDON, W.B., and TRUNK, G.V.: 'Maximum likelihood elevation angle estimates of radar targets using subapertures', *ibid.*, 1981, **AES-17**, pp. 213–221

3 GORDON, W.B.: 'Improved three subapertures method for elevation angle estimation', *ibid.*, 1983, **AES-19**, pp. 114–122

4 HAYKIN, S., and KESLER, J.: 'Adaptive canceller for elevation angle estimation in the presence of multipath', *IEE Proc. F, Commun., Radar & Signal Process.*, 1983, **130**, (4), pp. 303–308; also in CLARKE, J. (Ed.): 'Advances in radar techniques' (Peter Peregrinus, IEE Electromagnetic Waves Series no. 20, 1985), pp. 161–166

5 PEEBLES, P.Z.: 'Radar performance with multipath using the complex angle', *IEEE Trans.*, 1971, **AES-7**, pp. 171–178

6 WHITE, W.D.: 'Low angle radar tracking in the presence of multipath', *ibid.*, 1974, **AES-10**, pp. 815–852

7 SKOLNIK, M.: 'Introduction to radar systems' (McGraw-Hill, 1980, 2nd edn.), Chap. 8

Radar-87 Int. Conference
London 19-21 Oct. 1987

EFFECT OF SURFACE ROUGHNESS ON HIGH RESOLUTION ELEVATION ANGLE ESTIMATE IN MULTIPATH

A. Taha and J.E. Hudson

Dept. Electronic and Electrical Eng. University of Loughborough, U.K.

Much of the past work on improved radar algorithms for low flying targers has focused on the case of a simple specular multipath reflection from a nominally smooth, flat surface. However, in practice, diffuse multipath reflection as well as specular reflection exist and one must consider both when estimating the performance of any algorithm. So far, the maximum likelihood estimator by Cantrell et al. (1) is the best known algorithm for solving the coherent multipath problem in radar. However, a new interest in using the autoregressive/maximum entrophy method (AR/MEM) is shown in literature (2).

In this paper, input data from an equally spaced linear array, divided into three equal subapertures, is used to test the performance of the MLE and the AR/MEM over various rough surface environments. The diffuse reflection model by Barton (3) is used in these simulations and it is shown that the performance accuracy of the MLE decreases both as the surface roughness increases and when the surface rms slopes decreases. For a given radar-target geometry, the narrower the beamwidth of the aperture the better is the accuracy. The performance of the AR/MEM is shown to be much more accurate than the MLE over a rough surface for all values of phase difference between the direct signal and its coherent multipath. The performance of the AR/MEM over a medium surface is better than the MLE when the two coherent signals are close to phase quadrature and worse otherwise.

References

1. Cantrell B.H., Gordon W.B., Trunk G.V., 1981, IEEE Trans., AES-17, PP. 213-221.

2. Evans J.E., 1979, IEEE Trans., AES-15, PP. 891-895

3. Barton D.K., 1974, IEEE Proc., 62, PP.687-704

EFFECT OF SURFACE ROUGHNESS ON HIGH RESOLUTION ELEVATION ANGLE ESTIMATE IN MULTIPATH

A. Taha and J.E. Hudson

Dept. Electronic and Electrical Engineering, University of Loughborough, U.K.

INTRODUCTION

Much of the past work (1)-(5) on improved radar algorithms for low-flying targets has focused on the case of a single specular reflection from a nominally smooth, flat reflecting surface. However in practice, when the reflected signal from a low-flying target propagates over the surface (sea or land) towards a low sited radar, the field incident of the receiving array is composed of a free space component and a component due to the reflection and diffraction from the surface. The latter consists of a coherent part (specular multipath) and noncoherent part (diffuse multipath). Barton (6), (7) developed a detailed model which describes the diffused multipath power distribution in the four radar cordinates for a low-flying target and it shows that most of the diffuse power from the homogeneous, Gaussian wave-height distributed surface, will reach the receiving array from the region within a glistening area. This diffused power distribution is a complicated function of the wave length (λ), elevation angle (θ_t), rms surface height (σ_h), rms surface slope (β_ϕ), and the radar target geometry. Also, the value of β_ϕ is a complicated function of the wind speed and direction etc.

Cantrell et al. (1) have discussed a three subaperture maximum likelihood estimator (MLE) using a linear array to solve the coherent multipath problem for both symmetric (when the direction of the direct and the specular-multipath signals are symmetrically located about the centre of the array elevation pattern) and nonsymmetric cases. Gordon (2) improved the performance of this algorithm when the two coherent signals are in phase agreement by introducing new constraint related to the fact that the absolute value of the specular reflection is less than one.

Also, there has been a controversy in the literature between White (10) and Evans (9), (11) with regard to the utility of the maximum entropy method (MEM) in the radar multipath environment. Evans showed results from field tests to prove that the method works well, while White dismisses the idea of using it in radar and in the presence of specular multipath in particular.

In this paper the performance of the MLE and MEM are tested in the presence of diffuse and specular reflection environments. Barton's (6), (7) diffused power model is calculated for different surface slopes and roughness and used in simulation. The results show, that the accuracy of the MLE depends on three factors: first, the slopes of the surface, where higher slope values means less degredation of the angle estimation accuracy, second, the surface roughness, where the higher the roughness the worst the accuracy, and third, the beamwidth of the array, where the narrower the beam the better the angle estimation accuracy.

The paper is organized as follows: the next section presents the diffuse power model for a rough surface used in simulations with comments on the effects of some of the factors involved, followed by discussion of the MLE and MEM, and, finally simulation results and conclusions.

Diffuse Reflection Model For Low-flying Target Over Rough Surface

Various experimental and theoretical investigations of rough surfaces have proved that the scattered field can be represented by the sum of two components, a specular component and a diffuse component. The characteristics of the specular reflection component are the same as that from a smooth surface with two restrictions: first, the amplitude of the reflection coefficient is smaller than that for a smooth surface, and second, the reflection coefficient fluctuates. The specular scattering coefficient for a rough surface is given (13) by

$$\rho_s = \exp\left[-\left(\frac{4\pi\sigma_h \sin(\theta_t)}{\lambda}\right)^2\right] \qquad (1)$$

where, σ_h is the rms deviation of the surface height. The power from the target which reaches the rough surface and is not reflected specularly or absorbed, will be scattered in other directions. Part of this power will reach the receiving array of the radar from an extended "glistening surface" region extending from the neighborhood of the target to the neighborhood of the radar. This is called the diffuse reflection component and the basic scattering elements are small facets which overlie the main large-scale pattern or swell. The rms slope of the small surface facets is given by $\beta_\phi = 2\sigma_h/dc$, where d_c is the correlation distance (14). Common practice among engineers is to express the rms value of the diffuse scattering coefficient (ρ_d) as a simple function of ($\sigma_h \sin(\theta_t)/\lambda$) as shown in figure 1, which was drawn from practical data (13). Barton (7) showed however that figure 1 is not accurate, and the values of ρ_d shown are smaller than the real values because the antenna used in collecting the experimental data was very directive and part of the scattering surface was not accounted for.

For low-flying targets, the grazing angle (ψ) is small in comparison with rms surface slopes (β_ϕ). For such cases the theory by Spizzichino (14) predicted that the diffused power will be concentrated near the ends of the glistening surface and a simple diffuse reflection model has sometimes been used, where the total diffuse power is divided between a foreground component (just in front of the radar antenna) and a horizon component (just in front of and below the target). The values of ρ_d and ρ_s are taken, according to the surface roughness and grazing angle from figure 1. For long range targets the horizon component for this simple model may lie behind the horizon range with a curved earth so this simple model cannot accurately represent the diffuse scattering. In order to get a more accurate model for low-flying target, and to adapt the glistening surface theory to partialy rough surfaces, Barton (6) introduced a roughness factor (F_a) which would account for removal of reflected diffuse power by specular reflection at either grazing angle ψ_1 or ψ_2 as shown in figure 2. In this model, the target is considered to be an active transmitter, with non-directional antenna, illuminating the radar and the surrounding rough surface (ρ_s=0). For low-flying conditions assume that $\theta_t < \beta_\phi << 1$, $h_r < h_t << R$, $r_1 \approx x_1$, $r_2 \approx x_2$. The curve of the glistening surface boundary is then given by the following, from (6)

$$Y = \mp \frac{x_1 x_2}{x_1+x_2} \left(\frac{h_r}{x_1} + \frac{h_t}{x_2}\right) \sqrt{\beta_\theta^2 - \frac{1}{4}\left(\frac{h_r}{x_1} - \frac{h_t}{x_2}\right)^2} \qquad (2)$$

and it extends from $x_a = h_r/2\beta_\theta$ to $x_b = R - h_r/2\beta_\theta$. The total diffuse power is given by:

$$P_d^2 = \frac{1}{4\pi\beta_\theta^2} \int_{x_a}^{x_b} \frac{R^2 Y\, dx}{(R-x)^2 x^2} \qquad (3)$$

and $F_d^2 = F_{d1}\ F_{d2} = ((1-p_{s1}^2)(1-p_{s2}^2))^{\frac{1}{2}}$ (4)

and P_{s1} and P_{s2} are the specular reflection coefficients for the paths associated with r_1 and r_2 respectively.

When the roughness factor F_d is included in equation (3), the new value of P_d is given by:

$$P_d^2 = \frac{R^2}{2\pi\beta_\theta^2} \int_{x_a}^{x_b} \frac{F_d^2\, Y\, dx}{(R-x)^2 x^2} \qquad (5)$$

This roughness factor accounts for the specular power at low-elevation angle and the horizon effect for a round earth. No shadowing or masking correction factor is required.

A simulation has been carried out to calculate the diffused power at a receiving radar antenna of 5m height, created by the reflection from a target at 205m height and 10km range. The diffused power is calculated for a series of rectangular strips of 500m extent in x from x_o (the specular reflection point) to the end of the glistening surface at x_b. Figure 3-a shows the range distribution of the discrete diffuse power samples (Δp_{di}^2) with $\beta_\theta = 0.1$ for a completely rough surface while figure 3-b shows the effect of the surface roughness ($\sigma_h/\lambda = 5, 20$). The elevation angle associated with each diffuse scatterer is calculated from the centre of the strip concerned, relative to the horizon ($\theta_{td} = -\arctan(x/h_r)$). The total foreground diffuse power component (the component from x_a to x_o) which is not shown in figure 3-a is calculated to be 0.41 divided into three scatterers at angles -0.2, -0.1, -0.04 radians and their associated power is 0.2, 0.13, and 0.08 respectively. This procedure is repeated to calculate the range distribution and the surface roughness effect for the above target-radar geometry for $\beta_\theta = 0.2, 0.05$ (the curves are not shown here). In general, by reducing the value of β_θ, the glistening surface becomes narrower and its limits move farther from the terminal and vis-versa, leading to bigger values of p_d. The results from these simulation will be used to study the performance of the algorithms in relation to different surface conditions specified by β_θ and σ_h/λ.

The maximum Likelihood Estimator

The maximum likelihood estimator using all the individual array elements (5) is very costly due to the large number of receivers required and the difficulty in getting a closed-form solution. Therefore we use a simple, closed-form, three subapertures MLE found by Cantrell et al. (1) in which a linear array of equally spaced elements (elements spacing is $\lambda/2$) is divided equally into three subapertures as shown in figure 2. The output of each subaperture in the presence of specular and diffuse multipath over a rough surface is given by the following

$$S_n = A_1 \exp\left[(n-2)\mu_1\right] + A_2 \exp\left[(n-2)\mu_2\right] + \sum_{j=1}^{N_s} A(J) \exp\left[(n-2)\mu(J)\right] + N_n \qquad (6)$$

The first term in the above equation represents the n^{th} direct signal, the second represents the n^{th} specular multipath, the third represents the sum of the n^{th} diffuse reflection scatterers, and the last one, N_n, represents the n^{th} complex Gaussian noise with zero mean and variance σ^2. Also $A_1 = a_1 G_1$, $A_2 = a_2 G_2$, $A(J) = a(J) G(J)$, $\mu_1 = i2\pi d \sin(\theta_t)/\lambda$, $\mu_2 = i2\pi d \sin(\theta_r)/\lambda$, $\mu(j) = i2\pi d \sin(\theta(J))/\lambda$, and ($G_1$, G_2, $G(J)$) are the subaperture pattern responses in the 1,2 and J angular directions which can be approximated by the following:

$$G(\theta-\theta_p) = \frac{d}{\lambda} \frac{\sin \pi d(\sin\theta - \sin\theta_p)/\lambda}{\pi d(\sin\theta - \sin\theta_p)/\lambda} \qquad (7)$$

where θ_p is the pointing direction of the beam. The values a_1 and a_2 are the complex amplitudes of the direct and specular multipath signals respectively; a(J) is the complex amplitude of the J^{th} diffuse reflection scatterer and $\theta(J)$ its associated grazing angle with respect to the horizon; N_s is the number of the diffuse scatterers assumed within the glistening surface.

The three-subaperture MLE estimator is obtained by choosing the parameters $A_1, A_2, \theta_t, \theta_r$ to minimize the cost function L (1), (2).

$$L = \sum_{n=1}^{3} \left| S_n - A_1 \exp\left[(n-2)\mu_1\right] - A_2 \exp\left[(n-2)\mu_2\right] \right|^2 \qquad (8)$$

By replacing the sines of θ_t and θ_r by their small value approximations and letting $\theta_t = \theta_B + \theta_D$ $\theta_r = \theta_B - \theta_D$ where, θ_B and θ_D are the bisecting angle and the angular distance from the bisector respectively, then L is given by (1).

$$L = \left| S_1 - \mu_B(\mu_D + \mu_D^*) S_2 + \mu_B^2 S_3 \right|^2 / \left| (2 + |\mu_D + \mu_D^*|^2) \right| \qquad (9)$$

where, $\mu_B = i2\pi d\theta_B/\lambda$, $\mu_D = i2\pi d\theta_D/\lambda$. So, minimizing L with respect to μ_B and μ_D subject to the constraints $\mu_B \mu_B^* = 1$ and $\mu_D \mu_D^* = 1$, the values of μ_B and μ_D can be related to μ_1 and μ_2, and the angle of arrival can be estimated. Detailed discussion for the symmetric and nonsymmetric cases is presented in (1). This algorithm is the best known one for solving the coherent multipath problem in radar. Here, the performance of this algorithm will be tested in the presence of specular and diffuse multipath from different surfaces, and the results will be shown and discussed in the simulation section.

The Maximum Entropy Method

In general, time-series spectral estimation techniques are only applicable when the underlying process is stationary. If it is not, such as in the case of a low-flying target over a smooth surface where the direct and reflected signals are coherent, then the resulting wavenumber spectral estimate will not be meaningful unless the two signals are in phase quadrature (10), (15). Because this is not always the case one can conclude that these sorts of algorithms are inappropriate for solving such problems. However, Evans (9), (11) shows results from a field test on the performance of the Autoregressive maximum entropy method (AR/MEM), where it worked very well over an irregular surface, but he did not discuss the scale of irregularities. The filter coefficients were calculated according to the Burg method (8). When the surface is rough, the specular reflection coefficent of the reflected field is a function of σ_h/λ as we have seen earlier. For example, when σ_h/λ changes from 5 to 20, the value of p_s changes from 0.42 to 9×10^{-6} for an elevation angle of 0.021 radians. In such environments, the overall received signal at the array consists mainly from a strong direct field and a relatively very small (depending on σ_t an σ_h/λ) coherent multipath plus widely distributed diffuse scatterers within the glistening surface. As long as the diffuse reflection scatterers have different phases and amplitudes, using the subaperture techniques would

reduce their effect and increase the signal to noise-and-diffuse-power-interference ratio at the output of each subaperture. Hudson (12) shows that if the sources are known to lie close to the broadside of the array, then using subaperture techniques are very efficient numerically but cannot resolve the grating lobes ambiguities if they occur. The AR/MEM for wavenumber spectral estimation can be given by the following equation (8), (16).

$$P(\Theta)=\sigma_w^2/\left|1-\sum_{m=1}^{M} a_m z^{-m}\right|^2 \qquad (10)$$

where, $Z=\exp(i2\pi d \sin(\Theta)/\lambda)$, a_m is the m^{th} coefficient of the all-pole filter, M is the number of poles, σ_w^2 is the variance of the white noise input, and d is the subaperture spacing (or interelement spacing in the case that individual elements are considered). Using the three-subapertures technique mentioned in the previous section, the above equation can be written as follows for two poles-filter case.

$$P(\Theta) = \sigma_w^2/\left|1-a_1 z^{-1} - a_2 z^{-2}\right|^2 \qquad (11)$$

There are two practical methods for locating the peak position of the spectrum. The first is by calculating the roots of the characteristic equation of the preduction error filter (the quadratic equation in the denominator of the above equation), then finding the angles of the roots which correspond to each incident plane waves. The other method is to find the wavenumber spectrum and search for its peaks. In the simulation performed for this study of a low-flying target over a rough surface, the second method was chosen, since it is more likely to be used in a practical system.

Simulation Results

In this section we present the results of a computer simulation used to study the performance of the MLE in different nonsymmetric multipath environments, and to compare it with the AR/MEM method over a rough surface. For the results presented here, we used a linear array of 21 elements equally spaced by a half wavelength. This array is equally divided into three subapertures of 7 elements, unless otherwise specified. The signal to noise ratio used is always 30dB, calculated for the direct signal only, as received by the main beam of the whole array. The bisecting angle (Θ_B) and the angular distance (Θ_D) are taken to be 0 and 0.25 BW (BW is the 3dB beamwidth of the whole array), unless otherwise stated. The noisy signal model used is the one shown in equation 6, where the number, and values, of the diffuse reflection scatterers' power and angular position are calculated according to the model discussed earlier and for the same radar-target geometry and strip length. The value of the specular reflection coefficient can easily be found for each surface roughness from equation 1. The phase difference between the direct and specularly reflected signals (ϕ) is taken in steps of 22.5° from 0° to 180°. The direct angle of arrival rms errors are averaged over 1000 trials for each value of ϕ and normalized to the 3dB beamwidth.

Figure 4, demonstrates the performance of the nonsymmetric case of the MLE (1) over a surface with $\beta_\varnothing$=0.1 and surface roughness parameter (σ_h/λ) of 0, 5, 20 (see figure 3-a,b). When σ_h/λ=20 the direct angle estimation accuracy is almost the same at all values of ϕ, showing large degredation in accuracy for all phases in comparison with the smooth surface (σ_h/λ=0, P_s=0.9), except at ϕ=0° or 180° where improvement occurs. Figure 7 shows a histogram for this case where the direct angle of arrival rms error normalised to the beamwidth is shown to be less than 0.1 for about 50% of the time. When σ_h/λ=5, the rough surface accuracy degrades at all values of ϕ in comparison with the smooth one, except at ϕ=0° where a little improvement occurs, as can be seen from the curves. Thus, in general, the MLE performance degrades as the surface roughness increases.

Figure 5, presents the nonsymmetric MLE performance of a medium surface roughness σ_h/λ=5 and three different values of $\beta_\varnothing$ ($\beta_\varnothing$=0.05, 0.1, 0.2). The direct angle estimation accuracy decreases as $\beta_\varnothing$ decreases over all values of ϕ, except at ϕ=180° where the opposite occurs and at ϕ=0°, where the accuracy is better for $\beta_\varnothing$=0.1 than for $\beta_\varnothing$=0.2. Figure 6, presents the effect of the aperture beamwidth used on the accuracy of the direct angle estimation over a rough surface with σ_h/λ=5, $\beta_\varnothing$=0.05. Here a linear array of 42 elements ($\lambda/2$ spacing), equally divided into three subapertures, is used in the simulation in order to reduce the BW by half (from 0.084 to 0.042 radians). One can see from the curves, that the narrower the beam the better the performance over all values of ϕ except at ϕ=180° where a little decreas in accuracy is shown. The average improvement in rms error at ϕ=90° is about 0.13 of a beamwidths which is very substantial. This improvement can be related to two facts: first the MLE works better at higher angular separation between the two coherent sources (the angular distance is 0.5BW instead of 0.25BW for the 21 element array), and the second, and more important, is that the main foreground component of the diffuse reflection is getting closer to the first null of the subaperture beam pattern, greatly reducing its effect. So to get the best performance, one must use the narrowest possible beam to exclude the effect of the main foreground component of the diffuse reflection. Another way to reduce the effect of this component is by tilting the beam up to create positive nonsymmetry in the target-image geometry.

A histogram is used to demonstrate the performance of the AR/MEM over a rough surface, where the angle of arrival is located by searching for the peaks in the spectrum. The rms error of the direct angle of arrival ($\div$ beamsidth) is divided into 20 zones of accuracy from 0.0-0.05, 0.05-0.1,...,0.9 - 0.95,>0.95. The beam is scanned in steps of 0.01° to ensure high accuracy in locating the spectral peaks over all values of ϕ. The filter coefficients are calculated according to Burg's method (8) after modification to operate on complex data from the three subapertures' outputs. For the smooth surface case, the performance of the AR/MEM as a function of ϕ has been well studied in the literature (9),(10),(11) and its advantages and disadvantages pointed out, so these are not going to be repeated here where the main concern is about its ability to perform properly over a rough surface. Figure 7 shows the simulation results for a surface with σ_h/λ=20, and $\beta_\varnothing$=0.1 where the AR/MEM (solid line) performed perfectly well over all values of ϕ. The rms error of the direct angle estimation in beamwidths is better than 0.05, for 90% of the time while 9% of cases fall in the range 0.05-0.1. On the same figure a histogram for the same set of data is shown for the MLE (dashed line), where its accuracy is seen to be much less than that for the AR/MEM over all values of ϕ. One concludes that the performance of the AR/MEM is much better than the MLE over rough surface when p_s is very small. The main reason for this accuracy is that in such case the input signal will be dominated by a strong directly related signal with only very weak coherent multipath plus widely distributed diffuse reflection. These diffuse reflection scatterers will generate poles well inside the unit circle resulting in weak peaks, while the direct signal will generate poles close to the unit circle creating very sharp peaks.

Additionally, a histogram of simulation results for a surface with σ_h/λ=5 has been obtained. It shows that the AR/MEM works much better than the MLE for ϕ close to quadrature and worse when ϕ is far from quadrature. Table 1 shows a histrogram results for this case at different values of ϕ for both AR/MEM and MLE.

TABLE 1. Histrogram simulation results for the rms angle of arrival error per beamwidths, frequency of occurance out of 1000 trials for each value of ϕ, for medium surface with $\sigma_h/\lambda=5$, $\beta_0=0.1$.

Phase difference (degrees)	Frequency of occurances for the shown rms error bands.					
	0.00-0.05		0.05-0.10		0.10-0.15	
	MLE	AR/MEM	MLE	AR/MEM	MLE	AR/MEM
0.00	119	0.0	132	40	223	626
45.0	290	32	243	274	142	541
90.0	425	701	249	219	142	39
135	280	18	253	149	175	487
180	43	0.0	64	0.0	92	13

Conclusion

The performance of the MLE and the AR/MEM in a rough surface environment is investigated according to the low-flying target diffuse reflection model described by Barton (6). The effect of surface roughness, rms slopes, and the aperture beamwidth is shown in detail. The lesson learned from this study is that the angle estimation performance of the MLE, for a given target-radar geometry, depends heavily on the surface roughness and rms slopes. In general, the estimation accuracy decreases as the surface roughness increases, and also when the rms slopes decreases with some exceptions for multipath phase=0° and 180°. It has found that the aperture beamwidth has a great effect in limiting the diffuse reflection effects and the narrower the beam the better. The use of the AR/MEM to locate a low-flying target over a rough surface is of great potential and its accuracy is superior to the MLE over the range of all possible phase differences when the surface roughness is high i.e. the value of ρ_s is very small, ρ_s=0.2 or less. Also, the AR/MEM performs much better than the MLE when ϕ is close to quadrature phase over a medium rough surface (i.e. ρ_s=0.42), but works badly when ϕ moves away from quadrature toward 0° or 180°.

References

1 Cantrell B.H., Gordon W.B., Trunk G.V., 1981, IEEE Trans., AES-17, pp. 213-221.

2 Gordon W.B., 1983, IEEE Trans, AES-19, pp. 114-122.

3 Taha A., Hudson J.E., 1986, IEE Electronics Letter, 22, pp. 1116-1117.

4 Taha A., Hudson J.E., "Trigonometric high resolution method to resolve two close targets," IEE Proc., part F, 1987, to be issued.

5 White W.D., 1974, IEEE Trans, AES-10, pp.835-852

6 Barton D.K., 1974, IEEE Proc., 62, pp.687-704

7 Barton D.K., 1977, IEE Radar-77 Conf., 155. pp. 308-312

8 Anderson N., 1974, Geophysics, 39, pp.69-72

9 Evans J.E., 1979, IEEE Trans., AES-15, pp.891-895

10 White W.D., 1979, IEEE Trans., AES-15, pp.895-899

11 Evans J.E., 1979, IEEE Trans., AES-15, pp.899-903

12 Hudson J.E., 1985, IEE ICAP 85, 248, pp.237-240

13 Barton D.K. & Ward R.H., Handbook of radar measurement, Prentice-Hall, Inc., 1969.

14 Beckmann P., Spizzichino A., The scattering of electromagnatic waves from rough surfaces, Pergamon Press, 1963.

15 Kay S.M., Marpel S.L., 1981, IEEE proc., 69, pp. 1380-1419.

16 Reilly J.P., 1981, McMaster University PhD Thesis.

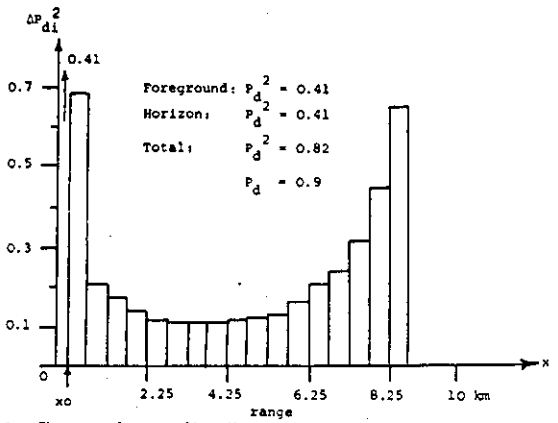

Fig.3-a: The ground range distribution of the scattered power for short-range target.

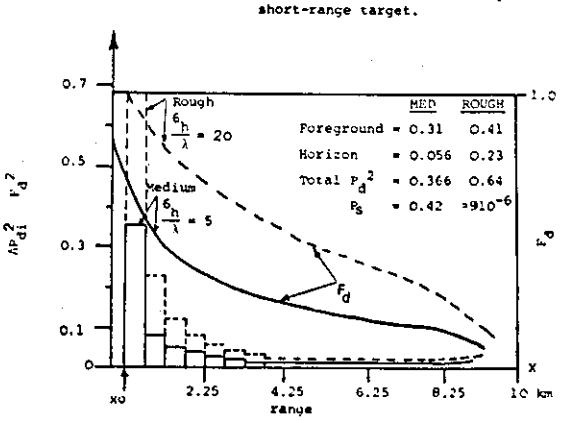

Fig.3-b: The effect of roughness factor on scattered power distribution for short-range target at β_o = 0.1, h_t= 205, h_r= 5m, R = 10km

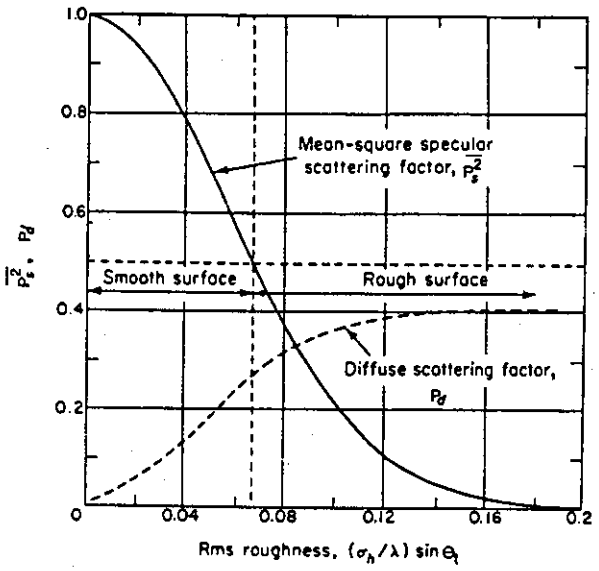

Figure 1 : Scattering factors vs roughness (after Beckmann and Spizzichino).

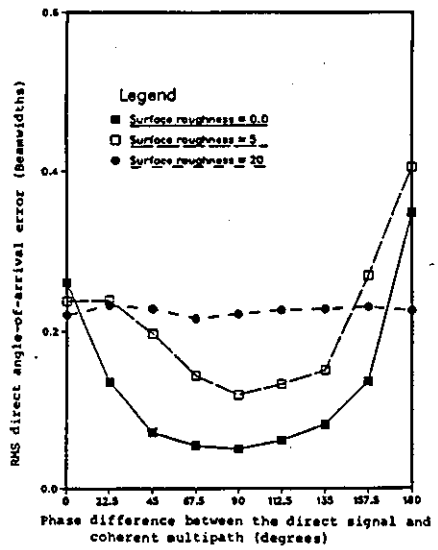

Fig.4: RMS error of nonsymmetric MLE estimate as a function of phase differences between signals for θ_B=0, θ_D=0.25BW, β_φ=0.1, S/N=30dB, and $\frac{\sigma_h}{\lambda}$ = 0.0,5,20 (when $\frac{\sigma_h}{\lambda}$ = 0, $|\rho_s|$= 0.9)

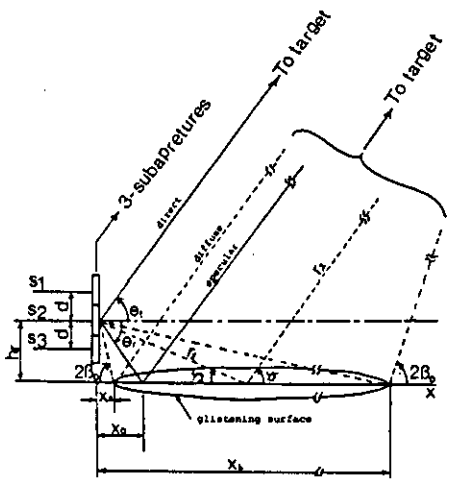

Figure 2. The radar target geometry over a rough surface where the dashed lines represent some of the diffuse reflection scatterers.

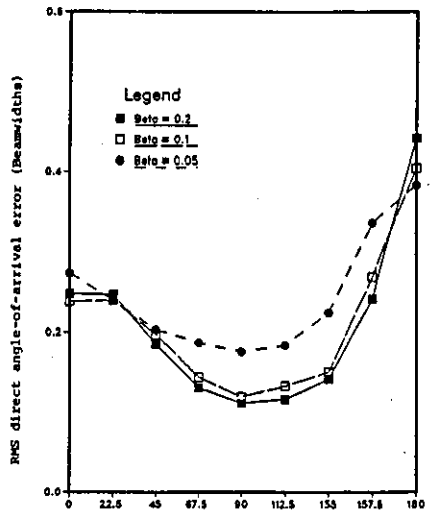

Figure 5 : RMS error of nonsymmetric MLE estimate as a function of phase difference between signals for θ_B=0, θ_D=0.25 BW, S/N=30 dB, σ_h/λ=5, and β_φ=0.05, 0.1, 0.2.

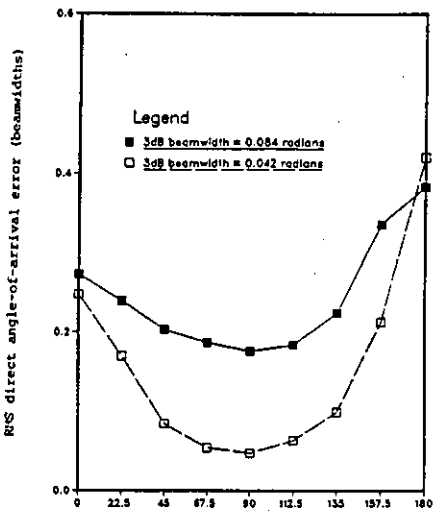

Figure 6: RMS error of nonsymmetric MLE estimate as a function of phase difference between signals for β_φ=0.05, S/N=30 dB σ_h/λ=5, θ_B=0, and θ_D=0.021 radians (beamwidth effect comparison).

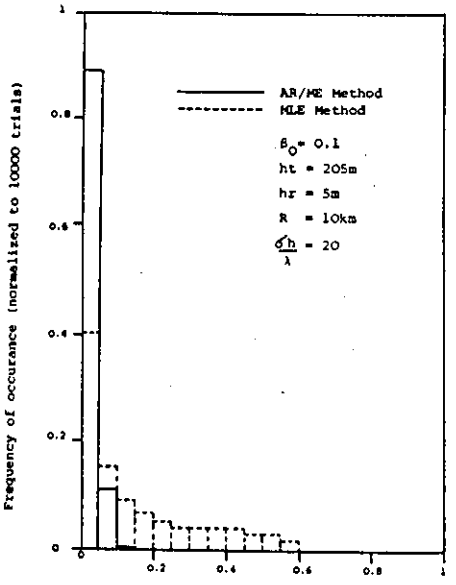

Figure 7. Histogram shows the performances of AR/MEM method and the MLE by Cantrel for θ_B=0, θ_D=0.25 beamwidths S/N=30 dB, β_φ=0.1 and surface roughness $\frac{\sigma h}{\lambda}$=20 for all phase differences.

SYMMETRIC TWO-TARGET MONOPULSE ANGLE ESTIMATOR

Indexing term: Radar

A simplified system for estimating the bearing difference of two symmetrical targets in a two-target monopulse radar is proposed. The technique requires only the envelope amplitudes of two RF signals to be measured, and the computation is very simple.

Introduction: Cantrell *et al.*[1] and Gordon[2] have discussed a three-subaperture monopulse antenna for estimating the directions of arrival of two coherent targets. In the special case of symmetric angles of arrival, relevant for low-angle tracking over the sea, they give a formula for the maximum-likelihood direction estimator which involves the solution of a quadratic equation. The purpose of this letter is to show that a simpler algebraic solution exists which, although not precisely maximum-likelihood, can be shown by simulation to have similar performance in spite of a much reduced work load and does not require phase-coherent digitisation of the element outputs.

Consider a three-subaperture uniformly spaced antenna with two signals symmetrically placed about broadside in the plane of interest. Neglecting the patterns of the subarrays (which can be included in the signals' amplitudes), the signals received at the three elements in a single data snapshot are:

$$s_1 = \alpha_1 e^{j\theta} + \rho\alpha_2 e^{-j\theta} + n_1$$

$$s_2 = \alpha_1 + \rho\alpha_2 + n_2$$

$$s_3 = \alpha_1 e^{-j\theta} + \rho\alpha_2 e^{j\theta} + n_3$$

where ρ is the reflection coefficient of the (smooth) sea surface. Suppose that the noises n_i are all zero; then these equations are trivially solved thus:

$$s_1 + s_3 = (\alpha_1 + \rho\alpha_2)\, 2\cos\theta$$

So

$$2\cos\theta = x = \frac{s_1 + s_3}{s_2}$$

In the presence of noise x can become complex-valued, and for simplicity it is proposed to use the modulus taking $\theta = \cos^{-1}(|x|/2)$ as an estimator for θ.

Simulation results: The estimation procedure has been simulated using a 21-element array divided into three subarrays of seven elements. Two sinusoidal signal target sources of separation 0·2 beamwidths (relating to the whole array) and $\rho = 0{\cdot}9$ were placed symmetrically about broadside and, with a beam SNR of 30 dB corresponding to element SNRs of 1000/21, 1000 samples of the field with random noise statistics were taken. Fig. 1 shows a graph of the RMS error of the estimated bearing of one target normalised by the 3 dB beamwidth for target phase differences in the range 0 to 180°. Errors for one target only are shown since $\theta_1 \equiv -\theta_2$ and errors are always equal.

Discussion: The estimator clearly gives identical results to the Cantrell symmetric system except for possibly one trial at 180° phase difference, and is therefore quite close to the Cramer-Rao bound. The hardware is simplified since coherent demodulators are not required; envelope amplitude detectors applied to $(s_1 + s_3)$ and s_2 are the only measurements. The computation load amounts to a division and a $\cos^{-1}$; the latter could be done rapidly by a look-up table. The variable θ is effectively the phase difference between adjacent subarrays, and the interval 0 to 90° will span one 3 dB width of the main aperture corresponding to target spacings of two 3 dB widths. The algorithm cannot estimate signal amplitudes except for the sum $\alpha_1 + \rho\alpha_2$ or even allocate the ρ coefficient to a particular target, but this is not of great importance in tracking applications.

A. TAHA
J. E. HUDSON

Department of Electronic & Electrical Engineering
University of Loughborough
Loughborough, Leics. LE11 3TU, United Kingdom

14th July 1986

References

1 CANTRELL, B. H., GORDON, W. B., and TRUNK, G. V.: 'Maximum likelihood elevation angle estimates of radar targets using subapertures', *IEEE Trans.*, 1981, **AES-17**, pp. 213–221
2 GORDON, W. B.: 'Improved three subaperture method for elevation angle estimation', *ibid.*, 1983, **AES-19**, pp. 114–122

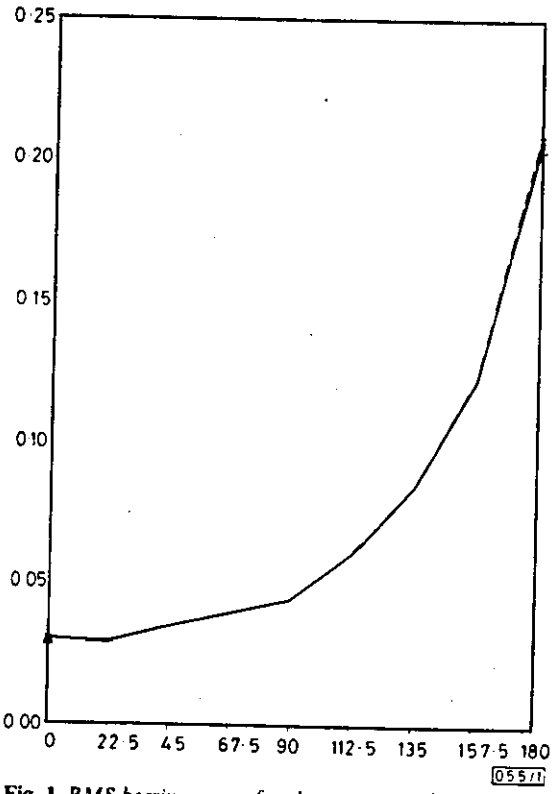

Fig. 1 *RMS bearing error of each target normalised by 3 dB beamwidth against relative target phases*

Solid line = new algorithm; broken line = Cantrell method

Refarances

1-1 Rhodes D.R., "Introduction to monopulse", Artech House Inc., 1958.

1-2 Skolnik M.I., "Introduction to radar systems", McGraw-Hill book company, second edition, 1980.

1-3 Schleher D.C.,"Introduction to electronic warfare", Artech House, Inc., 1986.

1-4 Dax P.R.,"Keep track of that low flying attack", Microwaves, Vol-15, april 1976.

1-5 Becker J.E. and Surean J.C., "Control of radar site environment by use of fences", IEEE Trans., AP-14, pp.768-773, 1964.

1-6 Guili D., "Polarization diversity in radars", IEEE Proc., Vol-74, pp.245-269, 1986.

1-7 Obe R.W., "The probability of detecting and tracking radar in clutter at low grazing angle", PhD. thesis, Loughborough University, U.K., 1982.

1-8 Sherman S.M., "The use of complex indicated angles in monopulse radar to locate unresolved targets", Proc. Natl. Electron conf., Vol-22,pp.243-248, 1966.

1-9 Sherman S.M., "Complex indicated angles applied to unresolved radar targets and multipath", IEEE Trans., AES-7, pp.160-170, 1971.

1-10 Peeples P.Z. and Goldman L. , "Radar performance with multipath using the complex angle", IEEE Trans., AES-7, pp. 171-178, 1971.

1-11 Symonds M.D. and Smith J.M., "Multi-frequency complex angle tracking of low-level targets", Radar Present and Future, IEE Conf. Publication No-105, pp.166-171, oct. 1973.

1-12 White W.D., "Low-angle radar tracking in the presence of multipath," IEEE Trans., AES-10, pp.835-852, 1974.

1-13 Nickel U., "Angular superresolution with phased array radar: a review of algorithms and operational constraints", IEE Proc., Vol-134, pp.53-59, 1987.

1-14 Kay S.M., Marple S.L., " Spectrum analysis-A modern perspective", IEEE Proc., Vol-69, pp.1380-1419, 1981.

1-15 Hudson J.E., "Adaptive array principles", Peter Peregrinus, 1982.

1-16 Clark J.,editor, "Advances in radar techniques", Peter Peregrinus, 1985.

1-17 Haykin S.,editor, " Array signal processing", Prentice-Hall, Eaglewood Cliffs, N.J., 1985

1-18 Childers D.G., editor, "Modern spectrum analysis", IEE Press, Inc., N.Y., 1978.

1-19 Monzingo R.A., Miller T.W., "Introduction to adaptive arrays", John Wiley & Sons, Inc., 1980.

1-20 Gabriel W.F., "Adaptive array - An introduction", IEEE Proc., Vol-64, pp.239-272, 1976.

1-21 Evans E.J., "Applicability of the angular power distribution to radar systems with coherent or incoherent interference" , IEEE Trans., AES-15, pp.899-903, 1979.

1-22 Greffiths J.W.R., "Adaptive array processing, Atutorial", IEE Proc., Vol-130, PP.3-10, 1983.

1-23 Mather J., "Least squars solutions in signal processing using singular value decomposition", RSRE memorandum, No.3864, 1986.

1-24 Gabriel W.F., " A high-resolution target-tracking concept using spectral estimation techniques", NRL Report-8797, May 1984.

1-25 Evans E.J., "Aperture sampling techniques for precision direction finding", IEEE Trans., AES-15, PP.891-895, 1979.

1-26 White W.D., "Angular spectra in radar applications", IEEE Trans., AES-15, pp.895-899, 1979.

1-27 Schmidt R.O, "Multiple emitter location and signal parametr estimation", IEEE Trans., AP-34, pp.276-280, 1986.

1-28 Gabriel W.F., "Spectral analysis and adaptive array superresolution techniques", IEEE Proc., Vol-68, PP.654-666, 1980.

1-29 Reilly J.P., Haykin S., "Maximum-likelihood receiver for low-angle tracking radar", IEE Proc., Vol-129, pp.331-340, 1982.

1-30 Haykin S., "Least squares adaptive antenna for angle of arrival estimation", IEEE Proc., Vol-72, pp.528-530, 1984.

1-31 Cantrell B.H., Gordon W.B., Trunk G.V., "Maximum likelihood elevation angle estimate of radar targets using sub-apertures", IEEE Trans., AES-17, pp.213-221, 1981.

1-32 Gordon W.B., "Improved three subaperture method for elevation angle estimation", IEEE Trans., AES-19, pp.114-122, 1983.

1-33 Reilly J.P., "Nonlinear array processing techniques with applications to correlated multipath", A thesis, McMaster University, Canada, 1981.

2-1 Rohan P., "Surveilance radar performance prediction", Peter Peregrinus Ltd, 1985.

2-2 Beckmann P., Spizzichino A., "The scattering of electromagnetic waves from rough surfaces", Pergamon Press, 1963.

2-3 Meeks M.L., "Radar propagation at low altitudes", Artech House Inc.,1982.

2-4 Long M.W., "Radar reflectivity of land and sea", Artech House Inc, 1983.

2-5 Barton K.D.,Ward R.H., "Handbook of radar measurement", Prentice-Hall, Inc., 1969.

2-6 Katz I,"Radar reflectivity of the ocean for circular polarization", IEEE Trans., AP-11, PP.451-453, 1963.

2-7 Katzin M.,"On the mechanism of radar sea clutter", IRE Proc., Vol-45, Jan., 1956.

2-8 Katzin M.,"Back scattering from the sea surface", IRE Conv. record V.3,Part 1, pp.72-77,1955.

2-9 Barton K.D., "Radar multipath theory and experemental data", IEEE International Conf., Radar-77,London,Oct., 1977.

2-10 Court G.W.G.,"Determination of the reflection coefficient of the sea, for radar-coverage calculation,by an optical analogy method", Am. Inst. Ph., pp.827-830, 1955.

2-11 McGarty P.T.,"Antenna performance in the presence oF diffuse multipath", IEEE Trans., AES-12, pp.42-54, 1976.

2-12 Beard I.C. & Katz I.,"Phenomenological vector model of microwave reflection from the ocean", IRE Trans. Antenna & Propagation, Vol-4, pp.162-167, April,1956.

2-13 Barton K.D.,"Low-angle radar tracking," IEEE Proc., Vol-62, pp.687-704, 1974

2-14 Mrstik V.A. & Smith G.P., "Multipath limitations on low-angle radar tracking", IEEE Trans. AES-14, 1978.

2-15 Twersky V.,"On the scattering and reflection of electromagnatic waves by rough surfaces", IRE Trans. Antenna And Propagation, Vol.5-7, pp.81-90, 1957.

2-16 Clarke J., "Advances in radar techniques", Peter Peregrinus Ltd, pp.246-249, 1985.

2-17 Beard C.I.,"Coherent and incoherent scattering of microwaves from the ocean", IRE Trans. Antenna & Propagation Vol-9, pp.470-483, Sept., 1961.

2-18 Skolnik M.I., "Introduction to radar systems", McGraw-Hill book company, second edition, 1980.

3-1 White W.D., "Low-angle radar tracking in the presence of multipath", IEEE Trans., AES-10, pp.835-852, 1974.

3-2 Cantrell B.H., Gordon W.B., Trunk G.V.,"Maximum likelihood elevation angle estimate of radar targets using sub-apertures", IEEE Trans., AES-17, pp. 213-221, 1981.

3-3 Gordon W.B.," Improved three subaperture method for elevation angle estimation", IEEE Trans., AES-19, pp. 114-122, 1983.

3-4 Skolnik M.I., "Introduction to radar systems", McGraw-Hill book company, second edition, 1980.

3-5 Hudson J.E., "Adaptive array principles", Peter Peregrinus, Stevenage, U.K., 1981.

3-6 Trunk G.V., Cantrell B.H., Gordon W.B., "Bounds on elevation error estimates of a target in multipath", IEEE Trans., AES-15, pp. 883-887, 1983.

3-7 Trunk G.V., Cantrell B.H., Gordon W.B., "Probability density of the maximum likelihood elevation estimate of radar targets", IEEE Trans., AES-15, pp. 288-290, 1979.

5-1 Childers D.G., Ed., "Modern spectrum analysis", IEEE Press, 1978.

5-2 Burg J.P.,"Maximum entropy spectral analysis", Proc. of the 37-th meeting of the society of exploration Geophysicists, 1967.

5-3 Lacoss R.T.,"Data adaptive spectral analysis methods", Geophysics, Vol-36, pp.661-675, 1971.

5-4 Haykin S., Ed., "Array signal processing", Prentice Hall Inc., 1985.

5-5 Monzingo R.A., Miller T.W., "Introduction to adaptive arrays", John Wiley & Sons, 1980.

5-6 Van de Bos A., " Alternative interpretation of the maximum entropy spectral analysis", IEEE Trans., IT-17, PP.493-494, July 1971.

5-7 Haykin S., Kesler S., "The complex form of the maximum entropy method for spectral estimation", IEE Proc., Vol-64, PP.822-823, May 1976.

5-8 Andersen N., "On the calculation of the filter coefficients for the maximum entropy spectral analysis", Geophysics, Vol.39, pp. 69-72, 1974.

5-9 Kay S.M., Marple S.L., "Spectrum analysis-A modern perspective", IEEE Proc., Vol.69, pp 1380-1419, 1981

5-10 McDonough R.N., "Maximum entropy spatial processing of array data", Geophysics, Vol.39, pp.843-851, 1974.

5-11 Kesler S., Haykin S.,"The maximum entropy method applied to the spectral analysis of radar clutter", IEEE Trans., IT-24, pp.264-272, 1978.

5-12 White W.D.,"Angular spectra in radar applications", IEEE Trans., AES-15, pp.895-899, 1979.

5-13 Evans J.E.,"Aperture sampling techniques for precision direction finding", IEEE Trans. AES-15, pp.891-895, 1979.

5-14 Evans J.E.,"Application of angular power distribution to radar systems with coherent or incoherent interference," IEEE Trans., AES-15, pp.899-903, 1979.

5-15 Skolnik M.I., "Introduction to radar systems", McGraw-Hill book company, second edition, 1980.

5-16 Rhodes D.R., "Introduction to monopulse," Artech house Inc, 1958.

5-17 Sinsky A.I. and Lew E.A.," Comparative analysis of a phase and amplitude processor for monopulse systems," IEEE Trans.,AP-13,pp.519-522, 1983.

5-18 Dax P.R., "Keep track of that low flying attack," Microwaves, April 1976.

5-19 Barton D.K., "Low-angle radar tracking," IEEE Proc., Vol.62, pp. 687-704, 1974.

5-20 Locke A.S.,"Guidance," D. Van Nostrand company, Inc., princeton, N.J., 1955.

6-1 Cantrell B.H., Gordon W.B., Trunk G.V.," Maximum likelihood elevation angle estimates of radar targets using subapertures", IEEE Trans., AES-17, pp.213-221, 1981.

6-2 Gordon W.B.," Improved three subaperture method for elevation angle estimation", IEEE Trans., AES-19, PP.114-122, 1983.

6-3 Taha A., Hudson J.E.,"Symmetric two-target monopulse estimator", IEE Electronic letter, 22, pp.1116-1117, 1986.

6-4 Taha A., Hudson J.E.,"Trigonometric high resolution method to resolve two close targets", IEE Proc., part F, Vol-134, pp. 597-601, Oct. 1987.

6-5 White W.D.,"Low-angle radar tracking in the presence of multipath", IEEE Trans., AES-10, pp.835-852, 1974.

6-6 Evans J.E.,"Applicability of the angular distribution to radar systems with coherent or incoherent interference", IEEE Trans., AES-15,pp.899-903, 1979.

6-7 Sinsky I.A. and Lew A.E.," Comparative analysis of a phase and an amplitude processor for amplitude monopulse systems",IEEE Trans. AP-31, pp.519-522, 1983.

6-8 Taha A., Hudson J.E.,"Effect of surface roughness on high resolution elevation angle estimation in multipath", IEE, radar conference 19-21 october 1987, London U.K.

6-9 Barton K.D., "Low-angle radar tracking", IEEE Proc., Vol-62, pp.687-704, 1974.